High Temperature Particle Deposition with Gas Turbine Applications

Peter Forsyth
St Catherine's College
University of Oxford

A thesis submitted for the degree of
Doctor of Philosophy

Trinity 2017

High Temperature Particle Deposition with Gas Turbine Applications

Peter Forsyth, St. Catherine's College, University of Oxford

A thesis submitted for the degree of Doctor of Philosophy, Trinity Term 2017

This thesis describes validated improvements in the modelling of micron-sized particle deposition within gas turbine engine secondary air systems. The initial aim of the research was to employ appropriate models of instantaneous turbulent flow behaviour to RANS CFD simulations, allowing the trajectory of solid particulates in the flow to be accurately predicted. Following critical assessment of turbophoretic models, the continuous random walk (CRW) model was chosen to predict instantaneous fluid fluctuating velocities. Particle flow, characterised by non-dimensional deposition velocity and particle relaxation time, was observed to match published experimental vertical pipe flow data. This was possible due to redefining the integration time step in terms of Kolmagorov and Lagrangian time scales, reducing the disparity between simulations and experimental data by an order of magnitude.

As no high temperature validation data for the CRW model were available, an experimental rig was developed to conduct horizontal pipe flow experiments under engine realistic conditions. Both the experimental rig, and a new particulate concentration measurement technique, based on post test aqueous solution electrical conductivity, were qualified at ambient conditions. These new experimental data compare well to published data at non-dimensional particle relaxation times below 7. Above, a tail off in the deposition rate is observed, potentially caused by a bounce or shear removal mechanism at higher particle kinetic energy. At elevated temperatures and isothermal conditions, similar behaviour is observed to the ambient data. Under engine representative thermophoretic conditions, a negative gas to wall temperature gradient is seen to increase deposition by up to 4.8 times, the reverse decreasing deposition by a factor of up to 560 relative to the isothermal data. Numerical simulations using the CRW model under-predict isothermal deposition, though capturing relative thermophoretic effects well. By applying an anisotropic Lagrangian time scale, and cross trajectory effects of the external gravitational force, good agreement was observed, the first inclusion of the effect within the CRW model.

A dynamic mesh morphing method was then developed, enabling the effect of large scale particle deposition to be included in simulations, without continual remeshing of the fluid domain. Simulation of an impingement jet array showed deposition of characteristic mounds up to 30% of the hole diameter in height. Simulation of a passage with film-cooling hole off-takes generated hole blockage of up to 40%. These cases confirmed that the use of the CRW generated deposition locations in line with scant available experimental data, but widespread airline fleet experience. Changing rates of deposition were observed with the evolution of the deposits in both cases, highlighting the importance of capturing changing passage geometry through dynamic mesh morphing. The level of deposition observed, was however, greater than expected in a real engine environment and identifies a need to further refine bounce-stick and erosion modelling to complement the improved prediction of impact location identified in this thesis.

For Grandfather

Acknowledgements

Completion of a thesis requires the support and help of many people along the way. Thanks must start with my supervisor, Prof. Matthew McGilvray, whose supervision balanced guidance and direction with the freedom to own the research, enabling me to develop as a researcher whilst enjoying the project until the end. Thanks also go to Prof. David Gillespie, with whom I have greatly enjoyed working over the last five years.

Thanks must also go to Rolls-Royce who supported the project, and those who were involved at various stages; to Vince Galoul, to Dougal Jackson, and to Miles Hawkyard. Their experience and input was always useful, and helped bring a different perspective to the research.

To those I've shared the time with at Osney, and at Catz, cheers. Life wouldn't have compared without you guys. And finally to my family, and to Caro; nothing more could have been wished for.

Contents

List of Figures

Nomenclature

Latin	
A	Area (m^2)
A_e	Thermophoretic energy constant (-)
A_{ii}	Drift correction (1/s)
A_m	Thermophoretic momentum constant (-)
C_{or}	Orifice constant (-)
C_0	Bulk aerosol concentration (kg/m^3)
C_c	Cunningham slip correction factor (-)
C_D	Drag coefficient (-)
C_e	Temperature jump coefficient (-)
C_m	Velocity slip coefficient (-)
C_m	Solution concentration by mass (kg_{NaCl}/kg_{sol}, ppm)
$C_{m,v}$	Solution concentration by mass (kg_{NaCl}/m^3_{sol})
C_v	Solution concentration by volume (m^3_{NaCl}/m^3_{sol})
c	Distribution coefficient (-)
$\bar{c}$	Mean gas molecular velocity (m/s)
D	Flow Diameter (m)
D_d	Droplet diameter (m)
d_p	Particle diameter (m)
dt	Integration time step (s)
E	Young's modulus (Pa)
F	Net force per unit mass on particle (m/s^2)
f	Friction factor (-)
f_a	Atomiser frequency (Hz)
f_d	Deposition fraction (-)
$\overline{f_d}$	Normalised deposition fraction (-)
$f_{k,\,1-4}$	Beresnev and Chernyak thermophoretic functions (-)
G	Solution conductivity (μS/cm)
g	Gravitational acceleration (m/s^2)
h	Channel half height (m)
IP	Impaction parameter (m^5/s)
J	Particle wall flux ($kg/m^2/s$)
k	Turbulent kinetic energy (m^2/s^2)
k_B	Boltzmann constant ($m^2kg/s^2/K$)
k_{diff}	Diffusion coefficient (-)
k_g	Gas thermal conductivity (W/m/K)
k_p	Particle thermal conductivity (W/m/K)
k_{sol}	Solution constant (µS/cm/ppm)
L	Length over which deposition occurs (m)
l	Particle length in bounce-stick model (m)
l_g	Gas mean free path (m)
m	Mass (kg)
$\dot{m}$	Mass flow rate (kg/s)
N_c	Total number of particles (-)
n_c	Particle count through OPS (-)
$\mathbf{n}$	Surface normal direction (m)
P	Pressure (Pa)
P^+_{Th}	Thermophoretic parameter
Q	Volume (m^3)
$\dot{Q}$	Volumetric flow rate (m^3/s)

R	Function ()
R	Specific gas constant (J/kg/K)
R_a	Arithmetic surface roughness (m)
R_{ii}	Reynolds stress (m^2/s^2)
r	Radius (m)
r_e	Boundary layer mesh ratio of expansion (-)
S_0	Brownian motion spectral density (W/Hz)
T	Temperature (K)
t	Time (s)
$\boldsymbol{\nabla} T$	Temperature gradient (K/m)
t_k	Kolmagorov time scale (s)
$\overline{U}_g$	Mean flow (gas) velocity (m/s)
U_R	Uncertainty in function R ()
$\tilde{u}$	Instantaneous gas velocity (m/s)
u^*	Friction velocity ($\sqrt{\frac{\tau_w}{\rho_f}}$) (m/s)
V	Particle velocity (m/s)
V_d	Particle deposition velocity (m/s)
V_{rel}	Relative particle-gas velocity (m/s)
$\tilde{v}$	Instantaneous particle velocity (m/s)
W	Energy, work (J)
w	Particle deformation (m)
X	Variable ()
$\mathbf{x}$	Node position (m)
y	Wall-normal distance (m)
z	Normal deposition growth height (m)

Dimensionless groups

C_f	Skin friction coefficient ($\frac{\tau_w}{\frac{1}{2}\rho_g \overline{U_g}^2}$)
Ep	Epstein number ($\frac{d_p \boldsymbol{\nabla} T_g}{T_g}$)
Ga	Galilei number ($\frac{g d_p^3}{\nu^2}$)
Kn	Knudsen number ($\frac{2l_g}{d_p}$)
Re	Reynolds number ($\frac{\rho_f \overline{U_g} D}{\mu}$)
Re_p	Particle Reynolds number ($\frac{\rho_g V_{rel} d_p}{\mu}$)
Re_τ	Friction Reynolds number ($\frac{\rho_f u^* D}{\mu}$)
Stk	Stokes number ($\frac{\tau_p}{U/D}$)
τ_p^+	Non-dimensional particle relaxation time ($Stk \cdot Re \cdot C_f$)
V_d^+	Non-dimensional deposition velocity ($\frac{V_d}{u^*}$)
y^+	Non-dimensional wall distance ($\frac{\rho_f u^* y}{\mu}$)
Λ	Thermal conductivity ratio (k_p/k_g)

Greek

α	Temperature compensation coefficient (%/ °C)
α_1	Impact angle (°)
α_2	Rebound angle (°)
α_e	Energy accommodation coefficient (-)
α_m	Momentum accommodation coefficient (-)
β	Ratio of Lagrangian to Eulerian time scales (-)
Γ	Particle to fluid velocity fluctuation scale
γ	Surface free energy (J/m^2)
δ	Node displacement (m)
δ_1	First prism layer height (m)
ϵ	Turbulent dissipation rate (m^2/s^3)
η_a	Atomiser efficiency (-)
η_c	Count efficiency (-)
η_s	Swabbing efficiency (-)
κ	Local velocity gradient (1/s)
μ	Dynamic viscosity (Pa.s)
μ_{imp}	Impulse ratio (-)
ν	Kinematic viscosity (m^2/s)
ρ	Density (kg/m^3)
σ	Root mean squares fluctuating velocity (m/s)
σ_y	Yield stress (Pa)
τ_E	Eulerian time scale (s)
τ_e	Eddy time scale (s)
τ_g	Flow characteristic time (s)
τ_L	Lagrangian time scale (s)
τ_p	Particle relaxation time (s) ($\frac{C_c \rho_p \rho_f d_p^2}{18\mu}$)

τ_w	Wall shear stress (Pa)
Φ	Thermophoretic coefficient (-)
ξ	Gaussian random number (mean: 0, variance: 1)
ω	Specific turbulence dissipation rate (1/s)

Abbreviations

ARD	Arizona road dust
CFD	Computational fluid dynamics
CoR	Coefficient of restitution
CRW	Continuous random walk
DES	Detached eddy simulation
DMM	Dynamic mesh morphing
DNS	Direct numerical simulation
DP	Dreeben and Pope
DRW	Discrete random walk
EIM	Eddy interaction model
EXPα	Experimental test piece A
EXPβ	Experimental test piece B
IH	Inline heater
JBPS	Jim Bridger power station sub-
SB	bituminous ash
KMM	Kim, Moin, and Moser
L&A	Liu and Agarwal
LES	Large eddy simulation
M	Million
MMD	Mass mean diameter
MFC	Mass flow controller
MX	Mixing chamber
OP	Orifice plate
OPS	Optical particle sizer
PRJ	Projected
PSD	Particle size distribution
ppm	Parts per million
RANS	Reynolds-averaged Navier-Stokes
SLPM	Standard litres per minute
TB	Test piece body
TI	Test insert
TP	Test piece
UDF	User defined function
UDM	User defined memory
VOAG	Vibrating orifice aerosol generator

Subscripts/Superscripts

1	Incoming/impacting
2	Outgoing/rebounding
amb	Ambient
b	Base
c	Composite
cont	Contact
crit	Critical
def	Deformed
d	Deposition
dep	Deposition (volume)
dil	Dilution
dis	Dispersion
disp	Displaced
g	Gas phase
h	Hydraulic
i	Index (*x, y, z, or u, v, w)*
i	Ideal
in	Inlet
jet	Mean jet values for impingement geometry
k	Kinetic
max	Maximum
n	Node
n	Wall-normal direction
op	Optical
or	Orifice
out	Outlet
p	Particle
py	Pyramidal
s	Surface
sol	Solution
T	Solution temperature
t	Wall-tangential direction
tet	Tetrahedral
ti	Test insert
ts	Test section
ve	Volume equivalent
w	Wall
ws	Washing solution
+	Non-dimensional form
^	Unit vector

Publications

The following four papers have been published alongside the DPhil. A technical report for Rolls-Royce was also produced.

P.R. Forsyth, D.R.H. Gillespie, and M. McGilvray. Development and applications of a coupled particle deposition dynamic mesh morphing approach for the numerical simulation of gas turbine flows. *Journal of Engineering for Gas Turbines and Power*, 140(2), 2018

P.R. Forsyth, D.R.H. Gillespie, and M. McGilvray. Experimental deposition of NaCl particles from turbulent flows at gas turbine temperatures. Paper no. 160. *ISROMAC*, 2017b. Recommended for publication in *International Journal of Turbomachinery, Propulsion and Power*

P.R. Forsyth, D.R.H. Gillespie, and M. McGilvray. Development and applications of a coupled particle deposition dynamic mesh morphing approach for the numerical simulation of gas turbine flows, GT2017-63295. *ASME Turbo Expo*, 2017a

P.R. Forsyth, D.R.H. Gillespie, and M. McGilvray. Validation and assessment of the continuous random walk model for particle deposition in gas turbine engines, GT2016-57332. *ASME Turbo Expo*, 2016

P.R. Forsyth and M. McGilvray. High Temperature Particle Deposition for Validation of Numerical Models. *Report to meet SILOET II deliverable D8.6.4.1*, 2015

Chapter 1

Introduction

> The jet engine has changed the way wars are fought, the way power is generated, and, with cheap and widely available air travel, it has changed the lives of millions... arguably it has altered everyone's perception of the world
>
> *The Jet Engine*
> Rolls-Royce

1.1 Gas turbine operation

The gas turbine engine is undoubtedly one of the most influential inventions of the twentieth century. From Whittle's first demonstration engine in 1937, through to the current generation of engines, the gas turbine's high specific thrust, net work, and overall efficiency have made it a mainstay of powered flight. Its high cycle efficiency led to its introduction into land-based electrical power generation, accounting for around 20% of world output. This study is based around the turbofan engine, but applications to other types of high temperature flows are equally valid.

The modern gas turbine turbofan engine is an extremely complex machine, operating with overall pressure ratios of 40:1, and turbine entry temperatures (TETs) up to 2 000 K. Components in the hottest regions in the main gas path are frequently manufactured from nickel-based superalloys; such TETs are significantly in excess of the melting temperature of materials employed ($\sim$ 1 600 K). Active and passive cooling techniques (Han et al., 2000) are used to reduce the thermal loading and stresses on these components, including thermal barrier coatings, and a range of methods using

air bled from the compressor as a coolant. These include air films wept onto the external (hot) surfaces, impinging jets on internal surfaces, and rib and pin-turbulated cooling passages within components. Up to 20 % of the core air mass flow rate is used to supply the secondary air system. Deposition within the secondary air system leads to reduced component coolant flow rate due to blockage, which in turn can lead to increased metal temperatures and drastically shortened component lifespans, and potential in-flight failure. A further damage mechanism for hot components is sulphidation, a high temperature corrosive attack. The major particulate damage mechanism for the fan and compressor regions is erosion of metal surfaces by impacting particles. A long term effect, particulate erosion roughens surfaces, reducing engine efficiency, and increases tip gap clearances, reducing stall margin.

1.2 Flight and operational experience

Over the last 30 years there has been an increase in interest in small particulate motion within the gas turbine industry. This has been largely driven by the threats to engine life and integrity caused by the ingestion of small particulates - sand, dust, salt, and volcanic ash. Fig. 1.1a shows a map of the world civil flight network, indicative of c.1980. It can be seen that the bulk of flying was done away from major areas of airborne particulate matter. Since, the vast expansion of civil aviation has driven a significant increase in the number of flight paths crossing through airspaces and atmospheres with potential to cause significant environmental damage to aero-engines. This is seen in the indicative modern world flight network, Fig. 1.1b. With the continuous increase of flights through more particulate-laden regions, the operational concerns regarding ingested particles only grow.

Some of the primary deposition sites within an engine are shown on Fig. 1.1c. The environmental damage mechanisms include fan and compressor blade erosion and fouling effects from sand and volcanic ash ingestion (Webley and Mastin, 2009; Casadevall, 1994) [marked 1], ice accretion on compressor stators [2], deposition on nozzle guide vanes [3] and high pressure turbine blades [4], deposition within the secondary air system [5]; blockage of film-cooling holes and deposition within cooling channels. Several encounters of civil aircraft with volcanic ash clouds, flights BA 009, 1982 (Chambers, 1985) and KLM 867, 1989 (Casadevall, 1994), have led to the aircraft involved experiencing stall and flame out of all four engines. During the enforced gliding descent, enough ash was removed from the nozzle guide vanes to allow engine restart, and both flights landed under limited power. Repair of the KLM

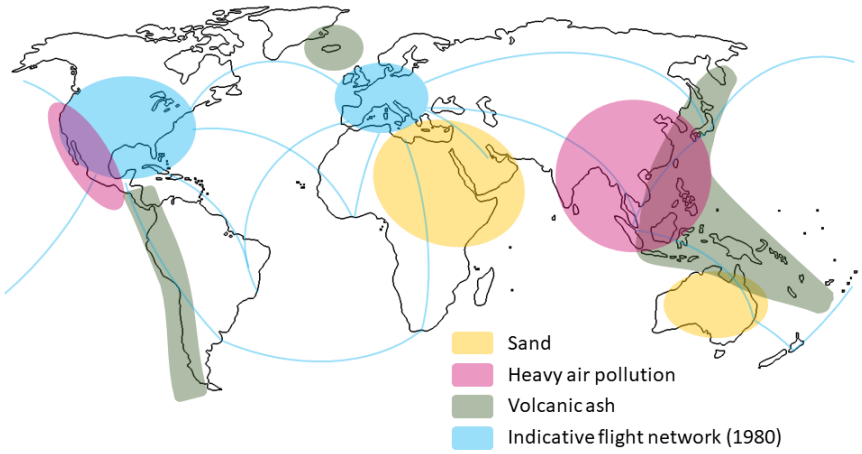

(a) Indicative world flight network and areas of high airborne particulate concentration (c.1980)

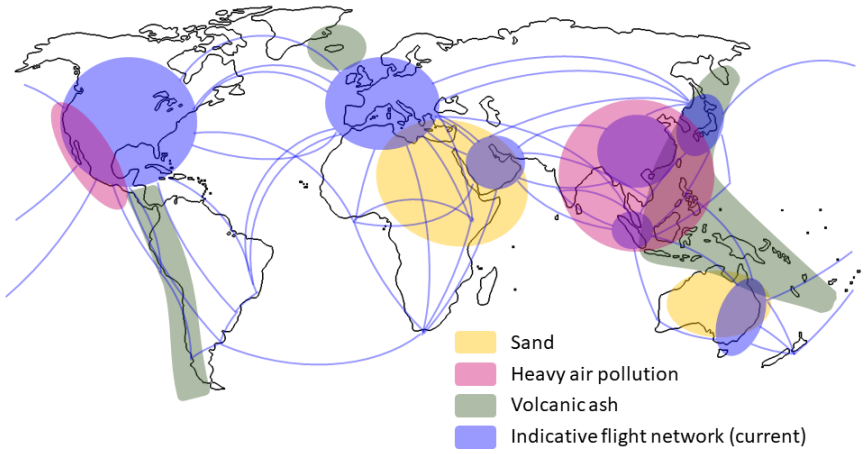

(b) Indicative world flight network and areas of high airborne particulate concentration (modern)

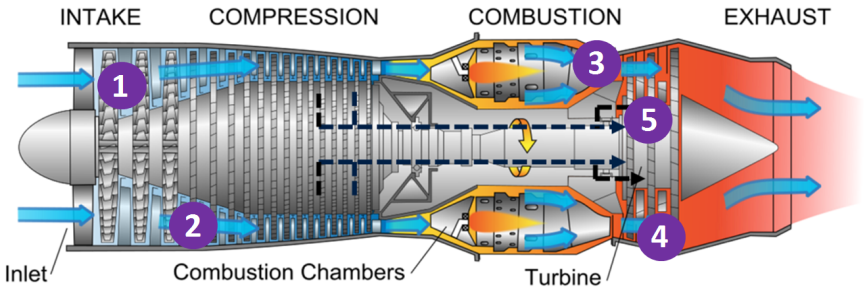

(c) Deposition locations of particulate matter within a gas turbine (turbojet). Dashed lines show secondary air system. 1. Fouling and erosion of compressor, 2. Ice accretion on stators, 3. Deposition on nozzle guide vanes, 4. Deposition on high pressure turbine blades, 5. Deposition within secondary air system. Background image: Jeff Dahl, FAA Handbook.

Figure 1.1: Airborne particulates and regions of deposition within gas turbine engines

aircraft and replacement of all four engines was estimated to have cost $80 million. Operation of helicopters during the first Gulf War (Cardwell et al., 2010) saw massive sand ingestion, which rendered engines inoperable after only a handful of missions. These incidents in particular were a catalyst for wider research into small particulate ingestion within the field of gas turbine technology.

1.3 Aerosol science

The bulk of the study of the characteristics of micron-sized particulate motion, dispersion, and deposition has been undertaken within the field of aerosol science, dating from the 1950s. Initially an experimental and theoretical field, numerical simulations now tend to dominate published output. The most widely referenced experimental data remain the early vertical pipe flow experiments (Friedlander and Johnstone, 1957; Sehmel, 1968; Liu and Agarwal, 1974), shown in Fig. 1.2. V_d^+ can be considered volumetric deposition rate per unit area, non-dimensionalised. τ_p^+ can be considered a particle characteristic time, non-dimensionalised. This is discussed in detain in section 2.1. Whilst there are a large number of experimental data in the open literature, there are very few at the high temperature conditions relevant to gas turbine secondary air systems (up to 900K), and for appropriate particle sizes and materials.

1.4 Motivation

The initial motivation for this study originates with sulphidation corrosion seen in the turbine section of a three-shaft civil gas turbine engine from the 2000s ('Engine A' in all following discussion). Significant corrosive damage has been seen in the shank pocket region of Engine A blades, Fig. 1.3. The shank pocket is a small region within the secondary air system, located between each pair of blades, below the blade platform and above the disc. Secondary air is pumped into the rotor cavity and up the disc. This provides air to form the main gas path seal to stop ingestion of hot gas under the blade platform, as well as coolant for the internal cooling passages within the turbine blades. The front of the shank pocket is open to the rotor cavity, with the back being sealed by the lockplate. Slight leakage out around the lockplate gives a net mass flow rate through the shank pocket from front to back.

Sulphidation is a high temperature corrosive reaction, where sodium (from evaporated sea salt, for example) mixes with airborne sulphur (jet fuel, industrial envi-

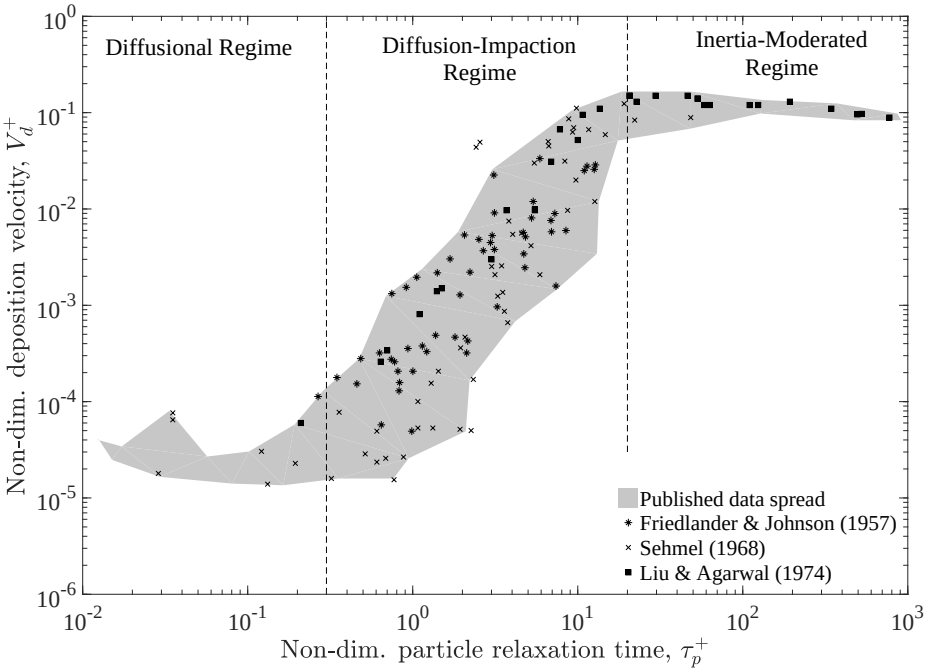

Figure 1.2: Summary of some key experimental data for particle deposition in vertical turbulent pipe at ambient conditions. Adapted from Young and Leeming (1997).

ronments), forming sodium sulphate, Na_2SO_4 (Lai, 2007). Two forms of sulphidation are noted, types I and II. The following discussion is a summary of Mason-Flucke (2011). Type I sulphidation occurs at temperatures 800-950 °C, above the melting point of Na_2SO_4. In this case the liquid salt dissolves the blade protective coatings, allowing sulphur to diffuse into the metal. Type II sulphidation occurs at lower temperatures (600-750 °C), where sodium chloride, NaCl, can combine with Na_2SO_4 to reduce the melting point of the mixture. The mixture penetrates the protective oxide layers of the blade metal. The blade metal substrate is nickel alloy with elements including tantalum, aluminium, tungsten, chromium, cobalt, molybdenum, and titanium. Where the NaCl-Na_2SO_4 mixture becomes liquid, the least stable of these alloying elements are able pass from the substrate to the surface of the liquid, where they oxidise. Unlike the original oxides, these new oxide layers are not protective to the blade metal. Temperature profiles for flight conditions indicate that Type II sulphidation would be prevalent in the region where cracking is seen (Fig. 1.3).

In comparison to an earlier engine of similar geometry, 'Engine B', Engine A has seen sulphidation attack after one tenth the flying hours in comparison to Engine B. Operating conditions (gas and metal temperatures, pressures) for Engine A are very similar to those in Engine B, however Engine B did not experience sulphidation corrosion to any significant extent. It was proposed internally that the sodium chloride

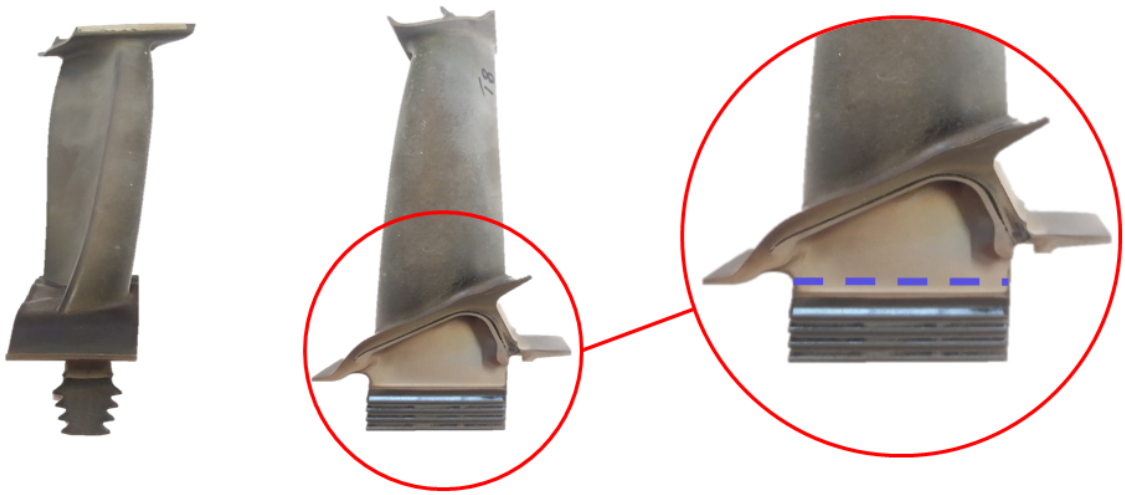

Figure 1.3: Engine A blade. *Left*: front view. *Middle*: suction surface surface. *Right*: close-up of shank pocket. Location of cracking is shown by dashed blue line. Front of cavity is on left of image, slot for lockplate can be seen on right hand side.

was transported to the shank pocket through the secondary air system, with the particles being small enough to remain suspended in the gas, and depositing within the shank pocket.

Initial simulations of rotor cavity geometries of both Engines A and B were carried out by Dougal Jackson (Rolls-Royce), using two discrete random walk models for the simulation of turbulent dispersion of particles - one available within ANSYS Fluent ('DRW'), and the other as an unvalidated user defined function ('Dehbi DRW', Dehbi (2008b)), a 'plug-in' for the ANSYS Fluent CFD software. Both models were unable to reproduce ambient experimental pipe flow data (see section 3.2.4). This led to the conclusion that higher-fidelity modelling was required, and would need validation at high temperatures.

As noted above, and seen in Fig. 1.1, a range of other particulates, namely sand, ash, and dust, also cause issues within gas turbine engines. These particulates behave in aerodynamic manner as those that catalyse sulphidation, but are generally larger, and at high enough concentrations to build-up substantial deposit features. The modelling of these particulates therefore should also consider temporal build up. Thick deposition on nozzle guide vanes is shown in Fig. 1.4a from the BA009 incident, where the throat area was calculated to be reduced by 10%. Thick deposition (5-8mm) was seen in the Calspan full engine tests, Figure 43 of Dunn (1990).

Blockage of film-cooling holes representative of a HPT blade leading edge has been seen in experiments (Fig. 1.5a) and full engine tests. The eruption of the Eyjafjallajökull volcano, 'Eyja', in Iceland, 2010, closed European airspace for six days,

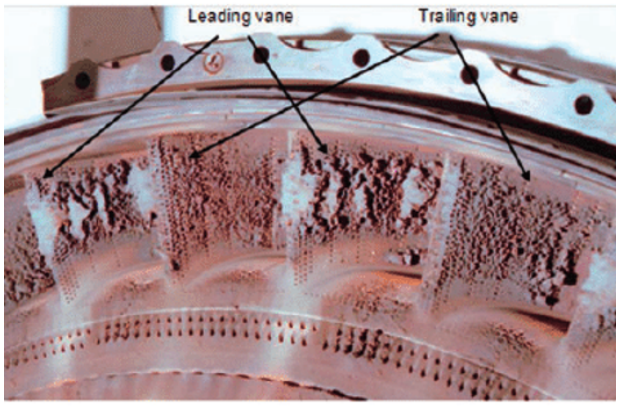

(a)

Figure 1.4: Ash deposition on nozzle guides vanes, flight BA009 (Clarkson et al., 2016)

caused the cancellation of around 95 000 flights, at an estimated economic cost to the airline industry alone of around £1bn. During, and following, the airspace closure there were substantial discussions regarding the maximum airborne ash concentration in which aircraft could be safely operated. A 'safe to fly' chart was produced by Rolls-Royce, attempting to put known incidents, experiments, and operating conditions into context on the chart. Following re-evaluation of the known events, this was reassessed, and an updated 'safe to fly' chart produced, Fig. 1.5b (Clarkson et al., 2016).

A fundamental problem for attempting to apply such methods and calculations is the lack of modern full engine data. The Calspan full engine tests used engines contemporary to c.1990; turbine entry temperatures have risen around 300 °C since (Clarkson et al., 2016). Inertial deposition has been shown to be well correlated to gas and surface temperatures above a particulate material-dependent temperature threshold by a number of experimentalists, meaning the older, lower temperature tests/encounters have reduced applicability to modern engines. This is problematic for engine manufacturers, as engine architecture has also changed significantly. Certification of gas turbine engines by the EASA and FAA has become more stringent with regards to particulate ingestion, requiring more consideration of particulate matters during the design process.

Whilst the above studies have shown that deposition can become large relative to component size, this is a facet that has previously been barely considered by numerical simulations carried out within the field. With only a couple of exceptions, numerical simulations have always considered deposition on a clean geometry, with deposition

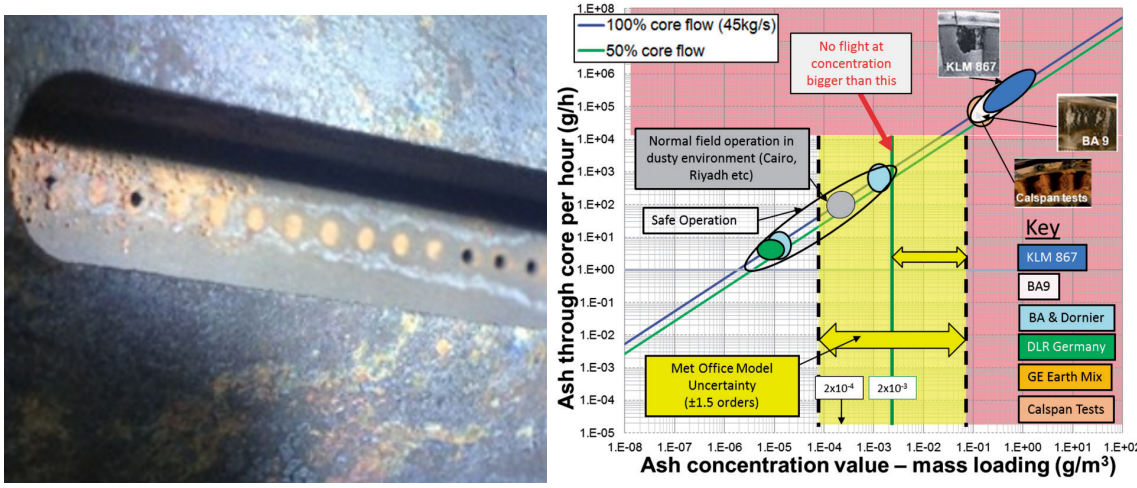

(a) (b)

Figure 1.5: *Left*: Ash blockage of experimental film-cooling holes (Wylie et al., 2017). Hole diameter: 0.6 mm. *Right*: Updated Rolls-Royce 'Safe to fly' chart (Clarkson et al., 2016).

trends assumed independent of time. This is unable to capture the transient nature of deposition within engine components - blockage of film-cooling holes, for example, would lead to decreasing coolant flow rate for a constant pressure margin. This would cause component temperatures to rise, potentially increasing the likelihood of particles depositing on impact.

1.5 Scope and outline

The scope of the thesis comprised three major aims. The first was to assess the models for turbulent dispersion of particulates available within commercial software and also the academic sphere. This led to conclusions that the continuous random walk model ('CRW', Dehbi (2008a)) provided significantly better predictions of deposition than other available, industry-friendly models. More detailed assessment and development of this model was carried out.

Validation of such a numerical model requires appropriate high temperature experimental data. Hence the second aim of the thesis was to design, build, and run an experimental rig to produce these data. A horizontal pipe flow configuration was used. The temperatures were chosen by Rolls-Royce to be representative of two flight conditions. A sodium chloride aerosol was chosen as a representative material of that found in gas turbines.

The third aim was to extend the numerical modelling to account for the effects of large-scale deposition on both the flow and particle impacts. This was done by integrating the deposition history, and updating the mesh to take account of this. To address question of whether a particle deposits or rebounds upon impact, a stick-bounce model from the open literature was applied.

The thesis is structured as follows:

Chapter two provides an overview of particle motion within, and deposition from, turbulent flows. A review of the open literature is presented, taking in both the gas turbine and aerosol science fields, and focusing on high temperature flows.

Chapter three concerns small particulate numerical modelling in further detail. The discrete and continuous random walk model for the turbulent motion of suspended particulates are discussed in detail. Further development of the CRW model is carried out. A dynamic mesh morphing technique to update the geometry of a numerical domain based on the deposition history is then developed. A model for wall-particle interaction at impact is implemented from the literature, and further assessed.

Chapter four presents the design, build, and results of an experimental test campaign for high temperature particle deposition. Experiments were carried out at ambient and high temperatures.

Chapter five presents the numerical modelling of the pipe flow experiments using the numerical techniques discussed in chapter three. Where the simulation does not reproduce experimental trends, investigations are carried out to reduce the disparity.

Chapter six applies the above numerical techniques to three engine-relevant test cases: a rotor-stator cavity and lower blade geometry, an impingement jet geometry, and a film-cooling geometry.

Chapter seven concludes the thesis, closing with a discussion of the directions which further research could take.

Chapter 2

Background and Literature Review

This chapter initially presents important background concepts related to the study. The open literature is then discussed and assessed. Published works of particular relevance and importance to this study are highlighted.

The characters $\tilde{u_i}$ and $\tilde{v_i}$ are used to indicate gas and particle velocities respectively. The velocities are split into time-averaged mean components, U_i and V_i, and instantaneous fluctuating components, u_i and v_i, following Reynolds decomposition.

$$\tilde{u_i} = U_i + u_i \tag{2.1}$$

$$\tilde{v_i} = V_i + v_i \tag{2.2}$$

2.1 Parameters and flow regimes

We begin from the expression for Stokes drag on a sphere of diameter d_p,

$$F_D = 3\pi\mu_g d_p V_{rel}, \tag{2.3}$$

where μ_g is the gas dynamic viscosity, and V_{rel} is the relative particle velocity,

$$V_{rel} = \tilde{u} - \tilde{v}. \tag{2.4}$$

Using particle mass,

$$m_p = \frac{1}{6}\pi d_p^3 \tag{2.5}$$

the acceleration of the particle due to Stokes drag is found,

$$a_D = \frac{18\mu_g}{\rho_p d_p^2} V_{rel}. \tag{2.6}$$

The particle relaxation time, τ_p, is defined as the ratio of relative velocity to particle acceleration,

$$\tau_p = \frac{|V_{rel}|}{a_D} = \frac{C_c \rho_p d_p^2}{18\mu_g}. \tag{2.7}$$

where C_c is the Cunningham slip correction factor,

$$C_c = 1 + \frac{2l_g}{d_p}\left(1.26 + 0.40e^{\frac{-0.55d_p}{l_g}}\right), \tag{2.8}$$

which is added to correct for slip effects for small particles.

The bulk gas characteristic time, τ_g, is the ratio of characteristic dimension l to characteristic velocity U,

$$\tau_g = \frac{l}{U}, \tag{2.9}$$

In the case of pipe flow, which will be widely discussed in this thesis, the characteristic dimension is the pipe hydraulic diameter D_h,

$$D_h = \frac{4A_{xc}}{P}, \tag{2.10}$$

where A_{xc} is the cross-sectional area of the flow, and P the wetted perimeter. The characteristic velocity is taken as the bulk mean velocity $\overline{U}_g$. The common expression for τ_g then follows:

$$\tau_g = \frac{D_h}{\overline{U}_g}. \tag{2.11}$$

The ratio of the particle to bulk fluid characteristic times, is the Stokes number,

$$Stk = \frac{\tau_p}{\tau_g} = \frac{\rho_p d_p^2}{18\mu_g}\frac{\overline{U}_g}{D_h}. \tag{2.12}$$

The Stokes number is widely used to describe particle response to a given flow condition. Stokes numbers less than one indicate that particle motion will be influenced by, and follow, fluid streamlines. Stokes numbers greater than one indicate that a particle is likely to have a ballistic trajectory and will be unable to follow changing fluid streamlines.

The friction velocity, u^*, is defined by,

$$u^* = \sqrt{\frac{\tau_w}{\rho_g}}, \tag{2.13}$$

where τ_w is the wall shear stress and ρ_g the gas density. Wall shear stress can be calculated from the Fanning friction factor f,

$$f = \frac{\tau_w}{\frac{1}{2}\rho_g \overline{U}_g^2}. \tag{2.14}$$

The Blasius expression for turbulent pipe flow is then used to relate friction factor to bulk Reynolds number,

$$f = \frac{0.0791}{Re^{0.25}}, \tag{2.15}$$

where Reynolds number in terms of a characteristic flow velocity and diameter as above,

$$Re = \frac{\rho_g \overline{U}_g D_h}{\mu} = \frac{4\dot{m}_g}{\pi \mu_g D_h}. \tag{2.16}$$

The second expression shows Re rearranged in terms of gas mass flow rate $\dot{m}$, which is a convenient form for use with experimentally-measured terms.

Wall shear stress can also be calculated from the pressure gradient,

$$\tau_w = \frac{D_h}{4}\frac{dP}{dz}, \tag{2.17}$$

where dP/dz is the axial pressure gradient over the region of interest. This derivation comes from considering the balance of wall shear stress and pressure over a control volume.

A near-wall flow characteristic time, $\tau_{g,w}$, can be defined,

$$\tau_{g,w} = \frac{\mu_g}{\rho_g \left(u^*\right)^2} = \frac{\nu_g}{\left(u^*\right)^2}. \tag{2.18}$$

where ν_g is the gas kinematic viscosity. The ratio of particle relaxation time to near-wall flow characteristic time gives non-dimensional particle relaxation time, τ_p^+,

$$\tau_p^+ = \frac{C_c \rho_g \rho_p d_p^2 (u^*)^2}{18\mu^2}. \tag{2.19}$$

The coefficient of skin friction is defined

$$C_f = \frac{\tau_w}{\frac{1}{2}\rho_g \overline{U}_g^2}, \tag{2.20}$$

being the ratio of wall shear stress to dynamic pressure. τ_p^+ can be rearranged in terms of non-dimensional groups Stk, Re, C_f,

$$\tau_p^+ = Stk \cdot Re \cdot C_f. \tag{2.21}$$

Expressed in more physical terms,

$$\tau_p^+ = \frac{\text{characteristic particle time}}{\text{characteristic flow time}} \cdot \frac{\text{gas inertial force}}{\text{gas viscous force}} \cdot \frac{\text{wall viscous force}}{\text{gas inertial force}}, \tag{2.22}$$

$$\tau_p^+ = \frac{\text{characteristic particle time}}{\text{characteristic flow time}} \cdot \frac{\text{wall viscous force}}{\text{gas viscous force}}. \tag{2.23}$$

It can be seen that the non-dimensional particle relaxation time is the Stokes number scaled by the ratio of wall to bulk viscous forces. Non-dimensional particle relaxation time gives an indication of a particle's response to changing flow conditions. Very low τ_p^+ ($\tau_p^+ \ll 1$) values indicate particles are responsive to the flow conditions, and are able to follow fluid streamlines. For $\tau_p^+ \sim 1$, particles are still able to follow fluid streamlines (to a lesser extent), but motion is significantly effected by turbulent eddies, which are able to 'kick' particles around, causing stochastic motion. As τ_p^+ increases ($\tau_p^+ \gg 1$), particles behave in a ballistic manner, similarly to large Stokes numbers, where the particle response to turbulent eddies decreases, and particles gain significant momentum from only the largest eddies. In wall-bounded flow, τ_p^+

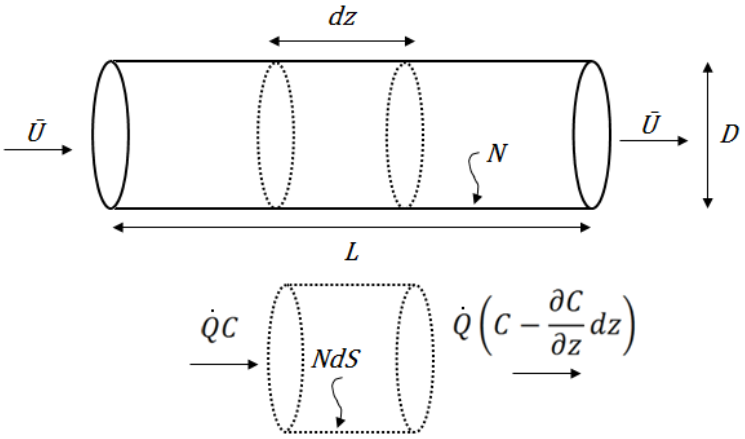

Figure 2.1: Control volume for derivation of deposition velocity

is a more appropriate parameter for characterising particle behaviour that Stk, as it accounts for viscous effects in the wall region in a manner the Stokes number does not.

Particle deposition flux J is the mass flow rate of particulate matter, $\dot{m}_{dep}$, to a surface of area A_s,

$$J = \frac{\dot{m}_d}{A_s}. \tag{2.24}$$

The mean bulk flow concentration of particulate matter over the area which deposition is occurring, C_0, is the ratio of mass of particulate in the bulk flow, m_0 to the flow volumetric flow rate,

$$C_0 = \frac{m_0}{\dot{Q}_g}. \tag{2.25}$$

The particle deposition velocity V_d is the ratio of deposition flux to mean bulk concentration,

$$V_d = \frac{J}{C_0}, \tag{2.26}$$

which describes the deposition rate of particles from a flow.

The deposition velocity, V_d, can also derived specifically for a pipe flow condition using a control volume analysis. Consider the length of pipe shown in Fig. 2.1, where $\dot{Q}_g$ is gas volume flow rate,

$$\dot{Q}_g = \pi \frac{D_h^2}{4} \overline{U}_g, \tag{2.27}$$

and C is concentration at a given axial position z, and N is particle deposition flux (N and C must in the same terms, either mass or number). An area-averaged mean axial velocity, $\overline{U}_g$, is used,

$$\overline{U}_g = \frac{\int_0^{D_h/2} urdr}{\int_0^{D_h/2} rdr}, \tag{2.28}$$

and an area-averaged concentration or count, C, which varies in the axial direction,

$$C = \frac{\int_0^{D_h/2} crdr}{\int_0^{D_h/2} rdr}. \tag{2.29}$$

Applying a control volume to an axial length dz, it is seen that

$$\dot{Q}_g C = \dot{Q}_g \left(C - \frac{\partial C}{\partial z} dz \right) + N dS \Rightarrow -\dot{Q}_g \frac{\partial C}{\partial z} dz = N dS, \tag{2.30}$$

where the increment of surface area is given by

$$dS = \pi D_h dz. \tag{2.31}$$

From the definitions of $\dot{Q}_g$, dS, and noting that as we are using area-averaged $\overline{U}_g$ and C, the partial derivatives become full derivatives in the axial direction, we have

$$-\frac{\pi D_h^2}{4} \overline{U}_g \frac{dC}{dz} dz = -N \pi D_h dz \Rightarrow -\frac{D_h}{4} \overline{U}_g \frac{dC}{dz} = -N. \tag{2.32}$$

Thomson (1987) defines particle deposition flux N as the product of C and V_d, the deposition velocity,

$$N = V_d C. \tag{2.33}$$

Substituting this into Eq. 2.32 gives

$$-\frac{D_h}{4}\overline{U}_g\frac{dC}{dz} = -V_d C. \tag{2.34}$$

Integrating from inlet to outlet axial positions and concentrations, an expression for V_d can be found,

$$-\frac{D_h}{4}\overline{U}_g\int_{C_{in}}^{C_{out}}\frac{dC}{C} = -V_d\int_0^L dz \Rightarrow -\frac{D_h}{4}\overline{U}_g ln\left(\frac{C_{out}}{C_{in}}\right) = V_d L, \tag{2.35}$$

therefore

$$V_d = \frac{1}{4}\frac{D_h\overline{U}_g}{L}\ln\left(\frac{C_{in}}{C_{out}}\right). \tag{2.36}$$

The deposition fraction, f_d, is the ratio of deposited mass, m_d, to the inlet mass, m_{in},

$$f_d = \frac{m_d}{m_{in}} = \frac{m_d}{m_d + m_{in}} = \frac{C_{in} - C_{out}}{C_{in}} = \frac{C_d}{C_d + C_{out}}, \tag{2.37}$$

where the second expression assumes a uniform particle density, ρ_p. Rearranging for C_{out} and substituting into Eq. 2.36,

$$V_d = \frac{1}{4}\frac{D_h\overline{U}_g}{L}\ln\left(\frac{1}{1-f_d}\right), \tag{2.38}$$

which is a form more convenient for experimental measurements. The appearance of the ln() term in Eq. 2.36 in comparison to Eq. 2.26 is due to the latter assuming a constant mean concentration across the whole area of deposition, whereas Eq. 2.38 accounts for variable C over the deposition length L.

V_d can be non-dimensionalised by the shear velocity to give non-dimensional particle deposition velocity,

$$V_d^+ = \frac{J}{C_0 u^*} = \frac{1}{4}\frac{D_h}{L}\frac{\overline{U}_g}{u^*}\ln\left(\frac{1}{1-f_d}\right). \tag{2.39}$$

In the absence of significant body forces except those due to relative gas motion, particle motion can be divided into three regimes, Fig. 2.2. This shows some of the most widely referenced experimental data including Friedlander and Johnstone

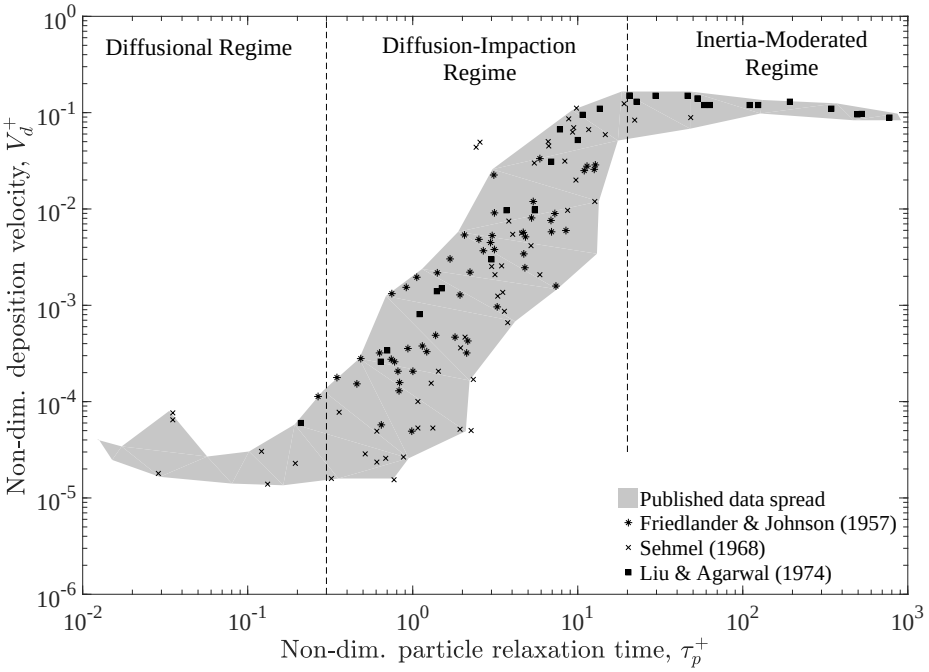

Figure 2.2: Summary of some key experimental data for particle deposition in vertical turbulent pipe at ambient conditions. Adapted from Young and Leeming (1997).

(1957), Sehmel (1968), and Liu and Agarwal (1974). These experiments were all carried out in turbulent vertical pipe flow for particle diameters 0.1-100 µm at Reynolds numbers of $4\,000 - 50\,000$, over a range of particle types, and at ambient temperatures and pressures.

Three distinct regimes of deposition can be seen. In the *diffusional* regime ($\tau_p^+ \leq 0.3$), Brownian diffusion of particles dominates deposition characteristics. Particles are small enough to have their motion affected by the momentum of impacting gas molecules. Very little dependence on particle inertia (τ_p^+) is seen. As τ_p^+ increases, particles enter the *diffusion-impaction* regime, ($0.3 < \tau_p^+ < 20$), where particles have enough inertia to be affected by turbulent eddies, which can give the particles sufficient wall-normal velocity to transit through the boundary layer, and deposit onto boundary surfaces. A strong dependence on τ_p^+ is seen, with $V_d^+ \propto \left(\tau_p^+\right)^2$ (Liu and Agarwal, 1974). A wide spread of data is seen, up to three orders of magnitude for $\tau_p^+ = 2$. The particles with the highest inertia are found in the *inertia-moderated* regime ($\tau_p^+ \geq 20$), where particle response to turbulence fluctuations decreases as particle inertia becomes to large too be affected by all but the largest eddies.

Based on expected particle sizes (0.5-10 µm) and standard secondary air systems conditions (T_g, ρ_g, u^*), τ_p^+ values are expected to lie within the *diffusion-impaction* and *inertia-moderated* regimes. This thesis focuses on particle motion in the *diffusion-*

impaction regime and the hugely significant effect that turbulence can have on deposition characteristics.

The vast majority of fundamental research into the motion of micron-sized particulates has been carried out in the field of aerosol science. Here simple flows, frequently pipe and channel geometries, and bends, have been analysed theoretically, and assessed experimentally and numerically. Flow conditions (T_g, P_g) are close to ambient, with both laminar and turbulent flows considered. Due to the highly turbulent nature of gas turbine flows, particle motion in laminar flows is not considered further here.

The definitions below are pertinent to the following discussions related to turbulence.

Isotropic: turbulence with fluctuations invariant with direction. Anisotropic turbulent fluctuations are unequal in space. For example bulk flow far from domain surfaces in pipes or channels is usually considered isotropic.

Homogeneous: turbulence which is invariant with position. In inhomogeneous turbulence, turbulent statistics vary with position. Bulk flows can often be considered homogeneous; boundary layer regions are inhomogeneous.

2.2 Particle motion theory

At gas turbine conditions the following forces are initially considered: drag, turbophoresis, thermophoresis, gravity, lift, and Brownian motion. Net particle acceleration is thus

$$\frac{d^2x}{dt^2} = a_D + a_{Tu} + a_{Th} + a_G + a_L + a_B, \tag{2.40}$$

where a_D is the acceleration due to drag, a_{Tu} that due to turbophoresis, a_{Th} due to thermophoresis, a_g due to gravity, a_L due to Saffman lift, a_B and due to Brownian motion. The individual accelerations are now discussed in detail.

2.2.1 Drag

Aerodynamic drag on a particle is the dominant force experienced in the flows of interest to this investigation. The general drag equation,

$$F_D = \frac{1}{2}\rho_g V_{rel}^2 C_D A_{pr}, \tag{2.41}$$

where V_{rel} is the relative relocity of the object, and A_{pr} the projected area of the moving object in the direction of motion. Drag coefficient C_D is specific to object's geometry. We limit ourselves here to spherical particulates. Equating this with Stokes drag (Eq. 2.3),

$$F_D = m_p a^D = \frac{1}{2}\rho_g V_{rel}^2 C_D A_{pr} = 3\pi\mu_g d_p V_{rel}, \tag{2.42}$$

where projected area $A_{pr} = \frac{\pi}{4}d_p^2$. With this substitution and rearranging for C_D gives an expression for the drag coefficient in Stokes flow:

$$C_D = 24\frac{\mu_g}{\rho_g V_{rel} d_p} = \frac{24}{Re_p}, \tag{2.43}$$

where particle Reynolds number is defined:

$$Re_p = \frac{\rho_p V_{rel} d_p}{\mu_g}. \tag{2.44}$$

Returning to Eq. 2.41, and substituting Eq. 2.5,

$$a_D = \frac{1}{2}\rho_g V_{rel}^2 C_D A \left(\frac{6}{\pi\rho_p d_p^3}\right) = \frac{6}{8} V_{rel} C_D \left(\rho_g V_{rel}\right)\left(\frac{1}{\rho_p d_p}\right). \tag{2.45}$$

Multiplying top and bottom by $\frac{d_p}{18\mu_g}$, and collecting terms, gives the familiar expression for particle drag,

$$a_D = \frac{1}{\tau_p}\frac{C_D Re_p}{24} V_{rel}. \tag{2.46}$$

In the case of Stokes flow, the expression reduces to Eq. 2.6. For larger Re_p, a different expression (Schiller and Naumann, 1935) for C_D is used:

$$C_D = \frac{24}{Re_p}\left(1 + 0.15 Re_p^{0.687}\right), \tag{2.47}$$

for $1 \leq Re_p < 400$. Whilst the drag coefficients discussed here are of a spherical formulation, a number of other formulations exist including non-spherical and Stokes-Cunningham.

2.2.2 Turbophoresis

Turbophoresis is a force experienced by particles due to fluctuating velocity gradients within the flow (Young and Leeming, 1997). This process is also often referred to as 'turbulent diffusion.' As particles gain more momentum from the regions of higher velocity fluctuations, particles move to regions of lower fluctuating velocity. Of particular importance for deposition are the wall-normal fluctuations, which can divert particles from following fluid streamlines though the boundary layer to walls.

For a particle with fluctuating velocity v_i in the i-th direction, Caporaloni et al. (1975) give the power dissipated against the viscous drag force (Eq. 2.3) as

$$P_{visc,\,i} = F_{D,\,i} v_i = 3\pi\mu_g \overline{v_i v_i}. \tag{2.48}$$

The energy dissipated by the motion is the product of viscous power and particle relaxation time,

$$E_{visc,\,i} = P_{visc,\,i}\tau_p = 3\pi\mu_g \overline{v_i v_i}\tau_p. \tag{2.49}$$

The force on the particle is the derivative of the change in energy, and is known as the turbophoretic force, $F_{Tu,\,i}$,

$$F_{Tu,\,i} = m_p a_{Tu,\,i} = -\frac{dE_{visc,\,i}}{dx_i} = -3\pi\mu_g\tau_p \frac{d\overline{v_i v_i}}{dx_i}. \tag{2.50}$$

Substituting for m_p and τ_p, and rearranging for $a_{Tu,\,i}$ gives the turbophoretic acceleration of the particle:

$$a_{Tu,\,i} = -\frac{d\left(\overline{v_i v_i}\right)}{dx_i}. \tag{2.51}$$

The turbophoretic force can be seen to move particles down the gradient of turbulence intensity to areas of low turbulence intensity. Modelling the particle Reynolds stress term, $\overline{v_i v_i}$ is difficult as it must be related to the equivalent fluid term, $\overline{u_i u_i}$. Young and Leeming (1997) suggest the following relation

$$-\frac{d\left(\overline{v_i v_i}\right)}{dx_i} = -\frac{d\left(\Gamma\overline{u_i u_i}\right)}{dx_i}, \tag{2.52}$$

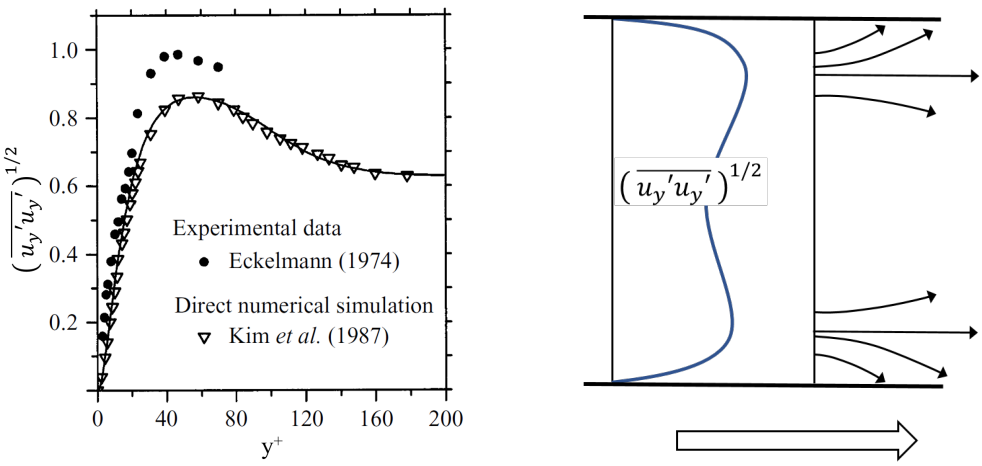

(a) (b)

Figure 2.3: Turbophoretic effects. *Left*: Indicative RMS fluid wall-normal velocity fluctuations. From Young and Leeming (1997). *Right*: Nominal particle tracks resulting from fluid wall-normal fluctuating velocity profile. Adapted from Young and Leeming (1997).

and took an expression for Γ from Reeks (1977), based on particle relaxation time and and eddy lifetime, τ_e,

$$\Gamma = \frac{\tau_e}{\tau_e + \tau_p}, \tag{2.53}$$

where τ_e is calculated from the turbulent kinematic viscosity, ν_t,

$$\nu_t = \overline{u_i u_i}\tau_e. \tag{2.54}$$

In the case of pipe flow, the most important fluctuating velocities are in the wall normal direction. The root mean square wall-normal fluctuating velocity profile against non-dimensional wall distance y^+,

$$y^+ = \frac{u^* y}{\nu} = \frac{\rho_g u^* y}{\mu}, \tag{2.55}$$

is shown in Fig. 2.3a, with the same profile and effect on particle motion sketched in Fig. 2.3b. Here the effect of the particles gaining wall-normal momentum in the near-wall region can be seen driving motion towards the walls. The effect in the bulk region is less strong due to smaller gradients within the flow.

Turbophoresis/turbulent diffusion is the primary reason for the increase of V_d^+ in the diffusion-impaction regime. Particles are large enough to gather sufficient wall-normal momentum from turbulent eddies to deviate from the fluid streamlines, but not large enough to follow ballistic trajectories.

Because of the difficulties in relating $\overline{v_i v_i}$ to $\overline{u_i u_i}$, as discussed above, capturing turbophoretic effects numerically (in a steady solution) is usually done by attempting to model the gas fluctuating velocities. This is then added to the mean flow velocity U to give instantaneous gas velocity $\tilde{u}$. Such models are discussed in detail in section 2.4.3.

2.2.3 Thermophoresis

Thermophoresis is a force due to momentum exchange from gas molecules impacting a particle. It is experienced by the particle in the negative direction of temperature gradient, and proportional to the gradient's magnitude, Fig. 2.4a. In the case of hot gas and cool wall, an increase in particle deposition rate is seen ('increasing' thermophoresis). In the reverse case with cool gas and hot wall, the rate of particle deposition is decreased ('decreasing' thermophoresis).

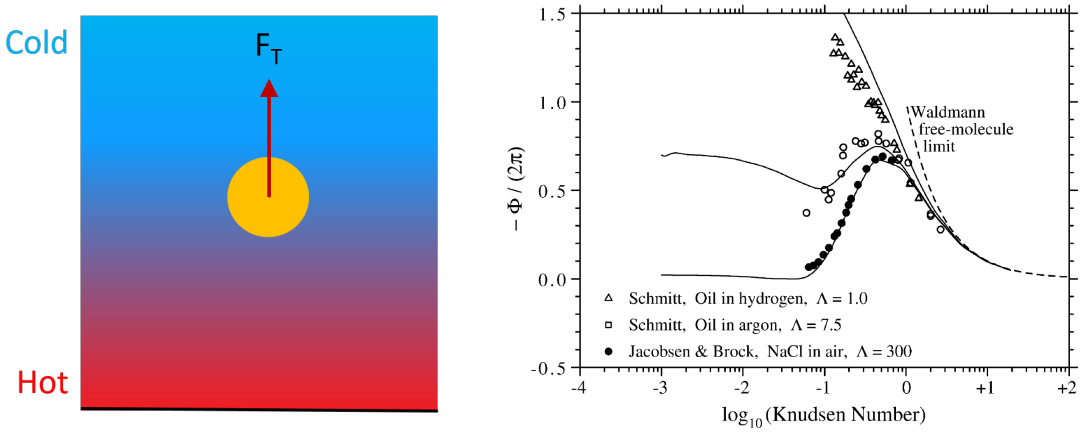

(a) Thermophoretic effect.

(b) Φ vs. Kn for varying Λ

Figure 2.4: *Left*: Thermophoretic effect; particle force down the temperature gradient. *Right*: Variation of thermophoretic coefficient with Kn and Λ. From Healy and Young (2010).

The thermophoretic force experienced by a particle is given by

$$a_{Th} = \Phi \frac{\mu_g^2 d_p}{2\rho_g m_p} \frac{\boldsymbol{\nabla} T_g}{T_g}, \tag{2.56}$$

where $\boldsymbol{\nabla} T_g$ is the gas temperature gradient, and Φ the thermophoretic coefficient. The thermophoretic coefficient is a function of thermal conductivity ratio, Λ, and Knudsen number, Kn. The thermal conductivity ratio is given by

$$\Lambda = \frac{k_p}{k_g}, \tag{2.57}$$

where k_p is the particle thermal conductivity, and k_g the translational component only of thermal conductivity,

$$k_g = \frac{15}{4}\mu_g R, \tag{2.58}$$

and R the specific gas constant (air: 287 J/kg/K). The Knudsen number is the ratio of molecular mean free path length l_g to particle radius r_p,

$$Kn = \frac{l_g}{r_p} = \frac{2l_g}{d_p}. \tag{2.59}$$

Various expressions for molecular mean free path length l_g exist; the following is used in this study from Healy and Young (2010),

$$l_g = \mu_g \sqrt{\frac{\pi}{2P_g\rho_g}}. \tag{2.60}$$

Four regimes of Knudsen number are usually identified. Low Kn (< 0.001) conditions are referred to as the 'continuum' regime. This describes 'normal' fluid dynamics. The 'slip flow' regime is defined as $0.001 < Kn < 0.1$, where the particle is approaching the gas mean free path length, with the 'transition' regime, $0.1 < Kn < 10$, above. The high Kn ($\gg 10$) conditions are referred to as the free molecular regime.

Early expressions for the thermophoretic coefficient were valid only for a particular Kn regime. Epstein (1929) was the first to address thermophoresis in this manner, producing an expression for Φ valid in the limit of low Kn,

$$\Phi = \frac{-12\pi K_{tc}}{2+\Lambda}. \tag{2.61}$$

where $K_{tc} = 1.10$ is the thermal creep coefficient. The expression is seen to be independent of Kn. At high Kn conditions, Waldmann (1959) produced an expression for Φ,

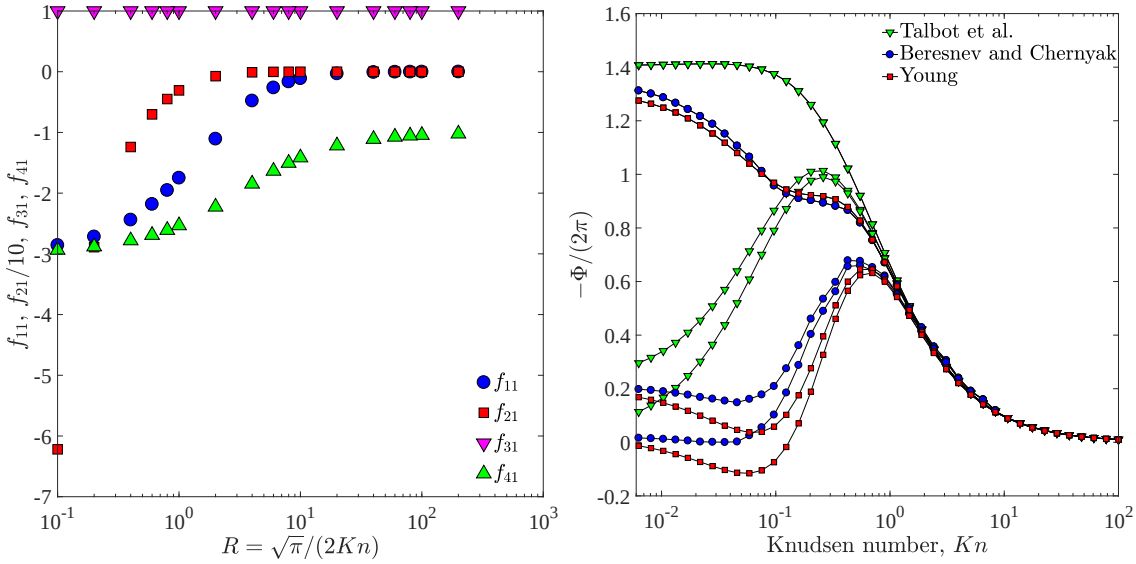

(a) Coefficients for Eq. 2.65

(b) Comparison of Φ expressions

Figure 2.5: *Left*: Coefficients f_{11}, f_{21}, f_{31}, f_{41} for the solution of the expression of Beresnev and Chernyak (1995) for Φ. *Right*: Differing expressions for Φ; Λ varies 3, 30, 300, top to bottom for each expression.

$$\Phi = \frac{-2\pi}{Kn} \tag{2.62}$$

which is seen to be independent of Λ. In this case, $d_p \ll l_g$, hence impacting molecules are assumed to only make contact with the particle once, and leading to the particle having no effect on the velocity distribution of gas molecules.

Neither the expression of Epstein, nor Waldmann is valid in the slip flow or transition regimes, in which a significant increase in Φ can be seen, Fig. 2.4b. Here thermal slip flow is the dominant cause of the thermophoretic force. Thermal slip flow occurs in slightly rarefied gases, where molecule-particle, rather than molecule-molecule impacts are more frequent. Upon impacting a particle, the molecule's temperature will tend towards that of the particle. This leads to molecules from a cold region increasing in mean velocity ($\bar{c} = k_B T_g$), and vice versa. This causes a flow of gas molecules close to the particle's surface from the cooler to hotter side of the particle, and hence an opposing force on the particle down the temperature gradient.

Brock (1962) produced an expression for Φ in the continuum and slip-flow regimes,

$$\Phi = \frac{-12\pi K_{tc}\left(1 + C_e \Lambda Kn\right)}{\left(1 + 3C_m Kn\right)\left(2 + \Lambda + 2C_e \Lambda Kn\right)}. \tag{2.63}$$

The constants were then adjusted by Talbot et al. (1980), which produced an interpolation valid (in theory) for all Kn. Here C_m and C_e are velocity slip and temperature jump coefficients,

$$C_m = \frac{2-\alpha_m}{\alpha_m} A_m; \quad C_e = \frac{2-\alpha_e}{\alpha_e} A_e, \tag{2.64}$$

where A_m and A_e are constants, ($A_m \cong 1.14$, $\mathrm{A}_e \cong 2.18$ from Beresnev and Chernyak (1995)). α_m and α_e are momentum and energy accommodation coefficients respectively which define the impact of gas molecules on the discrete particulate surface. These are usually assumed equal to unity as their 'values are seldom known' (Healy and Young, 2010). This expression reduces to the expressions of Epstein (Eq. 2.61) and Waldmann (Eq. 2.62) in the limits of low and high Kn respectively.

Widely referred to as the Talbot model, it has been extremely widely used (for example Romay et al. (1998); Luo and Yu (2006); Abraham et al. (2010)), due to the range of Kn, and ease of implementation for numerical calculations. However, whilst convenient for use, the Talbot formulation over-predicts Φ substantially in the slip-flow and transition regimes for high Λ particle-gas combinations.

Beresnev and Chernyak (1995) produced an analysis based on the S-model, a higher-order linearisation of the Boltzmann equation collision integral than the (more widely used) BGK equation. The formulation for thermophoretic coefficient Φ is dependent on a number of functions, $f_{k,1}$, for $k = 1-4$,

$$\Phi = \frac{-2\pi}{Kn}\left[\frac{f_{11} + \Lambda f_{21}}{f_{31} + (1 + 2.5\Lambda Kn)\, f_{41}}\right]. \tag{2.65}$$

Numerical solutions for $f_{k,1}$ are tabulated for varying R ($= \sqrt{\pi}/2Kn$) in the original paper. These are shown in Fig. 2.5a. This necessitates interpolation in order to use this formulation for Φ in any practical calculation, adding further complexity. Sagot (2013) assessed the Talbot and Beresnev and Chernyak expressions for the thermophoretic coefficient against a number of experimental datasets available in the literature. They came down firmly in favour of the Beresnev and Chernyak expression, which predicted the experimentally-measured Φ better for 16 of the 18 data sets. The remaining two were poorly predicted by both expressions. These particle-gas combinations had extremely low thermal conductivity ratios $\Lambda < 1$, which is not representative of the materials in this study ($\Lambda > 50$).

Attempting to rectify this drawback of the Beresnev and Chernyak formulation, Young (2011) used the Grad's 13-moment approach to produce an expression for the

thermophoretic coefficient at low Knudsen numbers ($Kn < 0.2$). An interpolation was constructed to link the new low Kn expression to the Waldmann free-molecular limit (Eq. 2.62). The complete expression of Young, valid for all Kn, is therefore

$$\Phi = \frac{-12\pi \left[K_{tc}\left(1 + \Lambda C_e Kn\right) + 3C_m Kn\left(1 - \Lambda + \Lambda C_e Kn\right)\right]}{\left[1 + 3Kn\exp(-C_{int}/Kn)\right]\left(1 + 3C_m Kn\right)\left(2 + \Lambda + 2\Lambda C_e Kn\right)}. \tag{2.66}$$

where $C_{int} = 0.5$ is a interpolation constant fitted by Young. The Talbot et al. (1980), Beresnev and Chernyak (1995), and Young (2011) expressions for Φ are plotted in Fig. 2.5b. Three values of Λ are shown, 3, 30, 300, top to bottom. Interpolation for the Beresnev and Chernyak function is done for Φ rather than f_{k1}, as the interpolation was found fluctuate significantly with the latter approach.

The differences between the expressions are significant in the slip-flow regime are substantial. The Talbot expression is large in comparison to the other expressions, and when compared to the experimental data in Fig. 2.4b, can be seen to be unrepresentative of high Λ conditions. The Beresnev and Chernyak, and Young expressions are closer over the range of Kn. The Young expression predicts reversed thermophoresis in the slip-flow and transition regimes for $\Lambda \geq 50$. The Beresnev and Chernyak expression predicts reversed thermophoresis for $\Lambda \geq 500$, though the magnitude is 20 times lower than that predicted by the Young expression. During reversed or 'negative' thermophoresis, particles are able to move up the temperature gradient due to the thermal creep flow changing direction (the 'second mechanism of thermophoresis'). Reversed thermophoresis has only been demonstrated by one published experimental work (Bosworth et al., 2016), and was found to be around 5% of the thermophoretic force in the 'usual' direction.

The literature is conflicted over which expression for Φ provides the best match to experimental data. One of the objectives of the experimental work within this study is to assess the above expressions for use with numerical calculations of high Λ aerosol particulates that can be found in engine environments, such as NaCl.

2.2.4 Gravity

Gravitational effects are included using acceleration due to gravity in the appropriate direction, scaled by the ratio of difference between particle and fluid density, to the particle density,

$$a_G = g\frac{\rho_p - \rho_g}{\rho_p}. \tag{2.67}$$

For the case of our solid particulates in air, $\rho_p \gg \rho_g$, therefore $a_g = g$ is used.

2.2.5 Lift

The Saffman lift force (Saffman, 1965) is lift due to shear flow. As it is proportional to the density ratio ρ_g/ρ_p, it is more appropriate to suspensions in dense fluids. The much-cited Kallio and Reeks (1989) work showed that the inclusion of the Saffman lift force gave closer numerical results to the Liu and Agarwal (1974) data for $\tau_p^+ \leq 5$, but over-predicted V_{dep}^+ for $5 < \tau_p^+ < 20$. The lift force is given by

$$a_L = 6.46 \frac{\rho_g}{\rho_p} d_p^2 \sqrt{\nu \kappa} V_{rel}, \tag{2.68}$$

where κ is the local velocity gradient. The lift force is not applied during this study as it is considered important only for sub-micron particles (ANSYS, 2011a; Dehbi, 2009; Slater et al., 2003; Chibbaro and Minier, 2008).

2.2.6 Brownian

Brownian motion is a stochastic process where solid particles of extremely low inertia ($\tau_p^+ < 0.3$) follow a randomised path due to impact of gas molecules. This process is prevalent in the diffusional deposition regime, and is modelled as a Gaussian random process,

$$a_B = \xi \sqrt{\frac{\pi S_0}{\Delta t}}, \tag{2.69}$$

where ξ is a Gaussian random number (zero mean, unit variance), and S_0 the spectral density,

$$S_0 = \frac{216 \nu k_B T_g}{\pi^2 \rho_g d_p^5 \left(\frac{\rho_p}{\rho_g}\right) C_c}, \tag{2.70}$$

where k_B is the Boltzmann constant. Due to the extremely low τ_p^+ values for such a force to become significant, it is not considered further in this study.

2.3 Experimental

Particle deposition experimental rigs work on a collectively similar basis, where a dispersed (solid or liquid) phase is suspended in a moving fluid (almost universally air). The amount of aerosol that is deposited on a specific area, the test section, is measured by one or more of the following techniques (section 2.3.4), from which the values of V_d^+ or deposition fraction can be calculated. Measurements of particle size or concentration are often made using optical laser-based equipment. Airborne concentration measurements can also be used in order to calculate deposition without using a 'wet chemistry' or optical approach.

2.3.1 Particle types

Dispersed phase particulates can be formed from a number materials. Engine-environment particulates include sand, dust, volcanic ash, and sea salts (Cardwell et al., 2010). These materials can be quite variable in composition, size distribution, and properties. Those materials used within aerosol science are frequently initially either in solution or powder form, including olive oil, aloic acid, dioctyle phythalate, salts, methylene blue, and sugar (TSI, 2009). Powder aerosols are produced and pre-ground to a particular size distribution, depending on specification. Liquid materials can also be tagged with fluorescent tracer (section 2.3.4.1).

2.3.2 Particle generation methods

A range of techniques for particle generation exists, depending on the required number, size, and distribution of particles. Generated particle distributions can be mono-disperse (nominally a single particle with a small standard deviation) or poly-disperse (diameters over a range). Depending on the testing requirement, either can be appropriate. Experimental work for model validation has generally used mono-dispersed particles, whereas engine-environment particles are generally sieved to a certain size range and are therefore poly-disperse.

2.3.2.1 Vibrating orifice atomisers

Vibrating orifice aerosol generators (VOAGs) produce aerosol particles from a solution containing the desired particle material as a solute. The solution is pumped through an orifice (10-40 µm diameter), which produces a (larger) droplet of solution. Air is then used to disperse the droplets and dry them to their final solid size. Solution

concentration is determined by required final particle diameter; mass flow rate of particulate is defined by solution flow rate. Orifice frequency is derived from solution flow rate (Eq. 4.12). Tuning of the frequency must then be undertaken to ensure that (a) particles are mono-disperse and (b) the mono-disperse particle size is the correct size. This is due to orifice manufacturing tolerances (TSI, 2009).

2.3.2.2 Powder atomisers

Powder-based atomisers produce aerosols from a pre-sized powder or particulate mass. The powder can be dispersed into the air stream in a number of ways (fluidised bed, venturi aspirator (TSI)), however these atomisers can struggle with agglomeration of the powder, in particular for very small particles ($< 1\,\mu m$). They can also be coated with various substances for calculation of particle deposition rates (section 2.3.4.1).

Many of the large or engine-representative experimental rigs use custom-built particulate dispersion systems: some form of rotating screw, disc, or valve is used to bring a metered amount of solid/powder particulate mass into an air stream, which is then mixed into the main flow (for example Walsh et al. (2006); Wylie et al. (2017); Prenter et al. (2016)). The higher temperatures and mass flow rates required by such experiments tends to make small-scale atomisers and techniques inappropriate.

2.3.3 Particle size and concentration

Real-time particle sizing can be achieved using optical methods. Optical particle sizers (OPS) use a laser-scattering principle (TSI, 2012). The aerosol particles pass individually though a laser beam, some of which is scattered. The intensity of the scattered light is measured, from this the number of particles present and their size is calculated, based on calibration. Particles are sorted into 'bins' of a specific width. Particle size resolution is inversely proportional to particle size; large particles have wider bins.

Aerodynamic particle size (APS) measurements give the volume equivalent particle diameter of unit density sphere, by measuring time of flight through the measurement volume. APS measurements are generally more accurate than those of an OPS, as they do not rely on laser-scattering, which can be affected by the particle material (refractive index). A volume-equivalent (density-adjusted) diameter can also be calculated. APS units are however 2-3 times more expensive than OPS ones, and also less portable.

Attempts have been made to transform OPS-measured distributions to APS sizes, for example Chien et al. (2016). Oleic acid and sodium chloride, NaCl, particles were

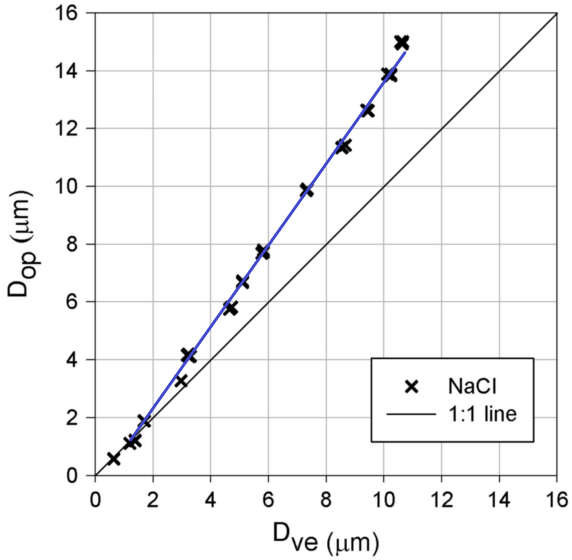

Figure 2.6: Optical vs. aerodynamic (volume-equivalent) particle sizing for NaCl, from Chien et al. (2016). Optically-measured particle size seen to be larger volume equivalent size. Linear fit shown in blue as used for Eq. C.1.

generated in the range 0.7-11 µm, and measured by both OPS and APS methods. For NaCl particles, the OPS measurements were found to be larger than those APS-calculated, Fig. 2.6. Here D_{op} is the optical particle diameter, and D_{ve} the volume-equivalent diameter.

Particle concentrations within the flow can be measured directly using the same equipment for sizing, as counting of the particles is necessary to form the distributions. More precise distributions can be made through the use of an isokinetic nozzle (Sippola and Nazaroff, 2014), where the air speed entering the nozzle is matched to the free stream velocity. This leads to the particle size distribution within the nozzle being equal to that in the main stream, rather than the inertial preferential selection of particles without matched velocities.

2.3.4 Deposition measurement techniques

Experimental methods for measuring particle deposition fall broadly into four categories: wet chemistry, optical, concentration, and mass-based. Each have particular advantages for given scenarios, and an appropriate choice of experimental measurement technique is important in order to gain valid data from any experimental particle deposition work.

2.3.4.1 Wet Chemistry

Wet chemistry is a widely used technique: a solvent is used to wash the deposited particles from the test piece (Sippola and Nazaroff, 2004; Healy and Young, 2010). Based on a known amount of the solvent, concentrations of deposited species in the washing solution are found, and deposited mass calculated. If an exit filter is employed to catch all non-deposited particles (Sun et al., 2013), the same process can be employed to verify the total mass of particles/species for deposition at domain exit. Fluoroscopic methods measure the resultant fluorescence of the washing solution (Liu and Agarwal, 1974; Healy and Young, 2010) using a fluorometer. Particles are initially tagged with a fluorescent tracer, for example uranine. An equivalent process using ultraviolet spectroscopy was used by Wilson et al. (2011). Long experimental times are sometimes required to deposit detectable amounts of the aerosol - Sippola and Nazaroff (2004) ran experimental times up to 144 hours.

Swabbing (and then mass spectrometry of the swab) of the affected areas is used when collecting data from engines, and has been applied as a technique in this laboratory for measuring particle deposition. There are some difficulties with this technique. Significant differences can be seen in swabbing efficiency (fraction of deposited substance collected) between different operators (Parry-Crooke, 2013). The possible spatial resolution is generally coarse, which limits the process to integral deposition measurements only. Swabbing efficiency is calculated from calibrations. A solution containing the test solute (NaCl, for example) is produced, at a known concentration. A known mass of the solution is deposited by syringe onto a test coupon, and allowed to evaporate. Swabbing of the surface is then undertaken. The reported collected mass is then compared to the initial mass of solute in the solution to give swabbing efficiency.

2.3.4.2 Optical methods

This approach uses imaging of the surface (either during or post-test) to size and count the particles present. The surface image can be post-processed using image recognition software to provide the particle statistics. This can then be easily turned into the standard deposition data knowing the imaged area and aerosol mass flow rate. Kvasnak et al. (1993) and Barth et al. (2013) developed such methods and applied them to isothermal channel flow. Barth et al. mounted the microscope directly beneath the test section so were able to assess temporal effects on deposition - this

was seen to be linear with time until agglomeration began to occur on the wall/lens at long experimental times.

Optical methods for particle deposition measurements have the advantage of giving a much finer spatial resolution than wet chemistry methods, and with on-experiment mounting can give deposition rates with time. However this requires optical access, which is challenging for high temperature experiments. Whilst high spatial resolution is achievable, this generally comes at the cost of imaging a small area at once. Particle agglomerates are difficult for computer vision to count, leading to high uncertainties when many particles are deposited.

2.3.4.3 Concentration-based methods

Measurement of particle concentration using optical methods (section 2.3.3) at inlet and outlet of the test section allows deposition rates to be calculated quickly, and for different particle sizes at once if a poly-disperse aerosol is used. There are advantages of speed (multiple flow rates can be undertaken in one run of the experiment), and integral deposition can be measured over a whole domain. This method has also been applied to complex domains (for example the mouth-throat geometry of Kelly et al. (2004)), though at the cost of spatial resolution. Lee et al. (2006) applied this technique to experimental temperatures up to 360 °C; the sampled high-temperature air was diluted 50:1 to reduce the temperature to levels acceptable to the OPS ($\leq$ 50 °C). Thermophoretic effects would have to be taken into consideration in the sampling system, as the tubes are likely to be significantly cooler than the flow at points, driving thermophoretic deposition and altering the sampled values.

2.3.4.4 Mass-based methods

Collecting the deposited mass from a surface and weighing it, or calculating the change in mass of a component is a simple method to measure integral deposition. The deposited mass must however be large enough to be measured without significant error on a balance. Deposition of this scale is found in some gas turbine experiments, and this method has been used in a number of studies, for example Whitaker et al. (2016b); Prenter et al. (2016).

3D scans of a test surface before and after the experiment occurs can be subtracted to give the deposition profile across a surface. This method gives high surface resolution, and is particularly appropriate for deposition onto complex surfaces where the spatial distribution may be highly non-uniform. Both the studies referenced above used such scanning before the deposited mass was weighed. A combined approach

could also be used to determine the mean density of deposits, useful for numerical studies attempting to simulate the thickness of such deposits.

2.3.5 Experimental data: simple flows

Much of the experimental data in the field of aerosol science has been obtained at ambient and isothermal conditions. The simplest geometries are straight pipes, Fig. 2.2, and channels/ducts. Deposition data is frequently presented as integral values over the whole test piece (or axial sections thereof). Particle sizes generally range from $0.1 - 200\,\mu m$, spanning the three deposition regimes as described in section 2.1. In many cases the liquid droplet aerosols generated can be approximated as giving an all-stick boundary condition.

The experimental data of Liu and Agarwal (1974) for turbulent pipe flow have become the most widely referenced experimental data in this field. Experiments were undertaken at ambient conditions, for $Re = 10\,000$ and $50\,000$. The test section was a vertical pipe, $L/D = 80.3$. Aerosol particles were produced from olive oil, with a fluorescent tracer (uranine). Mono-disperse particles $d_p = 1.4 - 21\,\mu m$ were generated ($0.21 \leq \tau_p^+ \leq 774$). Their data, Fig. 2.7a, showed almost no dependency of V_d^+ on Reynolds number. The authors reported $V_d^+ \propto \left(\tau_p^+\right)^2$ in the diffusion-impaction regime. No experimental uncertainty was reported, though repeated experiments showed differences $< 3\%$ in V_d^+, extremely low in comparison to other published experiments.

Other widely referenced experiments for ambient pipe flow include Friedlander and Johnstone (1957); Sehmel (1968), whose data are seen on Fig. 2.2. Their data are comparable to that of Liu and Agarwal (1974), but have a wider spread of up to three orders of magnitude.

Montgomery and Corn (1970) investigated deposition from horizontal turbulent flow at high Reynolds numbers ($48\,000 - 360\,000$). They showed their initial results, using a uranine-methylene blue aerosol, were strongly influenced by particle charge, increasing deposition by up to $30\times$ over their later, neutralised, experiments. The effect of particle charge decreased with increasing Re. The authors did not consider their V_d^+ results strongly correlated with τ_p^+, as vertical experiments have tended to show, which is possibly a characteristic of horizontal flows.

Sehmel (1972) used a large-scale horizontal wind tunnel (60×60 cm cross section), generating Reynolds numbers $92\,000 - 550\,000$, for particles 0.1-28 µm. Measurements were taken on the passage floor and ceiling. The increase in deposition velocity V_d between ceiling and floor for 2.5 and 13 µm particles was 28.0 and $2.6\times$ respectively.

Re-entrainment of particles from both surfaces was seen, but at a higher rate from the duct ceiling. When surfaces were make 'sticky' with petroleum jelly, re-entrainment of particles into the bulk flow was still observed for particle diameters greater than 20 µm.

Closely related are a number of horizontal channel flow experiments; Kvasnak et al. (1993) investigated deposition of varying solid particulate types in the size range d_p 1-45 µm, in turbulent horizontal duct flow ($Re = 15\,000$). The test section was made sticky to particles to attempt an all-stick boundary condition. Optical measurement techniques were used. Results, whilst showing significant scatter, indicate an increasing trend of deposition with increasing particle size, Fig. 2.7d. The data is self-consistent, and shows a reduced dependency of V_d^+ on τ_p^+ in comparison to the vertical orientation. Sippola and Nazaroff (2004) undertook experimental work to simulate deposition within an air conditioning duct. The duct was a square section, with Reynolds numbers in the range 28 400 - 116 200, and particle diameters $1 - 16$ µm. Their data was collected for ceiling, (vertical) walls and floor regions, allowing gravitational effects to be investigated. Generally good agreement with the Liu and Agarwal data is seen, though other experimental data has shown a rise in V_d^+ for $\tau_p^+ < 10^{-2}$, which is not seen here. The effect of gravity is clearly seen, with the floor of the passage seeing dimensionless deposition velocities two orders of magnitude higher than the ceiling in general. Experimental set-up was well-considered, and experimental uncertainty around 10%.

A different approach was taken by Barth et al. (2013), who used optical microscopy to measure the deposition rate with time of particles to the floor of a duct. Deposition rate was seen to be independent of time for all but the largest particles (5.8 µm), but deposition was seen to decrease for increasing bulk velocity, proposed due to a reduction in gravitational settling.

The early study of Matsui et al. (1974) showed that under gravitational (horizontal) conditions, deposition fractions on top and bottom surfaces of the pipe did not equalise until $Re = 30\,000$ for their 3.7 µm particles, a reasonable match for their calculations. Gravitational effects were strongest for $Re < 10\,000$, and their calculations also showed this was the case in general for smaller particles: deposition was predicted to be equal between top and bottom surfaces for 10 µm particles at $Re \sim 4\,000$, but not until $Re \sim 100\,000$ for 0.3 µm particles. Deposition velocity in low speed turbulent flows, $Re = 4\,000 - 10\,000$, was shown to be a much weaker function of Reynolds number than for higher speed flows, $Re > 10\,000$. These points indicate a highly complex interaction between turbulent diffusion and gravitational motion.

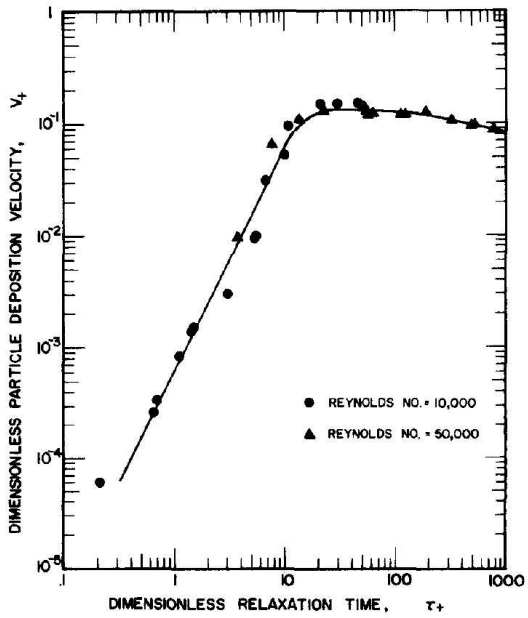

(a) Liu and Agarwal (1974).

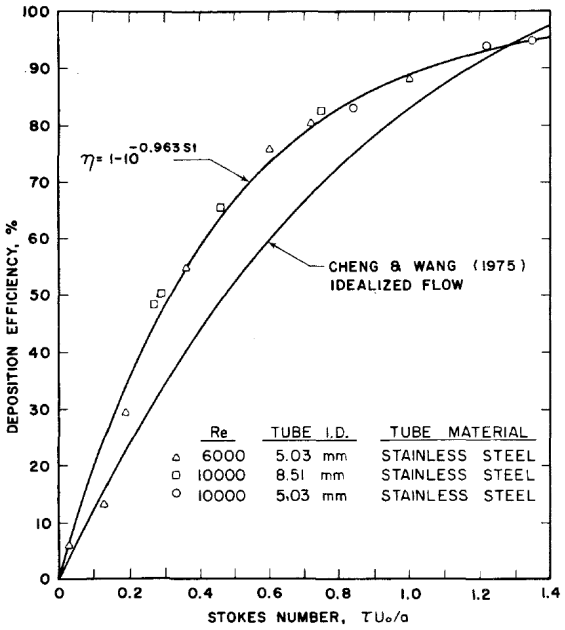

(b) Pui et al. (1987).

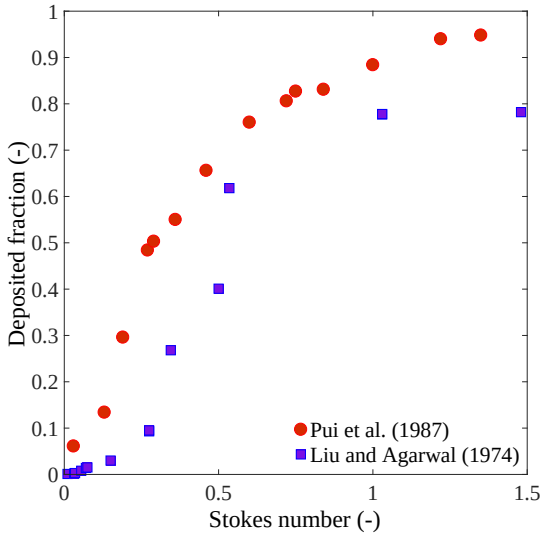

(c) Comparison of deposition fraction.

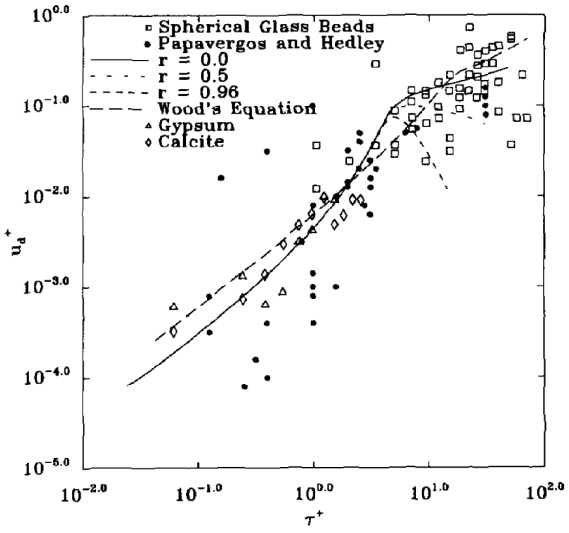

(d) Kvasnak et al. (1993).

Figure 2.7: (a): straight, vertical pipe flow. (b): flow through 90° bend. (c): comparison of the deposition fraction between vertical pipe flow and 90° bend geometries. (d): horizontal channel flow.

These studies agree on a number of points. Deposition increases with τ_p^+ in the diffusion-impaction regime when rebound or re-suspension of particles is not considered. Horizontal flows in general have higher V_d^+ for the same τ_p^+ than horizontal flows, and this can vary substantially between floor, wall, and ceiling measurements.

However, a number of effects are not so clear cut. The effect of Reynolds number is a significant area of disagreement, with some studies showing Reynolds-independence of deposition, whereas other show banding of data by Re on V_d^+ vs. τ_p^+ plots. The interaction between gravitational and turbophoretic effects is complex, and how this interaction changes with Reynolds number. Most experimental studies in pipe/channel/duct flows address particle rebound by attempting to reduce it using sticky surfaces - those studies that have 'allowed' rebound or re-suspension of particles are incoherent. This is likely due to such an effect being a complex interaction of factors, which the experiments were not designed to address.

A development of this is the introduction of bends to these flows. An increase in deposition fraction is generally seen with increasing particle Stokes number. In the absence of rebound this tends to full capture for $Stk > 5$; for example see experimental data of Pui et al. (1987), Fig. 2.7b. Here the centrifugal forces acting on the fluid set up two counter-rotating secondary flow vortices within the flow. Particle motion is also strongly affected by the centrifugal force experienced by the particle due to streamline curvature. A comparison of pipe and bend flows, Fig. 2.7c, shows that the bend-induced secondary flows increase deposition significantly in comparison to straight pipe flow at the same Stk, especially for small Stk. Sun et al. (2013) found similar results to Pui et al. (1987) for larger particles, but significantly higher deposition fraction for particles of lower Stk. Wu and Young (2012) produced an intensive study of inlet channel, 90° bend, and outlet channel, indicating that downstream deposition trends were significantly altered by the bend. The bend raised V_d^+ by around an order of magnitude for all τ_p^+ considered (0.8-46). After the bend, V_d^+ returned to pre-bend levels for the larger particles, but stayed elevated by 1-500% for $0.8 < \tau_p^+ < 7.8$ particles.

Thermophoresis has been investigated experimentally, again frequently for pipe flow. Healy and Young (2010) carried out experiments on annular flow between heated and cooled annular, concentric surfaces, and showed that a temperature difference of less than 30°C between surfaces can drive substantially different dimensionless deposition velocity statistics. The thermophoretic effect is shown to be strongest for smaller particles, in particular in the diffusional regime. Of particular interest in the secondary air system is the 'hot wall, cold gas' situation, where thermophoresis acts

to move particles from the hot wall region to the cooler bulk flow region, reducing deposition. Romay et al. (1998) investigated thermophoretic deposition for NaCl and PSL (polystyrene latex) spheres in vertical pipe flow. Attempts were made to decouple the turbophoretic and thermophoretic effects, an important but complex task. Assumptions made about the nature of the coupling seem to be somewhat arbitrary Deposition fraction data presented is an order of magnitude higher for isothermal conditions than has been published by others (see above), and it appears to be plotted erroneously, as their figures showing V_d^+ against τ_p^+ line up against that of Liu and Agarwal (1974), which is not the case based on the raw data of Romay et al.

The study of Tsai et al. (2004) developed this with further thermophoretic pipe flow experiments. Applications of the theory of Romay et al. (1998) with the thermophoretic coefficient of Talbot et al. (1980) showed good agreement with the experimental data for NaCl. Knudsen numbers were in the range 1-4, hence sitting in the transition regime. These data are not likely to be applicable to engine conditions, as the particles of interest at engine conditions are larger, and the gas mean free path lower.

The vast majority of published experimental data represents 'increasing' thermophoresis ($T_g > T_w$). Almost no experimental data is available for $T_g < T_w$, which is the main direction of interest for the study of particle deposition within the secondary air system. Only Healy and Young (2010) present such data, though this is of mixed use as the deposition rates were extremely low, leading to measurement difficulties and a number of possible inconsistencies within the data set. The authors were however able to develop a reasonably consistent gas temperature profile within the annular section, which itself is a challenge.

Other experimental studies include that of Zhang and Chen (2006), who made point concentration and velocity measurements of particle-laden flow within a full-scale room geometry. This was part of a combined experimental-numerical study, which showed successful simulations of their experimentally measured concentrations (section 2.4.6).

A number of studies have addressed oral delivery of pharmaceutical drugs by aerosol. Deposition fraction or efficiency is frequently reported against an impaction parameter IP,

$$IP = d_a^2 \dot{Q}_g, \tag{2.71}$$

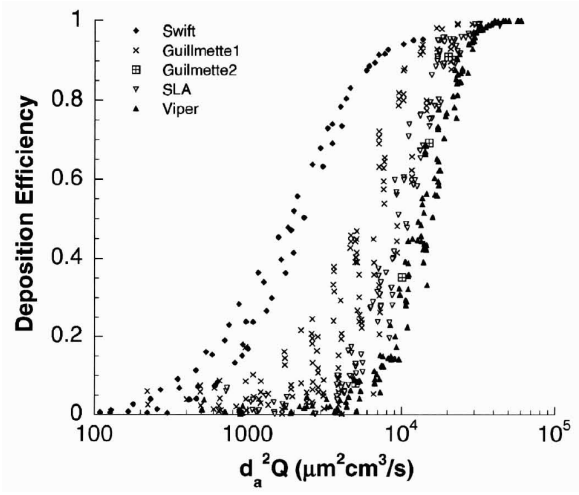

Figure 2.8: Five different experimental geometries from the same MRI scan of a nasal geometry indicating the huge dependency on manufacturing technique (surface finish/roughness). From Kelly et al. (2004).

where d_a is the particle aerodynamic equivalent diameter, and $\dot{Q}_g$ the gas volumetric flow rate. Eq. 2.71 is multiplied by ρ_p in some publications. Due to the complex nature of these geometries, it is often necessary to make simplifications, and deposition fraction is seen to vary significantly due to differing surface finishes. The work of Kelly et al. (2004) compared five physical implementations of a MRI (magnetic resonance imaging) nasal scan, the integral deposition results of which are seen in Fig. 2.8. Deposition occurred at IP values an order of magnitude lower for the roughest test piece, 'swift', than the smoothest, 'viper', indicating a huge dependency on surface finishes. However, the 'Guilmette' test pieces were smoother than the 'SLA' version, yet saw higher deposition. Spatial resolution of deposition, which was not measured, would help address such issues.

Most experimental studies have considered particle-wall impacts to be 'all stick', and have used a range of techniques to reduce rebound effects, when necessary. These include double-sided tape (Friedlander and Johnstone, 1957), petroleum and glycerine jellies (Sehmel, 1972), and Freon Tetrafluoride (Kvasnak et al., 1993). The latter study noted than marks were seen in the Freon coating, indicating particle rebound occurring in spite of it. Whilst studies have addressed particle rebound characteristics for various materials (section 2.3.6), few have given much consideration to the effects on net deposition rate. In many environments, including gas turbines, 'all stick' is not a necessarily a representative boundary condition. This area of the field that requires further investigation.

2.3.6 Experimental data: gas turbine flows

Engine-representative experimental work has investigated a range of main gas path geometries using engine(-scale) components at engine-representative temperatures. These studies have shown that particle temperature can have a significant effect on rate of deposition; above an adherence or softening temperature the rate of deposition has been seen to increase very significantly.

Previous studies connected to this thesis begin with the work of Ireland (2010), which set out the requirements for an experimental rig to produce validation data for the Dehbi DRW model. An experimental rig was designed and built (McGilvray et al., 2011), and several experimental campaigns carried out (Parry-Crooke, 2013; Wedd, 2014). These showed promise, but difficulties relating to particle generation, and control of the experimental conditions, were noted.

Engine-scale deposition, where more significant deposition structures are built, also is affected by particle-particle erosion, where impacting particles may have enough kinetic energy to remove sections of deposit. This adds a significant level of temporal complexity to such modelling. The effect was captured by Clum et al. (2014) experimentally using video recording of the build-up of mounds under impingement jets. This was observed to be an unsteady process, whereby deposit mounds increased and decreased in size, especially those growing down from a horizontal surface. It was seen by Whitaker et al. (2016a) larger particles (0-10, and 0-20 µm sievings) were able to remove blockage caused by smaller particles (0-5 µm sieving). These experiments were carried out up to 886 K, significantly below the sintering temperature of the Arizona road dust material ($\sim 1\,400$ K). In general particle removal of deposition has not received a great deal of research attention, likely due to the complexity of the problem.

The erosion of metal surfaces by particulate matter has, however, received more investigation. This is usually an aspect more considered in relation to the cold end of the engine, in particular fan and compressor erosion. Particles sizes at this point in the engine are in general larger than in the hot section, as the centrifugal effects of the fan and compressor tend to cause larger particles to be removed from the core flow. Hamed and Tabakoff (2006) provide a useful overview of erosion in turbomachinery. The Calspan full engine tests (Dunn (1990), summarised in Dunn (2012)) indicated significant compressor blade damage and performance deterioration; blade trailing edges were sharpened and blade tips eroded away. The removal rate of a surface undergoing erosion was investigated experimentally (for example Wakeman and Tabakoff (1982)). The removal rate is usually reported in terms of eroded volume

or mass of metal per unit mass of impacting particulate. This is useful in the case of fan/compressor studies, but less appropriate for the simulation of particle-deposit erosion, where a net change of deposited mass, the difference between deposited and eroded mass, $m_{dep,\,net} = m_{dep} - m_{ero}$, may significantly influence deposition rate and shape. In the related field of ice crystal deposition, where large-scale deposits are frequently seen, attempts to model erosive effects of ice on ice have used empirical and semi-empirical expressions, for example Currie et al. (2014). It is likely such an approach could be undertaken for particulates such as sand, ash, and dust, and would form a useful first step towards accounting for these effects. As appropriate validation data is not readily available, and it is outside the scope of this thesis to investigate particle-particle erosion experimentally, the subject is not considered further, except for discursive purposes.

Studies have been carried out on nozzle guide vane (NGV) geometries using the TuRFR experimental rig at Ohio State University. Initially build by Jensen et al. (2004) to test deposition on engine-scale NGVs, recent studies using this equipment include Casaday et al. (2014b) and Prenter et al. (2016), who both assessed the effects of combustor hot streaks on NGV deposition rates, Fig. 2.9. Unsurprisingly the hot streak was seen to increase deposition when clocked directly onto a vane, in comparison to a uniform temperature profile baseline case. Slot cooling of the vane reduced integral deposition by 3.5× in comparison to the hot streak deposition case. Interestingly deposition was also reduced upstream of the coolant slot. This may be indicative of the fact that the temperatures achieved experimentally were close to a particle sticking threshold temperature - deposition appears to stop abruptly in this region.

Whitaker et al. (2016b) investigated the effects of free-stream turbulence on NGV deposition. Fly ashes with mean diameters of 4.6 and 6.5 µm were used; increasing free-stream turbulence from 6 to 9% was found to increase deposition by factors of 1.77× and 1.84× respectively for the particle diameters. No uncertainty was reported for deposition rate/mass. Though not discussed in their paper, the traces of deposition thickness make interesting comparisons; for the larger 6.5 µm particles (Figure 10 of original paper, top) the increase in deposition is mainly at the leading edge, in contrast to the 4.6 µm particles (original figure, bottom) for which deposition was seen to increase fairly uniformly across the whole pressure surface. This may indicate that between these particle size distributions, turbulent diffusion and inertial effects are changing the deposition characteristics. This experimental rig has a tendency to

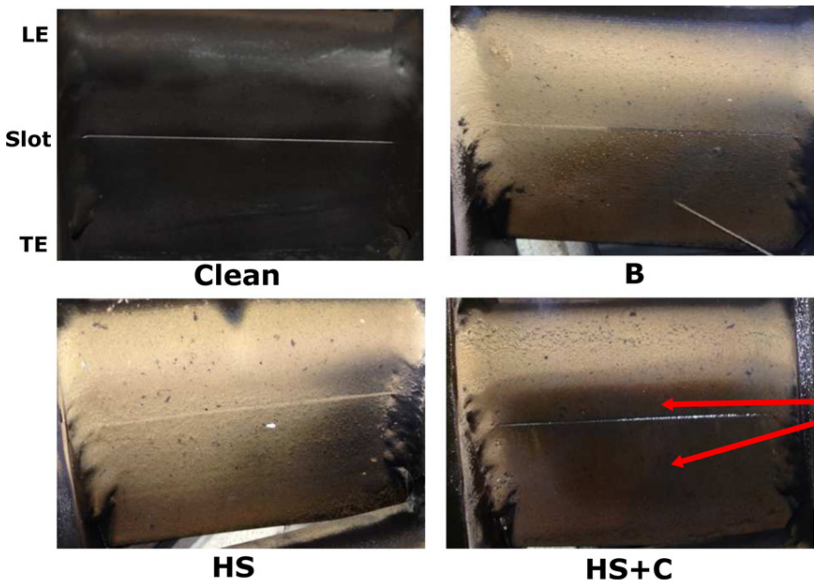

Figure 2.9

Figure 2.10: Deposition on NGV pressure surfaces for differing inlet temperature profiles. B: uniform; HS: hot streak; HS+C: hot streak and coolant slot. Taken from Prenter et al. (2016).

shed deposit during the cooling process (see Lundgreen et al. (2016) for example), which puts some doubt on their quoted values of deposited mass.

Clum et al. (2014) carried out experiments to assess build up of particulates underneath impingement jets. Rate of build up was found to be a function of composition and temperature. This work is simulated in chapter 6. These findings corroborate a number of studies of deposition in secondary air systems; Walsh et al. (2006) and Cardwell et al. (2010) investigated sand ingestion and blockage of film-cooling holes. Both reported increased rate of hole blockage with increasing metal temperature, above a threshold.

This approach was extended by Wylie et al. (2017), who compared blockage trends for varying volcanic ashes, film hole geometries, temperatures, and ash loadings for a high pressure turbine blade leading edge passage with film-cooling holes. Deposition was reported in terms of a reduction in flow parameter (RFP), where flow parameter is a normalised mass flow rate. The extensive study indicated that particle (gas) temperature was a first-order effect, with very substantial increases in RFP over threshold temperatures, which where themselves ash type dependent.

Whitaker et al. (2016a) assessed a NGV leading edge passage with an impingement liner and film-cooling. Deposition was reported in terms of blockage, a frac-

tional reduction in mass flow rate. Different PSDs were used, with the 0-5 µm sample increasing hole blockage, and 5-10, 0-10, and 0-20 µm distributions less likely to deposit, and able to remove previously formed deposits. Maximum temperatures of 866 K were used, significantly below those expected in a NGV leading edge passage. These temperatures would also be below expected sintering or melting temperatures of the particulate material, Arizona road dust.

The work of Kueppers et al. (2014) and Taltavull et al. (2016) demonstrated that ARD and such test dusts do not represent volcanic ash when treated thermally. Whilst both materials are high in silica (SiO_2) the silica component of volcanic ash (Eyja, matching the study of Wylie et al. (2017)) was found to be highly glassy, and hence amorphous and unstructured, whereas the silica component of ARD is highly crystalline. The glassy volcanic ash undergoes glass transition and softening at a significantly lower temperature (650-700 °C) than ARD melts ($\sim$ 1 700 °C). Onset of sintering was observed for volcanic ash at 850 °C, at 1 100 °C for ARD, and 1 400 °C for the MIL test sand, indicating that the materials have substantially different structures and responses to thermal conditions, and therefore substitution of one material for another must be done with consideration.

2.3.6.1 Wall-impact

The characteristics of particle rebound upon impact at gas turbine conditions - temperatures, velocities, materials - are highly complex, and is a field of research which remains largely empirical. A number of studies have addressed this problem experimentally, where data is usually presented as coefficient of restitution, CoR, the ratio of rebounding to incoming velocities. This is done for both the normal (CoR_n) and tangential (CoR_t) directions. Velocities and angles are defined in Fig. 2.11.

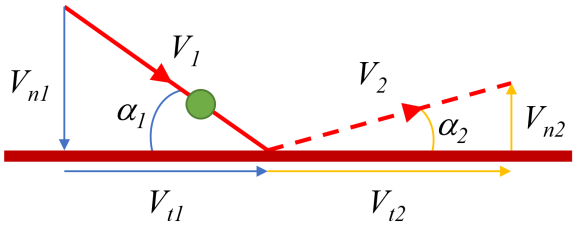

Figure 2.11: Particle rebound upon wall impact.

Early studies included Wakeman and Tabakoff (1982), and Tabakoff et al. (1987), who measured rebound characteristics as part of surface erosion. Gas turbine materials (Inconel, stainless steel, aluminium, titanium, and fly ash and sand) were tested,

at velocities up to 450 m/s and temperatures to 1 100 K. Tabakoff et al. (1987) also included the distribution of CoR values as a function of impact angle (β_1 in their paper), which indicates that the spread of CoR values at a nominal impact angle is a function of that impact angle.

A frequently used technique is particle shadow velocimetry (PSV), the particles pass between a high-speed video camera lens and a back-light before and after impact. The particle therefore leaves a shadow in each image, which is processed to give particle velocities. Bons et al. (2015) used such a technique to assess the impact of quartz on aluminium. They employed four differing but widely-used methods for the calculation of CoR values, demonstrating the advantages of individual particle tracking and calculation over field-averaging approaches, but at significantly higher computational cost.

Three fly ashes were assessed by Whitaker and Bons (2015) on stainless steel surfaces. Differences in CoR were reported with particle composition, but not with the two temperatures used, 295 K and 395 K. Reagle et al. (2014) carried out experiments for Arizona road dust (ARD) particles impacting a stainless steel surface. Gas temperatures up to 1 073 K were achieved, and particle velocities to 102 m/s. However their experiment was operated at a constant mass flow rate, temperature-velocity coupling the system, making it difficult to unpick the corresponding effects. Correlations of CoR as a function of impact angle were presented.

The above experimental works tend to come with the same caveats in relation to the demands of the current current study. Firstly, particle sizes used for rebound studies are typically large ($> 50\,\mu m$), for ease of capture on camera. As particle-wall adhesion is proportional to d_p^2, and particle kinetic energy proportional to d_p^3, the response of the smaller particulates (0-10 µm) in this current study is different. Secondly, experimental rebound conditions are attained to reduce the deposition of the particulate matter, as rebound is desired, hence there is little data available for the effects of particulate matter impacting previously deposited particulate matter. Thirdly, fly ash, which is frequently used for such experiments due to its availability, is not representative of the various volcanic ashes found across the globe. Fly ash, which is formed from the burning of pulverised coal during power generation, tends to be spherical in shape, whereas volcanic ashes are frequently shard-like (see figure 1 of Kueppers et al. (2014)). These considerations must be taken into account.

2.4 Numerical simulations

As within almost every field of engineering, the improvements in computing power and capability over the last 50 years have made numerical simulation of particulate-laden flows a significant area of research. Numerical simulations offer significantly better resolution of deposition data than experiments, be it spatial trends, concentration profiles, or particle tracks. Simulations of particle deposition tend to offer the usual numerical advantages over experiments regarding time/cost. If modelling on an engine-scale can be carried out this would be hugely advantageous.

However the fidelity of numerical simulations with regards to particle dispersion and deposition remains, on the whole, significantly lower than other fields (for example aerodynamics or heat transfer). This is in the main due to two factors. The first is the random nature of turbulence and therefore the stochastic interaction between suspended solid and continuous phases. This interaction is the most challenging aspect of current numerical modelling. The second factor is the mechanics of impact, whether a particle adherers or rebounds upon contact with a wall.

A wide range of solutions has been proposed for numerical modelling of particle motion in turbulent flows, with different levels of fidelity and tractability. Before making a choice of numerical approach, the desired 'cost' and output should be understood.

2.4.1 Continuous phase solution

The following is an overview of the general approaches for continuous phase modelling that have been applied to simulations of particle motion and deposition.

2.4.1.1 Reynolds-Averaged Navier-Stokes, RANS

The vast majority of published work on particle deposition, from both the aerosol science and gas turbine fields has used the Reynold-averaged Navier-Stokes (RANS) method. Here the Navier-Stokes momentum equations are time-averaged, hence solution provides a steady, mean flow solution. However the time averaging process introduces six mean fluctuating velocity components for three-dimensional flows, usually denoted $\overline{u_i u_j}$. These mean fluctuating velocity components are referred to as the Reynolds stresses. Attempts to provide further equations for the solution of the Reynolds stresses by taking moments of the RANS equations leads to an increasing number of products, which themselves must be solved.

A method for the solution of the RANS equations is to model the Reynolds stress terms, thus closing the equations, and rendering them soluable. Frequently this is done by making an analogy to molecular viscous stresses, by assuming a proportionality between the mean flow velocity gradients and the Reynolds stresses, with an effective 'turbulent viscosity'. This is known as 'first-order' closure. The two-equation eddy-viscosity turbulence closure models are the most widely used form of first-order closeure. The various formulations of the k-ϵ (standard, re-normalisation group, realisable, low-Reynolds) and k-ω (standard, SST) models are the most frequently used. Their utility lies in their stability and ease of use, and their shortcomings are well known. For certain classes of flows, they can produce good results in comparison to experimental or higher order model results.

To attempt to rectify the problem of anisotropic turbulence, Durbin (1991) produced the $\overline{v^2} - f$ model which solves for the wall-normal velocity fluctuations $\overline{v^2}$, in addition to turbulent kinetic energy and turbulent dissipation rate. The model has been shown to give good predictions in comparison to the Reynolds stress model (Lou and Razinsky), but it is not widely used in industrial applications due being less stable and less available than the two-equation models above.

The Reynolds stress model (RSM) solves the individual Reynolds stresses directly, leading to six extra equations. This is a second-order method. This increases computational time, however the RSM is able to capture anisotropy of turbulence. It performs significantly better for separated and rotating flows than the eddy viscosity models.

2.4.1.2 Large eddy simulation, LES

Large eddy simulation and the associated variants (detached eddy simulation, DES, hybrid methods etc.) have not seen widespread application to particle motion simulations in general. When LES has been applied to particle simulations, it has been in a similar manner to simulations employing RANS methods - a stochastic model is still required in the boundary layer (modelled) region. Dehbi (2011) simulated a throat geometry using LES, showing improvements over RANS solution in comparison to experimental data. Liu et al. (2007) also assessed a throat geometry, with their LES-based results indicating better comparisons to experimental data than either the eddy interaction model (EIM), for which deposition was too high, or mean flow tracking, for which deposition was too low. Berrouk et al. (2008) simulated the experimental work of Pui et al. (1987). The results were promising, however the application of a stochastic model for particle-turbulence interaction was shown to have very little

effect on the overall results, likely due to the particle body forces due to streamline curvature being significantly larger.

2.4.1.3 Direct numerical simulation, DNS

Within the field of aerosol science a number of researchers and groups have applied direct numerical simulation techniques to the solution of particulate flows. Due to the vast computational requirements ($N_{cells} \propto Re^{9/4}$) those seen have almost exclusively been for low speed flows in simple geometries, for example the pipe flow of Thakurta et al. (1998), or the channel flow of Marchioli et al. (2003, 2008).

Data extracted from DNS indicate the unsteady manner in which aerosol particles interact with and approach solid walls from a turbulent flow. In the diffusion-impaction regime this appears to be driven by 'sweep' and 'ejection' mechanisms, the former drawing particles down into the boundary layer, the latter removing them away to the bulk region. This data also provides important data against which the validity of lower-order codes can be assessed - for example fluid and particle normalised velocity profiles, particle-fluid covariances, and higher moments. Such data have been essential to the development and validation of Langevin-derived models for instantaneous fluid velocity as seen by a solid particle, discussed below.

The fidelity of DNS comes at a very significant computational cost, the $Re_\tau = 155$ channel flow simulations undertaken in Marchioli et al. (2008) were reported to have taken 8-10 months each. Here Re_τ is friction Reynolds number, based on shear velocity,

$$Re_\tau = \frac{u^* l}{\nu_g} = \frac{\rho_g u^* l}{\mu_g}, \tag{2.72}$$

where l is the channel half height for channel flow simulations. This time frame is clearly unacceptable in an industrial context, not accounting for the required increase in complexity of geometric and flow conditions.

2.4.2 Continuous-discrete phase coupling

The vast majority of researchers have applied a serial approach to numerical simulations of particle tracking, where the continuous phase is solved first, followed then by some manner of particle tracking. The assumption is made that particle concentration is low (volume ratio $< 1e^{-6}$), hence the discrete/solid phase has no effect on the continuous phase, allowing a one-way coupling.

When the simulated conditions have a volume ratio > 0.001, the effect of the particles on the bulk flow, and particle-particle interactions must be simulated. In the middle domain, volume ratio $10^{-3} - 10^{-6}$, the effect of the suspended phase on the bulk flow is small, and frequently ignored (Venturini and Rispoli, 2012).

2.4.3 Discrete phase

The formulation of the equations of particle transport in a flow can be described as Eulerian or Lagrangian. The fully-Eulerian formulation, as proposed by Kallio and Reeks (1989) treats the solid phase as a second continuous phase, solving ensemble-averaged conservation equations similarly to the fluid phase. The Eulerian approach is most suitable for high volumetric ratios, where particle-particle and particle-gas effects cannot be ignored (Dehbi, 2008b). Whilst less computationally intensive than Lagrangian tracking, Eulerian modelling has difficulties with implementation of boundary conditions and particle density discontinuities.

The Lagrangian approach, where the Newtonian equations of motion are solved for individual particles, is more widely utilised by researchers. Particles are tracked individually, solving the equation of motion along their path. In the case of turbulent flows, large numbers of particles must be tracked in order that stationary particle statistics are formed. This makes the Lagrangian approach more computationally expensive, however its relative ease of implementation and calculation, in combination with the continuous decrease in cost of computing power, has resulted in its widespread use.

Numerical simulations of particulate-laden gas turbine flows have almost exclusively been undertaken using a Lagrangian approach. Due to the low particle loadings experienced in operation (Whitaker et al., 2016a; Wylie et al., 2017) particle-particle interaction can be ignored, and a one-way coupling between gas and particle motion can be assumed (Venturini and Rispoli, 2012).

The most widely used stochastic methods are discussed in Table 2.1. The continuous random walk (CRW) model of Dehbi (2008a) was chosen for further assessment and use, based upon its good predictions of experimental deposition, and relative ease of use in industrial configurations.

2.4.4 Analytic models

The first major model for turbulent particle deposition was published by Friedlander and Johnstone (1957). Known as the 'free-flight' model, particles are transported by

Model	Authors	Description	Pros	Cons
Eddy Interaction Model (EIM/DRW)	Gosman and Ionnides (1983)	Uses isotropic turbulence assumption to calculate fluid fluctuating velocities. Particles remain in an eddy until the particle crosses the eddy, or the eddy expires.	Simple to implement, good predictions of dispersion in bulk flow (Zhang and Chen, 2006). Available within ANSYS Fluent and straightforward to use.	Over-predicts experimental deposition by orders of magnitude in diffusion-impaxtion regime. Insensitive to particle size.
Langevin	Langevin (1908); Obukhuv (1959)	Initial Langevin-based model. Increment in fluctuating velocity calculated from previous fluid velocity and a Gaussian random component.	Better performance than the EIM. Tian and Ahmadi (2006) successfully simulated deposition form channel flow in 2D.	Over-prediction of deposition in diffusion-impaction regime. A non-physical drift velocity causes spurious build up in boundary layer.
Normalised Langevin (CRW)	Iliopoulos et al. (2003); Dehbi (2008a)	Fluctuating velocity is normalised by the root mean square velocity. In bulk region assumes isotropic turbulence. In boundary layer uses normalised fluctuating velocity statistics from channel flow DNS.	Relatively straightforward computationally. Model was shown to reproduce a range of ambient experimental deposition results with good fidelity, by independent groups.	Does not reproduce Reynolds stresses correctly in the limit of tracer particles.
Generalised Langevin	Pope (1983); Arcen and Taniere (2009)	Based on drift and diffusion parameters, which are estimated from DNS data for inhomogeneous turbulence.	Reproduces higher order fluid, particle, and covariance statistics well in comparison to DNS.	Less tractable than other models due to necessity for substantial DNS-based data. No published work using the model of Arcen and Taniere (2009) has shown actual deposition predictions.
Sweeps and ejections	Jin and Reeks (2016a)	Models the coherent structures in the near-wall region, *sweeps* that bring particles close to the wall, and *ejections* or *bursts* that remove them to outer regions.	Cheap computationally, and models sweeps and ejections seen in experiments/DNS.	Comparisons to experimental data not favourable. Further development of the model (Jin and Reeks, 2016b) showed little improvement.
Particle cloud tracking	Corsini et al. (2013); Venturini and Rispoli (2012)	Groups of particles to travel in a 'cloud', normally distributed around a mean path. Ensemble-averaged equations of motion solved for mean path. Turbulent dispersion of the particles from cloud variance.	Efficiency of computation. Very large number of particles can be tracked. Good for non-wall bounded flows.	All particles in cloud behave as the centre point at rebound etc. Challenges when applied to internal flows.

Table 2.1: Varying models for the calculation of fluid fluctuating velocities from steady flows

turbulent mechanisms to a wall-normal distance defined as the 'stopping distance', S. The authors referred to this distance as an effective particle radius, based upon its inertia. The particle drifts in free-flight across the remaining distance (S) to the wall. The experimental work of a number of authors has disproved the free-flight theory, though it found use for a substantial period of time.

Wood (1981) published two analytic models for deposition to smooth and rough surfaces. These use the particle diffusivity from the Einstein equation to model deposition in the diffusional and diffusion-impaction regimes. Roughness is defined in terms of sand grain roughness. The model constants were tuned against the data of Liu and Agarwal (1974), and has found widespread use due to its simplicity and ease of calculation.

Fan and Ahmadi (1993) produced a model based on coherent turbulent vortical structures in the near-wall region. Limiting trajectories are calculated for particles in a turbulent sweep that just touch the wall before being returned to the bulk flow. The model provides 'reasonable predictions' of deposition velocity for a range of density ratios, Reynolds numbers, and roughnesses, according to the authors. The model was extended by Kvasnak et al. (1993), who accounted for particle rebound effects using an energy-based boundary condition, giving a critical approach velocity, above which rebound would occur.

2.4.5 Boundary conditions

2.4.5.1 All-stick

An 'all-stick' boundary condition captures all particles which come within one particle radius of the wall. Particles are then removed from the domain. This boundary condition is representative of many published studies on particle deposition where experimentalists have chosen to use either liquid aerosols, or have actively made surfaces sticky to particles. Whilst useful for the assessment of numerical models without consideration of impact effects at boundaries, it is not necessarily representative of the particle-wall impacts that occur in gas turbines, where particles are seen to rebound upon impact.

2.4.5.2 Rebound

A number of models for particle-wall impact have been developed, with ranging applicability. A number of critical viscosity models have been developed based on the

concept of Walsh et al. (1990). Here particle viscosity μ_p is related to particle temperature through the relation

$$\mu_p = AT_p \exp(B/T_p), \tag{2.73}$$

where A and B are constants. The 'critical viscosity', μ_c, is that at which it is deemed to become perfectly sticky. The probability of sticking (i.e. fraction of depositing mass) is then calculated from

$$p(T_p) = \begin{cases} \frac{\mu_c}{\mu_p} & \text{for} \quad \mu_p > \mu_c \\ 1 & \text{for} \quad \mu_p \leq \mu_c. \end{cases} \tag{2.74}$$

Tuning of parameters A, B, and μ_c must be done for particle/surface pairings.

Brach and Dunn (1992) produced a model for low-speed impacts which accounted for loss of kinetic energy due to deformation and adhesion in two independent processes, and was a step forward in terms of generality of model.

Kim and Dunn (2007) produced two models for particle impact, implementing them using a Fluent UDF. Alongside the material properties the model used a number of tunable constants, which are generally unknown a priori and were best-fitted by the authors. The validation cases shown indicated good reproduction of the experimental data chosen.

Singh and Tafti (2013) developed a model for particle rebound, dividing the process into four separate steps that occur in series: elastic deformation, elasto-plastic deformation, sticking, and rebound. Reproduction of experimental results was reasonable in general, though the calculation process quite involved.

Bons et al. (2016) attempted to produce a 'simple physics-based model' into which the relevant material properties could be inserted, and in theory used a priori. The model, discussed further in chapter 3, accounts for elastic and plastic deformation, adhesion, and shear removal. Good reproduction of a number of experimental cases relevant to gas turbine conditions was demonstrated, though the authors noted that tuning of the physical parameters (inc. particle material yield stress, composite Young's modulus, surface free energy) had been undertaken, in some cases significantly away from their nominal values. The model is however reasonably straightforward to implement as a Fluent UDF for CFD applications.

2.4.6 Numerical simulations: simple flows

Numerical simulations within aerosol science have been focused on internal flows in the main. Pipe, duct, and channel flows form the bulk of the published work, focusing on the simulation of a small number of well-referenced experimental results (in particular those of Liu and Agarwal (1974)). Kallio and Reeks (1989) also had success with modelling of the same data, but using an eddy-tracking approach. Their conclusions suggested a move towards a 'two-fluid', i.e. Eulerian-style, method should be pursued for reasons of computational efficiency. The work of Tian and Ahmadi (2006) indicated good reproduction of the Liu and Agawral experimental data, though simulations were carried out in 2D. Zonta et al. (2013) used DNS simulations with Lagrangian particle tracking of swirled gas flow in a stationary tube to show that the capture efficiency is increased under these conditions. Dehbi (2009) showed that the CRW model (discussed below) predicted experimental thermophoretic deposition (Dumaz et al., 1993; Tsai et al., 2004) with good fidelity, generally within experimental error (20%). Particle simulations without the CRW-calculated fluid fluctuations over-predicted deposition by around 1-400%. Across all test cases $\tau_p^+ < 0.24$, hence the CRW model has not been tested under thermophoretic conditions for larger particles or the diffusion-impaction regime, $0.3 < \tau_p^+ < 20$.

Other widely used internal flow geometries include those based on human thoracic and nasal passages, generally studying the effectiveness of aerosol drug delivery into the lungs. A thorough review of the subject is provided by Kleinstreuer and Zang (2010). Idealised geometries are generated based on CT scans of patients; these are usually averaged across a number of scans. Matida et al. (2003) simulated a mouth geometry; results, using the k-ω turbulence model and the EIM showed mixed success at reproducing experimental data, with their best comparisons occurring with a somewhat unlikely inlet velocity of 70 m/s. Feng and Kleinstreuer (2014) applied a dense discrete phase model (DDPM) to simulate particle-particle interactions, matching deposition efficiency reasonably in comparison to an experimental correlation. The DDPM model took around 1700× longer than one-way fluid-particle coupling, and around 17× longer than two-way fluid-particle coupling.

Ghahramani et al. (2014) applied the continuous random walk model (CRW) to an upper airway geometry. Matching to experimental deposition fractions at lower IP values was reasonable; at higher IP simulated values were significantly lower than experimental (2-10×). In comparisons to the continuous random walk, the discrete random walk model was not able to capture the shape of the deposition fraction-Stokes number curve. This study was repeated (Ghahramani et al., 2017) using LES.

Instantaneous velocities were set equal to the filtered velocity in the resolved regions of the simulation, and the fluctuations ignored in the modelled regions. Overall deposition trends were remarkably similar between the two publications/models, though still notably under-predicting experimental deposition. The regions in which specific particle sizes were depositing did however change between the models, though no comparisons were made to experimental data to indicate which simulation method might be preferred.

Zhang and Chen (2006) investigated vertical particle concentration profiles in a office-like room geometry. Simulations using the k-ϵ turbulence model and the Fluent DRW produced generally good replication of their own experimental work; the DRW model being successful in the isotropic region away from boundaries.

The recent work of Dehbi et al. (2017), recirculating particle-laden flow within a cubic cavity, showed that their LES simulation reproduced the decay in airborne particle concentration as seen in the partner experimental study to a high degree of fidelity. Their calculations indicated that thermophoresis only has a small effect on their particle motion calculations. For $d_p = 0.5\,\mu\text{m}$, thermophoresis was around one sixth of the strength of the drag force, for $d_p = 5\,\mu\text{m}$, it was a negligibly small fraction.

2.4.7 Numerical simulations: gas turbine flows

Numerical simulations of particulate-laden gas turbine flows have been carried out largely for external flows. Deposition within the combustor was considered by Dunham et al. (2011), who used a critical viscosity model to calculate deposition probability. An initial experimental test case was nominally used to assess the sticking model, though no comparisons were shown to experimental data. Compressor fouling was considered by Suman et al. (2014a,b), who developed sticking probability correlations based on a single set of experimental data (Poppe et al., 2000). This was applied to their compressor blade geometry, though no comparisons were made to experimental data. This work was extended within the same group (Suman et al., 2016), where a holistic model was formulated for the ingestion of particulate matter and fouling of compressor blades. Their methodology is outlined in Figure 1 of their paper, which includes a filtration profile, airborne particulate size distribution, and an adhesion probability, giving overall spatially-resolved blade contamination. Unfortunately, again no experimental data were used for validation of the computations.

Deposition onto nozzle guide vanes (NGVs) has been the subject of a number of computational papers. Casaday et al. (2014a) investigated the effects of hot streaks

on deposition build-up rate in comparison to experiments. Despite significant tuning of the critical viscosity model they were unable to match deposition trends around the full circumference of the vane, citing the model's independence from particle diameter and impact velocity. This was extended by Prenter et al. (2016) who computationally showed good matching of deposition rates (using the same critical viscosity sticking model as above), but erroneous high deposition rates near the trailing edge, where experiments showed negligible deposition. Whitaker et al. (2016b) assessed the effects of free-stream turbulence on NGV deposition rates; their simulations were not able to capture the full increase in deposition rate with increasing particle size and turbulence intensity. They noted that the discrete random walk model was not able to fully capture the physics of turbulent dispersion.

Borello et al. (2014) demonstrated a reduction in deposition onto film cooled NGVs, using a two-stage critical viscosity model, which gave different probabilities for sticking on a clean surface and also onto a previous deposit. No comparisons were made to experimental data. Agati et al. (2016) extended the sticking model of Thornton and Ning (1998) to high temperatures through the use of volume fraction-weighted component properties (Young's modulus and Poisson's ratio). Polynomial expressions for the temperature dependence of individual material properties were produced but only reported graphically.

Venturini and Rispoli (2012) numerically studied high temperature (1 293 K) deposition of pulverised coal ash onto a representative heat exchanger pipe. Thermophoresis was ignored. Particles sized 8-52 µm were injected into the U-RANS simulation. Deposition thickness was calculated by adding the deposition from the three discrete particle sizes. Comparisons to experimental data were limited to a single photograph from a referenced study.

Numerical simulations have also been carried out for internal geometries, representative of secondary air systems components. Wylie et al. (2017) carried out simulations of their experimental work for deposition in film-cooling holes. Qualitatively the results showed similar trends to the experiment, including the variation of deposition location/blockage with varying angle of hole.

2.4.8 Deposition thickness and domain updating

Two distinct methods are used for calculating the thickness of deposits on a surface after a specified mass of particulate has been injected into the domain. The first is to run particle tracking and calculate a scaled deposited mass based on the local deposition fraction from the particle tracking. The scaled deposited mass can then be

projected normal to the surface to calculate a deposited thickness. We refer to this as the 'projected thickness' method. Published works which have used such a method include Venturini and Rispoli (2012); Peng et al. (2016); Borello et al. (2012).

Although this projected thickness method is computationally cheap and simple to implement, it does not allow for unsteady trends in the development of the deposited profile. It has been noted, for example by Bons et al. (2016) that the grid should be regenerated at intervals to account for the aerodynamic effects of large scale particulate accretion. With reference to figure 19 of their paper, shown as Fig. 2.12 here, they state '*this deposit structure is large enough to modify the flow streamlines and thus the trajectories of subsequent particles. For the model to capture this effect, the vane surface would have to be modified and regridded at regular intervals during the steady solution. It is expected that this would result in a broader leading edge deposit structure as observed experimentally.*' It is immediately clear from Fig. 2.12 that there is a significant difference between the experimentally-observed deposition (grey profile, from Prenter et al. (2014)) and their calculations (black). Experimentally, the leading edge deposit spreads thickly onto both the suction and pressure surfaces, more than 20% of the way along the latter from the leading edge. The computational projected deposition thickness was very localised to the leading edge, only spreading down 5% of the pressure surface.

Such deposition would also be likely to negatively effect the capacity of the nozzle guide vanes, altering the engine operating point. Without being able to capture the thickening of the vane surface, this effect on engine operation cannot be simulated.

Updating of a CFD domain due to deposition has been implemented for ice accretion on compressor blades and engine cowls, for example Cao et al. (2016). The ice phase tends to be tracked in an Eulerian manner (similarly to the gas itself) due to the high number concentrations seen. Good reproduction of experimental results have been shown by Shen et al. (2013). However there have been limited attempts to apply such a scheme to deposition of ash or sand in hot stage components. The deposited thickness, shown to be non-negligible relative to component size in experimental and engine experience cases (Lundgreen et al., 2016; Prenter et al., 2016), is ignored, meaning that its effect on the continuous flow field, heat transfer distributions, and further particle trajectories is not accounted for. One notable exception was the work of Casaday et al. (2014a), who used a series of 2D axisymmetric simulations to explore deposition under an impingement jet. Calculation of surface adjustments was carried out in MATLAB before remeshing was undertaken. Simulation results matched the partner experimental study (Clum et al., 2014) reasonably well, however the critical

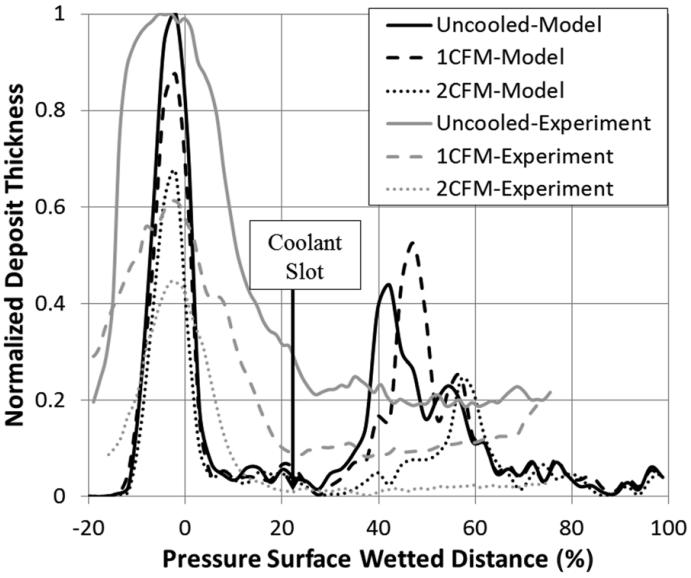

Figure 2.12: Normalised deposition thickness on a nozzle guide vane against wetted distance for experimental and numerical studies. Taken from Bons et al. (2016). Substantial difference seen between experiments (grey) and their simulated projected deposition thickness (black).

shear stress sticking model was tuned using fairly arbitrary parameters to match the experimental data. Remeshing the whole domain at every iteration was acceptable for this 2D axisymmetric geometry, but is considered a computationally expensive process for larger, more complex 3D domains.

The above calculations were done by exporting the geometry and deposition to external software, where the necessary geometric changes were made, and the domain fully remeshed in a third piece of software. A preferable approach would be to undertake the calculation and remeshing processes within the flow solution software itself (Fluent). We refer to this as 'dynamic mesh morphing.' This would be likely to significantly reduce calculation time and make the whole process more user-friendly. Such a scheme is described in section 3.3.

2.5 Summary

Based on the above review, a number of main points are pertinent to the thesis. Experimentally, a rig based on pipe flow conditions is the simplest to construct, and measure deposition from. Instrumentation of such a configuration is also more straightforward, with regards to measuring surface and flow temperatures. Differences are noted between vertical and horizontal pipe flow measurements, due to gravita-

tional effects. This must be considered. Particle generation from solution was seen to be the most reliable method to generate a highly mono-disperse aerosol, which makes comparisons to numerical simulations cleaner. Wet chemistry or optical assessment of test surfaces to measure deposition post-test appear to be appropriate methods.

Numerically, a large number of flow and particulate models are available. These should be limited to those appropriate for industrial applications, which places limits on the achievable fidelity of such simulations. This narrows the flow simulations to turbulence modelling (k-ϵ, k-ω, RSM etc.), rather than resolved simulations. Models for the fluid fluctuating velocities must be robust, and be limited in their dependence on DNS data that requires updating. This suggests the generalised Langevin models are not appropriate, favouring the normalised Langevin models. Lagrangian particle tracking, though more computationally expensive than a two-phase Eulerian solution, gives high resolution deposition predictions, and allows bounce-stick modelling to be applied with greater ease, important for capturing particle-wall interaction in gas turbine realistic flows.

Chapter 3

Numerical Models

This chapter presents detailed discussion of four key numerical models. Initially the eddy interaction/discrete random walk and continuous random walk models for calculation of the fluid fluctuating velocities are described. Further assessment and validation of the continuous random walk model is then undertaken.

Following this, the dynamic mesh morphing method is developed. This is a numerical approach for updating a numerical domain based on deposition history. This is able to capture the manner in which heavy deposition changes the surfaces on which it occurs.

The final section of the chapter concerns the implementation of a bounce-stick model from the literature for particle-wall impacts. Areas of model strength and weakness are discussed.

3.1 Eddy interaction model

The eddy interaction model (EIM), or discrete random walk (DRW) model was introduced in section 2.4.3. The development of the eddy interaction model was a first major step towards capturing the stochastic effects of turbulence on suspended particles (Gosman and Ionnides, 1983). Conceived in order to model the dispersion of fuel droplets in isotropic turbulence in internal combustion systems, it has found extremely wide-spread use within the gas turbine community. Individual particles exist in a series of capturing eddies. The particle remains within a specific eddy until the particle crosses the eddy, or the eddy expires.

The eddy velocity (instantaneous fluid velocity) in the i-th direction is calculated from the Reynolds stress $\overline{u_i u_i}$ and Gaussian random variable (zero mean, unit variance) ξ,

$$u_i = \xi_i \sqrt{\overline{u_i u_i}}. \tag{3.1}$$

When the EIM is applied to simulations utilising the two-equation turbulence closure models, isotropic turbulence is modelled. The mean square fluctuating velocities are equal, and derived from the turbulent kinetic energy,

$$\sqrt{\overline{u_i^2}} = \sqrt{\overline{u_x^2}} = \sqrt{\overline{u_y^2}} = \sqrt{\overline{u_z^2}} = \sqrt{\frac{2k}{3}}, \tag{3.2}$$

where k is the turbulent kinetic energy. The eddy lifetime, τ_e is calculated from the Lagrangian time scale T_L,

$$\tau_e = 2\tau_L, \tag{3.3}$$

or from

$$\tau_e = -\tau_L \ln(r), \tag{3.4}$$

where r is a uniformly distributed random number, $0 < r < 1$. The Lagrangian time scale is calculated

$$\tau_L = 0.15\frac{k}{\epsilon}, \tag{3.5}$$

where ϵ is the turbulent dissipation rate. The eddy velocity is constant whilst the particle is within the eddy, making it a zero-order function.

The EIM/DRW, whilst relatively straightforward to implement and use, has a number of drawbacks. The largest of these is a tendency to over-predict deposition by orders of magnitude (Tian and Ahmadi, 2006), in part due to the use of isotropic fluctuating velocities. In order to reduce this discrepancy, the continuous phase solution can be calculated using the Reynolds stress model, RSM. This allows anisotropic fluctuating velocities to be calculated from the principal (density-normalised) Reynolds stresses R_{ii},

$$u_i = \xi_i \sqrt{\overline{R_{ii}}}. \tag{3.6}$$

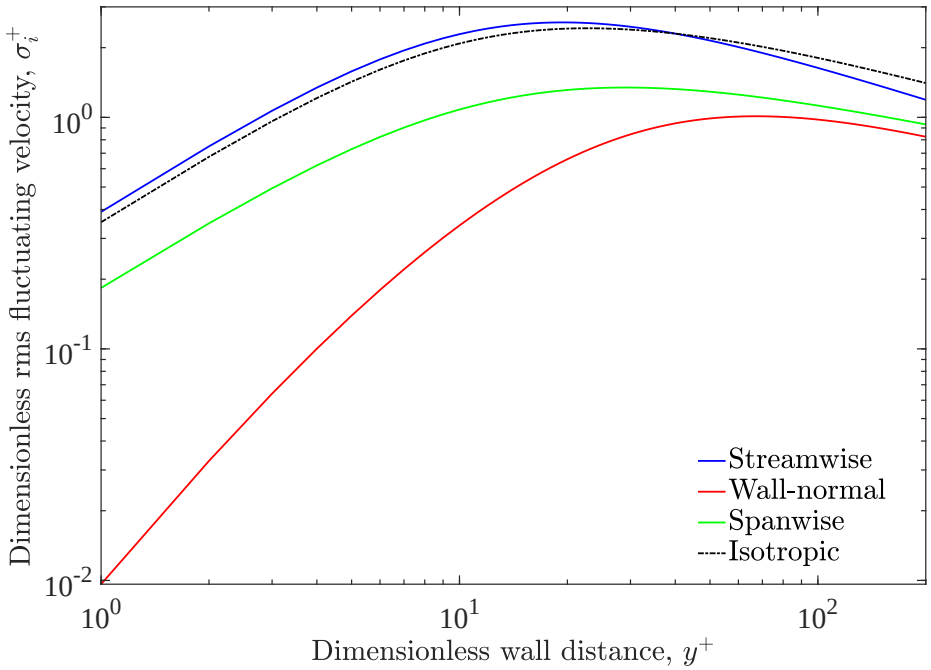

Figure 3.1: Comparison of non-dimensional fluctuating velocity components in three principle directions (streamwise, wall-normal and spanwise) from channel flow DNS data and equivalent calculated from isotropic turbulence.

It was noted that the use of isotropic fluctuating velocities was a primary cause of the over-prediction of deposition rates. Whilst an acceptable assumption in the bulk region where turbulence is largely isotropic, the assumption does not hold in the boundary layer region (defined as $y^+ < 100$) where the turbulence is strongly anisotropic. This can be seen in Fig. 3.1, where the normalised root mean squares fluctuating velocities σ_i^+ are plotted against non-dimensionalised wall distance y^+,

$$\sigma_i^+ = \frac{u_i}{u^*}, \tag{3.7}$$

where u_i is calculated from Eq. 3.6. Coloured lines show the three principle directions (streamwise, wall-normal, spanwise) from a direct numerical simulation of channel flow (Dreeben and Pope, 1997). The black dashed line shows the isotropic value as calculated from Eqs. 3.2 and 3.7. It can be seen that the isotropic value is representative of the streamwise value, but over-estimates both the wall-normal and spanwise components significantly. For $y^+ < 10$, use of the isotropic fluctuating velocity over-predicts the wall-normal component by more than an order of magnitude.

3.1.1 Simulations using DRW

To assess the numerical models in this chapter, simulations of the experimental data of Liu and Agarwal (1974) ('L&A') were carried out. L&A carried out particle deposition experiments for turbulent pipe for $Re = 9\,800$ and $50\,000$, in a 1.27 cm diameter $\times$ 1.08 m length pipe at ambient conditions. Particles were generated from an olive oil and uranine solution, over a range of sizes (1.4-21 µm).

3.1.1.1 Numerical simulation set-up

All numerical simulations were carried out using the ANSYS 14.5 suite; ANSYS ICEM 14.5.7 for grid generation and ANSYS Fluent 14.5 for simulation solution. A mesh sensitivity analysis for the simulations of the Liu and Agarwal experiments discussed below was carried out. The chosen grid was unstructured tetrahedral elements with 25 prism layers, an expansion ratio of 1.1, with an initial cell height of 30 µm. This gave a y^+ value of 0.8 for all but the first 5mm of the passage, which was not considered for deposition calculations, following Liu and Agarwal (1974). After comparisons to other turbulence models, calculations were undertaken using the realisable k-ϵ model. The energy equation was solved, density calculated from the ideal gas law, and dynamic viscosity calculated from Sutherland's law. Numerical convergence of residuals was obtained for continuity below 10^{-3}, and below 10^{-6} for x, y, z-velocities, energy, turbulent kinetic energy, and turbulent dissipation rate. A coupled pressure-velocity scheme was used, along with the third order MUSCL spatial discretisation scheme.

All simulations use injections distributed evenly over the inlet face of interest. Due to the strong dependence of deposition fraction on particle size, it was necessary to define finer injection grids (larger numbers of injections) for smaller particles in order to gain the required stationary deposition statistics. The finest grid was 126 000 particles, the coarsest 7 600 particles. The 'all stick' discrete phase boundary condition is used.

3.1.1.2 Sensitivity analysis

A mesh sensitivity study was carried out, which is shown in Fig. 3.2. Four meshes were constructed, 1.10 - 4.15 M cells. Axial velocity profiles (Fig. 3.2a) were seen to be almost invariant with mesh size. Wall shear stress values quickly approached an asymptotic value, the 1.1 M cell mesh was 2.5% higher on average than the 3.36 M mesh, with the 1.27 and 1.38 M cell meshes within 0.5% of the finest mesh.

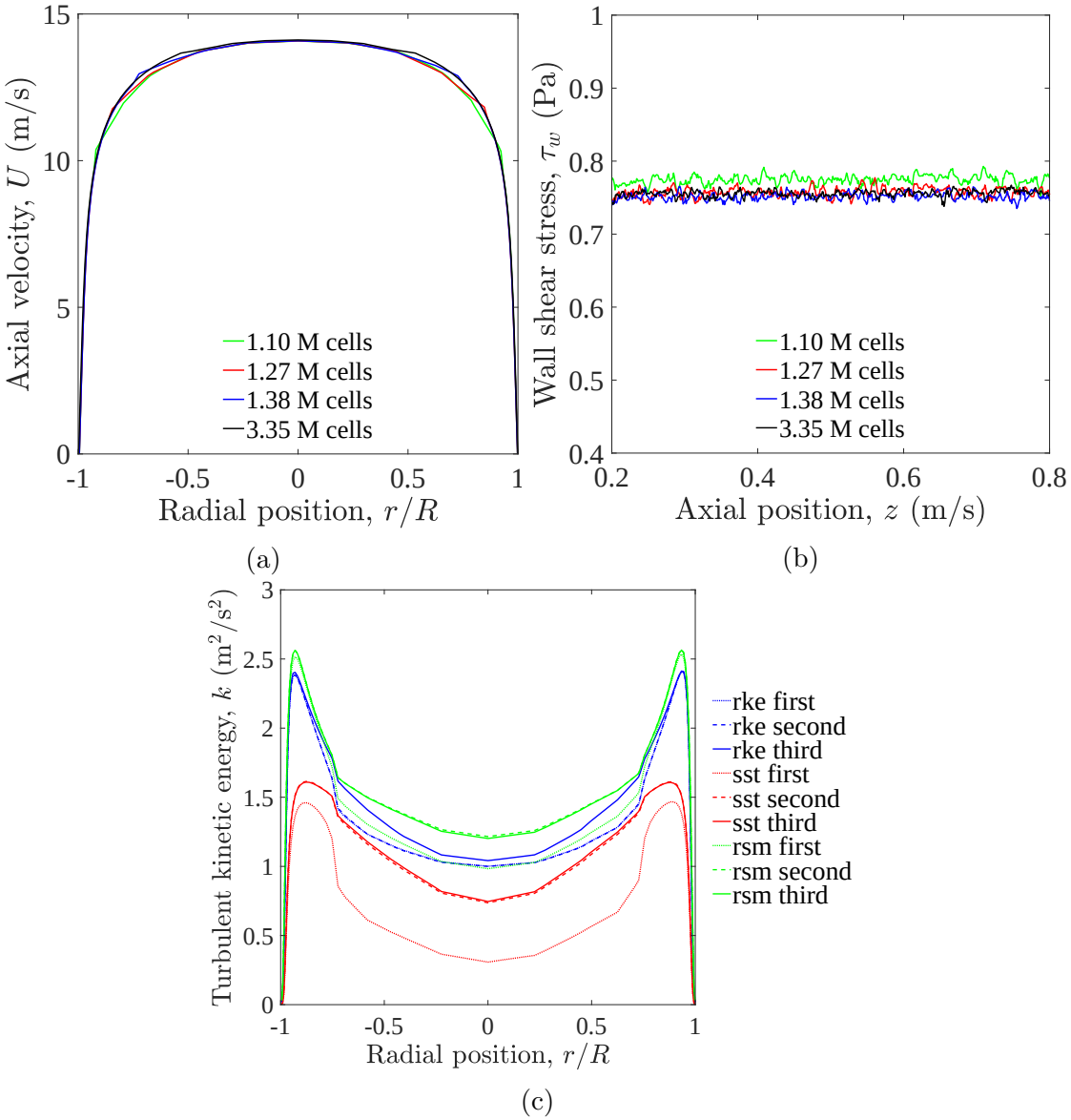

Figure 3.2: Mesh sensitivity study for L&A simulations. (a): Axial velocity profile at mid length of the pipe ($z = 0.50$ m). (b): Wall shear stress against axial position. (c) Turbulent kinetic energy profiles for varying turbulence models for 1.38 M cell mesh.

Profiles of turbulent kinetic energy against normalised radial position are shown in Fig. 3.2c. Three orders of spatial discretisation (first order upwind, second order upwind, and third order MUSCL, are used with the chosen turbulence models. The realisable k-ϵ model, 'rke', is able to match the peak in k in the boundary layer much more closely than the k-ω shear stress transport model, 'SST', in comparison to that calculated by the Reynolds stress model, 'RSM'.

The simulations presented below were therefore carried out using the 3.36 M cell

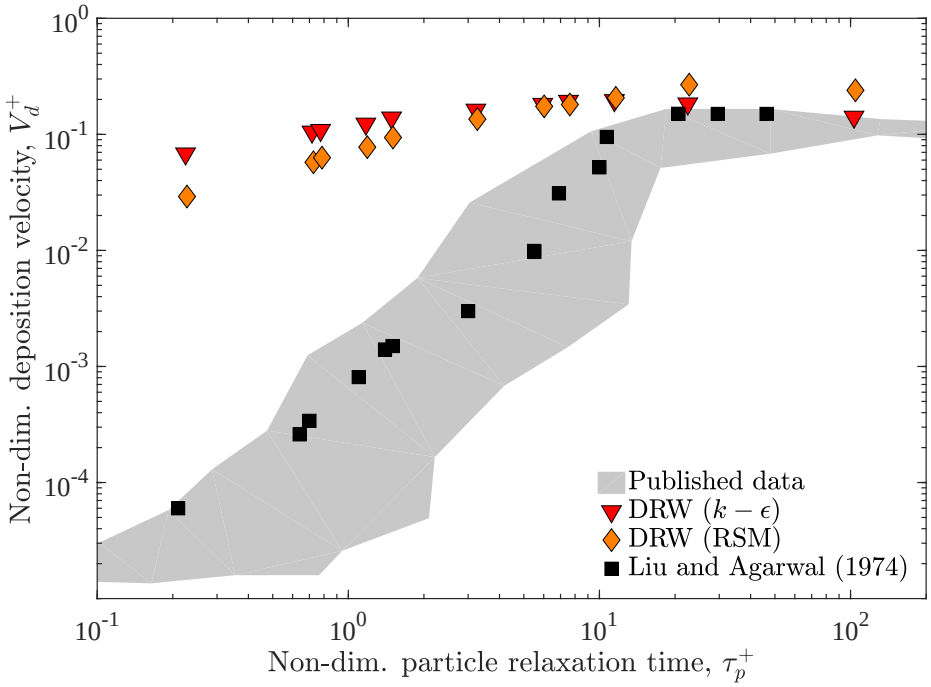

Figure 3.3: Non-dimensional deposition velocity V_d^+ against τ_p^+ for the CRW and DRW particle deposition models. Grey area shows extent of key published deposition data (Friedlander and Johnstone, 1957; Sehmel, 1968; Liu and Agarwal, 1974).

mesh, with third order spatial discretisation of the realisable k-ϵ model.

3.1.2 Simulation results

Simulations of the L&A data using the discrete random walk are shown in Fig. 3.3. Trials with both the realisable k-ϵ and RSM turbulence models were carried out; little improvement was seen in the RSM simulations. Obtaining a fully converged and stable continuous phase solution using the RSM turbulence model can be extremely challenging for engine-realistic flows, which places an inherent limit on the usability of the DRW model in combination with this model.

3.2 Continuous random walk

3.2.1 Model description

The CRW model of Dehbi (2008a) is another model for the instantaneous fluid fluctuating velocity as seen by a particle, based upon the normalised Langevin equation (Iliopoulos et al., 2003). The general form of the increment in normalised fluctuating velocity is given by

$$d\left(\frac{u_i}{\sigma_i}\right) = -\left(\frac{u_i}{\sigma_i}\right)\frac{dt}{\tau_L} + \sqrt{\frac{2}{\tau_L}}d\xi_i + A_i dt. \tag{3.8}$$

Here σ is root mean square fluctuating velocity, τ_L the Lagrangian time step, $d\xi$ a Gaussian random number with zero mean and variance dt, therefore is solved as an incremental Weiner process, $d\xi = \xi\sqrt{dt}$, and A_i the drift correction. The model is calculated in two layers, the bulk and boundary layer regions. The division is defined by $y^+ = 100$. The root mean square fluctuating velocity σ is defined differently for either layer. In the bulk region it is isotropic,

$$\sigma_1 = \sigma_2 = \sigma_3 = \sigma = \sqrt{\frac{2k}{3}}, \tag{3.9}$$

where k is the turbulent kinetic energy. In the boundary layer, turbulence is strongly anisotropic. The model accounts for this using normalised fluctuating velocities, σ^+,

$$\sigma^+ = \frac{\sigma}{u^*}, \tag{3.10}$$

which are functions of y^+. These correlations are calculated from ensemble averages of the Reynolds stresses in channel flow DNS, in the streamwise (index 1), wall-normal (2), and spanwise (3) directions:

$$\sigma_1^+ \equiv \frac{\sigma_1}{u^*} = \frac{0.40y^+}{1 + 0.0239(y^+)^{1.496}}, \tag{3.11}$$

$$\sigma_2^+ \equiv \frac{\sigma_2}{u^*} = \frac{0.0116(y^+)^2}{1 + 0.203y^+ + 0.0014(y^+)^{2.421}}, \tag{3.12}$$

$$\sigma_3^+ \equiv \frac{\sigma_3}{u^*} = \frac{0.19y^+}{1 + 0.0361(y^+)^{1.322}}. \tag{3.13}$$

To make these orthogonal directions applicable to an arbitrary geometry, a body-fitted coordinate system (BFCS, Fig. 3.4) is applied within the boundary layer region. The streamwise direction is calculated from the bulk flow. The wall-normal direction is calculated from the face normal vector of the nearest wall face. The spanwise direction is then calculated from the cross product of the first two vectors.

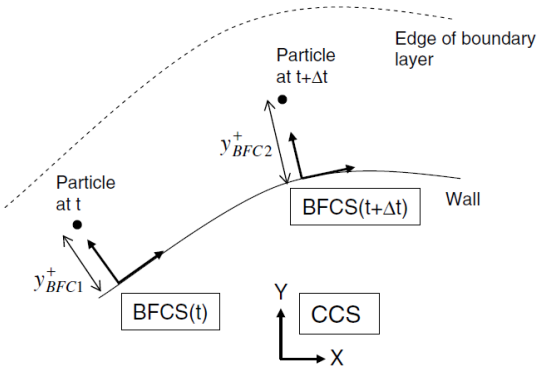

Figure 3.4: Body-fitted coordinate system for use in boundary layer. From Dehbi (2008a).

The Lagrangian integral time scale τ_L is a spatially-varying property of the fluid (turbulence), which characterises large-scale turbulent motion. The Lagrangian integral time scale is assumed isotropic following the DNS study of Bocksell and Loth (2001). Again the definition is split at $y^+ = 100$; for the bulk region,

$$\tau_L = \frac{2}{c_0}\frac{k}{\epsilon}, \tag{3.14}$$

where $c_0 = 14$, from the DNS of Mito and Hanratty (2002). In the boundary layer region, fits of non-dimensional Lagrangian integral time scale, τ_L^+ are used from Reeks (1977):

$$\tau_L^+ = \begin{cases} 10 & \text{for } y^+ \leq 5, \\ 7.122 + 0.5731 y^+ - 0.00129\,(y^+)^2 & \text{for } 5 \leq y^+ \leq 100, \end{cases} \tag{3.15}$$

where τ_L^+ is defined

$$\tau_L^+ = \frac{\tau_L}{\tau_{g,\,w}} = \tau_L \frac{\nu}{(u^*)^2}. \tag{3.16}$$

The drift correction A_i in the bulk region is defined as

$$A_i = \frac{\partial}{\partial x_i}\left(\frac{\overline{u_i u_i}}{\sigma_i}\right)\frac{1}{1+Stk} = \frac{1}{2\sigma_i}\frac{\partial \sigma_i^2}{\partial x_i}\frac{1}{1+Stk} = \frac{1}{3\sigma}\frac{\partial k}{\partial x_i}\frac{1}{1+Stk}, \tag{3.17}$$

where isotropic turbulence (Eq. 3.9) has been invoked to get from the second to third expression on the right hand side. In the boundary layer the drift correction formulation differs,

$$A_{i2} = \frac{\partial}{\partial x_2}\left(\frac{\overline{u_2 u_i}}{\sigma_i}\right)\frac{1}{1+Stk}. \tag{3.18}$$

Dehbi eventually only considers the drift correction in the wall-normal direction, due to difficulties calculating the product $\overline{u_1 u_2}$, stating that this assumption '*should not alter the predictions significantly since it is the turbulent motion in the wall normal direction which controls the overall particle dispersion and deposition physics.*'

The model algorithm is as follows. Two preliminary calculations are undertaken for each volume cell; to locate the nearest wall face and store that distance, vector, and the corresponding friction velocity, and secondly to store the gradients of kinetic energy.

For each particle step the model calculates the particle's non-dimensional wall distance, y_p^+,

$$y_p^+ = \frac{u^* y_p}{\nu} \tag{3.19}$$

where u^* is the friction velocity at the nearest wall cell, and y_p the distance from particle centre to that nearest wall cell. If $y_p^+ > 100$ the particle is considered to be in the bulk flow. If the particle is in the boundary layer region ($y_p^+ \leq 100$), the particle is transformed into the BFCS. Eq. 3.8 is solved for the increment of fluctuating velocity, with the appropriate values of σ_i and A_{ii}.

The increment of fluctuating velocity is transformed back to the global coordinate system if necessary, and is added to the mean flow velocity vector to give an instantaneous fluid velocity as seen by the particle. This introduces the turbophoretic acceleration to the particle's motion.

Numerical integration is carried out using the first order implicit Euler method, leading to the expression for the normalised fluid velocity fluctuation at the current time step n,

$$\left[\frac{u_i}{\sigma_i}\right]^n = \left[\frac{1}{1+\frac{dt}{\tau_L}}\right]^n \left(\left[\frac{u_i}{\sigma_i}\right]^{n-1} + \left[\xi_i\sqrt{\frac{2dt}{\tau_L}} + A_i dt\right]^n\right). \tag{3.20}$$

Trials using the Euler-Maruyama method showed the first order implicit Euler scheme to be preferable. Our initial implementation of the CRW model was provided by Ghahramani et al. (2014). This takes the form of a series of User Defined Functions (UDFs) for Fluent. Verification of the Ghahramani implementation against the Dehbi

original can be found in Ghahramani et al. (2014). This showed the that model reproduced the simulations as carried out by Dehbi with high fidelity.

The CRW model has been previously assessed in a number of configurations by its author, in the main. These are listed in Table 3.1, with a brief comment regarding the nature of the assessment. It can be seen that assessment of the CRW model is lacking for horizontal and gravitational conditions, and also for thermophoretic conditions for particles in the diffusion-impaction regime.

Flow/conditions	Publication	Comments
Vertical pipe flow	Dehbi (2008a)	Shown for $\tau_p^+ > 6$. Reasonable match to L&A data using a 3D structured grid.
Bends	Dehbi (2008a)	Good reproduction of the Pui et al. (1987) correlation, using RSM. Turbulent enhancement of deposition for medium-inertia particles. Low Reynolds number (4080) used.
Channel flow	Dehbi (2010b)	Good reproduction of the mean and root mean square particle velocity profiles in axial and wall-normal direction. Fluid-particle statistics were not considered. The gravitational force was zero.
Thermophoresis	Dehbi (2009)	Good prediction of two sets of experimental thermophoretic data, using the Talbot thermophoretic coefficient. Not tested for $\tau_p^+ > 0.24$.
Throat	Dehbi (2008a); Ghahramani et al. (2014); Dehbi (2011)	RSM and CRW closer to experimental data than LES. Deposition overpredicted at low Stk, Re, and underpredicted at high Stk, Re.
Mixing	Dehbi and de Crechy (2011)	RSM and CRW not successful, but use of DES (detached eddy simulation) indicated ability to capture the mixing of two scalars.
External	Dehbi and Martin (2011)	Deposition simulated onto array of spheres. For $Stk > 0.3$, results were very promising.

Table 3.1: Flow conditions under which the CRW has been validated against experimental data

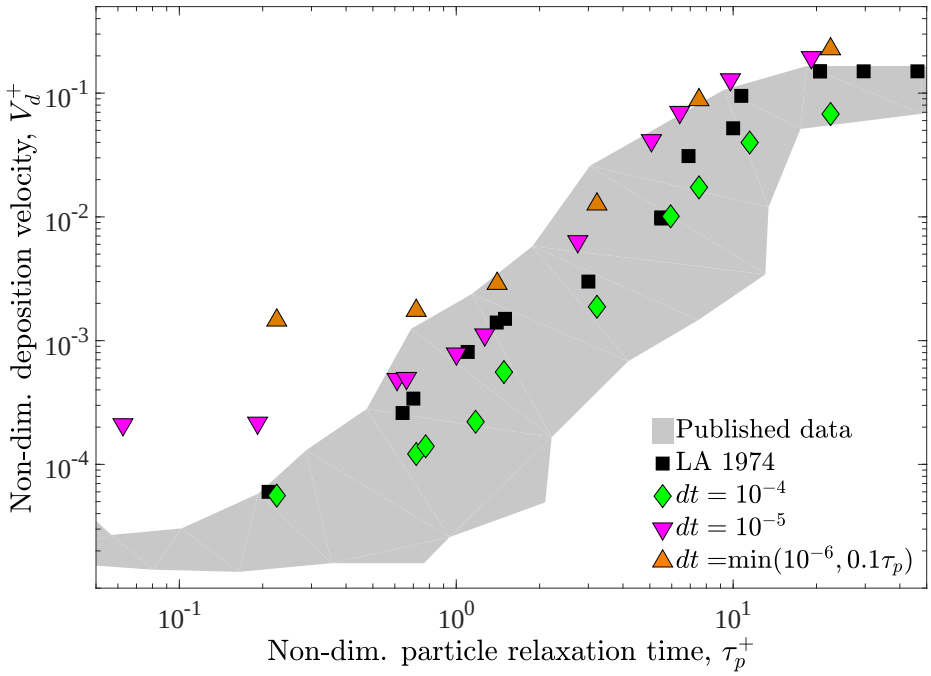

Figure 3.5: Plot of non-dimensional deposition velocity against non-dimensional particle relaxation time, showing the strong dependence on integration time step dt seen, for varying values of dt.

3.2.2 Integration time step

When solving the normalised Langevin equation (Eq. 3.8), the numerical integration time step dt must be correctly defined. A strong dependency of deposition fraction on time step was seen, as highlighted by Fig. 3.5. This presents simulated deposition statistics for the L&A experiments, as in the previous section. Here fixed values of dt are used, $dt = 10^{-4}$, 10^{-5}, $min(10^{-6}, 0.1\tau_p)$, where the latter is the time step criterion proposed by Dehbi. Ghahramani et al. proposed that $dt = \min(10^{-7}, 0.1\tau_p)$ fitted the selected data to a greater extent.

In response to this dependency, a new definition of the time step was formed. From the work of Sawford (1984, 1985), it is understood that $dt \ll \tau_L$, and as $t \gg t_k$ (τ_L and t_k are the Lagrangian and Kolmagorov time scales respectively) we assume $dt \gg t_k$. This then leads to

$$t_k \ll dt \ll \tau_L. \tag{3.21}$$

Taking a geometric mean of t_k and τ_L as a method to fulfil the inequality gives

$$dt = \sqrt{t_k \tau_L}. \tag{3.22}$$

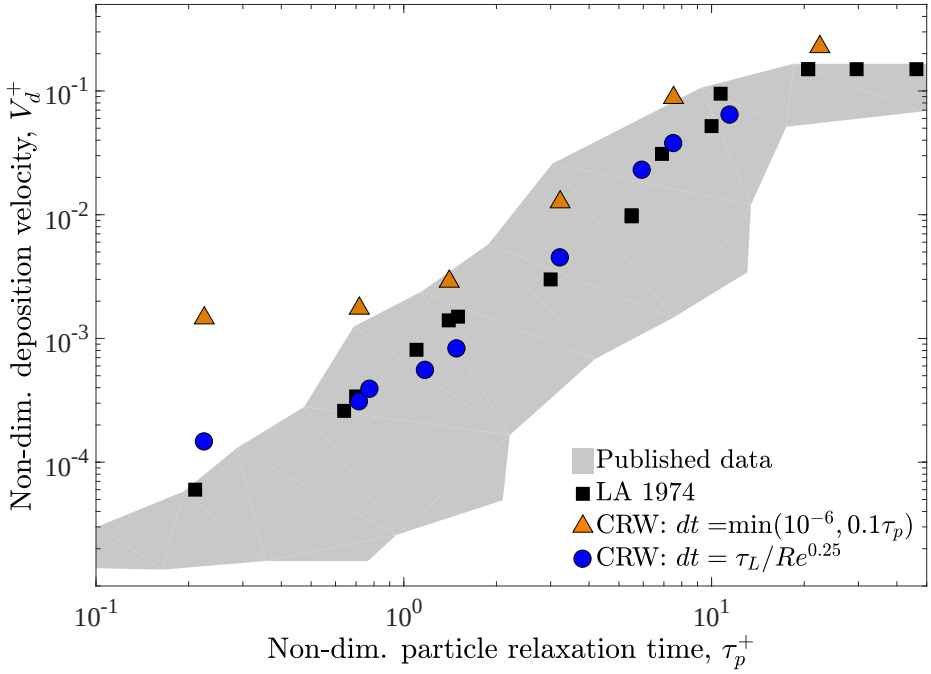

(a)

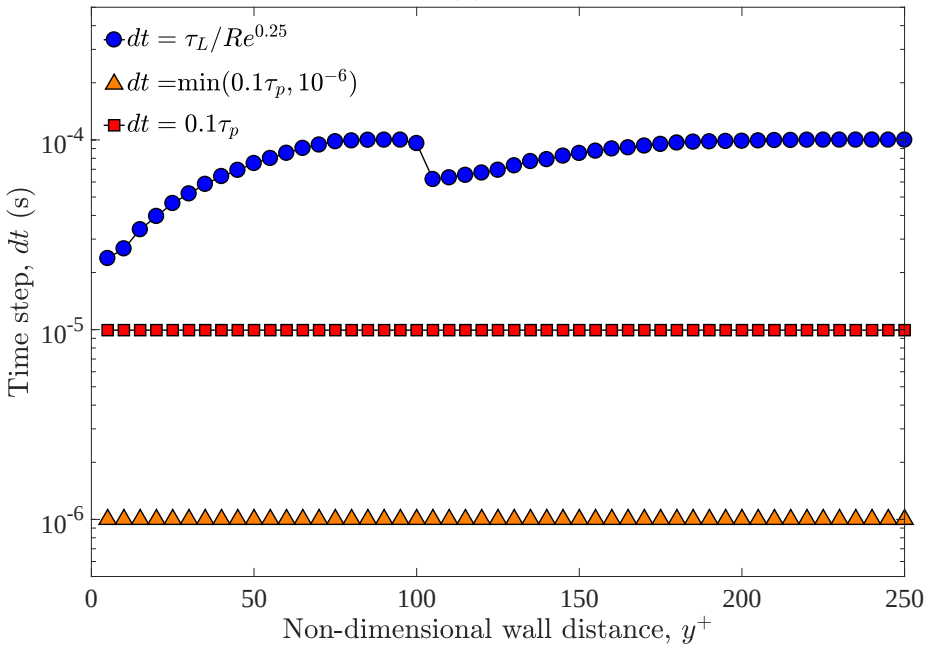

(b)

Figure 3.6: *Top*: Comparison of predicted deposition based on new and Dehbi time step criteria. Spread of published vertical pipe flow experimental data for reference. *Bottom*: actual time step values for above simulations (4 µm particle).

The definition $t_k = Re^{-0.5}\tau_L$ from Sawford (1985) is then into substituted Eq. 3.22, leading to

$$dt = \frac{\tau_L}{Re^{0.25}}. \tag{3.23}$$

This new definition of the integration time step was implemented within the CRW UDF and applied to the above simulation, Fig. 3.6a. A maximum time step of 10^{-4} s was allowed. A significant improvement can be seen over the whole diffusion-impaction regime. The actual values of the time step with y^+ are shown in Fig. 3.6b. A 4 µm particle is shown, however particle size does not affect the new time step definition, and only affects the Dehbi criterion for $d_p < 1.3$ µm in this flow. The dip in the new time step line (top) is due to the division of τ_L calculation (Eq. 3.15, 3.14). It is observed that the new time step definition is $20 - 100\times$ larger than the Dehbi criterion. The time step, and its effect on the results, is discussed more below.

Simulations were undertaken at varying Re in order to demonstrate the applicability of the new time step definition at a range of Reynolds numbers, as shown in Fig. 3.7. L&A's data for varying Re ($Re = 10\,000, 50\,000$) is also plotted to indicate the low-Re dependence on deposition that should be expected. The trend within the simulation results is extremely strong in general, with the exception of the lowest data points within both the $Re = 10\,000$ and $20\,000$ sets, which over-predict deposition by a factor of ~ 2.

That some dependency of the results on the time step exists may be partially a function of the model formulation. From inspection of Eq. 3.20 it can be seen that the stochastic and drift correction terms have different dependencies on $\sqrt{dt}$ and dt respectively. Hence, as dt becomes smaller, the drift term (Eq. 3.17-3.18) becomes smaller faster than the stochastic term, becoming negligible for small dt.

The drift correction term was noted (Dehbi (2008a) and citations therein) to significantly improve comparisons to experiments; simulations without the drift term (MacInnes and Bracco, 1992) showed non-physical drift or diffusion of tracer particles into the boundary layer region, which would increase the rate of deposition. The drift correction term is dependent on the reciprocal of Stokes number (Eq. 3.17-3.18), as smaller particles, towards the tracer limit, are more susceptible to the non-physical drift. Hence reduction of the $A_i dt$ term may reduce the effect of the drift correction.

An investigation was carried out into the magnitude of the drift correction by setting A_i to zero. The resultant simulations, Fig. 3.8, showed that without the drift correction, the CRW model over-predicts deposition similarly to the DRW. The

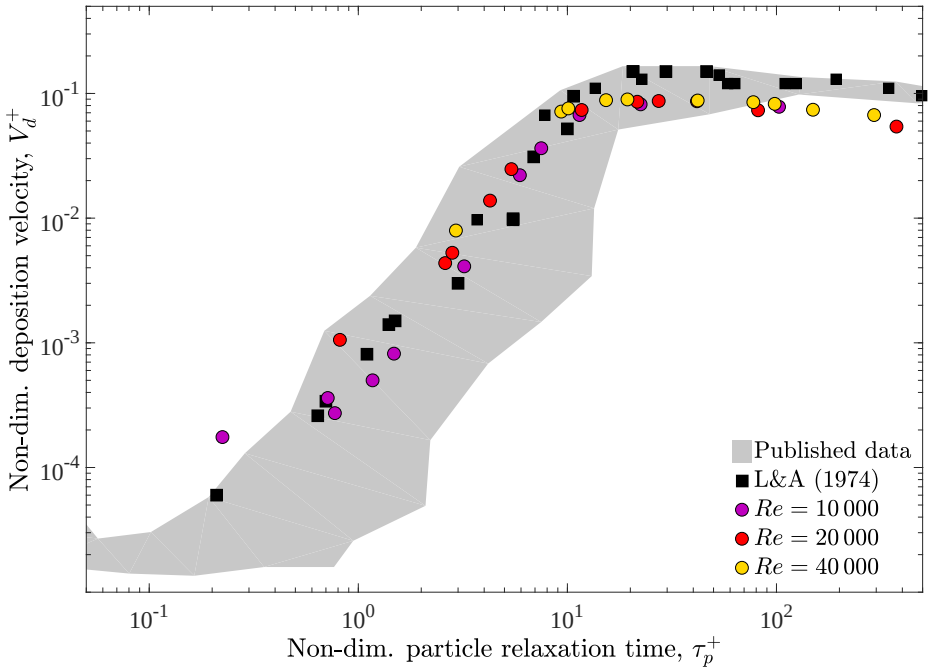

Figure 3.7: Deposition statistics at varying Reynolds number using new time step definition, showing applicability at a range of Reynolds numbers.

integration time step was also varied from $0.1dt$, dt, $10dt$, where dt is calculated as Eq. 3.23. Without the drift correction, there is almost no dependence on time step of the model; over the time steps shown the relative shift from the mean at each value of τ_p^+ was 0.6-7.5%. This implies that the different dependencies on dt in the CRW model are a possible cause of the observed time step dependency.

It is observed that the time step of Dehbi does not appear to reproduce the Liu and Agarwal experimental data particularly well in these simulations. Two main reasons are given for this. Firstly, Dehbi chose to publish his simulations for $\tau_p^+ > 5.5$, which excludes half of the diffusion-impaction regime. The reason for this is not given in his paper, though when Ghahramani showed a smaller τ_p^+ point ($\tau_p^+ = 1.7$), this simulation was an order of magnitude from the experimental data. A second point is that the Liu and Agarwal simulations shown in this chapter used the 3.36 M cell mesh, which the mesh sensitivity study showed produced convergence of the deposition results using the new integration time step. For the finer mesh, the Dehbi time step showed closer reproduction of the experimental results than larger time steps, which may be partly responsible for the disparity. Dehbi (and upon reproduction, Ghahramani) also appear to have used a finer boundary layer mesh back calculating from the given mesh description suggests an expansion ratio of ∼1.05, which was not trialled in this study. Such a mesh requirement would be

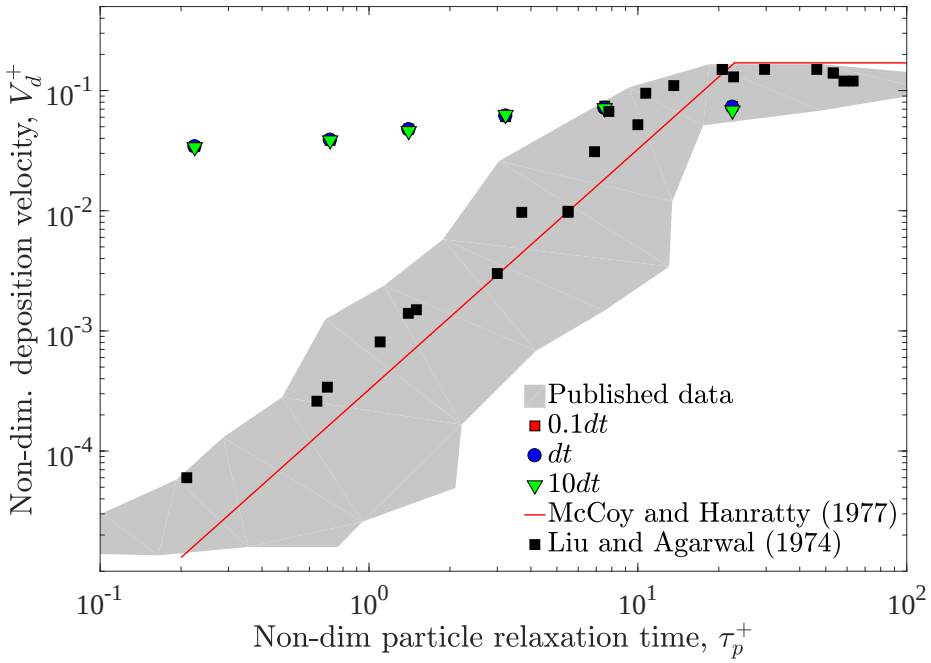

Figure 3.8: Effect of removing the drift correction, Eq. 3.18, 3.17, from the CRW model. Time step varied $0.1dt$, dt, $10dt$, where dt is calculated as Eq. 3.23.

prohibitive for industrial applications in terms of both size and difficulty. A further, intensive mesh study could address such issues.

It is also noted that the CRW model is not alone in showing a dependency of V_d^+ on dt. Investigations were carried out into the DRW model as implemented in Fluent, Fig. 3.9. Two particle sizes, 1 and 5 µm, were used. The integration time step was varied directly using the 'step length factor' option, Fig. 3.9a. Here the nominal value to dt is divided by the step length factor, and both axes are normalised to the value at a relative step size of 1.0. Whilst the larger particles (5 µm) showed a negligible dependency, the smaller particles (1 µm) showed a significant change in deposition fraction with changing dt, reducing by one fifth. When the eddy lifetime was (Eq. 3.3 was adjusted via the constant in Eq. 3.5, a strong dependency of deposition rate on eddy lifetime τ_e is noted, Fig. 3.9b.

It is seen that the approach taken to redefining the time step in the current study is different to that of Dehbi and Ghahramani et al., who chose to link theirs to the particle relaxation time, rather than to a fluid time scale, as done in this study. Other published models and simulations have followed attached their time step to τ_p; Dehbi (2010a, 2011) chose to use $dt = 0.1\tau_p$ in later publications using the same CRW model without comment as to the change. Arcen and Taniere (2009) used τ_p-linked time steps, though varied this with τ_p^+. However a number of other authors have linked

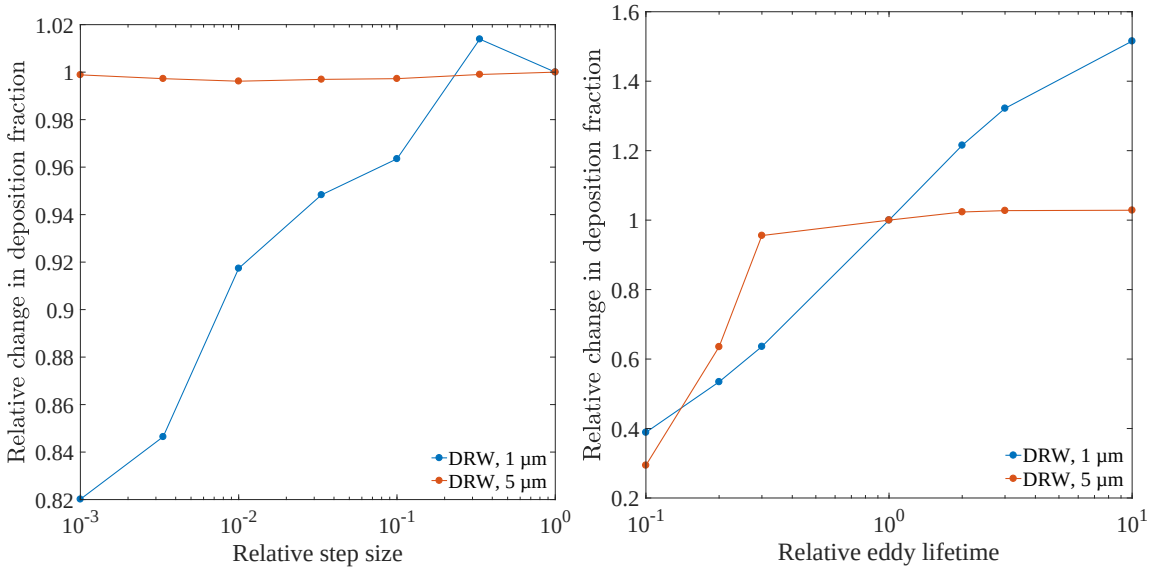

(a) (b)

Figure 3.9: Effect of changing integration time scale on deposition rate from DRW model. *Left*: scaling integration time step. *Right*: scaling eddy lifetime. Scaling is relative to the initial values proposed by in User Guide (ANSYS, 2011a).

their time step to the fluid conditions; Sawford (1985) used $dt = 0.1\tau_L$, and Taniere and Arcen (2014) used $dt^+ = 0.1$, where the non-dimensionalisation was undertaken using the fluid wall time scale $\tau_{g,w}$, Eq. 2.18. Sommerfeld (2003) used a criteria $dt = min\,(\tau_p,\, \tau_L,\, \tau_c)$, where the final term is a collision time scale. Finally, Mehel et al. (2010) used a fixed time step of $dt = 10^{-4}$. It can be seen that there are a range of approaches used within the literature, without any particular conclusion regarding the pros and cons of specific approaches.

3.2.3 Reynolds-independence of DNS statistics

The quoted statistics are taken from the simulation of Dreeben and Pope (designated 'DP', Dreeben and Pope (1997)) at $Re_\tau = 395$ ($Re = 13\,000$ based on bulk velocity and channel height). It is stated that these statistics show only a slight Re-dependence for two-dimensional flows. In order to investigate this assumption, the DNS of Kim, Moin and Moser (designated 'KMM', Kim et al. (1987)) and Moser, Kim and Moin (designated 'MKM', Moser et al. (1999) for channel flow were used to construct correlations of the same form as those used in the model. The KMM and MKM simulations were undertaken at $Re_\tau = 180, 395, 590$, ($Re = 5\,280, 12\,970, 20\,510$). Fig. 3.10 shows the dimensionless fluctuating velocity correlations.

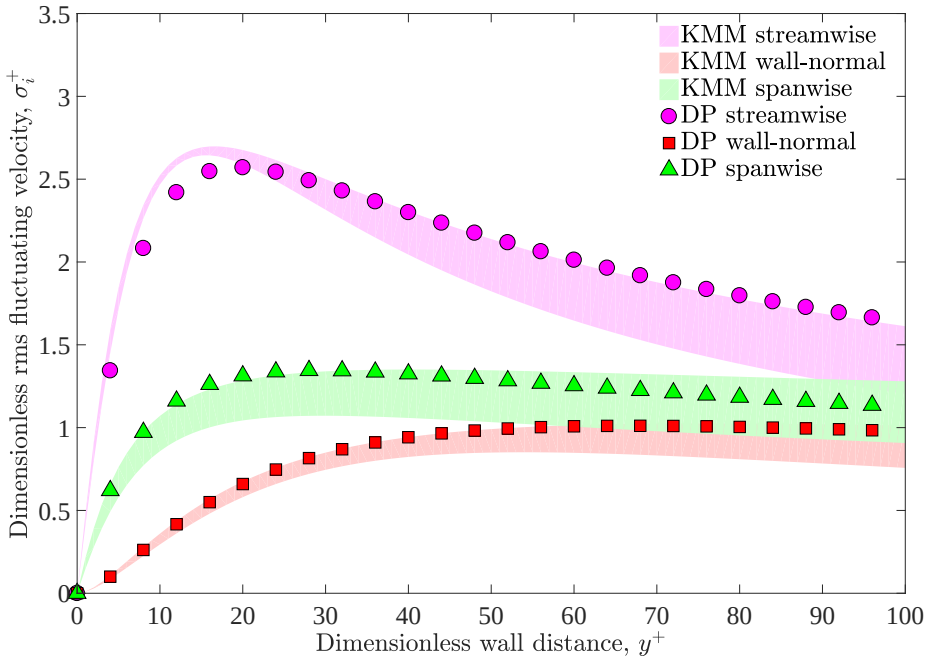

Figure 3.10: Variation of dimensionless fluctuating velocities (streamwise, wall-normal, spanwise) with friction Reynolds number Re_τ against dimensionless wall distance. Data from Dreeben and Pope (1997); Kim et al. (1987); Moser et al. (1999). Re_τ increases moving upwards through each coloured region.

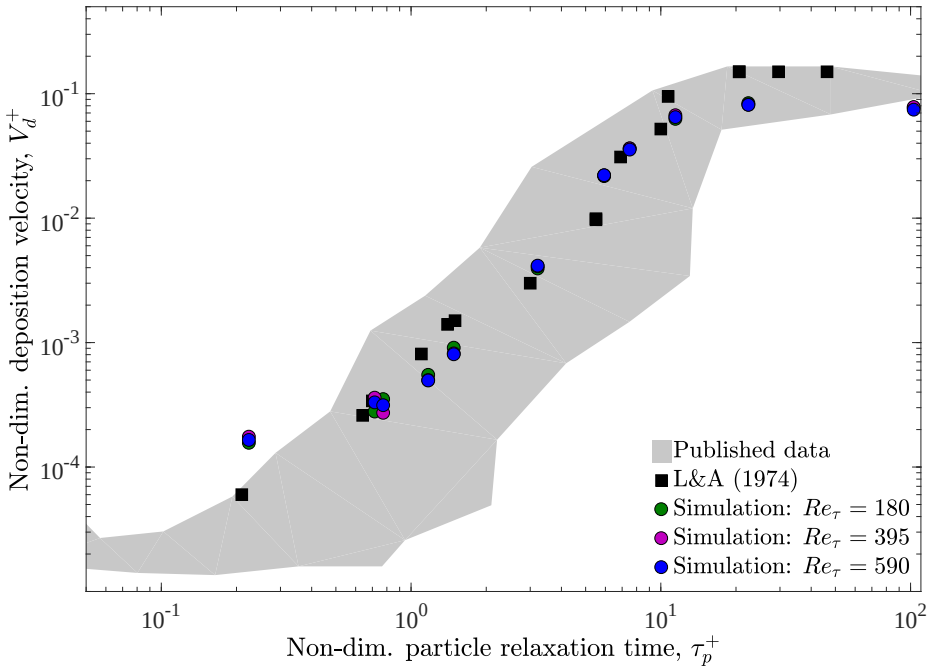

Figure 3.11: Simulation of L&A experimental data at $Re = 9800$. Correlations for $Re_\tau = 180$, 395, 590 used to demonstrate near-independence of deposition characteristics from DNS statistics used.

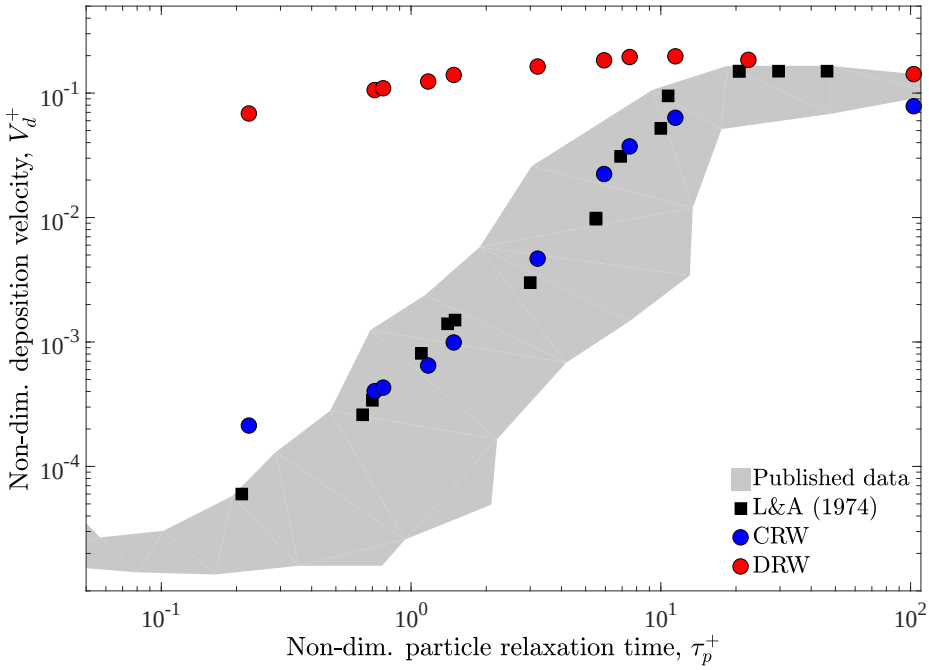

Figure 3.12: Non-dimensional deposition velocity V_d^+ against τ_p^+ for the CRW and DRW particle deposition models.

Simulations of the Liu and Agarwal vertical pipe flow experiments were carried out, varying the non-dimensional fluctuating velocity statistics used to investigate any potential dependence. The new correlations based on the data of KMM and MKM were implemented within the CRW user defined function. The L&A simulation results are shown in Fig. 3.11. Despite the Re-dependence seen in some parts of the boundary layer region, it appears that the deposition predicted is mainly dependent on the non-dimensional fluctuating velocity statistics in the near-wall region of the boundary layer ($y^+ < 10$), where correlations collapse to a single curve in each direction. This is particularly the case with the wall-normal profile; it is proposed that this direction dominates the deposition trends seen.

In light of this it is suggested that for ambient conditions, the assumptions of Re-independence are reasonable. However this may not be the case for high temperature flows; limited DNS data for applicable flows at high temperature could be found in the open literature, though the work of Duan and Martin (2011) indicates that high and low enthalpy boundary layers closely resemble each other.

3.2.4 Comparison of CRW and DRW models

The $Re = 10\,000$ simulations for both the continuous and discrete random walk models are shown in Fig. 3.12. Across the diffusion-impaction regime ($0.3 < \tau_p^+ < 20$),

the CRW model is seen to perform better, except at the diffusion-impaction/inertia-moderated junction. This matches the findings of other researchers, who have published similar findings. Hence going forwards, the CRW is preferred, as even in these simple flows is is seen to produce deposition predictions orders of magnitude closer to experimental data than the DRW.

3.3 Dynamic mesh morphing

This section describes the development of a dynamic mesh morphing method for updating a numerical domain based on the deposition history. This approach takes advantage of inbuilt functionality within Fluent for the transfer of boundary movement into the volume mesh. Capability was built to determine the motion of the boundary, using user defined functions. This domain updating method runs deposition simulations in pseudo time, allowing the assessment of unsteady deposition rate and trends with injected mass/time.

3.3.1 Description

In order to simulate the coupled effect that deposited particles have on the flow geometry and hence continuous phase solution, a method for moving the domain boundaries has been developed. This is integrated into ANSYS Fluent using the UDF capabilities, and makes use of existing dynamic mesh capabilities offered within Fluent (for fluid-structure interaction etc.). The advantages of such an approach are:

- *Speed*: carrying out the mesh adjustments within Fluent, rather than exporting the mesh to ICEM and re-meshing, is many times quicker.
- *Ease of calculation*: access to the required mesh data (surface points and face normals etc.) is simple in Fluent.
- *Ease of use*: scripting of the functions that carry out the mesh morphing process is straightforward and mean as many iterations as required can be looped.

Such an approach comes with the caveat that as the mesh is not fully regenerated at each mesh morphing iteration, the quality of the mesh can deteriorate over time. To some extent this can be offset by reducing the injected mass per iteration. Exporting the domain surfaces to ICEM and carrying out a full re-mesh is sometimes necessary to continue the simulation.

Initially the mesh and continuous phase solution are generated. The mesh-morphing iteration loop is then carried out (Fig. 3.13), made up of the following three parts: 1. particle tracking, 2. dynamic mesh morphing, 3. re-convergence of the continuous phase solution.

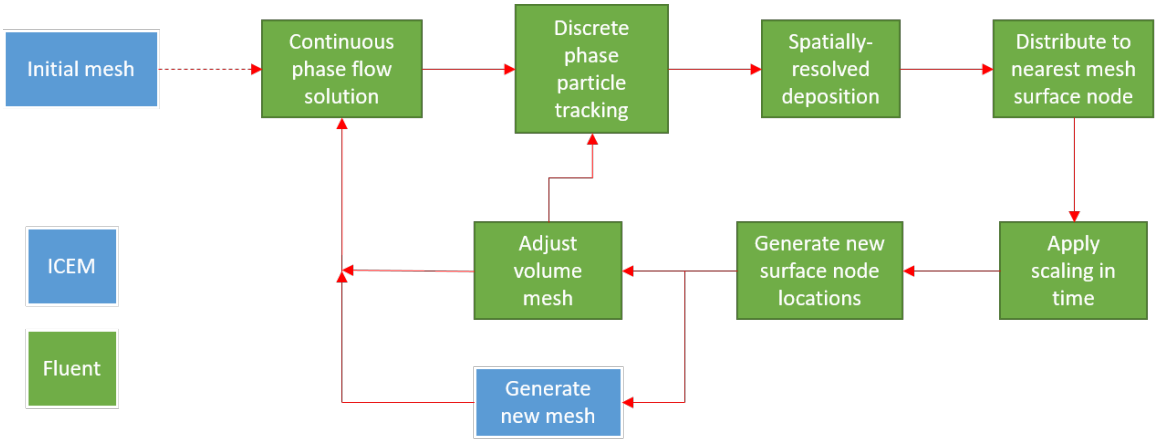

Figure 3.13: Diagram demonstrating dynamic mesh morphing approach

3.3.2 Implementation

The dynamic mesh morphing approach presented here requires two fundamental parts: firstly recalculation of the domain boundary, and secondly redistribution of this boundary movement into the volume mesh. The description below is done in reference to triangular surface elements (unstructured meshing); a similar method could be applied to the quadrilateral surface elements used in structured meshing.

3.3.2.1 Boundary node movement

The new boundary node locations are calculated based on the deposited mass assigned to each node. During the particle tracking phase, a mass flow rate per deposited particle is assigned by the solver (ANSYS, 2011c). This is integrated in time, assuming steady injection into the domain. Once a particle has deposited on a surface face, deposited mass m_{dep} is distributed to nodes. This is carried out based on location of particle, $\mathbf{x}_p$, node, $\mathbf{x}_n^i$, and deposited face centroid, $\mathbf{x}_c$. A distribution coefficient is defined, α; this splits the deposited mass either equally between nodes (if deposition has occurred centrally on the face) or assigns it to single node (if deposition has occurred close to a node):

$$\alpha = \frac{min\left(\mathbf{x}_p - \mathbf{x}_n^i\right)}{c\left(\mathbf{x}_p - \mathbf{x}_c\right)}. \tag{3.24}$$

Here c is a distribution constant to weight allocation of deposited mass towards a node ($c > 1$) or towards the centroid ($c < 1$). Index i are the nodes of the face on which deposition has occurred, the 'deposited face'. If $\alpha < 1$ all deposition volume due to the impacting particle is assigned to node i (nearest to deposition). If $\alpha \geq 1$ deposited volume is divided equally between all nodes of the deposited face. This approach reduces the likelihood of a 'spiky' mesh resulting from large individual node movement relative to surrounding nodes. It is reasonable to assume some distribution of deposition as each tracked particle represents a number of individual particles, depending on the specified injection mass flow rate. Individual node deposited masses are summed once per iteration, and stored in user defined memory (UDM) within Fluent.

Upon completion of particle tracking each node is checked for deposition in UDM. If deposited mass has been assigned to a node, displacement $\boldsymbol{\delta}_n$ is calculated. Node i is displaced in the direction $\hat{\mathbf{n}}_i$ given by an average of the (unit) face normals of the j surrounding faces,

$$\hat{\mathbf{n}}_i = \frac{\sum^j \hat{\mathbf{n}}_j}{\left|\sum^j \hat{\mathbf{n}}_j\right|}. \tag{3.25}$$

Deposited volume, Q_{dep}, is calculated from deposited mass and converted to individual node displacements. This assumes that the displaced volume generated from individual node displacements, Q_{disp}, can be combined using linear superposition, and hence that individual node displacements can be calculated individually. Displacing nodes individually relative to all surrounding nodes produces a j-sided pyramid deformation in the boundary mesh. An initial guess at node displacement δ_n (pyramid vertex height) can be made assuming a pyramid with a base formed from a regular j-sided polygon, base area A_b equal to the sum of the face areas surrounding the node. The vertex height for any such pyramid is given by

$$\delta = \frac{3Q_{py}}{A_b} = \frac{3Q_{dep}}{A_b}, \tag{3.26}$$

where Q_{py} is pyramidal volume. Hence the node displacement $\boldsymbol{\delta}_n$ is calculated, $\boldsymbol{\delta}_n = \delta_n \hat{\mathbf{n}}_i$. From the sum of initial node position $\mathbf{x}_n^0$ and $\boldsymbol{\delta}_n$, the displaced node position

$\mathbf{x}_n^1$ is calculated. The displaced volume is calculated by dividing the pyramid into j tetrahedra, each formed from the three nodes of a face and sharing $\mathbf{x}_n^1$ as the fourth vertex. Tetrahedral volume Q_{tet} is calculated from the scalar triple product,

$$Q_{tet} = \frac{1}{6}\left(\mathbf{x}_n^1 - \mathbf{x}_f^1\right) \cdot \left(\mathbf{x}_n^1 - \mathbf{x}_f^2\right) \times \left(\mathbf{x}_n^1 - \mathbf{x}_f^3\right), \tag{3.27}$$

where $\mathbf{x}_f^k$ are the nodes defining the initial position of the surface face j. Scalar triple product gives parallelepiped volume, twice the tetrahedral volume, hence the factor of 1/2.

Summing the individual tetrahedral volumes gives Q_{disp}, which is similar to Q_{dep}. Differences occur when the individual boundary face cells are not uniform in area. The ratio of Q_{dep}/Q_{disp} is then used to scale δ_n to produce an updated value, and hence $\boldsymbol{\delta}_n$, accounting for non-uniform face sizes. The final node position $\mathbf{x}_n^1$ is recalculated and returned to Fluent for every displaced node. Total deposited and displaced volumes were reported at the end of each mesh morphing iteration.

3.3.2.2 Volume mesh

Once the domain boundary has been redefined, the attached volume mesh is adjusted to accommodate the node displacements. This is carried out by feeding calculated node displacements into the dynamic meshing functions within Fluent. Two methods are available for transferring boundary movement to the volume mesh: boundary layer deformation and diffusion-based smoothing. Both are described in ANSYS (2011a). Boundary layer deformation, Fig. 3.14, is capable of retaining the prism layer structure to quite a high degree of fidelity; whole wall-normal stacks of prism nodes are moved, retaining the boundary mesh expansion ratio. This is highly desirable for continued solution of both the continuous and discrete phases. This method was capable of withstanding very large deformations, including individual iteration steps larger than the first cell height.

The second method for transferring boundary displacement into the volume mesh is diffusion-based smoothing. This absorbs the displacement based on either the local cell volume or cell centroid to wall distance, both relative to a mesh average.

Whilst diffusion-based smoothing was found to be in general more robust than boundary layer deformation, the actual boundary layer mesh is not retained to the same level of fidelity. Hence the boundary layer smoothing method was chosen for use in this study.

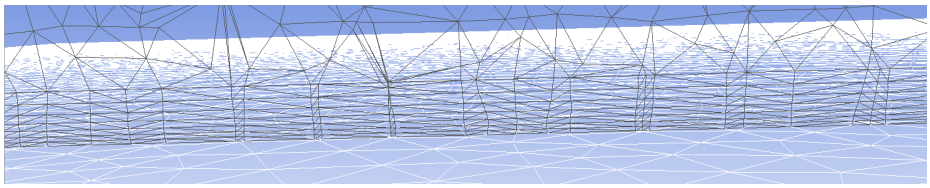

(a) Undeformed mesh

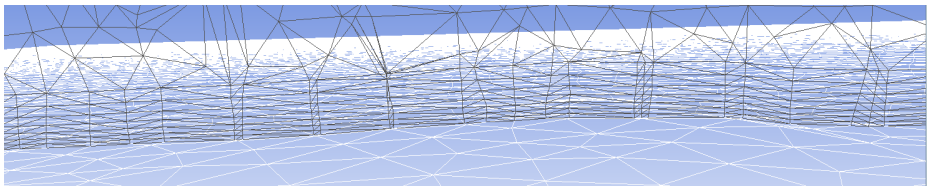

(b) After one mesh morphing iteration

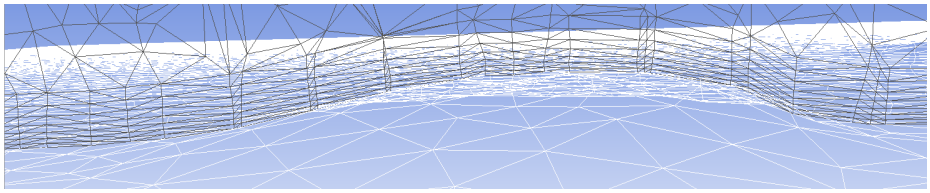

(c) After four mesh morphing iterations

Figure 3.14: 'Boundary layer smoothing' method demonstrating retention of boundary layer mesh despite significant deformation.

3.3.3 Initial demonstration of DMM technique

Particle-laden flow through a single impingement jet was used as an initial demonstration of the DMM technique, Fig. 3.15. Gas enters through the top surface, is impinged onto the bottom surface, and exits the domain through all sides of the lower box. Deposition and build-up occur on the dark blue portion of the bottom surface, where the mesh can be seen to be deformed. Flow conditions are as specified in section 6.2 where appropriate: impingement hole diameter $D_h = 0.71$ mm, spacing $z/D_h = 2.0$, $Re_{jet} = 1000$, particle size distribution as Fig. 6.4. The 'all stick' boundary condition is applied.

Fig. 3.16 shows six points in the build-up process. Plots are coloured by normalised deposition height $\bar{\delta}$: the ratio of deposition height δ to the impingement hole diameter D_h. As more DMM iterations are run, the mesh surface deforms upwards, into the domain.

3.3.4 Dependencies

The solution dependency on solver precision and mesh sizing was investigated. Solver precision was shown to lead to maximum differences of 1.8% in deposition height,

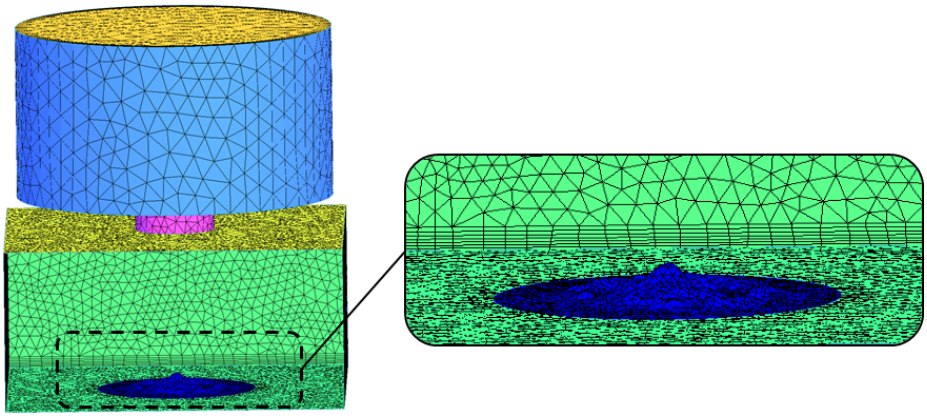

Figure 3.15: Geometry for single hole impingement geometry. Inlet is on the top surface, where particles are injected uniformly. DMM is applied on the lower surface. Gas is vented out of the domain from all four sides of the lower box. Region where DMM is occurring is enlarged on right.

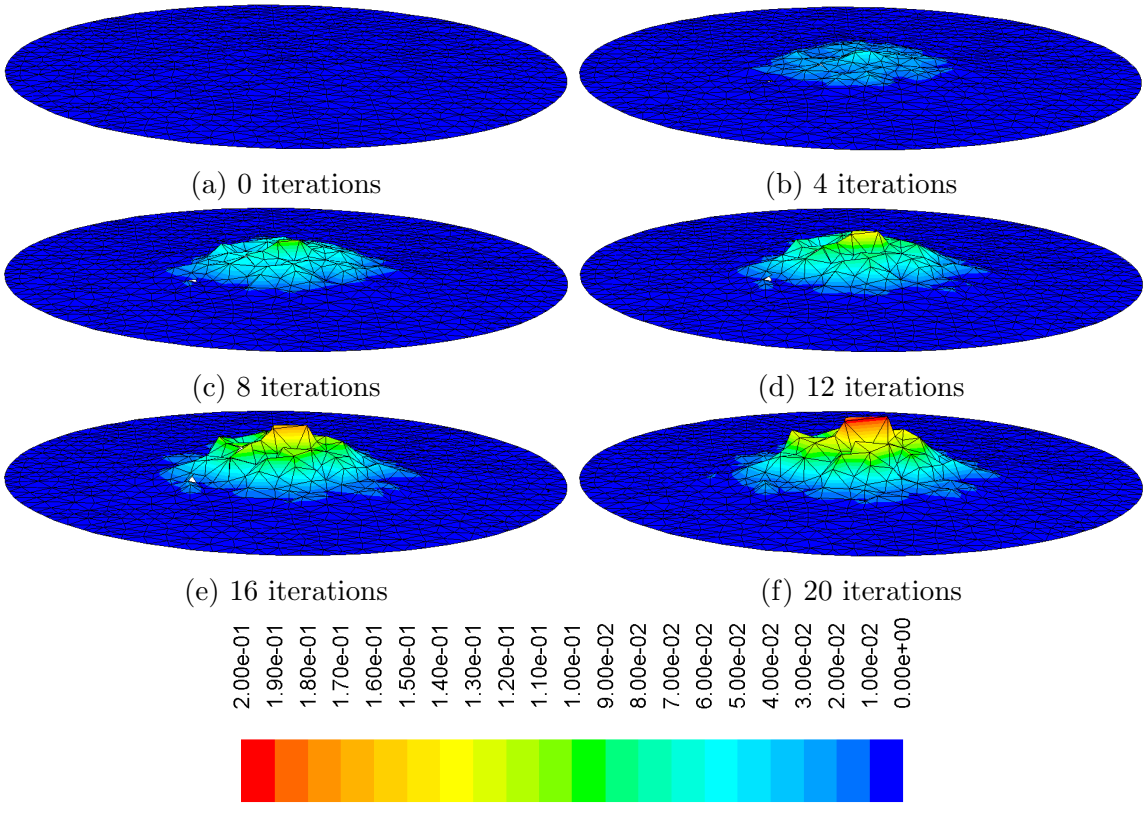

Figure 3.16: Build-up of surface with DMM iterations. Contour colour indicates deposition height normalised by impingement hole diameter, δ/D_h.

however the single precision calculation was 15% faster for the same calculation. Mesh size produced small ($< 5\%$) differences in deformed volume, and it was seen

than extremely fine mesh was likely to deform into negative volumes. Details of these investigations are given in Appendix A.

3.3.5 Discussion of modelling considerations

Based on experiences developing and implementing the dynamic mesh morphing method, a substantial amount of time was invested in finding appropriate modelling approaches. The following lists some of the fundamental considerations investigated.

3.3.6 Meshing considerations

Mesh size: it was generally found that an extremely fine surface mesh would not necessarily give a robust computational domain, as the mesh becomes folded more easily. Smaller particle injections are then required (see below), increasing computational time.

Tetrahedral volume mesh: Initial generation of an octree mesh, followed by remeshing using the Delaunay algorithm was seen to produce robust meshes in general, due to slower growth away from the boundary layer mesh.

Boundary layer mesh: It was generally seen that a fine boundary layer mesh with expansion ratio $r_e = 1.1$ was likely to withstand large deformation more successfully than meshes with higher expansion ratios as the boundary layer mesh can be deformed as a more homogeneous unit.

Inlet/outlet boundaries: avoiding morphing inlet or outlet planes where possible was found to be beneficial to solution stability. Movement of these boundaries was found to encourage divergence of the continuous phase solution. Adding 'buffer' surface zones where DMM was not occurring between a morphed zone and a boundary reduced this problem.

3.3.7 Particle injection considerations

Number of particles/mass/injection: each injected 'particle' in Fluent in fact represents a mass flow of particles to reduce computational effort. This is reported as 'frequency' by Fluent. We found a frequency of the order of 500 (each particle tracked by Fluent having the mass of 500 actual particles of that size and density) was a reasonable balance of resolution and computational time.

3.3.8 Simulation considerations

'Boundary layer' vs. 'diffusion' methods: the 'boundary layer' method offered by Fluent for transferring surface motion into the volume mesh was far preferred to the 'diffusion-based' smoothing method, discussion above. However it was liable to failure when two zones were selected to be morphed, due to a bug in Fluent (v.14.5.7). We avoided this through use of a single deforming zone, however this should be addressed in a more robust manner. The same problem was not detected for diffusion-based smoothing.

Continuous phase iterations: the continuous phase solution was updated every five mesh morphing iterations in general. This was found to be a reasonable compromise between accuracy and computational time. Significant differences were seen for the impingement geometry based on the number of mesh iterations between continuous phases solution; here the continuous phase was resolved every mesh iteration for the first ten mesh iterations. 50-80 continuous phase iterations were generally required to reduce residuals to their initial levels.

3.4 Bounce-stick model for particle-wall impact

Whilst an all-stick boundary condition has been used in the previous simulations in this chapter, and in fact widely within the field or aerosol science, it is not necessarily representative of particle-wall impacts in gas turbines. To address this, the particle-wall impact model of Bons et al. (2016), the 'bounce-stick' model, was implemented as a Fluent user-defined function, UDF. The 'simple physics-based model' offers a replacement to the various flavours of 'critical variable' options (shear stress, velocity, viscosity) available in the literature. The particle is modelled as a cylinder, impacting in an end-on orientation. Elastic-plastic deformation is modelled, with the effects of adhesion and shear-removal considered. The impact model considers all four elements of the impact to be occurring at once, rather than the sequential approach favoured by other authors (Singh and Tafti, 2013).

The model is adapted to particular particle/surface combinations through the use of a number of physical parameters: particle yield stress σ_y, composite Young's modulus E_c, surface free energy γ, and impulse ratio μ_{imp}. Coefficients of restitution in both the normal (CoR_n) and tangential (CoR_t) directions are calculated for application to the particle velocity.

The model is highly dependent on these key material properties. These are generally difficult to measure experimentally, and little data exists in the open literature.

They can be estimated from the rule of mixtures based on the data for the individual elements of the compounds. Bons et al. initially used the rule of mixtures, then tuned these constants for a range of appropriate materials for gas turbines based on the experimental data.

In this study, the bounce-stick model was initially implemented in MATLAB to confirm it was working as described, section 3.4.1. The implementation was then transferred to Fluent as a user defined boundary condition. A graphical user interface (GUI) was built to allow model physical constants to be varied easily.

3.4.1 Validation of implementation

Bons et al. published three validation cases for their model in the original paper. These were reproduced to demonstrate that the implementation used in this study matches the original. These are shown in Appendix B.2, indicating our version matches the original.

3.4.2 Further validation case

A further validation case was assessed, modelling the experimental work of Taltavull et al. (2016). This study investigated the effects of particle temperature, velocity, and impingement angle on deposition trends for volcanic ash on stainless steel. Gas and particles were heated with a plasma torch and impinged upon a stainless steel coupon at angles of 30-90°. Particle sizes were reported to span 1-150 µm, with a median value by volume of 30 µm. Particle temperatures and velocities at impact were calculated from CFD. Results were presented as integral deposited mass fraction. The calculated particle temperatures were demonstrated to span the glass transition region.

The particle size distribution, Fig. 3.17a, was sampled and linearly interpolated to a finer grid in d_p. Three cases were run, A ($T_p = 600$ °C, below glass transition), B ($T_p = 700$ °C, glass transition occurring), and C ($T_p = 900$ °C, above glass transition, but before melting). Variables a, b, and c were adjusted to give closer reproduction of the experimental data, $a = 0.7$, $b = 0.14$, $c = 0.1$. Material parameters used were $E_p = 136$ GPa, $\gamma = 0.3$ J/m^2. Yield stress was correlated and fitted based on the glass transition curve for the ash as published by the authors, Fig. 3.17b.

Model results for deposited mass fraction are presented in Figs. 3.17c-3.17e. The results reproduce the more normal impact angles well, but less well the oblique angle (30°). This is in keeping with the other validation cases which indicate the model is more successful for normal impaction angles.

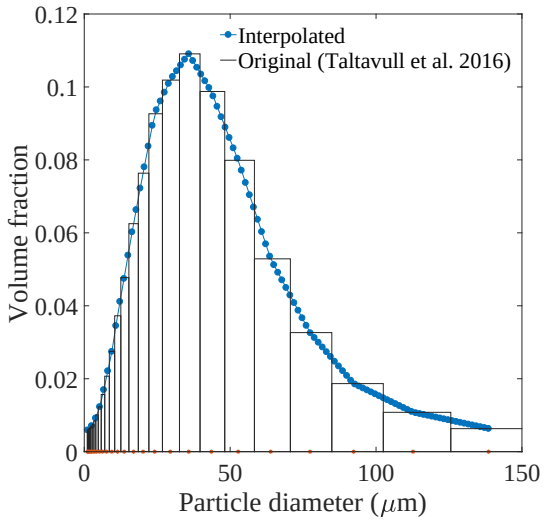

(a) Particle size distribution.

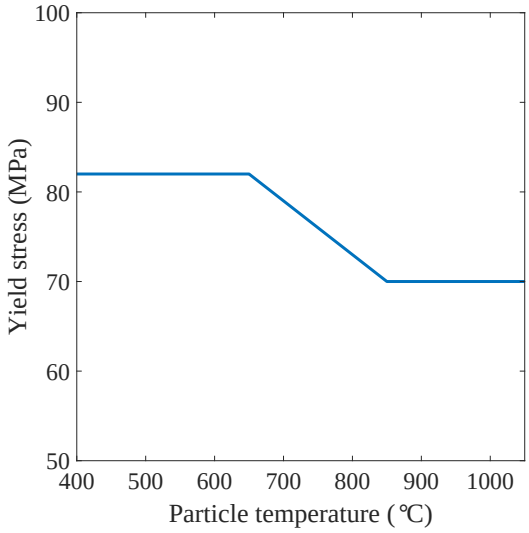

(b) σ_y temperature dependence

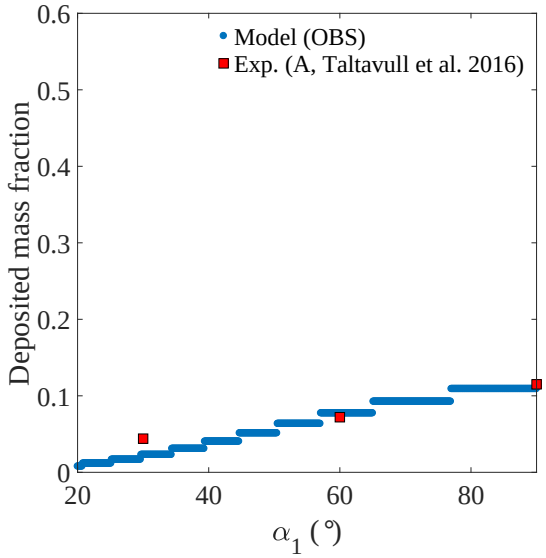

(c) Case A: $T_p = 600$ °C.

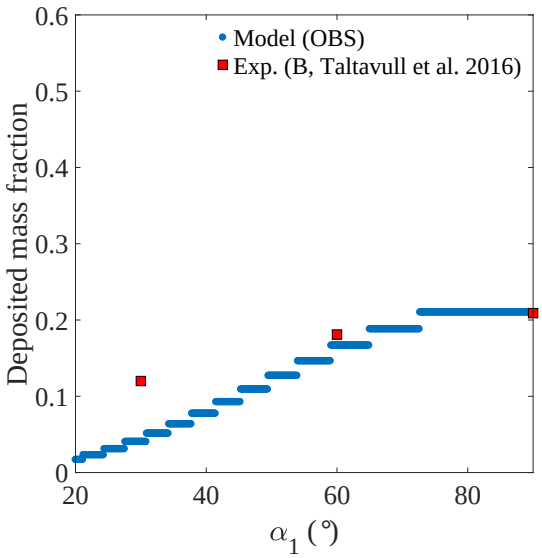

(d) Case B: $T_p = 700$ °C

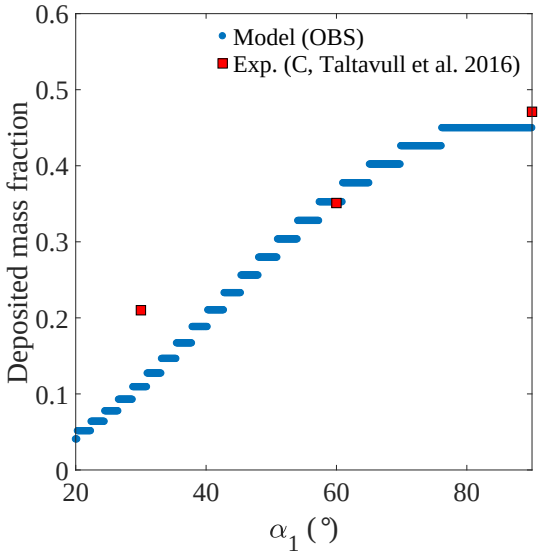

(e) Case C: $T_p = 900$ °C

Figure 3.17: OBS model applied to experimental work of Taltavull et al. (2016). Three experimental cases with increasing gas and particle temperatures.

3.4.3 Effect of main parameters

The effect of the six main physical parameters (d_p, ρ_p, σ_y, E_c, γ, μ_{imp}) on the normal coefficient of restitution is outlined below and in Fig. 3.18. The parameters are assessed for varying d_p within the range of interest.

3.4.3.1 Particle size

In the ideal case, $\gamma = 0$, particle size does not affect the normal coefficient of restitution, Fig. 3.18a. When adhesion is included, CoR_n becomes a strong function of d_p. Increasing particle size causes the distribution to tend towards the ideal case: CoR_n increases for given V_{n1}.

3.4.3.2 Particle density

Increasing particle density, Fig. 3.18b, decreases the normal velocity at which the maximum elastic deformation occurs, $V_{n1} = V_{n,\,crit}$. Peak values of CoR_n are not changed as both terms in Eq. B.1 scale with $1/\rho_p$.

3.4.3.3 Surface free energy

Increasing surface free energy (particle-surface adhesion), reduces CoR_n, Fig. 3.18c. By inspection of Eq. B.1(b), it is clear that the $\frac{2W_a \sin(\alpha_1)}{m_p}$ term is a function of $1/d_p$, hence adhesion becomes less significant for larger particles. It is adhesion that causes the 'kick down' in CoR_n visible at the boundary between regimes 3 and 4, Figs. B.1 & 3.18.

3.4.3.4 Yield stress

Increasing yield stress, Fig. 3.18d, increases the first term in Eq. B.1 relative to the second, hence reducing the influence of d_p and therefore adhesion. This is seen in the manner in which smaller particles are more significantly affected by the change in yield stress.

3.4.3.5 Composite Young's modulus

Increasing E_c makes the effective particle stiffer, which reduces w_{crit}, and hence CoR_n, Fig. 3.18e. The effect is more significant for smaller particles as proportionately the work of adhesion is larger compared to (critical) normal kinetic energy.

3.4.3.6 Impulse ratio

Impulse ratio μ_{imp} was defined by Brach (1991) as the ratio of tangential to normal impulses at impact. Two constant values of impulse ratio are plotted in Fig. 3.18f; the lower μ_{imp} gives a higher CoR_t for both particle sizes. The experimental data of Brach (1991) show μ_{imp} is not constant, but varies with α_1; increasing angle of impact decreases impulse ratio. Impulse ratio was also seen to vary strongly with particle/surface material, and should be measured experimentally for gas turbine materials.

3.4.4 Model parameters

The effect of the six main parameters used within the bounce-stick model, d_p, ρ_p, σ_y, E_c, γ, μ_{imp}, are not immediately apparent. An investigation of their effects is presented in Appendix 3.4.3, which highlights their effects on rebound characteristics, for particle properties relevant to this study.

3.4.5 Model discussion

Based on the above discussed validation cases it is clear that the current implementation of the bounce stick model is producing the same results as the published version. This gives a good initial point for use and development of the model. Whilst the model is a significant step forward from previous attempts at particle impact modelling, a number of questions remain regarding its design and implementation.

Particle size: the three cases above have all used experimental data where the particle size (d_p = 30-150 µm) is significantly larger than those of interest in our secondary air system flows (< 10 µm). Carrying out such experiments with these much smaller particles presents significant issues with regards to capturing and resolving the particles optically. The rebound characteristics of particles of this size might well be (significantly) more affected by surface roughness, where roughness R_a becomes of the order of particle size, leading to more dispersed rebound statistics.

Surface roughness: following from the above, randomness of rebound due to surface roughness could possibly be taken into account by sampling a Gaussian distribution and adding this random component to the calculated coefficient of restitution (in both directions), which could be inversely scaled by the ratio of d_p/R_a. Such a process could also be applied in general to the model, as it is clear from inspection of the raw experimental data as used above that there is significant scatter in the results.

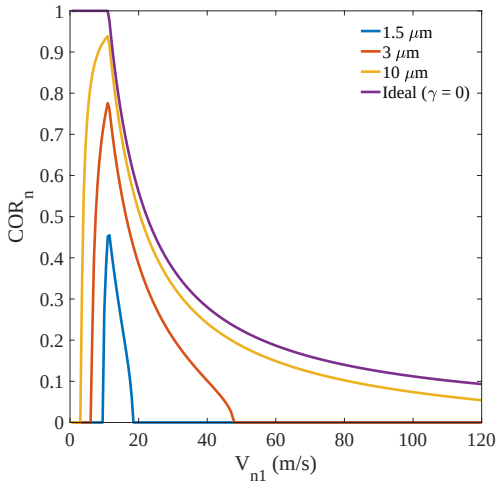

(a) Effect of d_p on CoR_n.

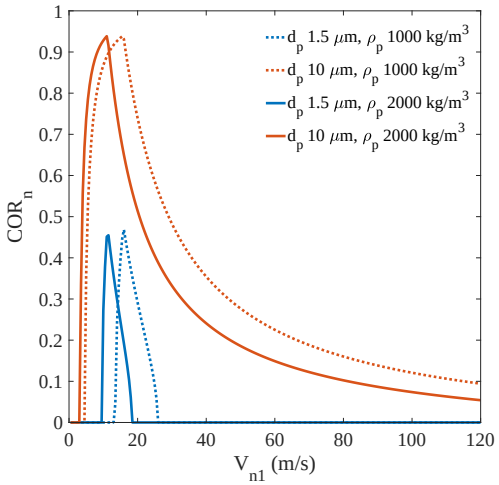

(b) Effect of ρ_p on CoR_n.

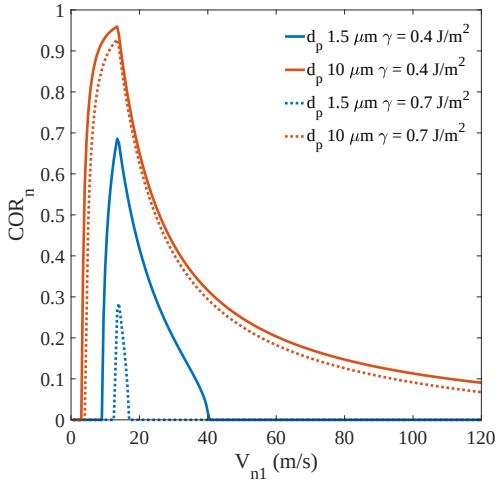

(c) Effect of γ on CoR_n.

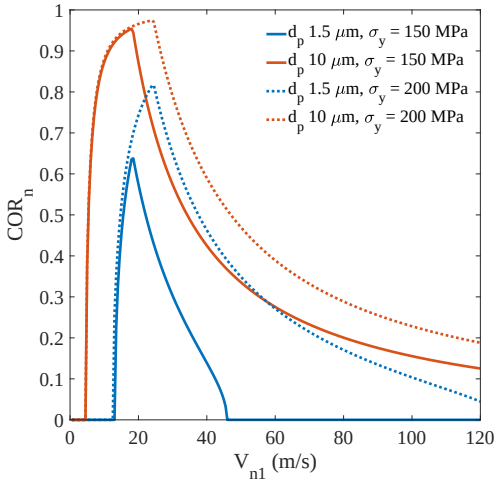

(d) Effect of σ_y on CoR_n.

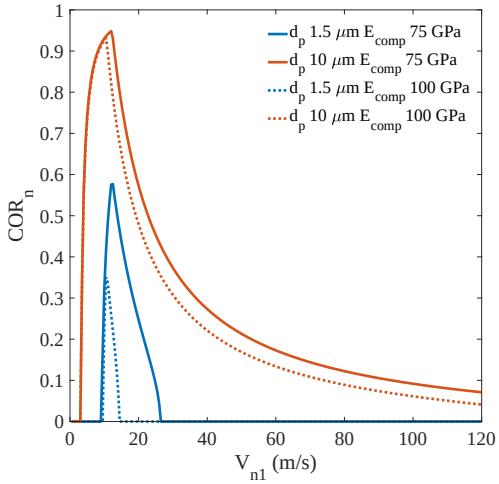

(e) Effect of E_c on CoR_n.

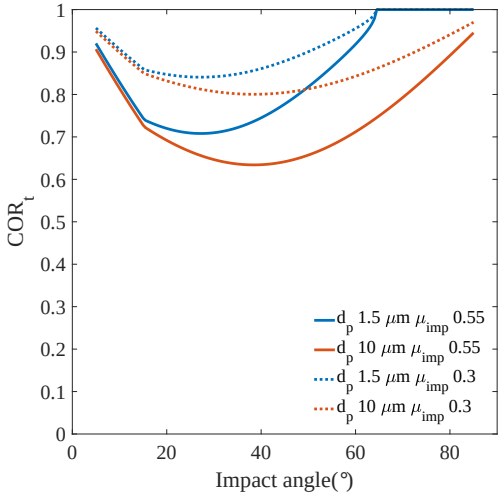

(f) Effect of μ_{imp} on CoR_t.

Figure 3.18: Effect of varying key model parameters on normal and tangential coefficients of restitution.

Contact area: for the undeformed cylinder, the face area of the cylinder is ∼21% of the equivalent sphere surface area. An empirical model was fitted by Bons et al. for calculating an effective contact area, as a fraction of the face area. As the model is tuned for large particles, for which the experimental conditions are designed to cause rebound, the model may not be well-tuned for small particles which are more sensitive to adhesion effects.

Tangential validation data: many of the researchers in this field have focused in the main on (highly) normal impacts, as these are largely expected in the main gas path. This has led to there being little CoR_t data for shallow (small values of α_1) angles. In the secondary air systems many impacts are oblique, which means the model validation is not necessarily as applicable.

3.5 Summary

Three approaches for numerical modelling of small particulates have been introduced. The first calculates a fluctuating fluid velocity as seen by a particle in the flow. This is added to the steady bulk flow velocity to give an instantaneous fluid velocity. Two models were discussed in detail; the discrete random walk model, which was shown to over-predict deposition rates by several orders of magnitude for the diffusion-impaction regime, and the continuous random walk model. This was shown to produce results within a factor of 3 within the diffusion-impaction regime, a very significant improvement. Further assessment and development of the model was carried out.

The second numerical approach was the development of a dynamic mesh morphing method to update a the boundaries of a computational domain based on the deposition which has occurred. This allows the effects of previous deposition on current deposition, fluid, and thermal characteristics to be assessed.

The third section of the chapter presented a model for particle-wall impact. Taken from the literature, this model was designed to be applied to Lagrangian particle tracking as part of CFD. The model implementation was validated, and applied to a further test case. The strengths and weaknesses of the model are discussed.

Chapter 4

High Temperature Experimental Campaign

Following the assessment of the continuous random walk model at ambient conditions, experiments were undertaken to provide data for validation of the model at engine secondary air system temperatures. The experimental rig used a horizontal pipe flow configuration, into which a sodium chloride, NaCl, aerosol was injected. Heating of the test piece body was undertaken using an oven. Gas was compressed air, pre-dried and supplied by the laboratory 7 barg line. Flow regulation and measurement was done using a pair of mass flow controllers and an orifice plate. Particles generated had diameters 2.0-6.5 µm. At ambient conditions, Reynolds numbers up to 27 000 were achieved. Heating of the rig produced gas temperatures of up to 480 °C, metal temperatures up to 730 °C, and Reynolds numbers up to 10 000. Experiments considered isothermal and non-isothermal conditions, the latter introducing thermophoretic effects.

4.1 Experimental domain

Gas and metal temperatures indicative of two flight conditions for the Engine A shank pocket region were provided. Experiments were to be carried out at both isothermal and non-isothermal conditions - the former to provide comparisons to published ambient temperature isothermal data, and the latter to provide assessment of thermophoretic conditions at high gas temperatures for micron-sized particulates, which has not been addressed in the literature.

Using the rotor-stator cavity simulations carried out in chapter 6, indicative engine conditions were found for the shank pocket. These are shown in Table 4.1. From these, a projected range of τ_p^+ relevant to gas turbine secondary flows was calculated. This is

T_g (K)	P_g (barg)	u^* (m/s)	d_p (µm)	ρ_p (kg/m^3)
670-1 000	8	< 8	0.5-10	$\sim 2\,000$

Table 4.1: Indicative engine conditions for shank region at varying flight conditions for experimental domain scoping.

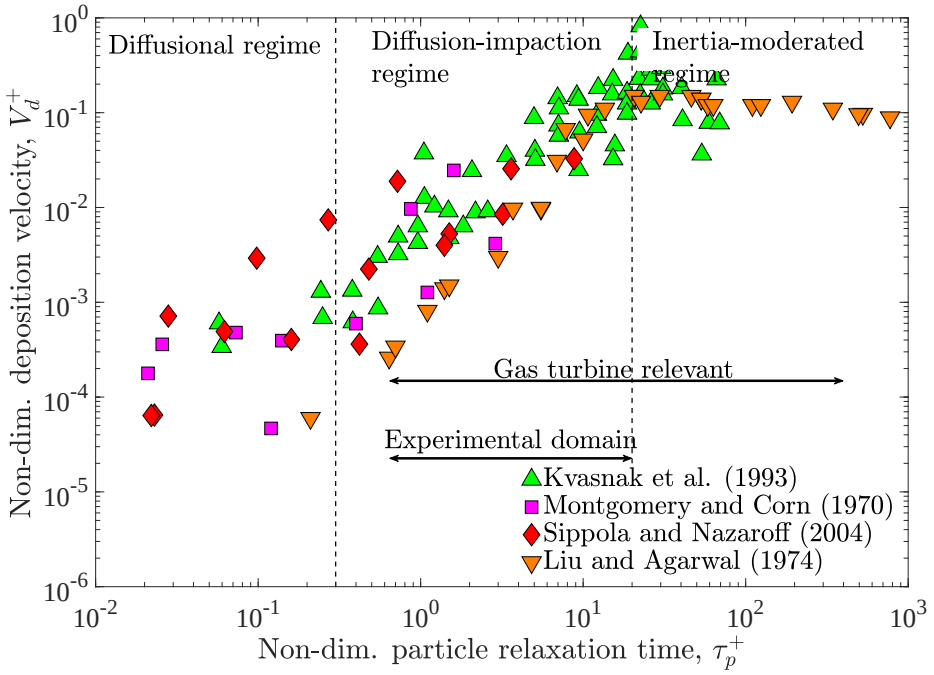

Figure 4.1: Domain of investigation in τ_p^+ based on indicative engine conditions. Background data for horizontal (Kvasnak et al., 1993; Montgomery and Corn, 1970; Sippola and Nazaroff, 2004), and vertical (Liu and Agarwal, 1974) pipe flow.

shown on Fig. 4.1. This spans parts of the diffusion-impaction and inertia-moderated regimes. As particle motion in the inertia-moderated regime is significantly better understood and simpler to model than that in the diffusion-impaction regime, the experimental domain is limited to τ_p^+ values within the diffusion-impaction regime. This is also shown on Fig. 4.1.

4.2 Dimensional analysis of particle motion

We consider the net force per unit mass F on a particle (d_p, k_p) suspended in a gas ($k_g, l_g, T_g, \boldsymbol{\nabla} T_g, \nu_g\,(=\mu_g/\rho_g)$), with particle slip velocity V_{rel}. It is assumed that only drag (inc. turbophoretic effects), thermophoretic, and gravitational forces (g) are influential. Following Buckingham's Pi Theorem, the ten variables and four dimensions reduce to the following six non-dimensional groups,

$$\frac{Fd_p^3}{\nu_g} = f\left(\frac{d_p \boldsymbol{\nabla} T_g}{T_g},\ \frac{g d_p^3}{\nu^2},\ \frac{l_g}{d_p},\ \frac{V_{rel} d_p}{\nu_g},\ \frac{k_p}{k_g}\right). \tag{4.1}$$

In terms of the groups' names this is expressed

$$\frac{Fd_p^3}{\nu_g} = f\left(Ep,\ Ga,\ Kn,\ Re_p,\ \Lambda\right), \tag{4.2}$$

where Ep is the Epstein number, Ga is the Galilei number, Kn the Knudsen number, Re_p the particle Reynolds number, and Λ the thermal conductivity ratio. As the aim of the experimental campaign is to provide deposition data at engine-representative conditions, it is desirable to match these non-dimensional groups experimentally to a range of engine conditions, taken from the Engine A rotor-stator cavity simulations, chapter 6).

4.2.1 Epstein number, Ep

The Epstein number is the ratio of the product of particle diameter and gas temperature gradient to the gas temperature,

$$Ep = \frac{d_p \boldsymbol{\nabla} T_g}{T_g}. \tag{4.3}$$

The Epstein number can be thought of as the ratio of difference in mean molecular kinetic energy across the particle to the mean molecular kinetic energy of the gas, $kd_p \boldsymbol{\nabla} T_g / kT_g$, where k is the Boltzmann constant (1.38×10^{-23} J/K).

Simulation (Engine A)			Experiment			
d_p (µm)	$\boldsymbol{\nabla} T_g/T_g$ (1/m)		d_p (µm)	$\boldsymbol{\nabla} T_g/T_g$ (1/m)		
	50	200		-50 ($T1_A$)	100 ($T1_D$)	250 ($T2_E$)
0.1	5×10^{-5}	2×10^{-4}	2.5	-5×10^{-5}	3×10^{-4}	6×10^{-4}
5.0	2.5×10^{-4}	1×10^{-3}	5.0	-3×10^{-4}	5×10^{-4}	1×10^{-3}

Table 4.2: Epstein numbers from the Engine A simulation and experimental conditions for differing particle diameters and thermal conditions, $\boldsymbol{\nabla} T_g/T_g$

Interrogation of the Engine A simulations indicates that the projected experimental conditions will be able to match a range of relevant engine Epstein numbers, Table 4.2.

4.2.2 Galilei number, Ga

The Galilei number can be described as the ratio of gravitational to viscous forces,

$$Ga = \frac{g d_p^3}{\nu^2}. \tag{4.4}$$

A range of Ga taken from the Engine A simulations is shown in Table 4.3. The experimental conditions are seen to be able to span a significant range of the expected engine Ga values.

Enigne A simulation ($\nu = 1 \times 10^{-5}$)		Experiment T1 ($\nu = 6 \times 10^{-5}$)	
d_p (µm)	Ga	d_p (µm)	Ga
0.1	10^{-10}	3	10^{-9}
5.0	10^{-5}	6	10^{-6}

Table 4.3: Galieli number from engine simulation and experimental conditions

4.2.3 Knudsen number, Kn

Knudsen number is the ratio of molecular mean free path length l_g to particle radius r_p, Eq. 2.59. The importance of matching Kn regimes is highlighted by Fig. 4.2. In the region $0.1 \leq Kn \leq 10$ the Knudsen number regime has a strong influence on the thermophoretic coefficient, Eq. 2.63. For $Kn < 0.1$ the theories of both Beresnev and Chernyak (1995) (solid lines on Fig. 4.2) and Talbot et al. (1980) (not shown) indicate that the thermophoretic coefficient is approximately constant and independent of Kn.

Indicative Kn are given in Table 4.4 for representative engine, taken from simulations in chapter 6.1, and experimental conditions. It can be seen that the experiment is generally able to match Kn, though the smallest Kn at engine conditions are not achievable due to the low pressure at which the experiment operates. As the thermophoretic coefficient is thought to be close to constant in this region, the inability to achieve these smallest Kn is of less significance.

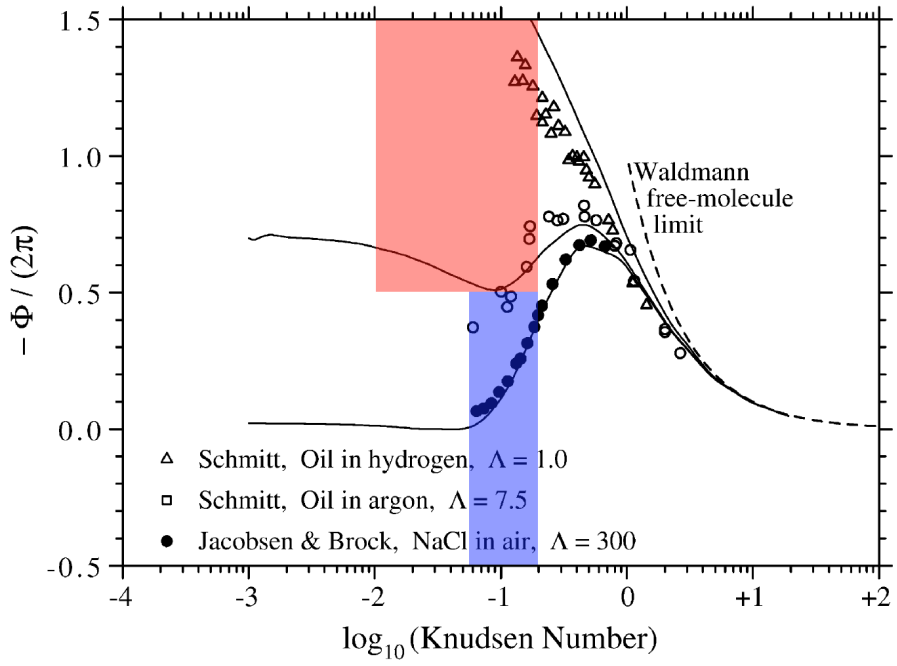

Figure 4.2: Effect of Knudsen number Kn and thermal conductivity ratio Λ on thermophoretic coefficient Φ. Red region indicates engine-representative Kn, blue region indicates Kn conditions achievable experimentally (see Table 4.4). Background taken from Healy and Young (2010), where solid black dots indicate sodium chloride, as used in this study, and the solid lines the expression of Beresnev and Chernyak (1995).

Engine conditions						
Case	T_g (K)	P_g (bara)	l_g (µm)	Kn		
				$d_p = 0.5\,\mu m$	$d_p = 1.0\,\mu m$	$d_p = 5.0\,\mu m$
T2	810	8.7	0.025	0.10	0.050	0.010
T1	730	3.5	0.058	0.23	0.12	0.023
Experimental conditions						
Case	T_g (K)	P_g (bara)	l_g (µm)	Kn		
				$d_p = 2.0\,\mu m$	$d_p = 4.0\,\mu m$	$d_p = 6.0\,\mu m$
T2	753	1.0	0.20	0.20	0.10	0.068
T1	663	1.0	0.18	0.18	0.088	0.059

Table 4.4: Knudsen number for varying particle sizes for both indicative engine conditions (taken from simulations in chapter 6) and proposed experimental conditions.

4.2.4 Particle Reynolds number, Re_p

Reynolds number based on particle diameter and particle slip velocity is used here,

$$Re_p = \frac{V_{rel} d_p}{\nu}. \tag{4.5}$$

From the Engine A simulations undertaken in chapter 6.1, a range of conditions are extracted, Table 4.5. It can be seen that the experiment will be able to match the lower Re_p values, however it will not be able to match the higher values. These are driven by the different pressure conditions, but also the high streamline curvature seen within the cavity, which we do not attempt to produce experimentally.

Engine A simulation			Experiment (sim)				
d_p (µm)	Re_p		d_p (µm)	Re_p, $T1_C$		Re_p, $T1_E$	
	$< 95\%$	mean		$< 95\%$	mean	$< 95\%$	mean
0.1	1.9	0.13	3.0	0.54	0.21	0.51	0.19
0.5	12.8	0.81					
1.0	27.0	2.12	6.0	1.4	0.50	1.2	0.45
5.0	133.0	17.5					

Table 4.5: Particle Reynolds numbers simulations of the engine, chapter 6, and experiments.

4.2.5 Thermal conductivity ratio, Λ

The thermal conductivity ratio, significant for defining a particle's response to a gas temperature gradient, is given by the ratio of particle to gas thermal conductivity, Eq. 2.57. With reference to Fig. 4.2 it can be seen that Λ has a very significant effect on the thermophoretic coefficient Φ. High-Λ pairings, which represents the NaCl-air situation in the following experiments show a much lower Φ than low-Λ particle-gas pairings. As Λ increases the Φ - Kn curves appear to approach an asymptotic high-Λ case.

As we are matching gas temperatures, hence μ_g (Eq. 2.58), and particle material, Λ will be matched across the experimental range (values in the region 150-300 with varying T_g, based on constant particle thermal conductivity of 4 W/m/K).

4.2.6 Normalised deposition fraction, $\overline{f_d}$

A normalised deposition fraction $\overline{f_d}$ is defined as the ratio of deposition fraction (in a temperature gradient) to deposition fraction at isothermal conditions,

$$\overline{f_d} = \frac{f_{d,\,thermophoretic}}{f_{d,\,isothermal}}. \tag{4.6}$$

This is used in conjunction with the thermophoretic parameter P^+_{Th} , below, to assess the change in deposition due to specific thermophoretic conditions.

4.2.7 Thermophoretic parameter, P^+_{Th}

A normalised thermophoretic parameter P^+_{th} was defined to attempt to collapse the deposition curves at varying thermophoretic conditions. Starting from the equation for thermophoretic acceleration, Eq. 2.56,

$$\mathbf{a}^{Th} = \Phi \frac{3\mu^2}{\pi \rho_g \rho_p d_p^2} \frac{\boldsymbol{\nabla} T_g}{T_g}, \tag{4.7}$$

this is non-dimensionalised by $(u^*)^2/d_p$,

$$P^+_{Th} = \frac{\mathbf{a}^{Th}}{(u^*)^2/d_p} = \Phi \frac{3\mu^2 d_p}{\pi \rho_g \rho_p d_p^2 (u^*)^2} \frac{\boldsymbol{\nabla} T_g}{T_g}. \tag{4.8}$$

This can then be expressed in terms of τ_p^+ and the Epstein number,

$$P^+_{Th} = \frac{\Phi}{6\pi} \frac{Ep}{\tau_p^+}, \tag{4.9}$$

or in physical terms as the ratio of particle thermophoretic force to a particle inertial force, based on shear velocity,

$$P^+_{Th} = \frac{\text{Particle thermophoretic force}}{\text{Particle (shear) inertial force}}. \tag{4.10}$$

The thermophoretic parameter is signed, i.e. positive values indicate the 'increasing' thermophoretic direction, negative values the 'decreasing' direction. Thermophoretic data was extracted from Romay et al. (1998) and Healy and Young (2010), and is presented as $\ln\left(\overline{f_d}\right)$ against P^+_{Th} in Fig. 4.3. $\ln\left(\overline{f_d}\right) > 0$ indicates thermophoresis increasing deposition, $\ln\left(\overline{f_d}\right) < 0$ indicates the reverse. The thermophoretic coefficient Φ is calculated as Beresnev and Chernyak (1995). The data of Romay et al. (1998) (NaCl in air, Fig. 4.3a) shows a convincing collapse to a single curve for the

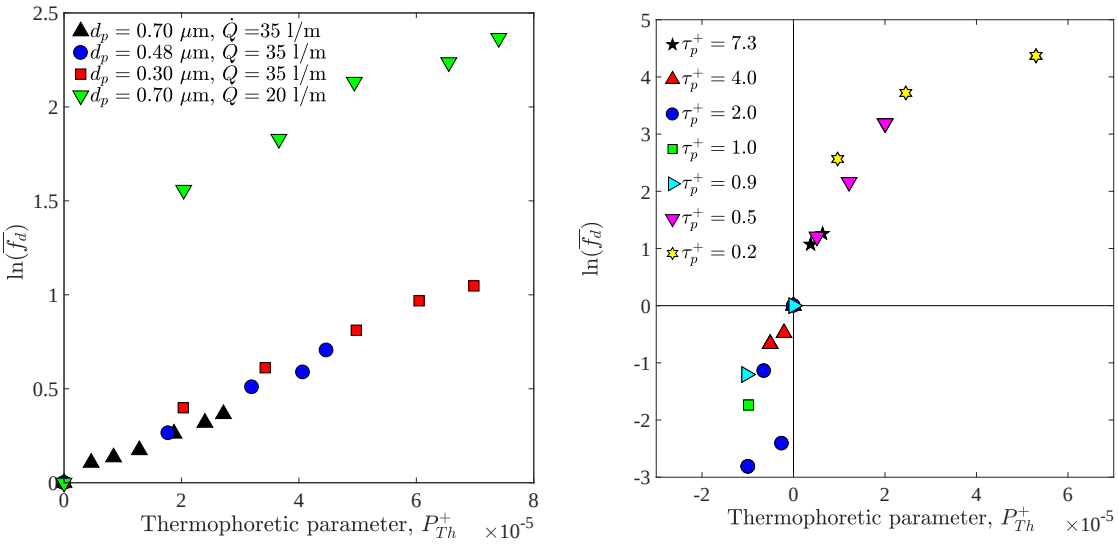

(a) Data of Romay et al. (1998)

(b) Data of Healy and Young (2010)

Figure 4.3: Normalised deposition fraction against thermophoretic parameter for published experimental data

higher gas flow rate data, $\dot{Q} = 35$ l/min, $Re = 9\,000$. The lower gas flow rate, $\dot{Q} = 20$ l/min, $Re = 5\,000$, shows a line of the same gradient, but translated, possibly related to the transition Reynolds number, or difficulties picking points off the published graph (figure 4 of the above paper).

The data of Healy and Young (2010) (uranine and oleic acid in air, Fig. 4.3b) also shows a good collapse to a single curve over the majority of the spread of data. Two outliers to a linear fit are observed, $[5.3 \times 10^{-5}, 4.4]$, and $[-2.6 \times 10^{-6}, -2.4]$, the latter also far from the prevailing trend in figure 9 of the original paper.

These published experimental data indicate that the thermophoretic parameter is able to characterise the effects of thermophoretic deposition for a range of Λ and Kn appropriate to engine conditions and materials.

4.3 Experimental rig design

4.3.1 Experimental measurements and instrumentation

From the discussion in section 4.1, particle deposition is to be presented in terms of τ_p^+ and V_d^+. The measurements required to calculate these values are given in Table 4.6. Where a value is a derived value, the other measurements required are listed. Discussion of the individual equipment is given in the following section, with further details in Appendix C.

Property	Method	Technique
Experimental time, t	Measured	Labview
Gas pressure, P_g	Measured	Pressure transducers
Gas temperature, T_g	Measured	K-type thermocouples
Gas density, ρ_g	Calculated	$\rho_g = P_g/RT_g$
Gas dynamic viscosity, μ_g	Calculated	Sutherland's law
Gas mass flow rate, $\dot{m}_g$	Measured	Mass flow controller
Gas bulk velocity, $\overline{U}_g$	Calculated	$\overline{U}_g = \dot{m}_g/\rho_g/A_{xc}$
Gas friction velocity, u^*	Calculated	$u^* = \overline{U}_g\sqrt{f/2}$
Wall/surface temperature, T_w	Measured	K-type thermocouple
Particle diameter, d_p	Measured	Optical particle sizer
Particle concentration, C_{out}	Measured	Optical particle sizer
Solution concentration, G	Measured	Electrical conductivity meter
Solution mass, m_{sol}	Measured	Balance
Particulate deposited mass, m_d	Calculated	$m_d = m_{sol}G_{sol}/k_{sol}$
Particulate outlet mass, m_{out}	Calculated	$m_{out} = C_{out}\dot{m}_g t/\rho_g$

Table 4.6: Properties to be measured experimentally and the methods by which this was done

4.3.2 Experimental rig layout and equipment

The rig layout is shown in Fig. 4.4. Dried, compressed air enters the system regulated to 2-3 barg, depending on mass flow rate requirement. Three gas paths are used. Paths 1 and 2 are controlled by mass flow controller 1 (MFC1). Gas path 1 (GP1) is the heated bulk flow, accounting for around 70% of the gas mass flow rate. This is heated by the inline heaters (IH), and passes into the mixing chamber (MX). This is mixed with gas path 2 (GP2), carrying the generated particles. The combined heated, particulate-laden flow then passes through the test section (TS), where some particles deposit on the test insert (TI). The gas is then exhausted to atmospheric pressure inside the oven. An extraction unit is used to remove the exhaust gas from the experimental room. The whole rig is protected by a 4 barg pressure relief valve at inlet.

Gas path 2 (GP2) passes through the atomiser, diluting the generated particles and passing these into the mixing chamber. This flow is measured using an orifice plate (OP) before entering the atomiser, and is not actively heated. A 2.0 barg pressure relief valve is used to protect the atomiser. A third gas path (GP3) is

an auxiliary gas path, used to bypass the atomiser whilst the rig is brought up to experimental temperature. This is controlled by mass flow controller 2 (MFC2). It is necessary that the atomiser is run for around half an hour before each test to stabilise its output. Once the rig is at temperature and the atomiser conditions are stable, flow into the mixing chamber is switched from GP3 to GP2, which allows the particles to be injected without disturbing the thermal conditions in the rig.

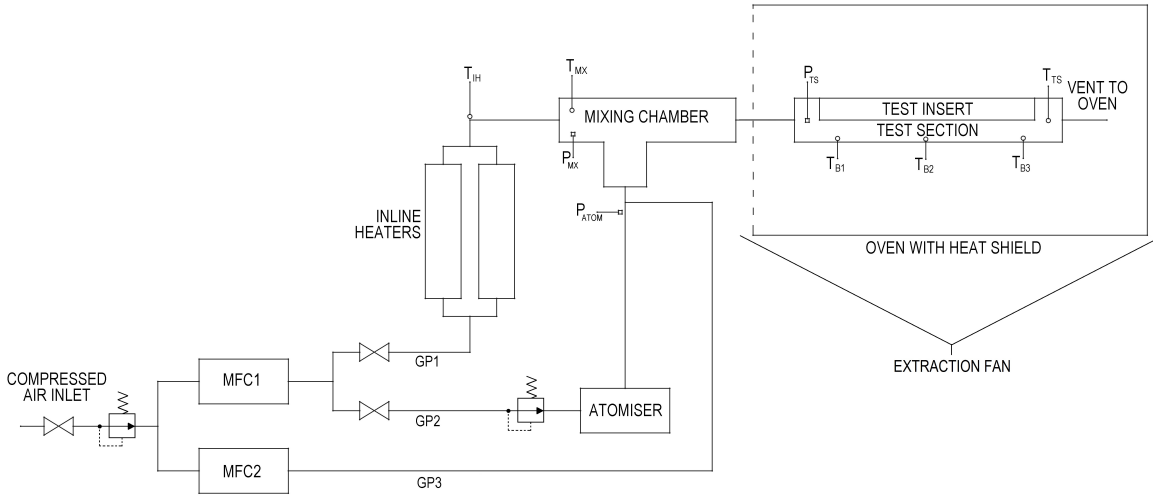

Figure 4.4: Schematic of experimental rig

Individual elements of the experimental rig are outlined below. Further detail is included in Appendix C.

4.3.2.1 Test piece

A two-part test piece was designed for measurement of particle deposition, Fig. 4.5. The two part design uses a main test body (TB) with a removable test insert (TI), on which deposition was measured. The test insert is clamped to the TB, and sealed using a high temperature gasket. Both the TB and TI were manufactured from stainless steel, with final gun drilling and honing processes being undertaken with both parts in place, to produce an extremely smooth joint between the concentric surfaces to reduce any tripping of the flow. Internal diameter is 18 mm, test insert length is 160 mm. Full dimensions are given in Table C.1.

The test piece sits within the oven, closed by a heat shield. Gas temperature is measured using a centreline gas thermocouple 10 mm downstream of the test insert. Body temperature measurements are taken in three locations in the test section body

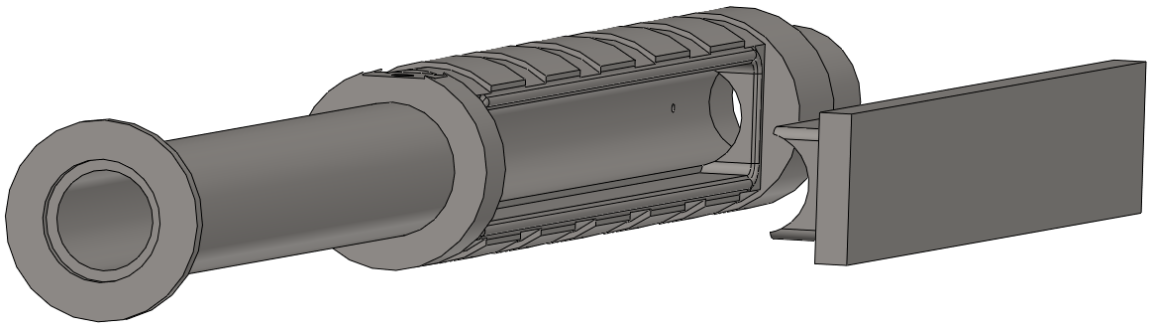

Figure 4.5: Test piece showing removable test insert (gasket and clamps omitted for clarity). Flow direction left to right.

within the length of the test insert, and averaged. A static pressure reading is taken 5.5 mm upstream of the test insert, on the opposite wall to the TI.

Two internally identical test pieces were manufactured from different grades of stainless steel, grades 304 and 310. These are referred to as EXPα and EXPβ , and only differ by their surface roughnesses (R_a = 0.22, 1.12 µm respectively). Further details in Appendix C.

4.3.2.2 Mixing chamber

The mixing chamber is of a diverging-straight-converging design, Fig. 4.6. Injection of NaCl particles from GP2 into the bulk heated (GP1) flow is done in the straight section. A gas thermocouple measures bulk flow temperature before mixing occurs, and a static pressure reading is taken at the same axial location; both are 90 mm upstream of the particle injection location. The mixing chamber is wrapped with a heater tape (Omega Ultra-high temperature heater tape STH052-100, 783 W, rated to 760 °C) to increase body and gas temperature. High-temperature insulation is wrapped around the outside of the heater tape. The heater tape is operated via a custom-built voltage phase angle control box.

4.3.2.3 Mass flow controllers

Two Omega FMA series mass flow controllers were used. MFC1 is model FMA-2612A (0-500 SLPM). MFC2 is model FMA-2609A (0-50 SLPM). MCF1 is controlled and read via a National Instruments VI.

The orifice flow meter is calibrated against MFC1 for the expected range of mass flow rates. Upstream and differential pressures are measured. Gas temperature is taken from MCF1 ($\sim$ 300 mm upstream). Mass flow rate is calculated from

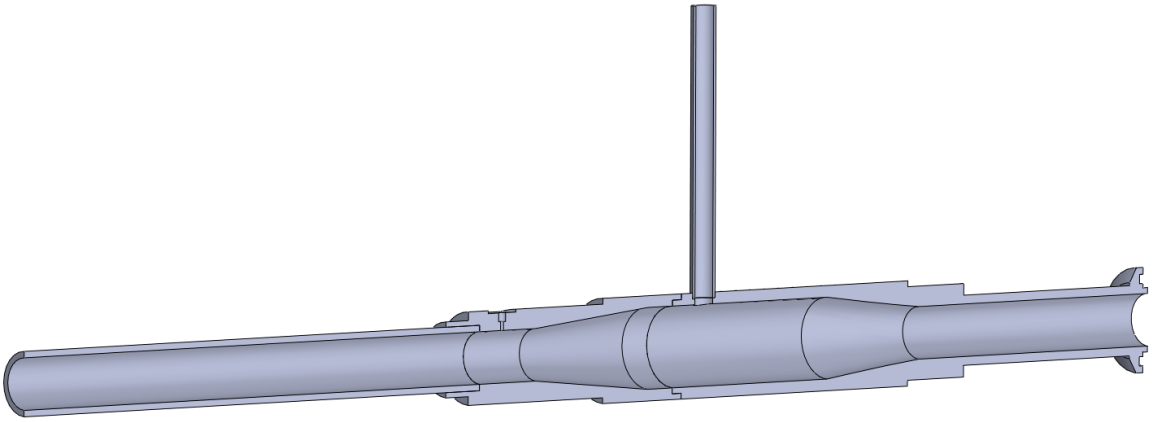

Figure 4.6: Cross-sectional view of mixing chamber. Flow direction left to right. Bulk (heated) gas enters from GP1 on left, particulate-laden flow from GP2 from top. Flanged joint to test section with slot for O-ring seen on right hand side.

$$\dot{m} = C_{or} A_{or} \sqrt{2 \rho_g P_{diff}}, \tag{4.11}$$

where the product $C_{or}A_{or} = 0.00137$ (C_{or}: orifice flow coefficient; A_{or}: orifice area) was calibrated against MFC1.

4.3.2.4 Inline heaters

Two Omega AHP-7562 heaters, designated IH, (rated to 540 °C, max flow rate 567 l/min) are used in parallel to provide heating to GP1. These are run using a heater control unit, as for the mixing chamber heater tape.

4.3.2.5 Optical particle sizer

The optical particle sizer (OPS), TSI model 3330, was used to provide both particle size distributions and bulk concentration measurements. The OPS uses a laser scattering/shadow principle to measure optical (rather than aerodynamic equivalent) size. The OPS samples 1.0 l/min air, reporting the size distribution and total count, n_c. The total number of particles is then calculated by multiplying by the actual volume flow rate of the flow from which the sample is drawn. Appendix C.1.1 has further details.

4.3.2.6 Atomiser

A TSI model 3450 vibrating orifice aerosol generator (VOAG) was used to provide mono-dispersed NaCl particles from a saline solution. The atomiser pumps the solu-

tion through an orifice, which is oscillated using a signal generator and piezoelectric crystal. A single droplet is produced per cycle, hence from the frequency the number of potential particles is known.

Tuning of the vibrational frequency f_a to the volumetric flow rate of the solution $\dot{Q}_{sol}$ and final (dried) particle diameter d_p can produce highly mono-disperse droplets,

$$f_a = \frac{6\dot{Q}_{sol}C_v}{\pi d_p^3}. \tag{4.12}$$

The droplets are dispersed into a drying column, where the solute evaporates, leaving a solid NaCl aerosol. Particle diameter is dependent on solution volumetric concentration C_v of NaCl,

$$C_v = \left(\frac{d_p}{D_d}\right)^3. \tag{4.13}$$

As the droplet diameter is a function of the orifice diameter, Eq.s 4.12 and 4.13 indicate that atomiser frequency is only a function of solution volume flow rate once the orifice has been chosen. Knowing the solute density, the mass concentration of solute per unit volume of solvent, $C_m v$, can be calculated,

$$C_{m,v} = C_v \rho_{solute}. \tag{4.14}$$

Preliminary testing was undertaken to understand the atomiser's operational characteristics. A minimum volume flow rate of 55 l/min was found to ensure particles were transported to the mixing chamber, and didn't settle out of the flow in the drying column. Particle generation is discussed further in Appendix C.1.2.

4.3.2.7 Oven

A Wild Barfield oven/electric furnace was used to increase body temperature. The oven is capable of heating in excess of 1 200 K. The oven is opened in a front-loading manner, with a hinged door. The oven is closed by a heat shield, which significantly reduces heat loss from the oven to the room environment.

4.3.2.8 Pressure transducers

Pressures were measured at the mixing chamber bulk inlet, atomiser-mixing chamber joining block, test section, and orifice meter upstream and differential, using Sensortechnics pressure transducers (0-5 mbar, 0-10 mbar, 0-2 mbar, 0-2 bar, 0-350 mbar respectively). A National Instruments (NI) card (NI9205) and chassis (NI-cDAQ-9174) was used to connect to the Labview VI. Pressure tapping locations are shown on Fig. 4.4.

4.3.2.9 Scales

Kern KB-1200-2N scales (max: 1 210 g, resolution: 0.01 g) were used for producing the NaCl solution. When a low mass of NaCl was needed (of the order of the instrument's resolution), an intermediate solution was produced initially, then a portion of this intermediate solution diluted, to reduce measurement uncertainty.

4.3.2.10 Thermocouples

Stainless steel sheathed K-type thermocouples (TC Direct) read by National Instruments card NI9214 were used for all temperature measurements. The inlet compressed air temperature was read from MFC1. Thermocouple locations are shown on Fig. 4.4.

4.3.3 Prime measurements

From the operational range of the experimental equipment, and predicted deposition trends based on Fig. 4.1, indicative prime measurements of τ_p^+, d_p, Re, u^*, and V_d^+ were calculated, Table 4.7. These are based on an assumed particle size range of 2.5-6.5 µm, and are for isothermal conditions. Under thermophoretic conditions, V_d^+ values are likely to vary significantly in comparison to isothermal conditions.

Condition	τ_p^+	d_p (µm)	Re	u^* (m/s)	V_d^+
Ambient	0.4-20	2.5-6.5	$9\,400 - 23\,000$	0.50-1.08	0.0005-0.2
T1	0.5-15	2.5-6.5	$5\,300 - 12\,000$	1.2-2.4	0.0005-0.1
T2	0.5-10	2.5-6.5	$4\,900 - 9\,200$	1.2-2.4	0.0005-0.1

Table 4.7: Prime measurements for ambient and high-temperature isothermal experiments

4.3.4 Particle charge from generation

Charging of aerosol particles during generation is common, and effects many widely used aerosol materials. Particle charge, in number of elementary charge units varies strongly depending on method, and material. A number of experimentalists have used radioactive sources to neutralise their generated aerosols. In the case of NaCl and atomisation from solution, the mean charge reduces with increasing solution concentration (Tsai et al., 2005). Kousaka et al. (1980) indicated that deposition due to electrical diffusion of their NaCl particles was negligible on the grounded section of their experiment. As the experimental rig for this study was also grounded, and high concentration solutions of NaCl used, Table C.3, a neutraliser was not employed.

4.3.5 Measurement of deposited mass

The previously used measurement technique (McGilvray et al., 2011) was found to introduce significant uncertainty into the measurement of deposited mass. Prior experiments had used a saline solution formed from BS9300 sea water corrosion test mix. Swabs were used to clean the test surface post-experiment, which were then individually bagged and sent for mass spectrometry analysis. Based on this, the deposited mass per unit area was calculated. Issues were found with this method; a new method for measuring the deposited mass was therefore designed, calibrated, and proven.

4.3.5.1 Salt material

Pure sodium chloride (Sigma Aldrich BioXtra, S7653), was chosen in preference to the previously used BS9300 sea water corrosion test mix. Making a solution from pure NaCl had several significant advantages. NaCl produces cubic crystals, which are easier to approximate to the numerically modelled spheres than the sharper crystals formed from sodium sulphate, from the BS3900 sea salt mix solution. Problems were also previously found with completely dissolving the BS3900 into solution. When swabbing calibrations were undertaken with the sea salt mixture, differing amounts of the mixture's components were detected when compared to the make up of the initial mixture. Making solutions from NaCl, the single compound in solution allowed the new measurement technique based on solution electrical conductivity to be used.

4.3.5.2 Swabbing technique

A surface swabbing technique was used to measure surface depositions. Standard swabs produced by Intertek were used, washed in deionised water. Integral measurements over the whole surface (both test insert and test body) were made.

Surfaces were swabbed and the swab itself rinsed in the measurement solution a number of times (4-8 in general), until the reading made with a solution electrical conductivity meter, sec. 4.3.5.3, stabilised. This was defined as the change in reading not exceeding 1% of the total reading for two consecutive swabs. This produced two significant advantages over the previously used mass spectrometry system:

1. Deposition measurements can be read at the time of swabbing, meaning that the operator can be more sure they have collected all (asymptotically) of the sample, reducing the reliance on a swabbing calibration (Appendix D.4).

2. Turn around time is significantly reduced, reducing risk to the experimental campaign.

4.3.5.3 Deposition measurement technique

A new method for the measurement of particle deposition was developed. It uses the dissociative nature of Na^+ and Cl^- ions in solution; salts in solution change the electrical conductivity (G) of the solution. In the case of NaCl in deionised water, the electrical conductivity of the solution is linearly related to the mass concentration (C_m) of NaCl,

$$G = k_{sol} C_m, \tag{4.15}$$

where coefficient k_{sol} must be calibrated for solutions of known concentration and measured conductivity. Electrical conductivity is measured in units of conductance/distance; S/m, or frequently µS/cm. Pure deionised water is used as it has an extremely low conductivity ($\sim 1\,\mu S/cm$ at 25 °C).

The conductivity of a saline solution is highly temperature dependent, hence conductivity values are referenced to a temperature datum-based value, G_{datum}. A linear temperature correction is valid for a small range of temperatures around a reference temperature T_{datum}, frequently 25 °C,

$$G_{datum} = G_T \frac{1}{1 + \alpha\,(T - T_{datum})}, \tag{4.16}$$

Range	0.001µS/cm - 1000 mS/cm (five sub ranges, four digit display)
Resolution	0.001µS/cm
Uncertainty	±1% reading ±0.01µS/cm

Table 4.8: Electrical conductivity meter details

where T is the measured solution temperature (°C), G_T the measured solution conductivity, and α a temperature compensation coefficient, in the range 0.02-0.04/°C for solutions of NaCl in deionised water at the concentrations and temperatures of interest.

Measurement was carried out using a swab of the surface of interest. After each pass, the swab was rinsed in a beaker of deionised water to remove the NaCl from the swab. The electrical conductivity and temperature of this solution were then measured and recorded. When the conductivity reading tended to a maximum, defined as less than 1% change of total reading over for two consecutive swabs, a final reading was taken. Care was taken to clean the beakers thoroughly after each test in the ultrasonic bath, and both the beakers and probe were rinsed with deionised water before and after each test was measured.

4.3.5.4 Electrical conductivity meter

A Hanna Instruments model HI5321 electrical conductivity meter (ECM) was chosen, following successful preliminary trials of the concept with a more affordable instrument. The instrument has a thermocouple built into the probe to allow temperature adjustment to be carried out. Instrument details are given in Table 4.8. The standard operating procedure, as described by the instrument's manual, was followed.

4.3.5.5 Calibration of measurement technique

The three aspects of the electrical conductivity meter were calibrated: for the cell constant against standard solutions, for solution temperature coefficient at varying solution concentrations, and for conductivity at varying solution concentrations. This is discussed in detail in Appendix D.

4.3.6 Experimental uncertainty

An assessment of the uncertainties in individual experimental measurements was carried out, in preparation for overall uncertainties for the key reported experimental

values (V_d^+, τ_p^+). Experimental uncertainty has not always been reported by experimentalists in this field, however those who did indicated values in the region 5-30%. A large fraction of published experimental data has tended to show significant spread in V_d^+, often in the region of an order of magnitude for matching τ_p^+. This suggests that the particle deposition process is in general highly stochastic. For V_d^+ and τ_p^+ this leads to total uncertainties of 11.5% and 10.4% respectively. The analysis is reported in detail in Appendix E.

4.3.7 Experimental procedure

An experimental procedure to give repeatable experimental data was developed. Around 5 hours were required for each test: 1.5 hours for preparation and heating, 1.5-2 hours experimental run time, 1 hour cooling time, 1 hour for dismantling experiment, measuring deposition, and processing data. Cold tests excluded heating and cooling processes. The procedure is listed in detail in Appendix F.

4.3.7.1 Particle concentration calculation

It was possible to use the OPS to measure bulk particle concentration at two locations in the experiment: at the inlet to the mixing chamber, $C_{0,\,in}$, and at the exit from the test section, $C_{0,\,out}$. The inlet concentration could only be measured pre-test, and the outlet concentration only during a test. Calculation of deposition fraction using the outlet concentration is preferred,

$$f_d = \frac{m_d}{m_d + m_{out}}, \tag{4.17}$$

where m_d and m_{out} are the deposited and outlet masses respectively. As the OPS had a maximum operating temperature of 50 °C , it was not possible to measure outlet concentration during the hot experiments, hence V_d^+ must be calculated via $C_{0,\,in}$. Ambient results are presented based on $C_{0,\,out}$.

4.4 Ambient temperature experimental campaign

4.4.1 Test matrix

A summary of the ambient experimental conditions is given in Table 4.9. Reynolds numbers ranged $8\,500 - 26\,000$, and particle diameters 2.5-6.5 µm. The full test matrix is given in Appendix G, where the individual tests are given with their conditions.

Reynolds number	$8\,400 - 26\,000$
Mean velocity	7.1-22.9 m/s
Friction velocity	0.46-1.3 m/s
Temperature (gas and metal)	22 °C
Nominal particle size	2.5-6.5 µm
Test length	0.8-2.5 hours
Surface roughness	0.22, 1.12 µm
Non-dim. particle relaxation time	0.7-14.2
Non-dim. deposition velocity	0.0019-0.056

Table 4.9: Summary of operating conditions for ambient temperature tests. Full test matrix in Appendix G.

The main independent variables were d_p, Re, and surface roughness R_a. The effects of test time and the gravitational force were also investigated, to a lesser extent. It was not possible to decouple Re and u^* at constant T_g with the current experimental geometry. The maximum Reynolds number tested was limited by the maximum gas pressure at which the atomiser could produce a good quality monodispersed aerosol.

4.4.2 Results - ambient temperature

A large number of ambient temperature tests (69) were carried out. These are plotted in Fig. 4.7, where repeated tests are plotted as a single, averaged value. The data of Kvasnak et al. (1993); Montgomery and Corn (1970); Sippola and Nazaroff (2004) for horizontal pipe/channel flow, and the vertical pipe flow data of Liu and Agarwal (1974) are plotted in addition for comparison. The Kvasnak et al. (1993) data is taken from the floor of the passage, the Montgomery and Corn (1970) from the full annulus, and the Sippola and Nazaroff (2004) data from an average of the four duct surfaces. The current experimental data show a little scatter, though this is almost universally the case with particle deposition experiments. They, in general, sit within the other published works on horizontal turbulent flows. It can be seen than the horizontal experiments see higher V_d^+ for given τ_p^+ than is seen in vertical experiments for $\tau_p^+ < 7$; above this the horizontal and vertical data overlay.

The data is now presented by Re, d_p, and R_a to discuss these aspects and effects in details. Secondary investigations into a number of other variables can also be found in Appendix H.3.

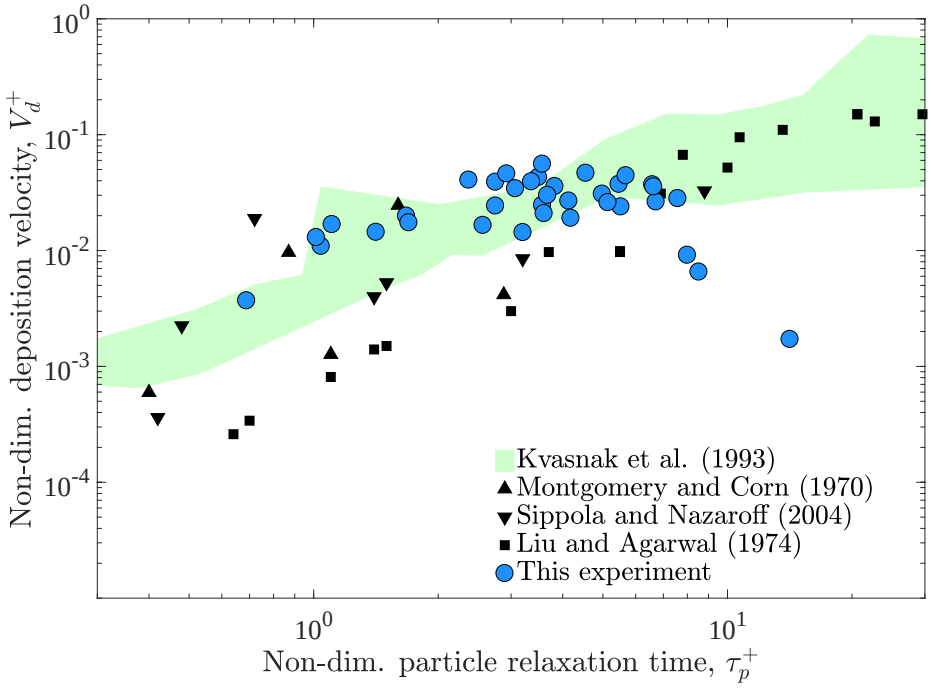

Figure 4.7: V_d^+ against τ_p^+ for all ambient temperature tests from this campaign, compared to the horizontal duct/pipe flow data of Kvasnak et al. (1993); Montgomery and Corn (1970); Sippola and Nazaroff (2004), and the vertical pipe flow data of Liu and Agarwal (1974).

4.4.2.1 Effect of flow Reynolds number, *Re*

The experimental data are plotted by Reynolds number and particle diameter in Fig. 4.8, and are shown in plots at discrete particle diameter in Fig. 4.9. From the lowest values of τ_p^+ it can be seen that increasing Re increases V_d^+ for $\tau_p^+ < 7$. Above this value of τ_p^+ the tail-off of V_d^+ can be seen, dropping to 1.5-2 orders of magnitude (OoM) lower than would be expected for the largest τ_p^+ value (14.1). Some stratification by Reynolds number is observable, with the lower Reynolds number tests having higher V_d^+ values for the same τ_p^+ . This is inline with the work of Sippola and Nazaroff (2004), who saw a similar trend for horizontal duct flow.

This effect has been reported to some extent in published literature reviewed above, though discussion of particle rebound or re-suspension is limited (see section 2.3.5). It is almost certainly due to the fact that the majority of experimentalists have chosen to make their particles or surfaces in some manner 'sticky', effectively giving an 'all-stick' boundary condition. As this is not the case in our experiments with dry NaCl particles on a dry stainless steel surface, it appears that some rebound of particles is occurring at impact. This highlights the need to consider such rebound

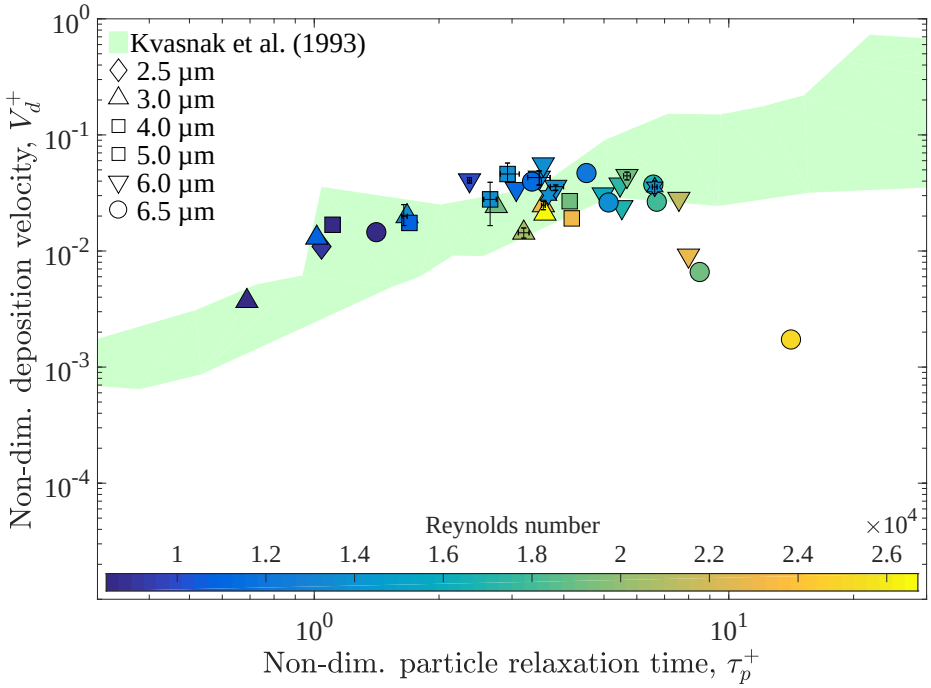

Figure 4.8: V_d^+ against τ_p^+ for all EXPα ambient temperature tests. Markers by d_p, coloured by Re. Error bars show the spread for all repeated tests.

effects when carrying out validation experiments.

The error bars on Fig. 4.8 indicate experimental repeatability. For all repeated tests, the plot marker shows an averaged value of V_d^+ and τ_p^+, with the error bar indicating the spread of the individual tests. An enlargement of the plot is shown in Fig. H.2 for clarity. Ten sets of repeat tests were done: eight pairs of repeats and two triple repeats.

It is notable that the experiments are highly repeatable; only one of the repeat tests has an error bar which extends beyond its plot marker. Across the repeated experiments, the mean deviation from the ten individual means was 14%, with a standard deviation of 11%. A maximum individual deviation of 40% was seen (d_p = 4.0 µm, Re = 14 000, point at [2.7, 0.0278]), with the remainder ranging 3.4-26%. In comparison, the repeated experimental data of Kvasnak et al. (1993) indicate an order of magnitude spread for nominal identical conditions (individual measurements shown in Fig. 2.7d). It is considered that the experimental repeatability of the current study makes the above assertion regarding apparent Reynolds dependence of V_d^+ acceptable.

The same data are coloured by kinetic energy E_k, Fig. 4.10. Here a nominal particle kinetic energy is calculated $E_{k,p} = 0.5 m_p \overline{U}_g^2$, based on the gas bulk velocity

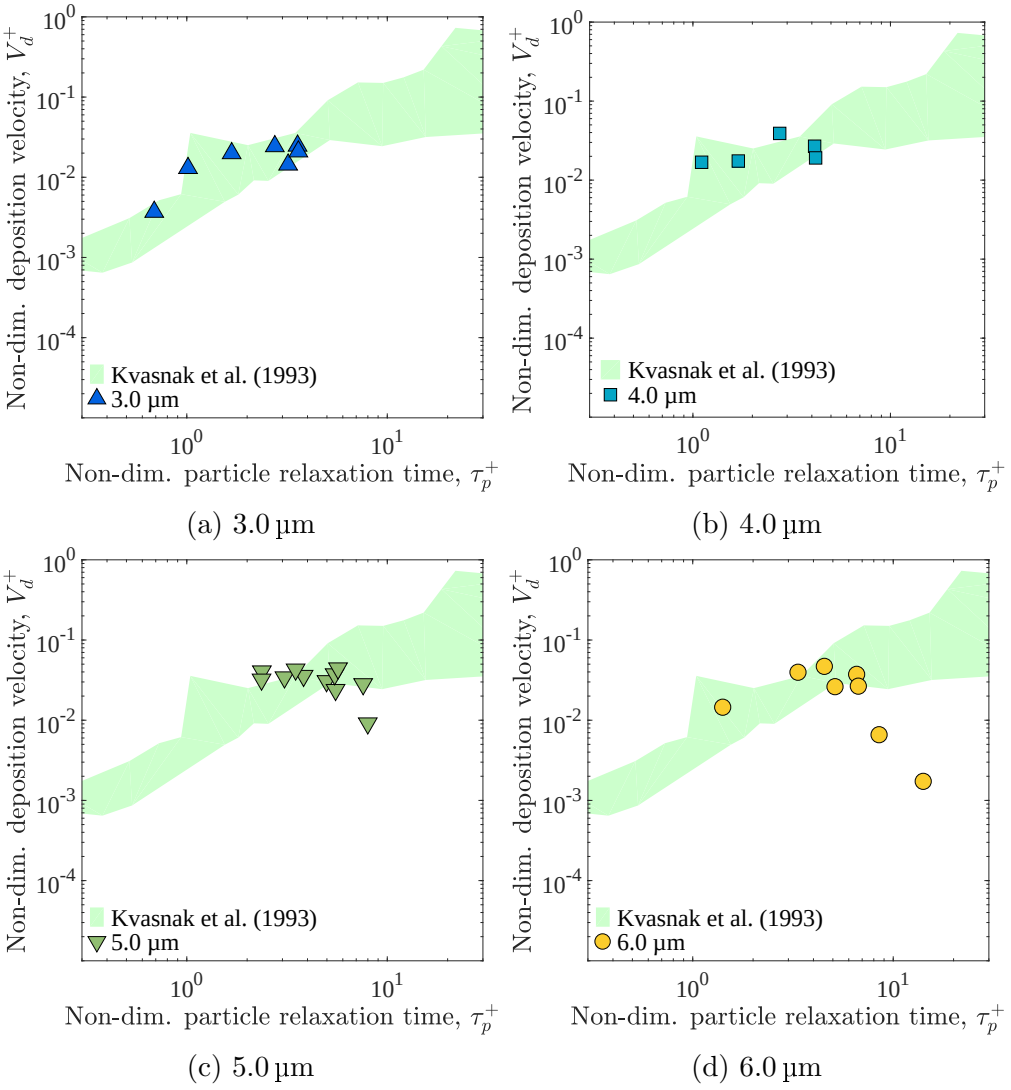

(a) 3.0 µm (b) 4.0 µm

(c) 5.0 µm (d) 6.0 µm

Figure 4.9: Experimental deposition with varying Reynolds number at discrete particle diameters.

$\overline{U}_g$. A strong trend is seen of decreasing V_d^+ for $E_{k,p} > 2.5^{-11}$ J. Along with their experimental data, Kvasnak et al. developed an analytic model for rebound, which is shown for varying coefficient of restitution r on Fig. 4.10 with the experimental data coloured by $E_{k,p}$. It is clear that the tail off of the NaCl data is close to the simulated '$r = 0.96$' line, which gives support for the rebound theory.

Another explanation for the tail off of V_d^+ could be related to shear removal or re-suspension of particles. The process of re-suspension has been studied experimentally by, amongst others, Barth et al. (2014), who deposited aerosols onto a microscope lens, then re-suspended them by increasing the flow velocity. For a given particle size, at a critical friction velocity instant re-suspension was found to occur. The authors

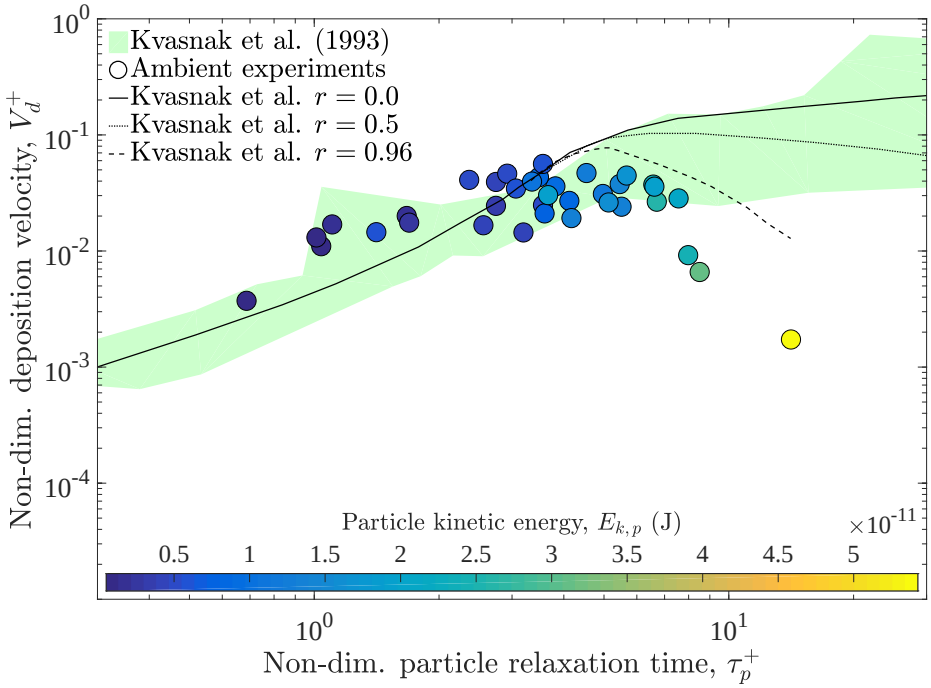

Figure 4.10: V_d^+ against τ_p^+ for all ambient temperature tests, coloured by nominal particle kinetic energy $E_{k,p}$. Lines indicate impact model of Kvasnak et al. (1993) based on constant coefficient of restitution r values.

used two aerosol materials, glass and polypropylene, with a distribution of particle sizes. The authors found that larger particles re-suspended at lower friction velocities than smaller particles. They correlated remaining fraction of the aerosol, f_r against friction velocity,

$$f_r = 0.5\,(1 - \mathrm{erf}((u^* - a)\,b))\,, \tag{4.18}$$

where erf is the error function, and a and b are fitting constants, valid for a range of particle diameters. For the relevant particle sizes: $2.8 < d_p \leq 5.2\,\mu\mathrm{m}$: $a = 0.84$, $b = 3.4$; $5.2 < d_p \leq 7.6\,\mu\mathrm{m}$: $a = 0.72$, $b = 3.9$. The function is plotted for the two particle size distributions in Fig. 4.11a.

Eq. 4.18 was applied to the a number of the experimental cases for which deposition was lower than expected. Based on the particle size distribution measured experimentally, piecewise calculations of the the fraction that would be expected to deposit in the absence of 'removal' were carried out, and a back-calculation of a possible overall V_d^+ for each experiment. As Barth et al. showed that re-suspension effects were strongest for large particles and high shear velocities, only these experiments are shown on Fig. 4.11b as the hollow shapes.

The results are somewhat mixed; the values for the 6 µm particles are all plausible, relative to the other experimental data, however for the smaller particles at high velocities the theory over-predicts V_d^+ substantially. As Barth et al. used polypropylene spheres with a substantially lower density ($\rho_p = 1\,200$ kg/m^3) the surface mechanics and particle response would be expected to differ. Applicable experimental data are scarce in the literature. If removal by shear was acting, it would be expected to act at particle impact, rather than removal at a later point in time. A similar study to that of Barth et al. using NaCl particles would be extremely useful to address this facet of particle motion, but was outside the scope of the current study. This shear removal/re-suspension process is therefore considered to be potentially occurring and contributing to the tail off seen in the experimental data, however until more applicable experimental data are available it remains speculative.

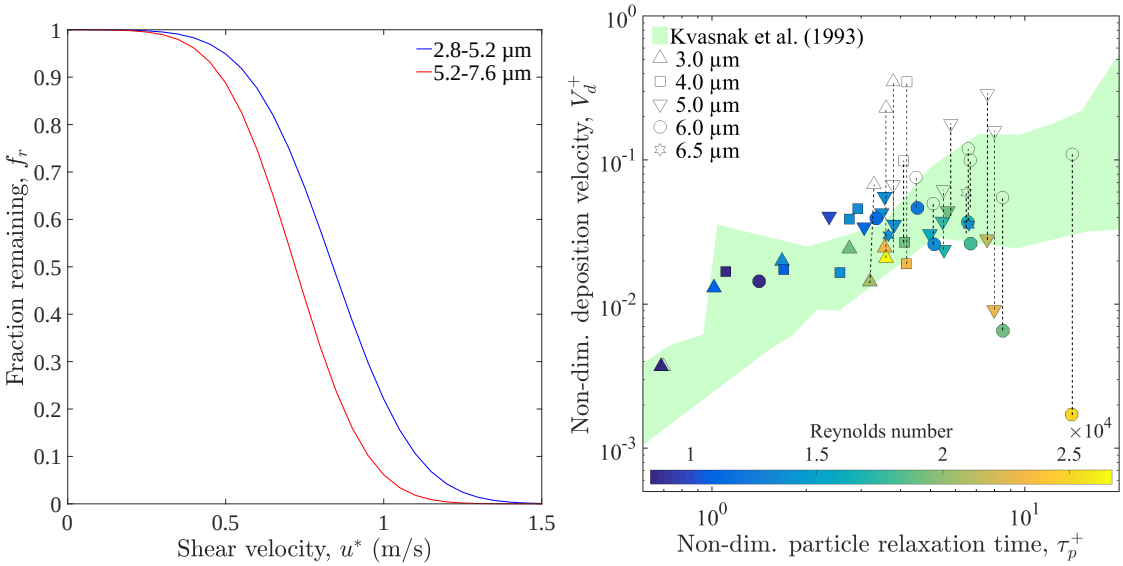

(a) (b)

Figure 4.11: *Left*: Fraction of deposition remaining as a function of shear velocity, from experimental work of Barth et al. (2014). *Right*: Calculated effect of 're-suspension'. Hollow shapes indicate recalculated V_d^+ if the re-suspension based on Barth et al. (2014) had not occurred.

4.4.2.2 Effect of particle diameter, d_p

Referring back to Fig. 4.8, the results are seen be independent of particle size in general, with no observable banding based on d_p noticeable. It is observed that only the 5-6.5 µm particles were affected by the proposed bounce effect, with the potential trend for smaller particles being within the scatter of the data. As $E_{k,p} \propto d_p^3$, higher

bulk velocities than were achieved would be required to test out the kinetic energy threshold prediction.

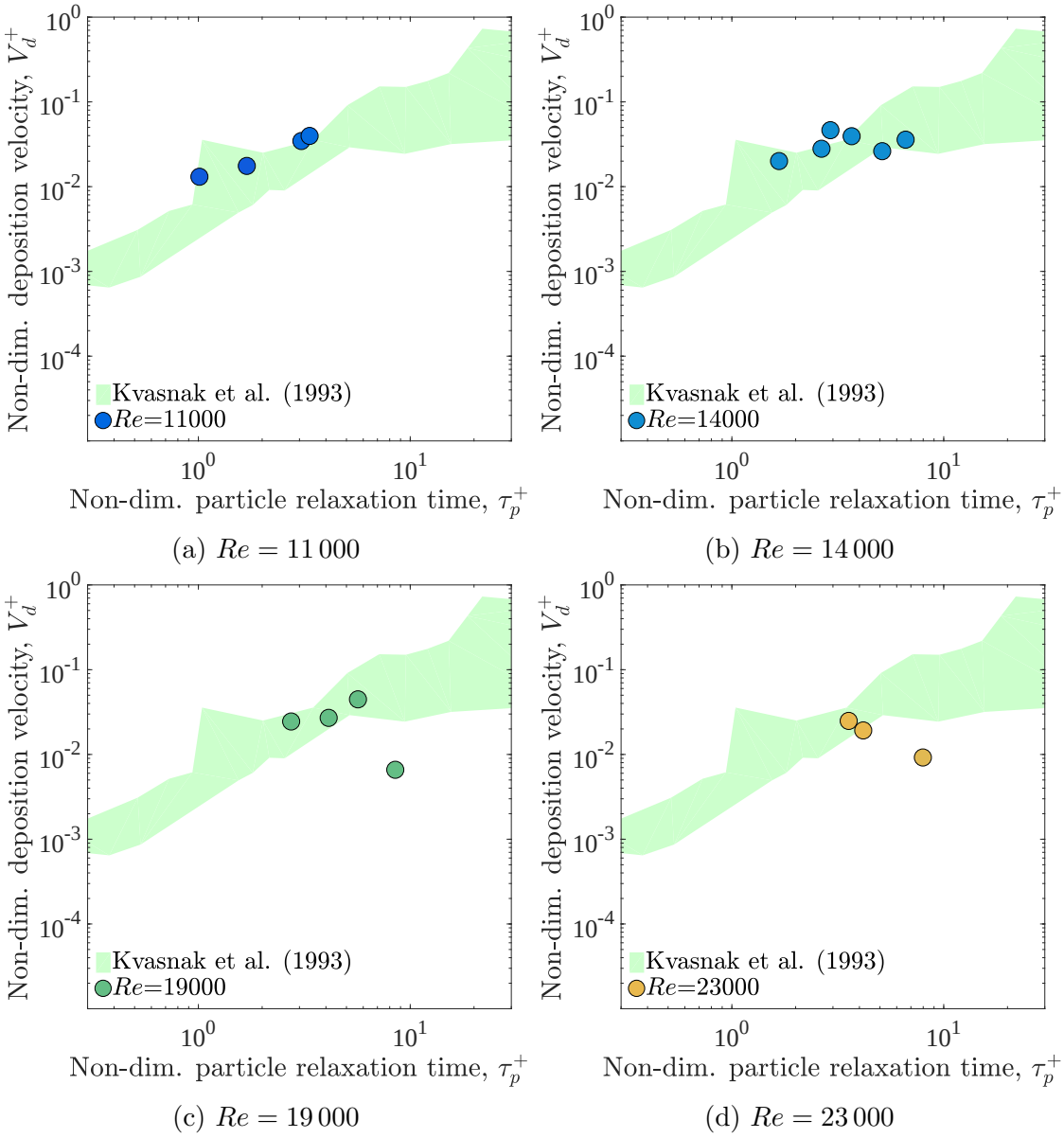

(a) $Re = 11\,000$ (b) $Re = 14\,000$

(c) $Re = 19\,000$ (d) $Re = 23\,000$

Figure 4.12: Experimental deposition with varying particle diameter at discrete Reynolds numbers.

Fig. 4.12 shows varying d_p at fixed Re. Over the four Reynolds numbers shown, the deposition trends are easily seen. At the lower Reynolds number, $Re = 11\,000$, deposition increases with τ_p^+, and at a gradient matching the Kvasnak et al. data. As the Reynolds number increases, $Re = 14\,000$ the larger particles show reduced increase with increasing τ_p^+. This is more evident at $Re = 19\,000$ where the bounce effect is noticeable for the largest particles (6 µm), and at the highest Reynolds number,

$Re = 23\,000$ the trend is strongly for decreasing V_d^+ with increasing τ_p^+, where particle rebound becomes more significant.

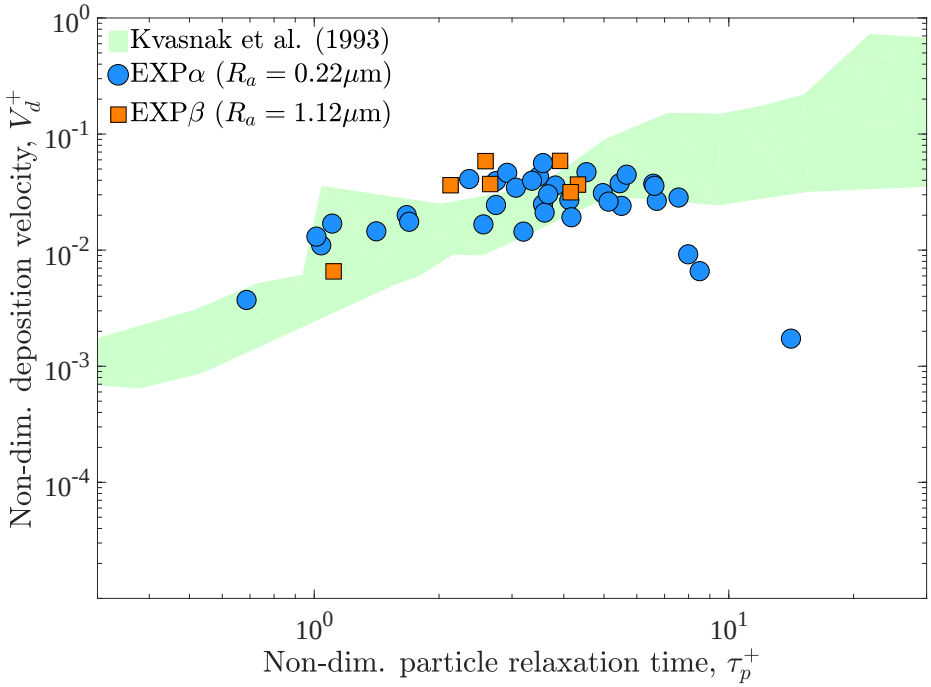

Figure 4.13: V_d^+ against τ_p^+ for all ambient temperature tests, comparing surface roughnesses. EXPα: $R_a = 0.22\,\mu$m. EXPβ: $R_a = 1.12\,\mu$m.

4.4.2.3 Effect of surface roughness, R_a

Test piece EXPα underwent some oxidisation at the maximum temperatures exposed to during the high temperature experimental campaign. A second, identical, test piece was manufactured in the same manner, EXPβ, for surface finish comparisons. Measured surface roughnesses were EXPα : $R_a = 0.22\,\mu$m, EXPβ: $R_a = 1.12\,\mu$m, where R_a is the arithmetic mean roughness. Details and surface profiles are given in Appendix H.1. Expected engine component finishes of 0.8-1.2 µm (machined) and $\sim 1.4\,\mu$m (shot peened) indicate that a comparison between deposition on test pieces EXPα and EXPβ is relevant to engine conditions. The difference in surface finish was likely due to the cleaning procedure: EXPα was scrubbed post-test, effectively polishing it. In order to maintain the different roughnesses, EXPβ was not scrubbed. Swabbing of EXPβ between cleaning and reassembly showed no NaCl remained, despite the difference in cleaning method.

Fig. 4.13 indicates that surface roughnesses of this magnitude have a noticeable effect on V_d^+. The EXPβ V_d^+ data are generally higher than those for EXPα. This

τ_p^+	1.1	2.1	2.6	2.7	3.9	4.2	4.3
d_p (µm)	2.5	5.0	4.0	4.0	5.0	5.0	5.0
Re	14 000	10 000	14 000	14 000	14 000	19 000	19 000
$V_{d,\beta}^+/V_{d,\alpha}^+$	0.51	0.88	2.1	1.3	1.4	1.2	1.4

Table 4.10: Fractional change in V_d^+ brought about by rougher test piece EXPβ ($R_a = 1.12\,\mu m$) over smoother test piece EXPα ($R_a = 0.22\,\mu m$).

is quantified in Table 4.10, which shows the fractional increase in V_d^+ for the EXPβ over EXPα. These were matched d_p and Re experiments between the two test pieces.

For the smallest values of τ_p^+, a decrease in V_d^+ was seen when the roughness increased. With increasing τ_p^+, the rougher test piece saw $1.2 - 2.4\times$ the deposition of the smoother, which is seen to become fairly constant. Over the seven EXPβ tests, the mean increase over EXPα was $1.2\times$. This is clearly a highly relvant issue with regards to real engine components, and should be investigated further.

4.5 High temperature experimental campaign

The high temperature experimental campaign was carried out at engine-representative temperatures for both gas and wall in the disc cavity and shank pocket regions. Within these secondary air systems flows, $T_w > T_g$, which formed the initial basis of the testing. This direction of temperature gradient reduces deposition of particulates on walls, referred to as 'decreasing' thermophoresis. Isothermal conditions were also assessed for comparisons to the data gathered at ambient conditions. 'Increasing' thermophoresis ($T_g > T_w$) was then assessed. This effect increases particulate deposition, which could potentially be used to filter small particulates upstream of regions where high temperature corrosion can occur.

4.5.1 Test matrix

A summary of the experimental conditions is given in Table 4.12. The full test matrix for high temperature testing is given in Appendix I.

4.5.2 Results - isothermal

The high temperature isothermal data are shown in Fig. 4.14, discriminated by d_p and Re. All results shown used the EXPα test piece. These were undertaken at the T1 condition of 390 °C, with the exception of the [2.5, 0.022], which was

Reynolds number	$6\,500 - 10\,000$
Mean velocity	21.7-33.1 m/s
Friction velocity	1.44-2.13 m/s
Temperature (gas)	390 °C (T1), 480 °C (T2)
Temperature (metal)	353-730 °C
Nominal particle size	2.0-5.0 µm
Test length	1.3-2.0 hours
Surface roughness	0.22, 1.12 µm
Non-dim. particle relaxation time	0.7-3.5
Non-dim. deposition velocity	0.000039-0.022

Table 4.11: Summary of operating conditions for high temperature tests. Full test matrix in Appendix I.

T2, 480 °C. It can be seen that the data are very comparable to those at ambient temperatures in general. For $\tau_p^+ < 3$ the hot V_d^+ values are in general lower than the ambient experiments at similar τ_p^+. A similar tail off appears in V_d^+ for larger τ_p^+ akin with the ambient temperature experiments. It is clear that once again this is due to increasing Re. Both the $Re = 10\,000$ data points show this effect. The two points at $\tau_p^+ = 3.4$ make a useful comparison: $d_p = 4\,\mu m$, $Re = 10\,000$ (yellow square), and $d_p = 5\,\mu m$, $Re = 7\,800$ (turquoise triangle). The higher Re case reduced V_d^+ by 46% when compared to the 5 µm/7 800 case. In the case of the ideal/'all stick' boundary condition implemented by many experimentalists, and following the Reynolds-independence proposed by Liu and Agarwal (1974), the two cases would be expected to be far closer.

Hot and ambient experiments are compared by nominal particle kinetic energy in Fig. 4.15. An earlier peak and tail off of V_d^+ with τ_p^+ is seen for the high temperature experiments, but at significantly higher nominal particle $E_{k,p}$ - the particles in high temperature experiments have around 4-5× more kinetic energy than those in experiments carried out at ambient conditions. Following the above theory for rebound at ambient conditions based on particle kinetic energy it would be expected that almost all of particles would rebound, as their kinetic energies are significantly higher than the proposed threshold ($\sim 10^{-11}$ J). A change in the material properties of sodium chloride would be expected with temperature; as discussed in chapter 5, the yield stress has been seen to fall with increasing particle temperature experimentally. This would be likely to cause larger particle deformations at high temperature, allowing sticking at higher impact velocities than at ambient conditions.

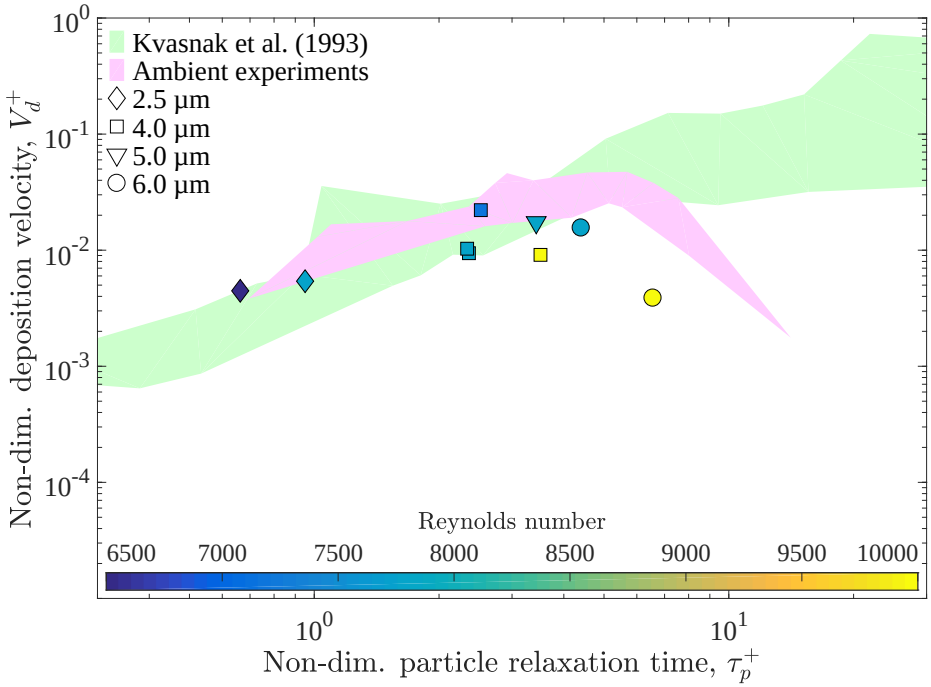

Figure 4.14: Hot isothermal data plotted by d_p and Re. Gas and metal temperatures for T1: 390 °C; for T2: 480 °C.

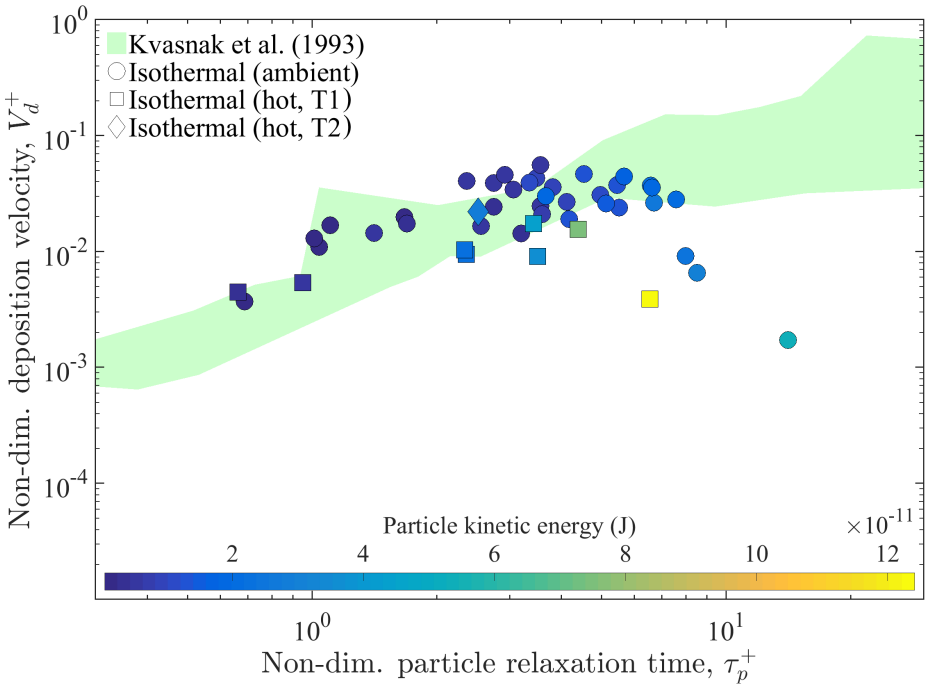

Figure 4.15: Comparison of all isothermal hot data with ambient temperature experiments. Coloured by nominal particle kinetic energy. Gas and metal temperatures for T1: 390 °C; for T2: 480 °C.

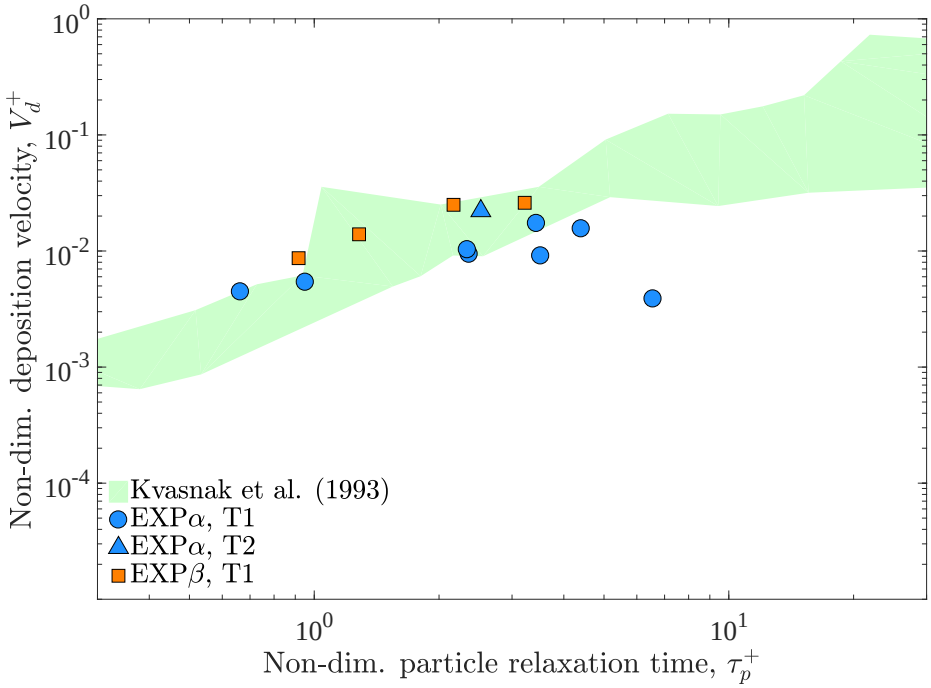

Figure 4.16: Surface roughness effects on deposition for isothermal high temperature experiments. EXPα : $R_a = 0.22\,\mu$m, EXPβ: $R_a = 1.12\,\mu$m. Gas and metal temperatures for T1: 390 °C; for T2: 480 °C.

Experiments were carried out with the second test piece EXPβ to investigate surface roughness effects seen at high temperatures, Fig. 4.16. It is seen here that the difference between the two test pieces is more significant at high temperatures than ambient, with the rougher test piece returning higher deposition across all values of τ_p^+ tested. For the tests undertaken at $\tau_p^+ = 0.9, 2.2, 3.2$, the increases in V_d^+ for EXPβ over EXPα were 1.6, 2.5, 1.5× (mean 1.9×). For comparison, at ambient conditions the mean increase with the rougher test piece was 1.2×. The effects of surface roughness and temperature should be investigated further.

4.5.3 Results - thermophoresis

Non-isothermal experiments were undertaken with temperature pairings A,B,D,E as outlined in Table 4.12. Gas temperatures were kept constant for T1 (390 °C), T2 (480 °C) conditions.

Results are presented as V_d^+ vs. τ_p^+ as throughout the thesis in Fig. 4.17, and also as $\overline{f_d}$ vs. τ_p^+ in Fig. 4.18. This second figure clearly indicates how the thermophoretic conditions change the deposition characteristics in relation to the isothermal case.

Tests T1$_A$ and T1$_B$ were carried out with increasing thermophoresis, $T_g > T_w$, at

Case	T1			T2		
	T_g (°C)	T_w (°C)	P^+_{Th} $\times 10^{-6}$	T_g (°C)	T_w (°C)	P^+_{Th} $\times 10^{-6}$
A	390	355	0.68	-	-	-
B	390	383	0.14	-	-	-
C	390	390	0.00	480	480	0.00
D	390	480	-1.9	480	530	-0.92
E	390	630	-5.0	480	730	-6.3

Table 4.12: Gas and wall temperature pairings A-E for high temperature tests. Indicative P^+_{Th} values shown for the tabulated gas temperatures with $d_p = 4\,\mu$m, $Re = 7\,800$ (T1), $Re = 7\,200$ (T2).

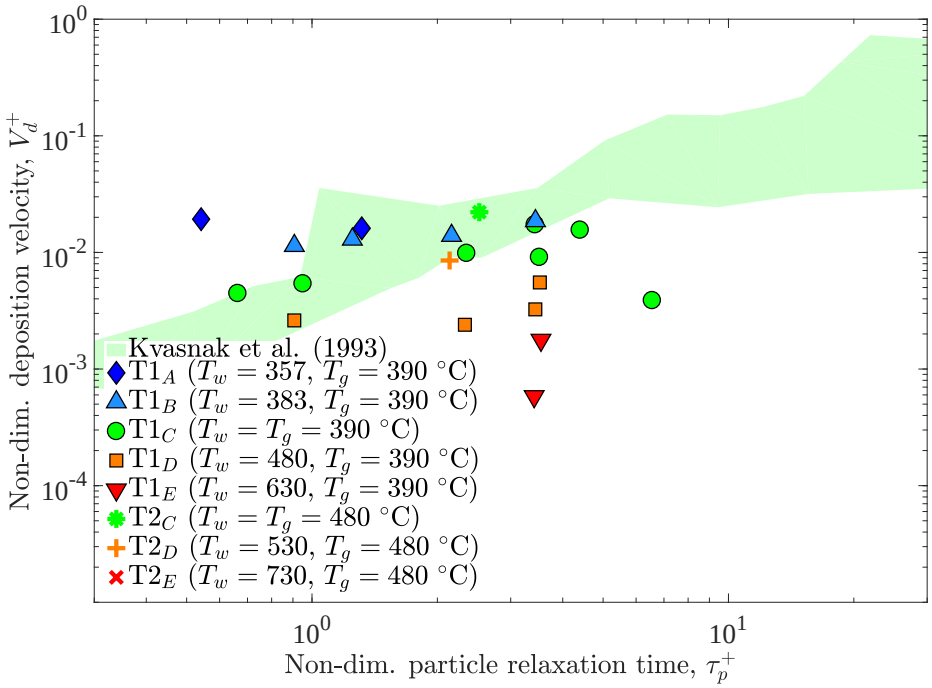

Figure 4.17: Non-dimensional deposition velocity vs. non-dimensional particle relaxation time for thermophoretic experiments. T1 (blue): $T_g = 390$ °C . T2 (red): $T_g = 480$ °C .

$Re = 7\,800$. Substantial increases in V_d^+ are seen for small gas temperature gradients relative to the magnitude of that in the decreasing thermophoretic direction. The T1$_B$ data show fairly constant V_d^+ values across the range of τ_p^+ investigated, with V_d^+ values increasing $1.1 - 2.5\times$ compared to the isothermal case. At T1$_A$ conditions, stronger thermophoretic conditions are seen to increase V_d^+ 4.8× over isothermal values.

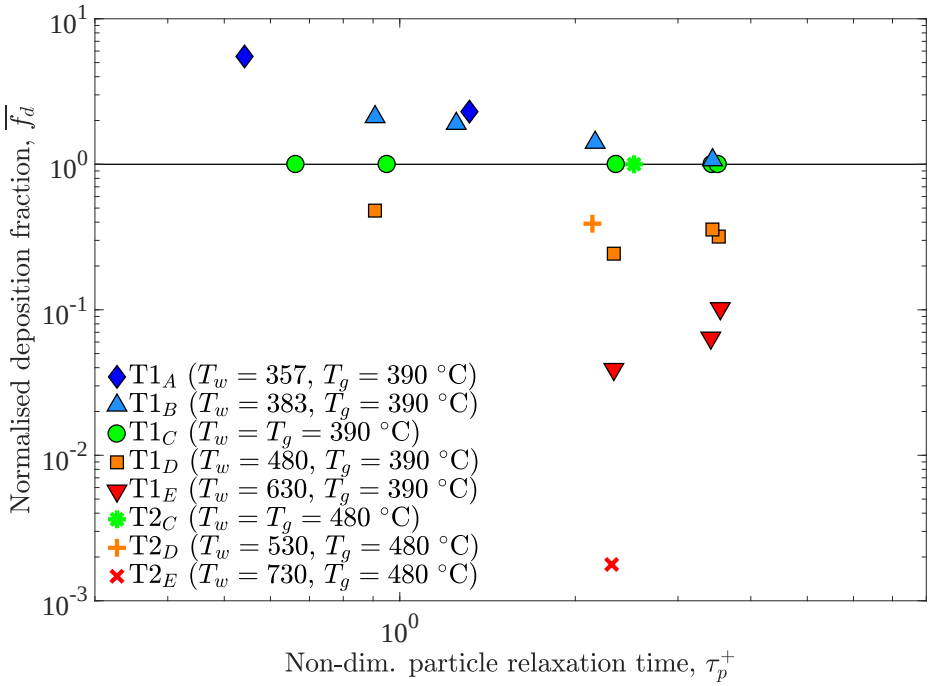

Figure 4.18: Normalised deposition fraction vs. non-dimensional particle relaxation time for thermophoretic experiments. T1: $T_g = 390$ °C . T2: $T_g = 480$ °C .

Temperature conditions T1$_D$ and T1$_E$ were undertaken at temperature gradients which gave decreasing thermophoresis. T1$_D$ shows significant reduction in V_d^+ in comparison to the isothermal data. At low $\tau_p^+ (< 2.5)$, V_d^+ stays fairly constant with τ_p^+, then increases for $\tau_p^+ > 2.5$, tending back towards the isothermal data line. The effect of varying d_p, Re at constant τ_p^+ showed a reduction in V_d^+ of 42% between the $d_p = 5\,\mu$m, $Re = 7\,800$ and $d_p = 4\,\mu$m, $Re = 10\,000$ cases. This is similar to the reduction at isothermal conditions (46%).

The T1$_E$ experiments used a larger temperature gradient than T1$_D$; these show a similar trend to the T1$_D$ experiments but of larger magnitude. A larger reduction of 68% between the two varied d_p, Re experiments at constant τ_p^+ is seen for this higher temperature gradient.

The T2 experiments were undertaken at higher gas and wall temperatures than T1. They show a similar trend to T1; although the T2$_C$ (isothermal) and T2$_D$ data points sit higher than the equivalent T1 points, the reduction in deposition fraction is comparable. The T2$_E$ experiment showed extremely low deposition, close to the detection limit of the conductivity meter. Deposition was 0.18% of that seen at isothermal conditions.

Natural log of normalised deposition fraction is plotted against thermophoretic parameter P_{Th}^+ for the six thermophoretic conditions in Fig. 4.19. Particle thermal

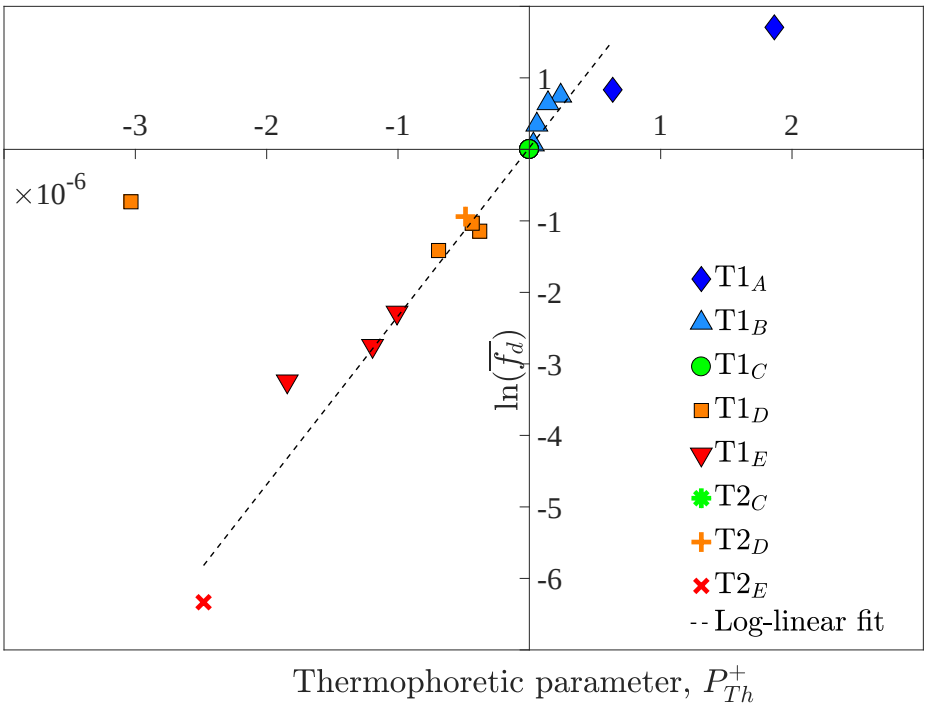

Figure 4.19: Log of normalised deposition fraction $\ln(\overline{f_d})$ against thermophoretic parameter P^+_{Th}.

conductivity is $k_p = 4.9$ W/m/K for $T_g > 120$ °C. The Beresnev and Chernyak (1995) expression is used for the calculation of thermophoretic coefficient Φ.

It can be seen that the relationship between $\overline{f_d}$ and P^+_{Th} is reasonably (log-) linear over the whole experimental domain, in both the increasing and decreasing thermophoretic directions. It is noted here that the data contain a range of particle sizes and Reynolds numbers. A first order correlation by linear regression is calculated,

$$\overline{f_d} = 1.02e^{2.38\times10^6 P^+_{Th}}, \tag{4.19}$$

and is shown on Fig. 4.19. The (log-) linear fit is good for both increasing and decreasing thermophoresis, with only two points significantly deviating. These are not included in the correlation calculation. Based on this, with a knowledge of the isothermal deposition fraction for the same aerosol, and the expected thermal conditions, the change in deposition due to thermophoresis can be estimated.

4.6 Secondary investigations

4.6.1 Gravitational effects

The hot and ambient experiments showed some salient differences. The ambient experiments showed no visual sign of gravitational effects. One trio of experiments was undertaken with the test insert sequentially orientated at the top, middle, and bottom of the passage. Experimental conditions were ambient, $d_p = 4\,\mu m$, $Re = 14\,000$. Results are shown in Table 4.13. As would be expected, the ratio of deposition on the insert to the whole passage is lowest in the top orientation, and highest in the bottom orientation, indicating that some gravitational effects are occurring. In general, ambient deposition was seen to be extremely fine and uniform across the surface, with no visible entry/exit trends. The variation in full passage V_d^+ is noted; variation of this magnitude is not uncommon in repeated experiments, and has been observed in many published works.

Orientation	Test insert	Full passage	Insert:passage
Top	0.026	0.035	0.74
Side	0.029	0.026	1.12
Bottom	0.031	0.022	1.41

Table 4.13: Effect of test insert orientation on measured V_d^+ values. Conditions: $d_p = 4\,\mu m$, $Re = 14\,000$.

The hot experiments showed complex interaction between thermophoretic and gravitational forces. The decreasing thermophoresis ($T_g < T_w$) temperature gradient experiments showed some traces of gravitational effects, Fig. 4.20, with qualitatively higher deposition seen on the bottom half (in the vertical direction), though it wasn't quantified with swabbing. Some apparent clumping or agglomeration of particles appeared to occur in the hot tests, which was not seen in the cold tests. This can also be seen in Fig. 4.20. It is proposed that in these hot tests the particles accrete preferentially where deposition has previously occurred, rather than in-flight agglomeration, as particles were in the range 2.5-6.5 µm at injection into the system, and the volumetric density ratio is low ($\mathcal{O}(10^{-9})$). The agglomeration was more noticeable at the higher wall temperatures, though almost no deposition was visible for the highest wall temperatures (highest temperature gradients).

With the lack of comparable published data it is difficult to assess this in terms of other studies, and would potentially require optical/imaging techniques to assess

more fully. These trends were seen more strongly in tests where the generated particle diameter was high, which may show some interaction between drag-thermophoresis-gravity due to particle density that, to the author's knowledge, has not been investigated previously.

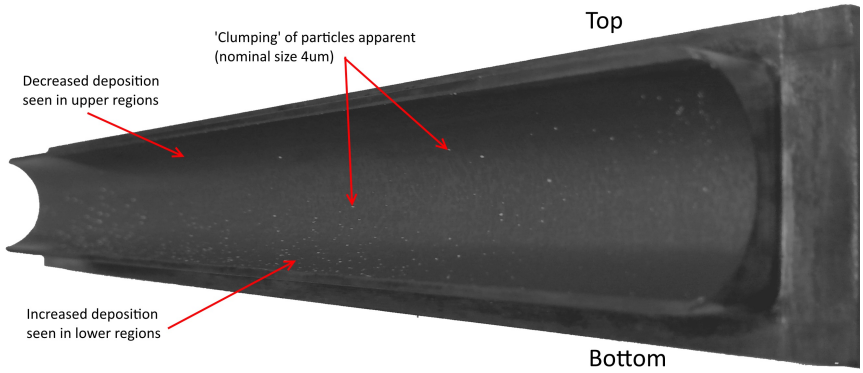

Figure 4.20: Visible gravitational effects and some 'clumping' of particles in experiment (temperatures $T2_D$, $d_p = 4\,\mu m$, $Re = 7\,800$). Qualitatively higher deposition is seen on the bottom/lower half of the insert.

4.6.2 Lift off of deposited particles

Several pairs of tests were carried out to assess the effect of the method of cooling the test piece post-test. The first of each pair of tests let the test piece cool with no internal flow. A fan was used to externally cool the test piece. The second half of each pair of tests repeated the deposition experiment, but left the gas running post-test, with the atomiser and heaters switched off, giving internal convective cooling. This in detailed in Appendix H.3.1. Results were somewhat inconclusive as to whether leaving the coolant on was lifting off particles. It was chosen to only cool the high temperature experiments externally following this investigation.

4.6.3 Experimental test length

A small number of the tests varied experimental length. These allowed the effect of experimental length to be assessed, a facet of such experimental work missing from the literature. The results, detailed in Appendix H.3.2, indicated tentatively that the EXPα test piece was not affected by the experimental length, whereas three of the four suitable EXPβ tests were. This may be an effect related to the roughening of the test piece surface due to deposition during the experiments due to deposition

occurring. This is an area of experimental work that requires more study. EXPβ data presented above are those closest to the corresponding EXPα test lengths.

4.7 Summary

A new experimental rig has been designed and built, and shown to be operating in line with other similar experiments for horizontal channel flow at ambient conditions. A mono-dispersed sodium chloride aerosol was used. Repeatability of integral deposition characteristics was seen to be good between tests. A new experimental method for the measurement of the deposited NaCl particles was developed and validated in a series of calibration tests.

Experiments carried out at ambient conditions indicated an increase of V_d^+ with τ_p^+ for $\tau_p^+ \leq 7$, and a reduction with $\tau_p^+ > 7$. This has been attributed to particles having enough kinetic energy at impact to overcome adhesive forces and rebound into the flow, reducing deposition. A similar effect was noted in the high temperature isothermal results, but initiating at a lower τ_p^+ threshold ($\tau_p^+ = 5$).

Experiments carried out under with wall-gas temperature gradients introduced significant thermophoretic effects. Under decreasing thermophoretic conditions, V_d^+ was seen to fall by up to three orders of magnitude in comparison to isothermal conditions. Under increasing thermophoretic conditions increases of 400% were seen for smaller temperature gradients. The various effects are summarised in Table 4.14.

Parameter	Effect on V_d^+
Re	For given τ_p^+, V_d^+ falls for increased Re
d_p	For given τ_p^+, V_d^+ increases with increased d_p
R_a	For given τ_p^+, V_d^+ increases with increasing surface roughness
g	Gravitational force increasing deposition on bottom surface, and decreasing on top surfaces. Visible effects for thermophoretic decreasing conditions
$\boldsymbol{\nabla} T_g$	Increases ($T_g > T_w$) or decreases ($T_g < T_w$) deposition rate. Effect increases with magnitude of gradient and decreasing τ_p^+

Table 4.14: Effects of parameters investigated experimentally on deposition rate

Chapter 5

Simulations of Pipe Flow Experiments

This chapter presents simulations of the experimental work from chapter 4. These were undertaken at both ambient and high temperatures. The continuous random walk model is applied from chapter 3, and developments are discussed based on the findings of the simulations.

5.1 Numerical set-up

The numerical domain for simulations of the experimental work in chapter 4 is shown in Fig. 5.1. Bulk heated flow is injected at I_1, particulate-laden gas enters at I_2. Walls $W_{1,\ldots,6}$ have appropriate thermal boundary conditions as measured or inferred from the experimental measurements (see Fig. 4.4). Boundary conditions are listed in Table 5.1. Gas and wall temperatures are updated as necessary to match the specific cases $T_{A,\ldots,E}$.

The realisable k-ϵ turbulence model was used for closure of the Reynolds-averaged Navier-Stokes equations. Trials with the Reynolds stress model (RSM) did not indicate significant differences to particle statistics. Spatial discretisation of scalars was carried out using the second-order upwind scheme. The 'coupled' pressure-velocity coupling scheme was used for its efficiency and Green-Gauss Node-Based gradient discretisation.

Gas density was calculated from the ideal gas law. Gas viscosity was calculated by Sutherland's law. Gas specific heat capacity was correlated against gas temperature (K), Hurley (2008),

$$c_p = 716.8 + 0.812\,T_g - 5.334 \times 10^{-5}\,T_g^2 + 1.445 \times 10^{-7}\,T_g^3. \tag{5.1}$$

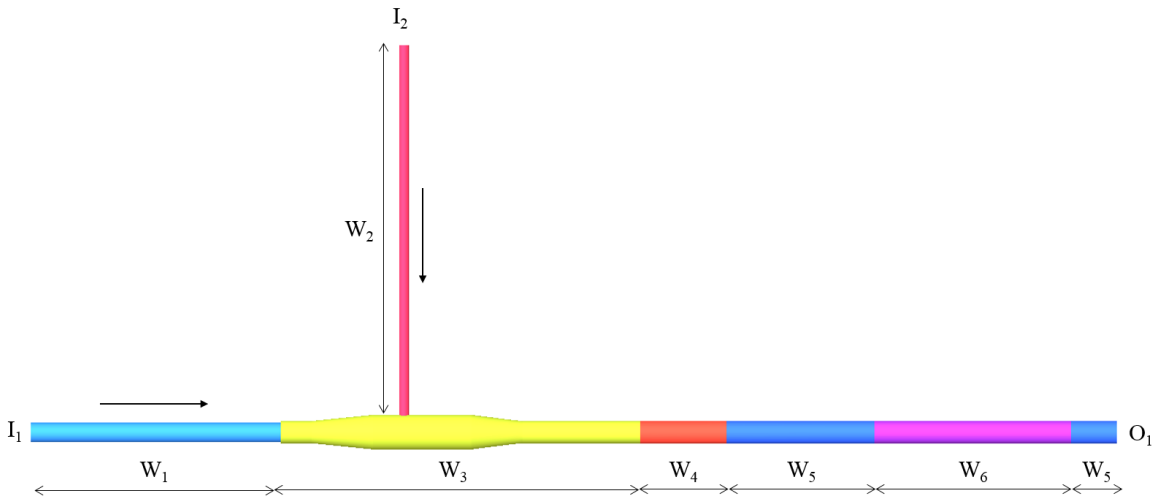

Figure 5.1: Numerical domain for simulations of experimental work. Gravity included in the vertical direction. Arrows indicate flow direction. I_1: bulk inlet; I_2: atomiser inlet; W_1: bulk tube; W_2: atomiser tube; W_3: mixing chamber; W_4: insulated section; W_5: test piece (oven); W_6: test insert (measurement region); O_1: outlet.

The gas thermal conductivity was also correlated against temperature (K), Hilsenrath (1955),

$$k = 0.0169 + 5.113 \times 10^{-5}\, T_g. \tag{5.2}$$

The single-precision solution option was used. Scaled residuals were of the order of 10^{-5} (continuity), 10^{-6} (turbulence properties), and 10^{-7} (energy and velocities). Maximum net mass flow rate was of the order of 10^{-7} % of inlet mass flow rate. The gravitational force was switched on.

Particle tracking used the CRW model, chapter 3. Particles were injected in uniform grid on the atomiser inlet plane (I_2), with a UDF written to match particle velocity and temperature to the gas conditions at each injection point. $5{\times}10^5$ particle steps were found to reduce incomplete particles to a negligible number. The thermophoretic force was switched on for the high temperature tests, and the thermophoretic coefficient of Beresnev and Chernyak (1995) applied as a UDF function, linearly interpolating the tabulated data for $R\,(=\sqrt{\pi}/2Kn)$ from their paper. The Fluent implementation of the Talbot thermophoretic coefficient, and the expression of Young were also used for comparison.

Boundary	Name	Condition	Value
I_1	bulk inlet	Mass flow inlet	$\dot{m}_g$, T_g as exp.
I_2	Atomiser inlet	Mass flow inlet	$\dot{m}_g$, T_g (ambient) as exp.
O_1	Outlet	Pressure outlet	0 Pa as exp.
W_1	Bulk tube	Temperature	Adj. to give T_{mx}, T_{ti} as exp.
W_2	Atomiser tube	Temperature	Amb. (295 K) as exp.
W_3	Mixing chamber	Temperature	Adj. to give T_{ti} as exp.
W_4	Insulated tube	Adiabatic	Insulated as exp.
W_5	Oven (two sections)	Temperature	T_w as exp.
W_6	Test insert	Temperature	T_w as W_5

Table 5.1: Boundary conditions for experimental simulations

5.2 Grid independence study

A grid independence study was carried out. Four meshes were generated, from 1.74-8.74 M cells, Table 5.1. Scale factor indicates relative cell size in relation to the 'medium' mesh. Conditions were to match case $T1_C$ $Re = 7\,800$ (isothermal at 390 °C). The realisable k-ϵ model was used with second-order discretisation of spatial gradients. A pressure-velocity coupling was used. The mean pressure on the test insert, Fig. 5.2a, and net convective heat flux into the domain through walls, Fig. 5.2b were used for grid convergence assessment. Both parameters show the medium grid density was enough to allow calculation of a grid-independent continuous phase solution.

Mesh	Cells (M)	Prism layers	r_e	Scale factor
Coarse	1.74	10	1.25	1.26
Medium	2.86	10	1.25	1.00
Fine	6.08	15	1.10	0.80
Very fine	8.74	15	1.10	0.63

Table 5.2: Grids for independence study. Scale factor is cell size (length) relative the medium mesh. The total prism height was fixed at 1 mm; this was seen to be sufficient to not limit the growth of the boundary layer. r_e is the prism layer expansion ratio.

Investigation of V_d^+ with relation to the grid showed reasonable convergence between the medium and fine meshes. $7\,600 - 69\,000$ particles were injected, depending on particle size. The very fine mesh indicated significantly lower deposition across the

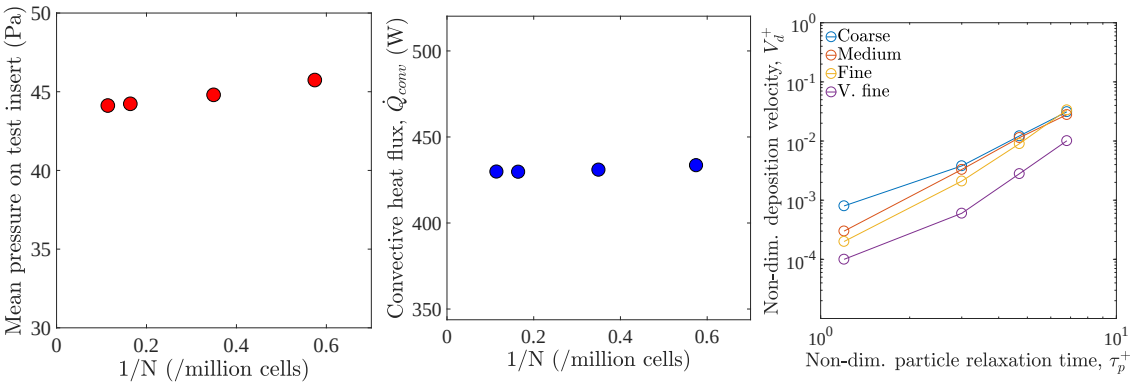

(a) Test insert pressure (b) Convective heat flux (c) V_d^+ vs. τ_p^+

Figure 5.2: Grid independence study for experimental numerical simulations

entire domain of τ_p^+ investigated. The other three meshes converged best for largest particles, but convergence is acceptable for all but the smallest particles. The very fine mesh results are a distance from experimental data, so were disregarded; this is possibly due to diffusion errors. The medium mesh was used as it showed good convergence to the fine grid.

5.3 Ambient temperature simulations

Simulations were carried out of the ambient experimental results at five Reynolds numbers, $8\,400 - 23\,000$. Four particle sizes were injected, matching those used experimentally; 2.5, 4.0, 5.0, 6.0 µm. The first simulations used the CRW and DRW models, with an all-stick boundary condition.

The results of these simulations are shown in Fig. 5.3. The CRW simulations are seen to under-predict the experimental deposition by an order of magnitude on average, for $\tau_p^+ < 2$. For $3 \leq \tau_p^+ \leq 8$, the CRW simulations are closer to the experimental results, under-predicting by a maximum factor of four. Above $\tau_p^+ = 8$, the simulation does not produce the tail off of V_d^+ seen experimentally; this is to be expected as it is thought to be a rebound effect, which is not captured by the all stick boundary condition (see section 5.3.2).

As would be expected from chapter 3, the discrete random walk model predicts deposition that is close to independent of τ_p^+ . Over the entire range of τ_p^+, V_d^+ only increases by 1.4×, whilst the Kvasnak et al. (1993) data indicates an increase of around 70×, based on the mid line of the shaded region for that τ_p^+range (0.51-17).

The CRW simulations of the experimental work predict deposition trends very similar to those presented for the simulations of the Liu and Agarwal vertical pipe

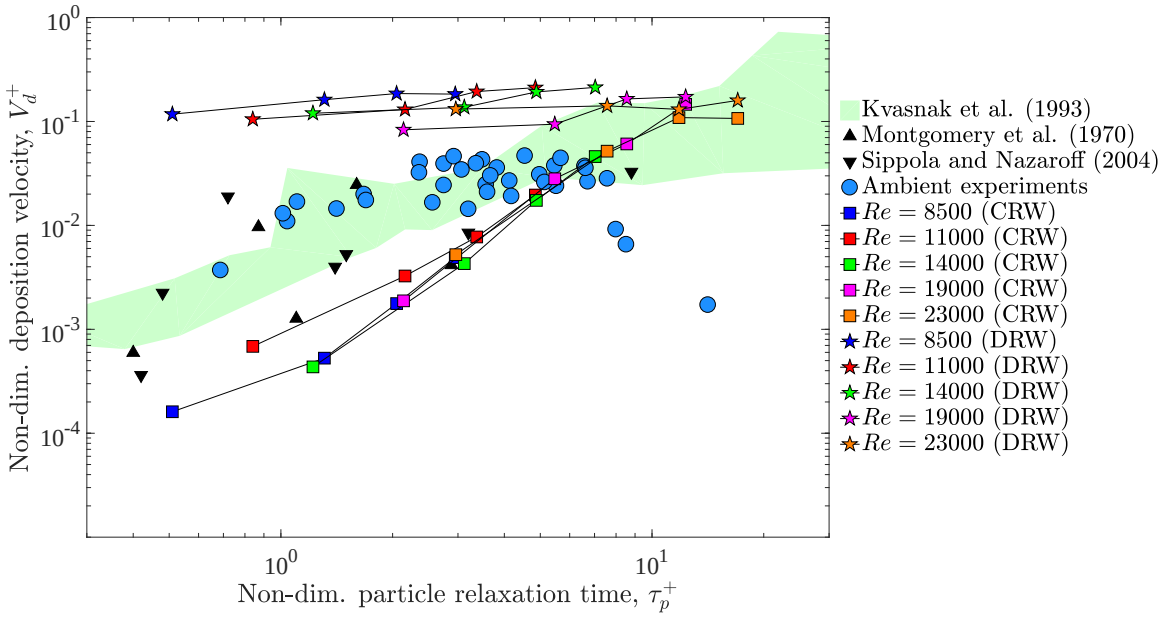

Figure 5.3: Initial numerical simulations of experimental rig at ambient conditions, using CRW (squares) and DRW (pentagrams) models

flows in chapter 3. Despite the gravitational force being used, this has almost no effect on the simulation integral deposition results. The CRW model does not appear to have been tested for horizontal flows previously, hence why this has not been noted.

To assess the effect of gravity on the simulations, the circumferential distribution of deposition over the test insert was calculated, Fig. 5.4. Radial scale indicates fraction of total deposition occurring in that sector. Gravity acts vertically downwards as viewed. It is seen that gravity has an extremely strong effect on deposition, in particular for lower Re and smaller particles. That gravity would affect slower speed flows more than higher speed is expected; g remains constant, whilst a_D varies with Re_p. At the highest Re, deposition becomes increasingly uniform as particle diameter increases, but the smaller particle sizes are still strongly dominated by the gravitational force. The same simulations were repeated without the gravitational force, Fig. 5.5. These indicate that without the gravitational force, deposition is closer to uniform around the circumference of the test section, with stochastic variation seen. This scatter is more significant for lower τ_p^+ particles, as fewer deposit. Simulations using the DRW model with the gravitational force, showed the turbophoretic effects due to the fluid fluctuations as calculated by the DRW model was stronger the gravitational effects. Close to uniform distribution was seen around the passage circumference.

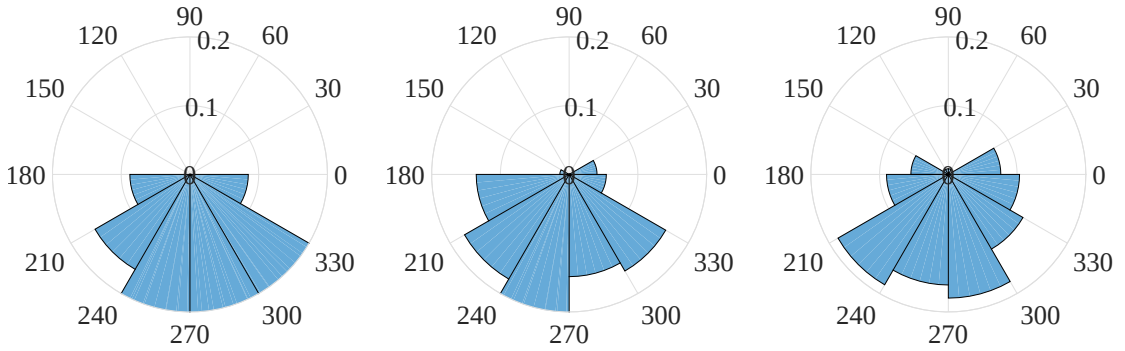

(a) $Re = 8\,500$, $d_p = 2.5\,\mu m$ (b) $Re = 14\,000$, $d_p = 2.5\,\mu m$ (c) $Re = 23\,000$, $d_p = 2.5\,\mu m$

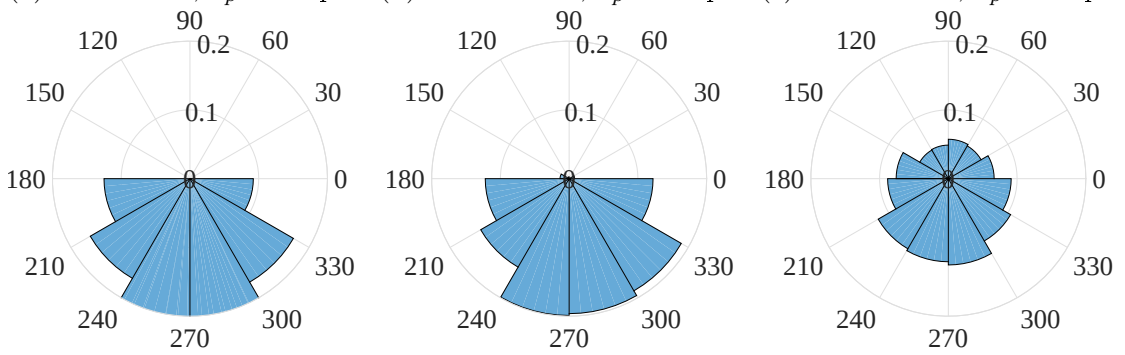

(d) $Re = 8\,500$, $d_p = 4.0\,\mu m$ (e) $Re = 14\,000$, $d_p = 4.0\,\mu m$ (f) $Re = 23\,000$, $d_p = 4.0\,\mu m$

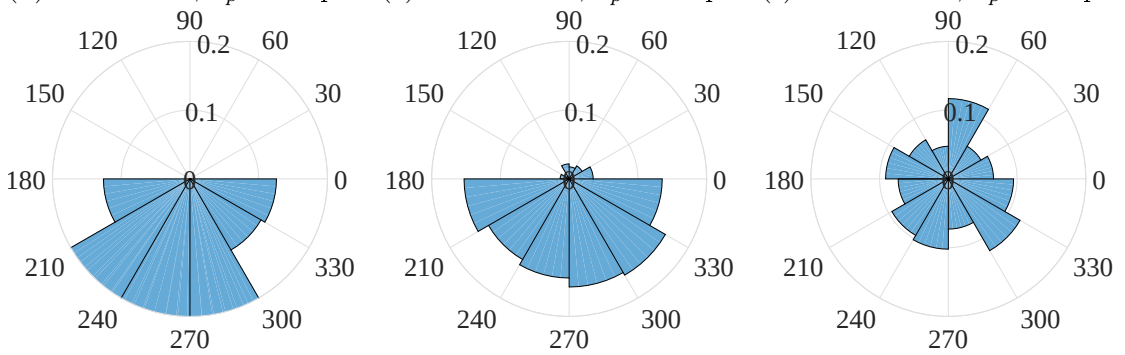

(g) $Re = 8\,500$, $d_p = 5.0\,\mu m$ (h) $Re = 14\,000$, $d_p = 5.0\,\mu m$ (i) $Re = 23\,000$, $d_p = 5.0\,\mu m$

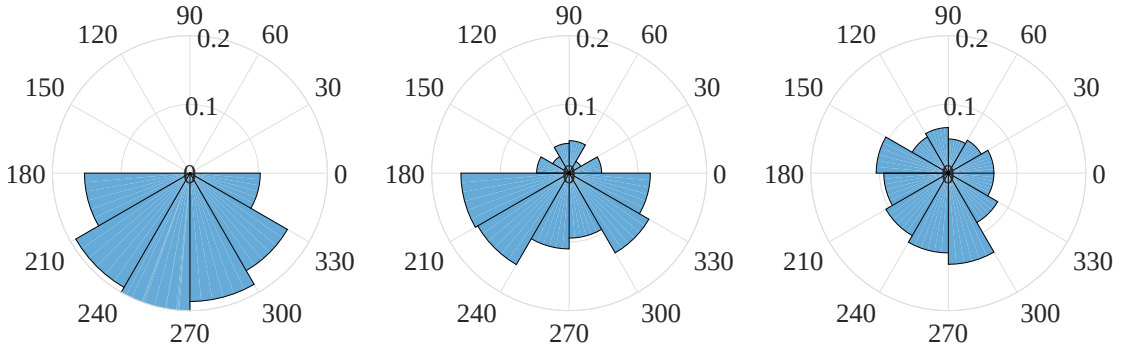

(j) $Re = 8\,500$, $d_p = 6.0\,\mu m$ (k) $Re = 14\,000$, $d_p = 6.0\,\mu m$ (l) $Re = 23\,000$, $d_p = 6.0\,\mu m$

Figure 5.4: Circumferential distribution of deposition using CRW model. Radial scale indicates fraction of total deposition in segment. Columns (left to right): $Re = 8\,500$, $14\,000$, $23\,000$. Rows (top to bottom): $d_p = 2.5$, 4.0, 5.0, $6.0\,\mu m$. Ambient conditions, $dt = dt^*$.

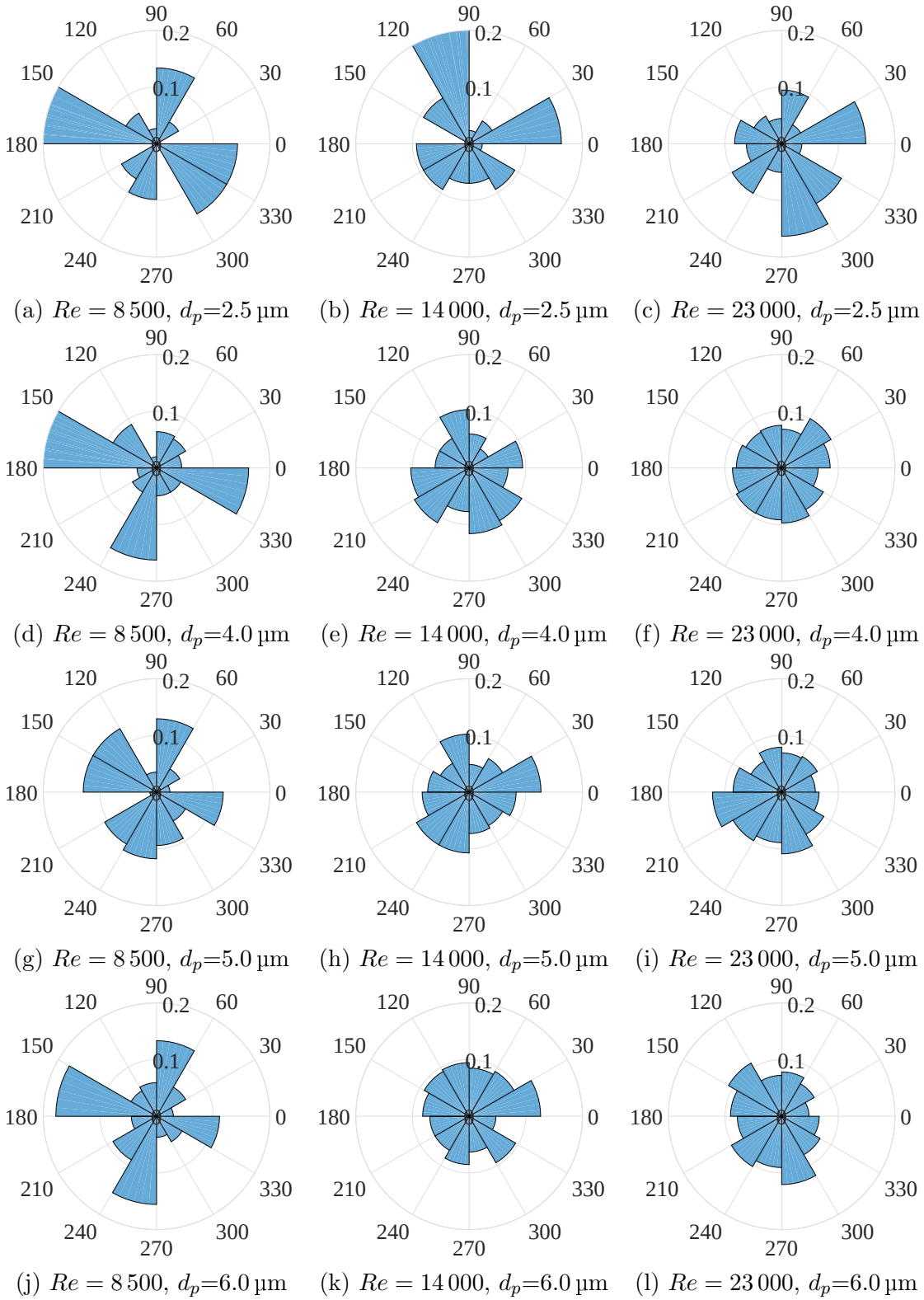

(a) $Re = 8\,500$, d_p=2.5 µm (b) $Re = 14\,000$, d_p=2.5 µm (c) $Re = 23\,000$, d_p=2.5 µm

(d) $Re = 8\,500$, d_p=4.0 µm (e) $Re = 14\,000$, d_p=4.0 µm (f) $Re = 23\,000$, d_p=4.0 µm

(g) $Re = 8\,500$, d_p=5.0 µm (h) $Re = 14\,000$, d_p=5.0 µm (i) $Re = 23\,000$, d_p=5.0 µm

(j) $Re = 8\,500$, d_p=6.0 µm (k) $Re = 14\,000$, d_p=6.0 µm (l) $Re = 23\,000$, d_p=6.0 µm

Figure 5.5: Circumferential distribution of deposition using CRW model but without gravity. Radial scale indicates fraction of total deposition in segment. Columns (left to right): Re = 8 500, 14 000, 23 000. Rows (top to bottom): d_p = 2.5, 4.0, 5.0, 6.0 µm. Ambient conditions, $dt = dt^*$.

5.3.1 Updated integration time step

Whilst the integration time step derived in section 3.2.2, hence referred to as dt^*, was seen to produce good results for vertical pipe flow, the effect of the gravitational force could not be accounted for in its initial form.

Two improvements to the modelling were made. The first was to allow the Lagrangian time scales to be anisotropic. Whilst Dehbi (2008a) initially assumed the Lagrangian time scales were isotropic, the DNS of Iliopoulos et al. (2003); Choi et al. (2004); Arcen et al. (2005) have shown that this is not the case. Figure 1 of Arcen et al. (2005) plots non-dimensional Lagrangian time, $\tau^+_{L,ii}$, against non-dimensional wall distance, y^+, in the $i = 1,\ 2,\ \&\ 3$ directions (streamwise, wall-normal, and spanwise respectively, as chapter 3). For use in this study these were correlated against y^+, and are shown in Fig. 5.6a. In comparison to the Kallio and Reeks-based fits used by Dehbi (Eqs. 3.14 and 3.15), the anisotropic fits are 1.31× higher (streamwise), 2.44× lower (wall-normal), and 1.39× lower (spanwise). These correlations were implemented in the CRW model. It is noted that in the bulk region, the definition of τ^+_L remains as Eq. 3.14, and hence $\tau^{g,+}_{L,ii} = \tau^+_L$.

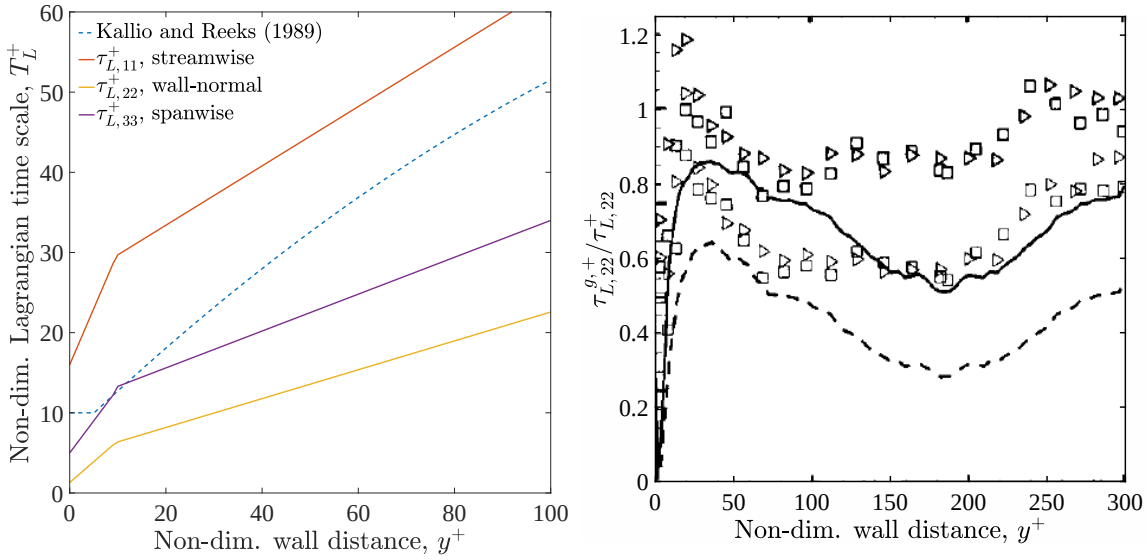

Figure 5.6: Lagrangian integral time scale effects. *Left*: Anisotropy of non-dimensional Lagrangian time scales. Directions: 1. streamwise, 2. wall-normal, 3. spanwise. *Right*: Ratio of $\tau^{g,+}_L/\tau^+_L$ in the wall normal direction, background from Arcen et al. (2005). Lines from their calculations based on Eq. 5.3, markers from their own DNS.

The model was then updated to account for the crossing trajectory effect. Here

particles trajectories cross fluid path lines due to the influence of an external force (gravity). This has the effect of decorrelating particle and fluid motion, decreasing the Lagrangian time scale. This concept was first introduced by Yudine (1959), who described the propensity of particles to fall in the gravitational direction from eddy to eddy faster than the average rate of eddy decay (Wells and Stock, 1983). This analysis showed that the effective non-dimensional Lagrangian time scale under gravitational conditions, $\tau_L^{g,+}$ becomes small relative to the isotropic non-dimensional Lagrangian time scale in the absence of gravity, τ_L^+. The reduction in the gravitational direction is given by

$$\frac{\tau_L^{g,+}}{\tau_L^+} = \frac{1}{\sqrt{1 + \left(\beta \frac{V_{rel,g}}{\sigma_g}\right)^2}}, \tag{5.3}$$

where β is the ratio of Lagrangian to Eulerian time scale, $V_{rel,g}$ is the particle relative velocity in the direction of gravity, and σ_g is the root mean squares fluid fluctuating velocity in the same direction. Hence for an increasing relative velocity due to the gravitational acceleration, the effective non-dimensional Lagrangian time scale decreases. The effect of crossing trajectories in the wall-normal (22) direction is seen in Fig. 5.6b, taken from Arcen et al. (2005). The ratio $\tau_{L,22}^{g,+}/\tau_L^+$ is seen to be highly dependent on y^+, with a very large decrease seen in the near wall region. Lines show Eq. 5.3 applied to their DNS calculations, markers show direct calculation of the time scales from sampling the DNS.

The above changes to the Lagrangian time scale calculations were applied to the integration time step. Rather than using the isotropic Lagrangian time scale, as Eq. 3.23, the gravitationally-affected Lagrangian time scale in the wall-normal direction, $\tau_{L,22}^g$, was used:

$$dt = dt_{L22} = \frac{\tau_{L,22}^g}{\sqrt[4]{Re}}. \tag{5.4}$$

This time step is referred to as '$dt_{L,22}$'. For comparison, a third, simpler, time step was defined to mirror the reduction in Lagrangian time scale given by Eq. 5.3, scaling dt^* by 0.01,

$$dt = 0.01 dt^*, \tag{5.5}$$

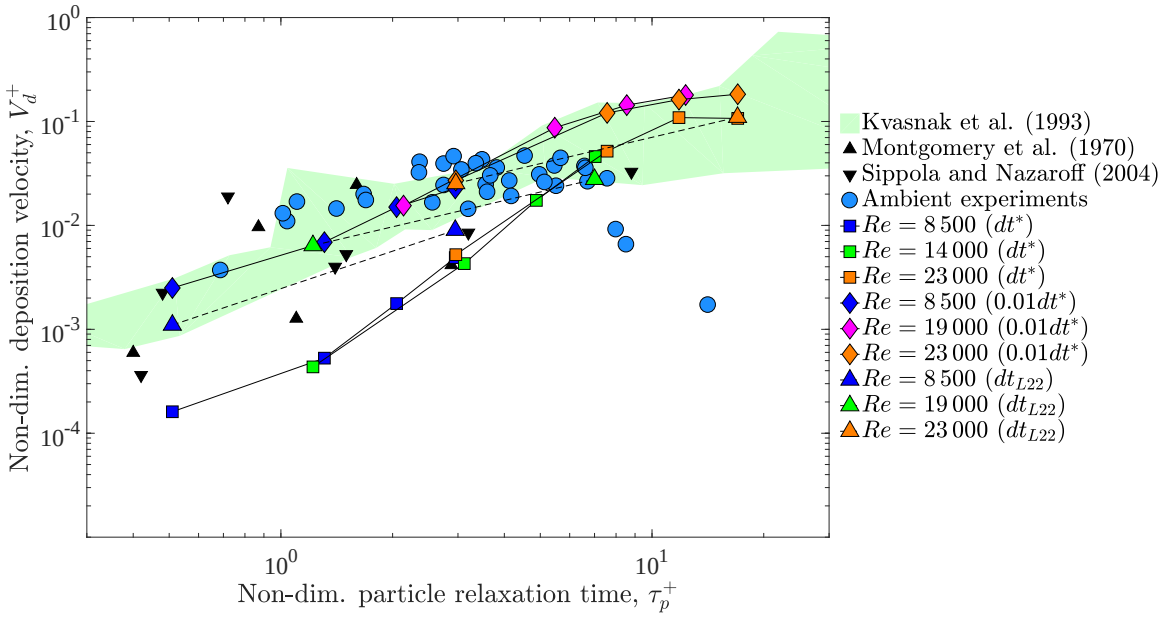

Figure 5.7: Anisotropic non-dimensional Lagrangian time scales and related time step dt_{L22} applied to the experimental ambient temperature simulations.

which is referred to in the discussion below as '$0.01dt^*$.' Time steps $dt = dt_{L,22}$ and $dt = 0.01dt^*$ were applied to the experimental simulations. Comparisons of all three time steps are shown in Fig. 5.7. The time step based on the effective non-dim Lagrangian time in the wall-normal direction, $dt_{L,22}$, produces simulations closer to the experimental data that dt^* for $\tau_p^+ < 8$, and similar to dt^* above this value. The uniform scaling of time step $dt = 0.01dt^*$, is seen to provide similar results to those given by $dt = dt_{L,22}$.

Some Reynolds number effects are seen for the $dt_{L,22}$ simulations, which aren't apparent in the dt^* or $0.01dt^*$ simulations. A similar effect was noted in the experimental data of this study, and also that of Montgomery and Corn (1970), though both sets of experimental data indicated that deposition matching τ_p^+ at higher Reynolds number gave lower V_d^+ , the reverse of the trends seen here.

The gradient of the V_d^+ to τ_p^+ dependency is seen to be more representative of both the experimental work of this study, and also Kvasnak et al. (1993), for $dt = dt_{L,22}$ than $dt = dt^*$. This suggests that a reasonable approximation comes from making the time step close to $dt_{L,22}$. The $0.01dt^*$ simulations showed an increase of $1.08 - 2.50\times$ the deposition seen in the $dt_{L,22}$ simulations, which may be considered small relative to the fidelity of other models.

5.3.2 Application of the bounce-stick model

To attempt to simulate the reduction of V_d^+ for $\tau_p^+ > 7$, the bounce-stick model, chapter 3, was applied. The bounce-stick model is applied to the $dt = 0.01dt^*$ simulations. Finding appropriate NaCl material properties for use with the model was not straightforward. The following initial material properties were used: $\sigma_y = 10$ MPa (Narita et al., 1989), $E_p = 40$ GPa (Yamamoto et al., 1987), $\gamma = 0.1$ J/m^2 (Mulheran, 1994; Kendall et al., 2011), $\mu_{imp} = 0.3$ was left as used by Bons et al.; no data were available for this parameter. The bounce-stick model was applied to the surfaces W_{3-6}.

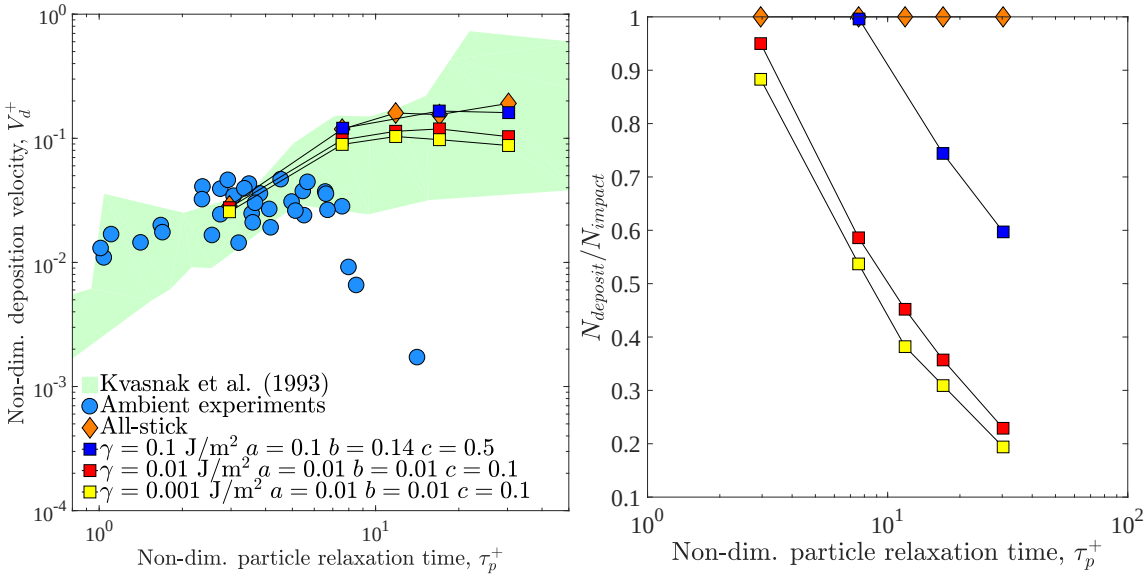

(a) (b)

Figure 5.8: Bounce-stick model applied to experimental rig ambient simulations. Material properties: $\sigma_y = 10$ MPa, $E_p = 40$ GPa, $\mu_{imp} = 0.3$. Left: V_d^+ vs. τ_p^+, showing all-stick vs. varying bounce-stick cases. Right: Ratio of number of deposited particles to number of impacting particles, $N_{deposit}/N_{impact}$. $dt = 0.01dt^*$.

The bounce-stick model was applied to the $Re = 23\,000$, $0.01dt^*$ simulation, with particle sizes 2.5-8.0 µm to emphasise the model effect. Results are shown in Fig. 5.8a. Maximum reductions of $\sim 50\%$ are seen in V_d^+ for the largest particle size (8 µm), whereas the fraction of particles depositing upon impact is seen to fall below 20%, Fig. 5.8b. The reason for this can be seen in comparisons of the impaction distributions for 2.5 and 6.0 µm particles, Fig. 5.9. The top row shows the distributions for all-stick, whilst the bottom row shows the distributions with the bounce-stick model applied (yellow squares; $\gamma = 0.001$ J/m^2, $a = 0.01$, $b = 0.01$, $c = 0.1$). In general,

deposition is seen to occur at small angles of incidence, $\alpha_1 < 10°$. The smaller particles (2.5 µm) show some shift towards lower impact angles and velocities when the bounce stick model is applied. The large particles (6.0 µm) show a much larger shift to smaller values, in particular the impact velocities. It is seen that the particles that re-impact multiple times do so at progressively lower velocities and angles, making them increasingly likely to stick.

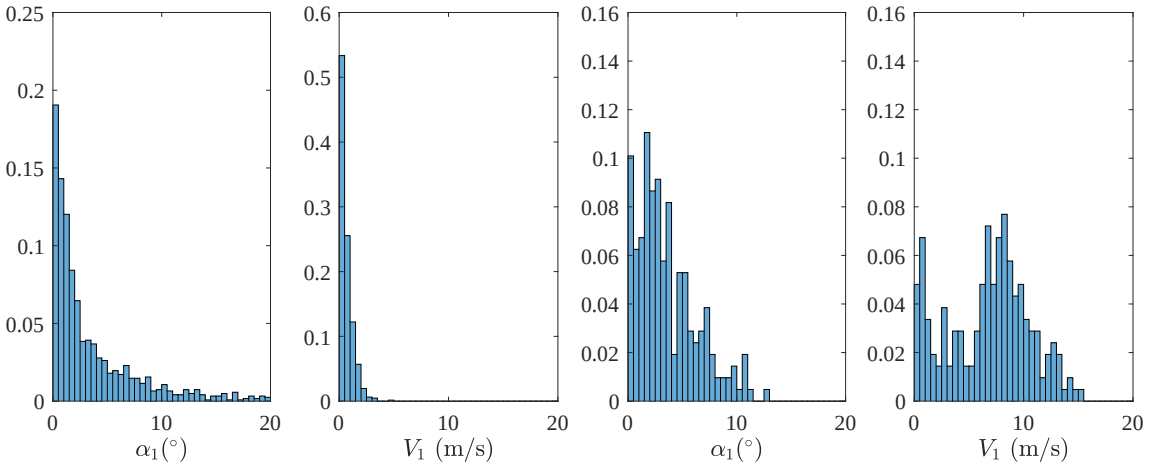

(a) 2.5 µm , all-stick

(b) 6.0 µm , all-stick

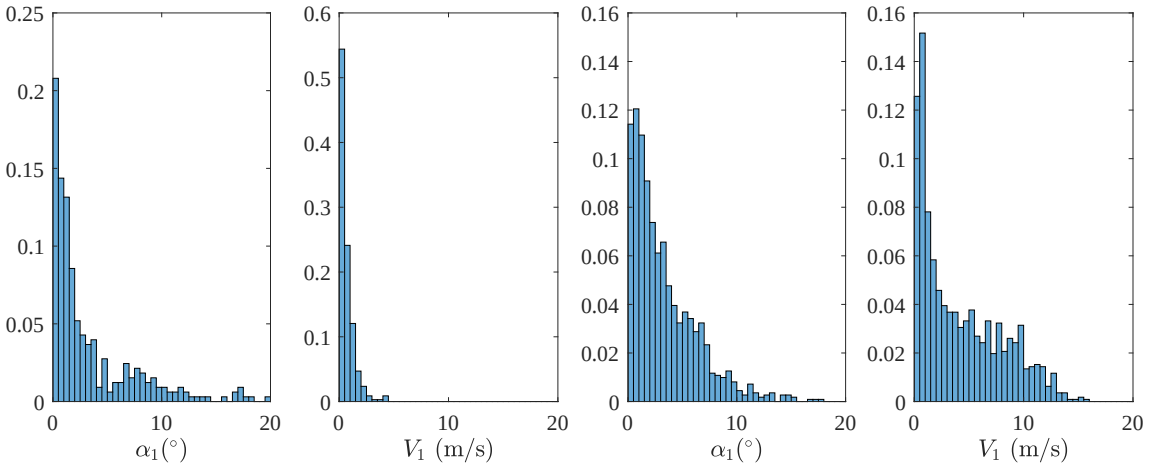

(c) 2.5 µm , bounce-stick

(d) 6.0 µm , bounce-stick

Figure 5.9: Variation of impact angle and velocity distributions with particle size for ambient $Re = 23\,000$, $dt = 0.01dt^*$ simulations. *Top*: all-stick (initial impacts only). *Bottom*: bounce-stick (particle rebound and multiple impacts allowed). $dt = 0.01dt^*$.

This analysis indicates why initial attempts to tune the model based on the yield stress and composite Young's modulus indicated a small dependency on these parameters for integral V_d^+ across the test section. The rebound characteristics were most affected by changing the parameters relating to deformation at impact (a, b, c), and sticking (γ).

Even tuning the parameters several orders of magnitude away from their expected values was not able to bring the simulated values to match the experimental tail off trend. This confirms the discussion in section 3.4.5, regarding the tuning and assessment of the model at larger angles of impact: the model does not appear to be suitable for the simulation of the low impact angles seen from these types of flow.

In conclusion, use of the Bons et al. bounce-stick model did not reproduce the 'tail-off' seen in the experimental data for V_d^+ at high τ_p^+. Whether this is due to deficiencies in the model when simulating impacts at oblique angles, being used away from its tuned point, or whether some other removal mechanism is also occurring cannot be said without further experimental investigation. Initial corroboration against other appropriate bounce-stick models, for example those of Kim and Dunn (2007) or Singh and Tafti (2013), would indicate whether the lack of tail-off prediction is an artefact of the model, or an indication that a further process is occurring. Use of an experimental imaging technique such as PIV (particle imaging velocimetry) or PSV (particle shadow velocimetry) could capture the necessary particle motion data for further investigation. However, as individual particles would ideally be tracked for multiple impacts, this would likely require a high aspect ratio field of view, which is challenging to capture with such techniques.

5.4 High temperature simulations

5.4.1 Isothermal

The simulations of the high temperature isothermal experiments are shown in Fig. 5.10. Three Reynolds numbers were simulated ($Re = 6\,500, 7\,800, 10\,000$), and four particle sizes tracked for each simulation ($d_p = 2.5$, 4.0, 5.0, 6.0 µm). Boundary conditions were all-stick for the mixing chamber and all downstream parts, and elastic rebound in the atomiser tube, as no deposition was observed here during the experimental campaign.

The CRW model was applied with the initial dt^* integration time step, Fig. 5.10a. The simulations are seen to substantially under-predict the deposition rates for the smallest particles, by over an order of magnitude in places. As τ_p^+ increases, the disparity reduces. For the largest τ_p^+ values seen, the simulation does not predict the tail off of V_d^+, as the boundary condition is all stick. Applications of the DRW model to simulations using realisable k-ϵ turbulence closure performed no better than at ambient conditions: V_d^+ was over-predicted by factors of 15-28. Application of the

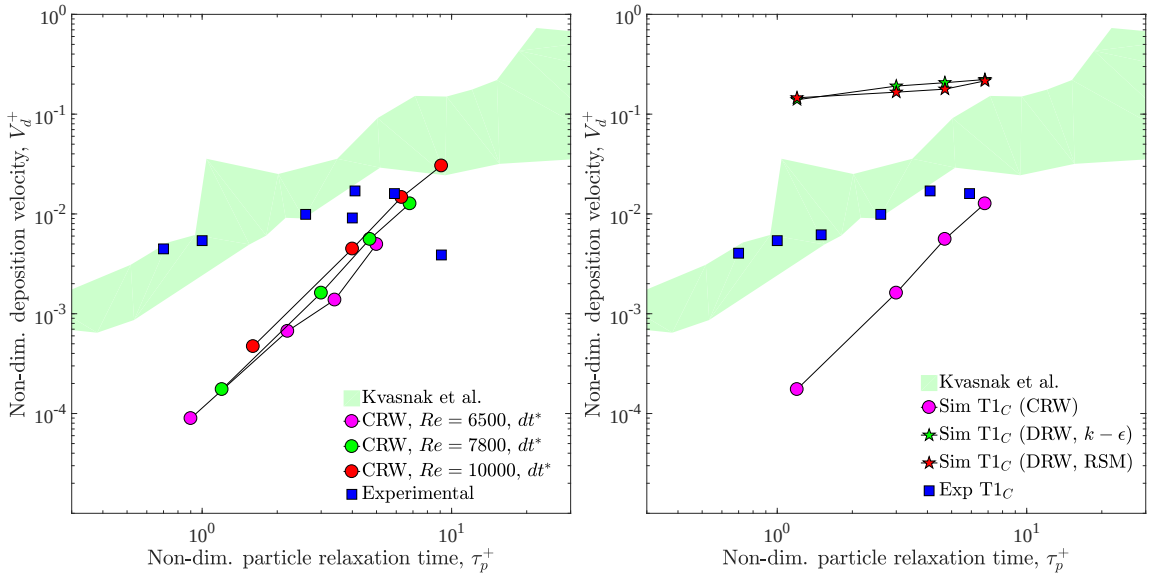

(a) CRW, $Re = 6\,500 - 10\,000$ (b) CRW and DRW, $Re = 7\,800$

Figure 5.10: Simulations of isothermal high temperature experiments. Experimental Re match the simulations shown in each figure. *Left*: CRW, using initial time step definition dt^* at varying Re. *Right*: Comparison to DRW simulations, using realisable k-ϵ and RSM models.

Reynolds stress model changed V_d^+ by 0.86-1.05 times relative to the realisable k-ϵ case, which did not noticeably change the simulation results.

To address the disparity, an investigation was carried out into the particle distribution at the exit of the mixing chamber. It was proposed that the particle distribution might be non-uniform at the exit from the mixing chamber. Fig. 5.11 shows scatter plots of cross sectional particle location and a histogram of particle concentration against radial position, for 2.5 and 6.0 µm particles. It is observed that the distribution for the smaller particles is highly uniform across the majority of the passage, with a reduction seen close to the wall. The larger particles show a less uniform distribution, with a peak towards the wall region. This distribution as a whole is reasonably constant. With neither distribution being particularly skewed, it appears that the simulation of the mixing chamber is not a likely cause of the discrepancy. Trials with setting the uniform injection plane at this location, matching particle temperatures and velocities to gas values, indicated negligible differences in V_d^+ .

The updated time steps, $dt = dt_{L,\,22}$, and $dt = 0.01dt^*$, as discussed in section 5.3, were applied to the isothermal, high temperature simulations. It can be seen, Fig. 5.12, that these adjustments also improves the matching to the experimental data for high temperature, isothermal conditions. Matching between the $dt_{L,\,22}$ and $0.01dt^*$

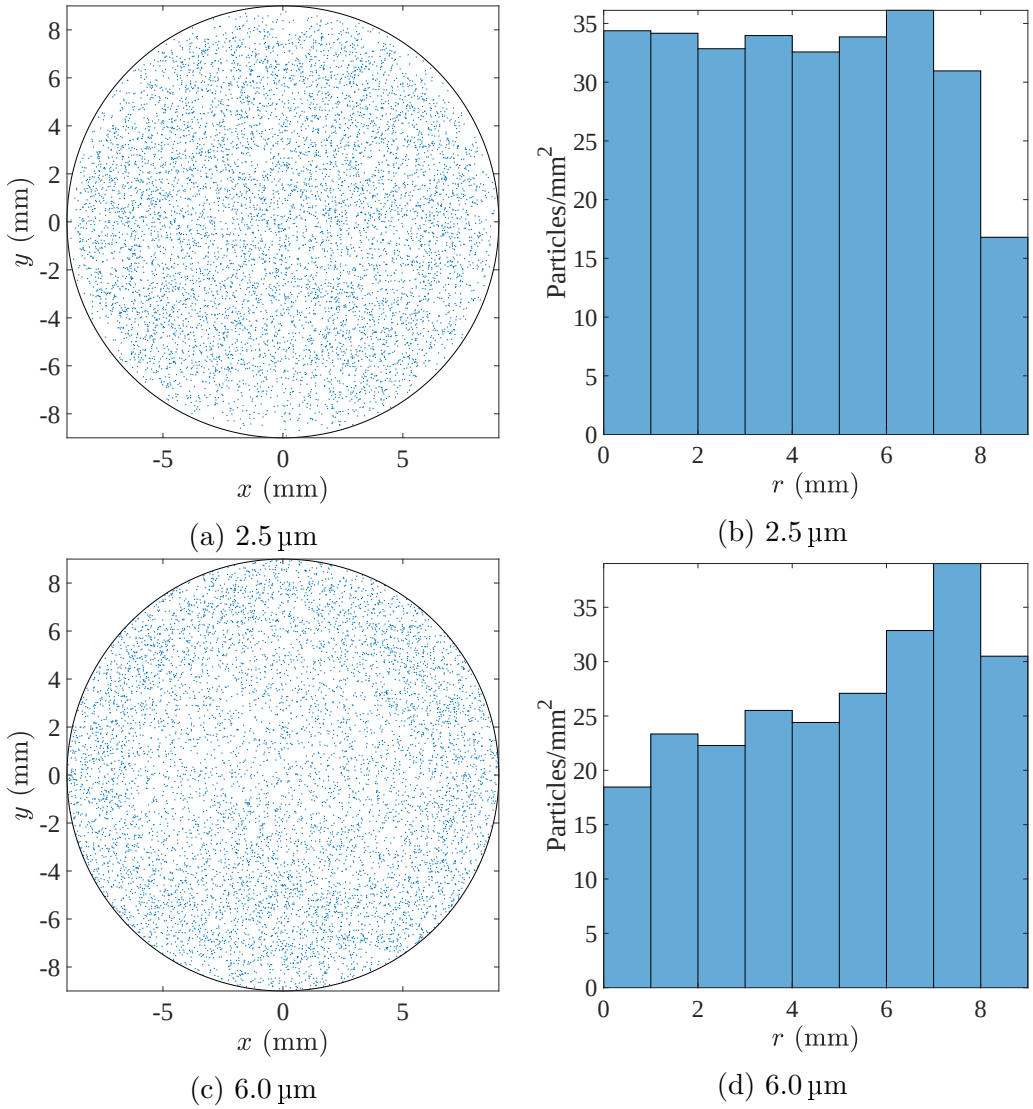

(a) 2.5 µm (b) 2.5 µm

(c) 6.0 µm (d) 6.0 µm

Figure 5.11: Scatter plots and histogram indicating particle distribution at mixing chamber exit. Gravity acting in the negative y direction. Stokes numbers: 0.031 ($d_p = 2.5\,\mu\text{m}$) and 0.18 ($d_p = 6.0\,\mu\text{m}$). $dt = dt^*$.

time steps is remarkably good, though the gradient of the V_d^+ on τ_p^+ dependency is higher than that seen experimentally.

5.4.2 Thermophoretic

The thermophoretic data are initially presented as normalised deposition fraction $\overline{f_d}$ against τ_p^+ in Fig. 5.13. The simulations were carried out using the expressions for thermophoretic coefficient Φ of Beresnev and Chernyak (1995); Talbot et al. (1980) and Young (2011), and are compared to the experimental data. In order to maximise the availability of the experimental data for comparisons, the isothermal experimental

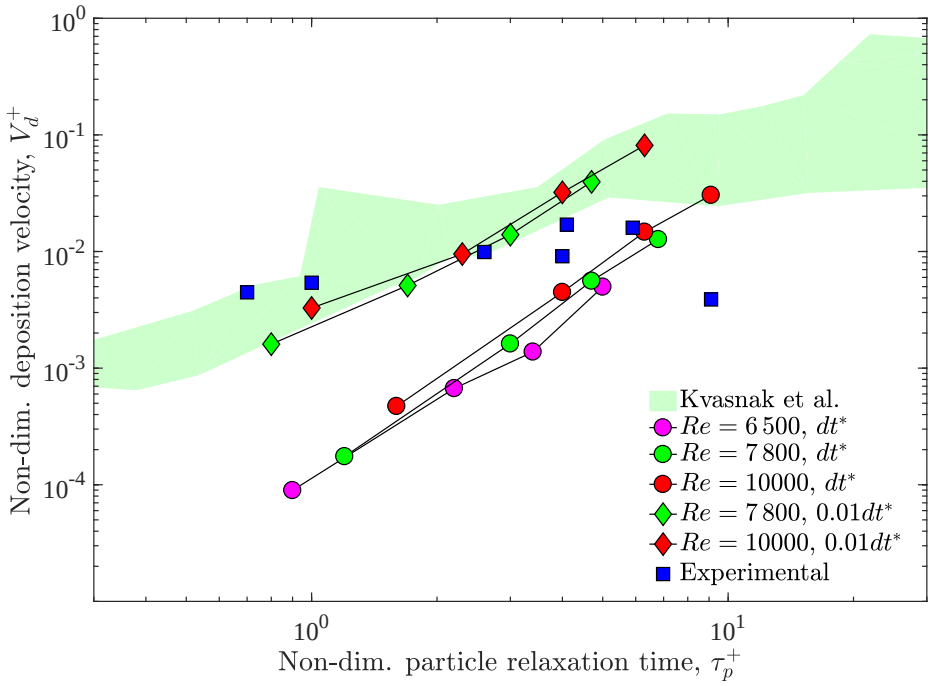

Figure 5.12: Comparison of dt^* and $0.01dt^*$ integration time steps for high temperature, isothermal simulations

deposition is extrapolated/interpolated linearly for the $\tau_p^+ = 0.70$, 1.50 points, corresponding to d_p =2.0, 3.0 µm, for which there were thermophoretic, but no isothermal, data.

The expressions for Φ produce significantly different trends in $\overline{f_d}$. The simulations using the expression of Beresnev and Chernyak (1995) is seen to reproduce the experimental data with the most success across the whole range of particle sizes. In the increasing thermophoretic direction the simulations are very close to the experimental data. In the decreasing direction the simulations are not as close to the experimental data; in particular the response of the smaller particles is not well captured, and for the highest temperature gradient ($T1_E$), the simulation under-predicts the experimental results by 1-2 orders of magnitude.

Simulations carried out using the widely-applied Talbot et al. (1980) expression for Φ, as implemented within Fluent, showed generally poorer comparisons to the experimental data, Fig. 5.13c. Note that the scale has been expanded here. Across all conditions the simulated $\overline{f_d}$ values are more extreme than those obtained experimentally. This is unsurprising to a certain extent as it can be seen from Fig. 2.5b that the Talbot expression generates significantly higher values of Φ for NaCl than has been seen experimentally.

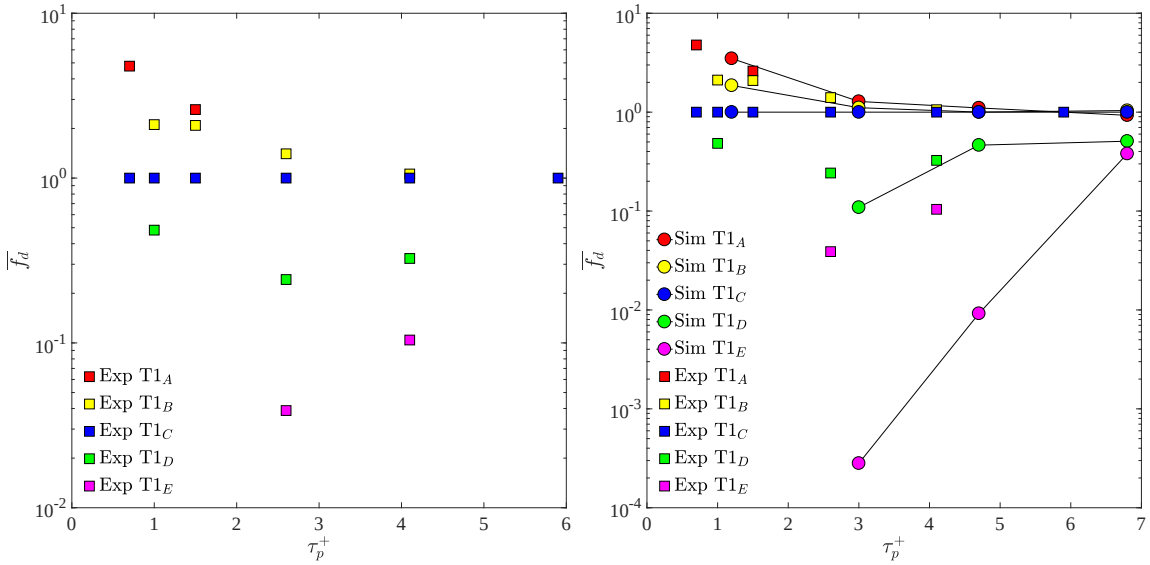

(a) Experimental

(b) Φ of Beresnev and Chernyak (1995)

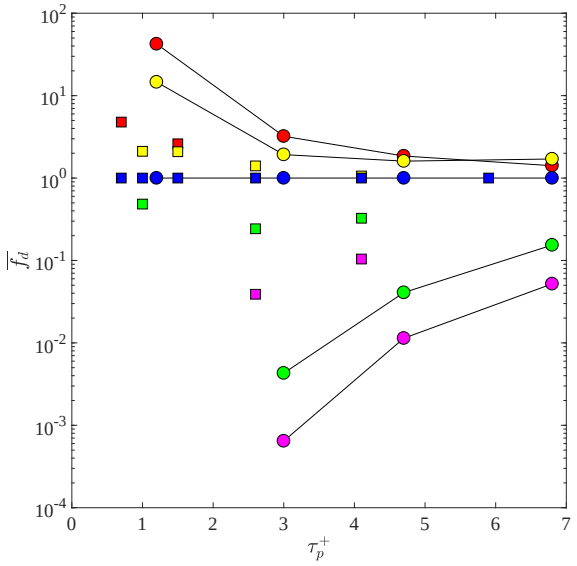

(c) Φ of Talbot et al. (1980)

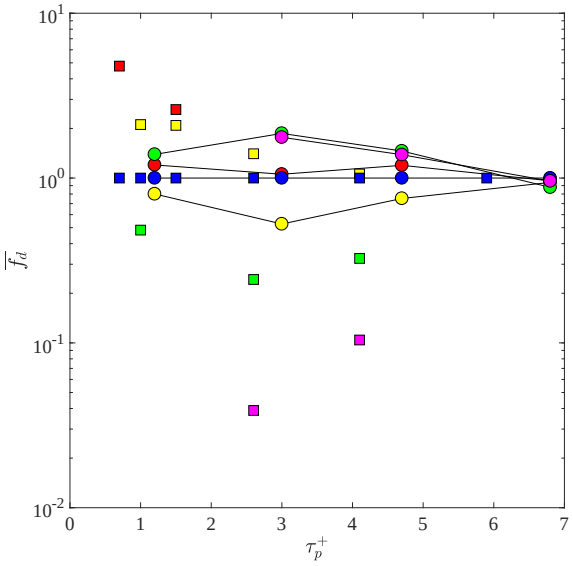

(d) Φ of Young (2011)

Figure 5.13: Normalised deposition fraction vs. τ_p^+ for thermophoretic tests. Experimental and varying expressions for thermophoretic coefficient Φ. Squares are experimental results, circles are simulation results in all plots. $dt = dt^*$. Note differing scale in plot Fig. 5.13c.

The simulations which applied the expression of Young (2011) showed very mixed results. Three of the four thermophoretic cases (B, D, and E) show reverse thermophoretic effects. This is due to the Young expression reversing sign for conditions of high Λ and slip-flow Kn, conditions seen within these experiments. This is seen in Fig. 2.5b. Experiments in the literature at these Kn/Λ conditions have not reported reversed thermophoresis, making such predictions doubtful. It is clear that

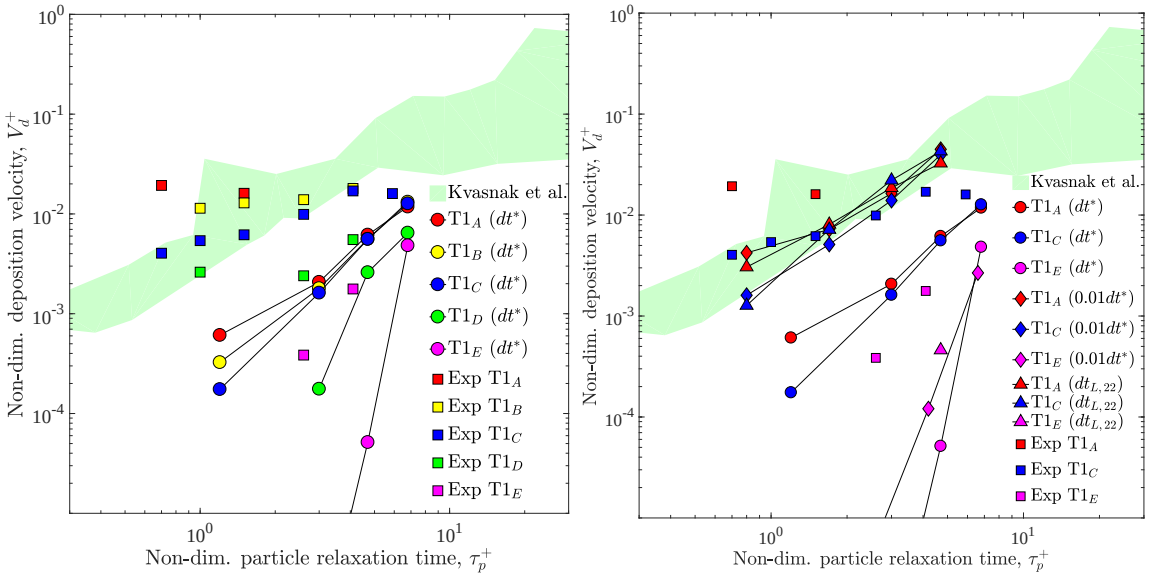

(a) (b)

Figure 5.14: V_d^+ vs. τ_p^+ for thermophoretic experimental simulations using differing integration time steps. *Left*: $dt = dt^*$. *Right*: comparison of all three time steps for cases T1$_{A,C,E}$. Expression of Beresnev and Chernyak (1995) for Φ used for all simulations.

this expression for Φ is not appropriate for the simulated conditions.

Simulations of the four thermophoretic conditions (A, B, D, and E) are shown alongside the isothermal simulations with the experimental data in Fig. 5.14a. The Beresnev and Chernyak (1995) expression for the thermophoretic coefficient is used for calculation of the thermophoretic force. As with the ambient temperature simulations, the integral deposition simulation results are seen to be substantially lower than the experimental data for smaller particles for $dt = dt^*$. The difference between simulation and experiment reduces as particle size increases. The thermophoretic simulations show the same general trend of the thermophoretic effect reducing with increasing τ_p^+ as the experimental data. At the highest temperature gradient, condition E, magenta, the simulations predict extremely low deposition for the smallest particles, far below experimentally measured values.

When the adjusted time steps, $dt = dt_{L,22}$ and $dt = 0.01dt^*$, were applied, Fig. 5.14b, matching between simulated and experimental deposition improved in general, as for the isothermal simulations. Comparison of normalised deposition fraction for these simulations, Fig. 5.15, shows that the T1$_E$ simulations produce better predictions of the experimental results, relative to the dt^* case (Fig. 5.13b), whereas the T1$_A$ simulations are not as close to the experimental results as the dt^* simulations.

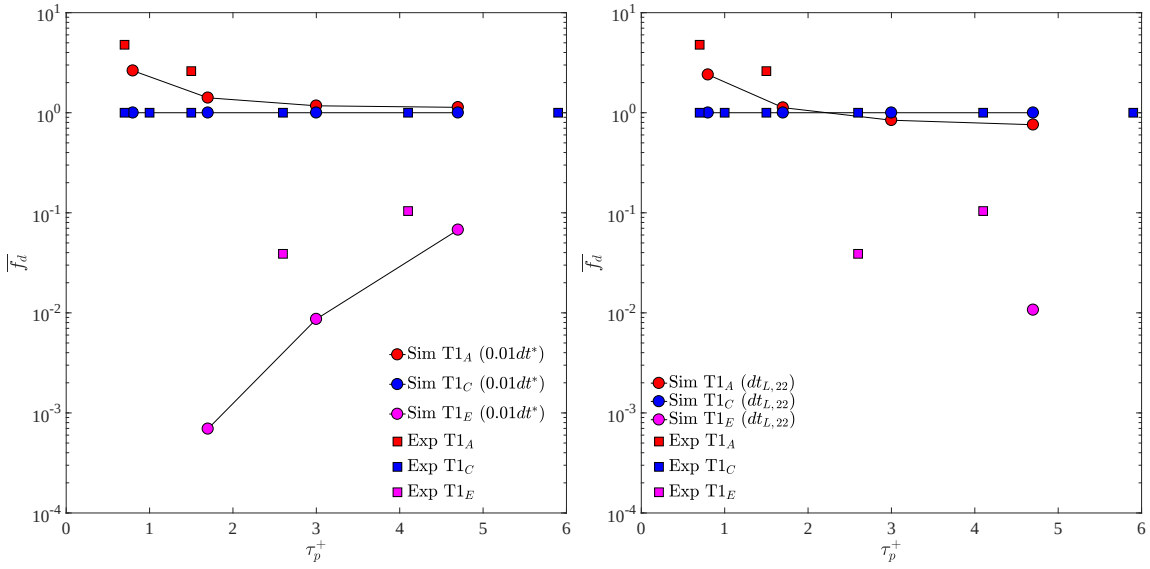

(a) (b)

Figure 5.15: $\overline{f_d}$ vs. τ_p^+ for thermophoretic experimental simulations using differing integration time steps. *Left*: $dt = 0.01dt^*$. *Right*: $dt = dt_{L,22}$. Expression of Beresnev and Chernyak (1995) for Φ used for both.

5.5 Summary

Simulations of the experimental work presented in chapter 4 have been carried out. Assessed for the first time under gravitational conditions, continuous random walk model was shown to under-predict deposition from flows where gravity is perpendicular to flow direction. Adjustments to the integration time step defined in chapter 3, based on the crossing trajectories effect, showed significantly improved matching to the experimental data at ambient conditions.

At high temperature conditions, the same issue of the original dt^* under-predicting deposition was encountered for the isothermal data. The updated time steps, $dt = dt_{L,22}$, and $dt = 0.01dt^*$, were shown again to improve prediction of the experimentally measured deposition. When the non-isothermal conditions were simulated, the relative changes in deposition due to the thermophoretic force were shown to be best simulated by the Beresnev and Chernyak (1995) expression; the very widely used Talbot et al. (1980) expression over-predicted the relative changes for all simulations, whilst the expression of Young (2011) was shown to predict mixed results, including reverse thermophoresis, which has never been demonstrated experimentally for the Λ values generated in this experiment ($50 - 200$).

Chapter 6

Simulations of Applications

Three relevant engine-representative test cases are simulated. The first is a sector of rotor-stator cavity from Engine A. The second test case is build-up of particulate under an array of impingement jets. The third case is blockage of film-cooling holes, representative of those in a HPT blade leading edge passage. The continuous random walk and bounce-stick models, and the dynamic mesh morphing method are applied, and comparisons made between them and standard techniques discussed in this thesis.

6.1 Test case 1: Engine A rotor-stator cavity

Simulations are presented of the application of the CRW, DRW, and Fluent standard (mean flow tracking, without stochastic effects) models to particulate-laden flow within the Engine A rotor-stator cavity. This allows for comparisons of the instantaneous fluid fluctuating velocity models in a more relevant and significantly more complex flow domain and field. In flight, the distribution of particle sizes is not known a priori, however an indicative maximum d_p can be calculated, based on upstream geometry. These simulations show the inherent risk of particulates depositing in engine subsystems, causing failure of cooling technologies, corrosion and coating degradation. All radial positions are normalised by maximum radial location of interest, r_{max}, which corresponds to the top of the shank pocket,

$$r^+ = \frac{r}{r_{max}}. \tag{6.1}$$

The 'Fluent standard' model referred to in the following is the the mean flow tracking onto which the instantaneous fluid fluctuating velocity as calculated by the CRW or DRW is superimposed. Hence for the same particle injection and flow, the Fluent standard model produces the same particle track when repeated. It is used

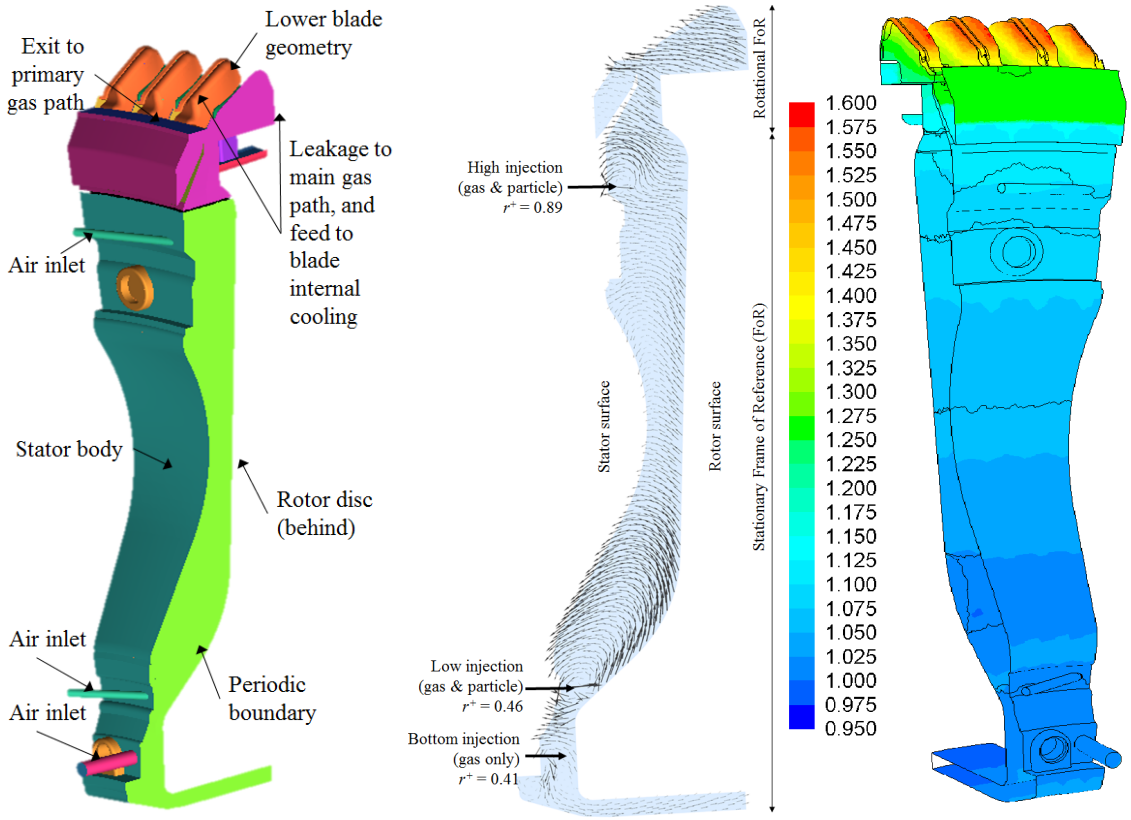

(a) Simulation geometry (b) Fluid path lines (c) Wall temp. profile

Figure 6.1: *Left*: Secondary air systems geometry used for particle deposition simulations. *Middle*: Flow patterns seen in the cavity, along with an indication of the locations of the two frames of reference used. *Right*: normalised wall temperature profile applied to simulation as boundary condition.

in these simulations to indicate how the turbulent fluctuations from the CRW/DRW models are affecting particle motion, relative to other forces (drag, rotation).

6.1.1 Simulation set-up

Fig. 6.1a shows the 3D engine geometry used; an 8.6° sector of rotor disc-stator cavity. Due to the complexity of the geometry, an unstructured tetrahedral grid was generated, with 10 prism layers. In order to achieve the recommended boundary layer resolution of $y^+ \approx 1$ across the whole geometry, barring inlet tubes, it was necessary to adjust the initial cell height to 1 µm. This leads to y^+ values significantly lower than 1 in many locations, with an expansion ratio of 1.64. The mesh comprises 2.52 M nodes and 9.20 M cells; mesh generation and flow solution was again carried out with the ANSYS suite. A temperature profile, Fig. 6.1c, shown here normalised by the static mean inlet gas temperature, was used as a wall temperature boundary

condition, with the mean gas to wall static temperature ratio being 0.94 (volume and area-weighted averages respectively). The CRW integration time step, as defined by Eq. 3.23, was used for these simulations as the gravitational force was not used.

Solution of the continuous phase was carried out using the realisable k-ϵ model. Periodic boundary conditions were used in the circumferential direction, and the solution carried out in two frames of reference, using the Multiple Reference Frame (MRF) or 'frozen rotor' approach. Three mass flow rate fluid inlets were implemented, at normalised radial positions of $r^+ = 0.41$, 0.46, 0.89, along with nine outlets. Outlets were conditioned using the 'mass-flow-inlet' boundary condition with the flow normal direction correctly aligned with an outflow direction. Density was calculated from the ideal gas law, and specific heat capacity c_p, thermal conductivity k_g, and viscosity μ_g calculated in a piecewise linear manner in 100 K increments. A coupled pressure-velocity scheme was used, along with Green-Gauss Node-Based gradient discretisation, standard pressure discretisation, and the second order upwind discretisation scheme for density, momentum, energy, turbulent kinetic energy and turbulent dissipation rate. Convergence of residuals was obtained for x, y, z-velocities, energy and turbulent kinetic energy below 10^{-3}, and below $3\text{x}10^{-3}$ for continuity and turbulent dissipation rate. Net mass flow rate was of the order of 0.02% of inlet mass flow rate.

Flow structure in the cavity is complex and shown schematically in Fig. 6.1b. Positions given are radial distances, matching Fig. 6.2. All flow from the bottom injection exits though a low outlet beneath the disc, and consequently no particles are injected via this inlet. The bulk of the flow, from the middle and high injections, moves radially upwards to exit the domain to the primary gas path via the main annulus seal as purge flow, as the blade internal coolant, or as simulated leakage flow. Gas injection occurs at normalised radial positions 0.46 (low injection), 0.89 (high injection). From $r^+ = 0.43 - 0.57$, a pair of counter-rotating vortices push flow up the centre of the cavity (radially), scrubbing down particularly on the stator surface. From $r^+ = 0.57 - 0.89$, flow moves generally radially upwards, through the converging-diverging section of the cavity. At the third gas injection point ($r^+ = 0.89$) a pair of counter-rotating vortices are again seen. Flow moves over these, scrubbing the walls ($r^+ = 0.85 - 0.93$). From $r^+ = 0.93 - 1.00$, flow moves radially, where it moves around the underside of the main seal and into the main gas path, or into lower blade geometry.

Particles are released from the upper two inlets (high and middle injections) only, as flow from the lowest inlet is all seen to move radially inwards and exits the back

of the domain and is hence not of interest. Particle tracking is undertaken in the absolute frame of reference, as recommended in ANSYS (2011b). Particles are released from the centroid of each inlet surface cell, giving an approximately uniform distribution. 1 553 particles are released for each particle size, one from the centroid of each inlet face. A ratio of ρ_p/ρ_f of 600 was used, representative of various environmental particulates (sand, sea salt, ash, dust) at relevant engine temperature and pressure. The *all stick* deposition wall condition was utilised, as differences seen between the CRW/DRW/Fluent standard models are solely due to these instantaneous fluid fluctuating velocity models, and not any particle-wall impact effects. Hence deposition and impaction fractions are equivalent in this case. Particle injection occurs at $r^+ = 0.46, 0.89$. The majority of the mass flow exits the domain around the main cavity seal into the primary gas path; this occurs at $r^+ = 0.98$.

6.1.2 Simulation results

Fig. 6.2 shows the performance of the CRW against the DRW and also the Fluent standard (non-stochastic) models. The left hand side of each pair of plots shows the distribution of deposition radially; on the stator on the left and rotor disc on the right. The right hand plot shows calculated τ_p^+ values at the deposition locations, based on the CRW model deposits (τ_p^+ is independent of the particle motion model used). The diffusion-impaction regime is highlighted in grey. The τ_p^+ plot is used to indicate which deposition regime is expected in reference to Fig. 2.2: $\tau_p^+ < 0.3$ diffusional regime (D.R.), $0.3 < \tau_p^+ < 20$ diffusion-impaction regime (D.I.R.), or $\tau_p^+ > 20$ inertia-moderated regime (I.M.R.). It is thought that these regimes may, however, be significantly altered by the local flow field, in particular streamline curvature effects, and are indicative only. The general trend is to see higher τ_p^+ values for stator-depositing particles; this is expected as higher wall shear stress values are seen on the stator compared to the rotor. These plots quickly highlight differences between the models, and can be used to show areas which future experimental work could target.

Particle tracking was undertaken with and without the thermophoretic force. Little difference was seen in deposition statistics; it is thought that this is caused by strong inertial effects due to high streamline curvature dominating particle motion in this case. In other flows within the gas turbine environment it is considered that thermophoresis may be a significant particle force, and hence its inclusion is relevant to the discussion.

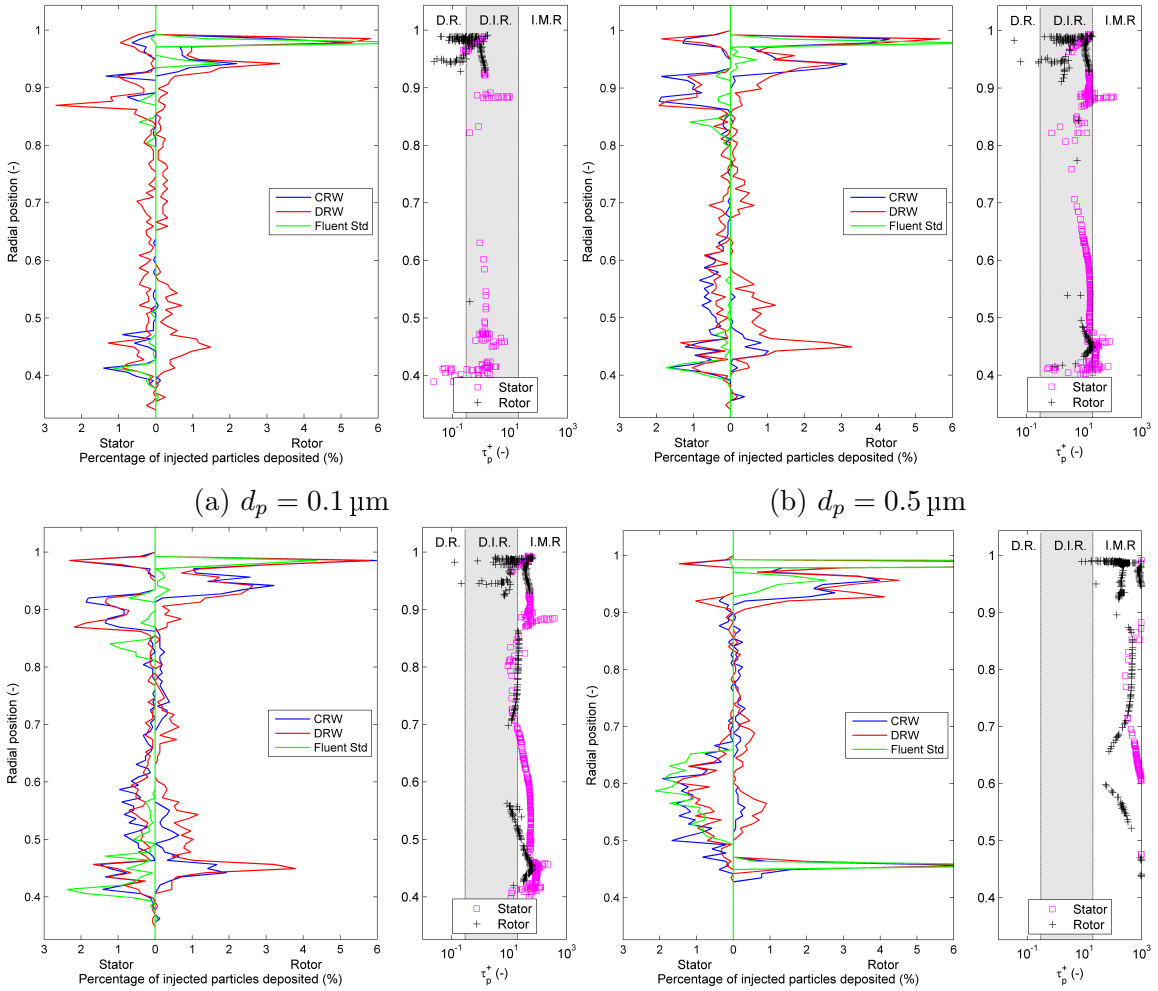

(a) $d_p = 0.1\,\mu m$ (b) $d_p = 0.5\,\mu m$

(c) $d_p = 1.0\,\mu m$ (d) $d_p = 5.0\,\mu m$

Figure 6.2: For each pair of plots: *Left*: Deposition trends on stator (left) and rotor (right) surfaces. *Right*: non-dimensional particle relaxation time τ_p^+ values for deposited particles (from CRW simulations only). Particle diameters $d_p = 0.1$, 0.5, 1.0, 5.0 µm. 'D.R.': Diffusion regime; 'D.I.R': Diffusion-impaction regime; 'I.M.R': Inertia-moderated regime, based on pipe flow definitions. Particle injection occurs at $r^+ = 0.46$, 0.89.

Fig. 6.2a shows 0.1 µm particles lying in the diffusion and diffusion impaction regimes. For pipe flow numerical simulations, the DRW was shown to over predict deposition fraction for these regimes. In the engine simulations it can clearly be seen that the DRW model predicts a significantly higher deposition fraction over almost the entire stator/rotor surfaces, in particular in the mid-disc region ($r^+ = 0.50 - 0.87$). Here the majority of deposited particles are calculated to have non-dimensional relaxation times $0.1 < \tau_p^+ < 1$, for which turbulent deposition effects are not expected to be strong. Particular differences are seen on the rotor ($r^+ = 0.41 - 0.78$), and on

the stator ($r^+ = 0.85 - 0.89$). It is interesting to note that all three models predict similar deposition above $r^+ = 0.91$ on the rotor; here extremely strong streamline curvature is seen as the gas passes though the main seal, and it is proposed that these inertial effects are dominating turbulent particle deposition in these locations, regardless of the low τ_p^+ values reported.

Fig. 6.2b shows 0.5 µm diameter particles. The τ_p^+ plot demonstrates that most particles are expected to lie in the diffusion-impaction regime, and into inertia-moderated regime in places. Some similar trends are seen to 0.1 µm particles; the CRW model predicts lower deposition than the DRW over the majority of the rotor ($r^+ = 0.48 - 0.89$). In this region the relative flow direction is positive radial, with low relative streamline curvature, hence it it thought that turbulent deposition is being over-predicted by the DRW model here. On the stator, around the lower particle injection point ($r^+ = 0.39 - 0.48$) close matching is seen between the CRW and DRW. From the τ_p^+ plot it can be seen that the majority of particles depositing on the stator are now in the low inertia-moderated regime, where the two models predict similar deposition trends (Fig. 3.12) for pipe flow. The counter-rotating vortices drive strong streamline curvature in this region, hence secondary flow effects may also significantly effect deposition. Above $r^+ = 0.87$, deposition trends are similar between models, which is expected from stator τ_p^+ values ($r^+ = 0.87 - 0.93$), and cavity secondary flow features ($r^+ = 0.93 - 1.00$). Comparisons to the Fluent standard (non-stochastic) model show that it is not predicting deposition in non-inertial areas ($\tau_p^+ > 20$, or from secondary flows).

Fig.s 6.2c and 6.2d show generally closer results between the CRW and DRW models. This is not unexpected, with τ_p^+ values for 1 µm particles generally high in the diffusion-impaction and into the inertia-moderated regime, and 5 µm particles almost solely within the inertia-moderated regime. Fig. 6.2c shows reasonable matching between CRW and DRW on the entire stator, following the τ_p^+ inertia-moderated trend. Rotor deposition trends are again not well-matched in the regions where τ_p^+ values fall below the inertia-moderated regime ($r^+ = 0.50 - 0.72$).

The deposition statistics for 5 µm particles, Fig. 6.2d, show close matching between the three models over the majority of the domain. This suggests that almost all deposition is now inertial, and that it is unlikely that many particles of this size would be able to penetrate this deep into the engine. All models predict that no 5 µm particles are drawn below the low injection ($r^+ = 0.43$), whereas deposition is seen in this region for other particle sizes. High deposition is seen on the rotor at

Model	Particle diameter (µm)			
	0.1	0.5	1.0	5.0
CRW	0.26	0.60	0.76	0.93
DRW	0.72	0.84	0.90	0.93
Fluent Std	0.16	0.20	0.25	0.89

Table 6.1: Integral particle deposition fractions for varying d_p (0.1-5.0 µm) for the CRW/DRW/Fluent standard (non-stochastic) deposition models.

equal radial locations to the particle injections; streamlines show that particles have enough momentum to directly cross the cavity, impinging on the rotor disc.

Table 6.1 summarises deposition fractions across the whole domain. This highlights the general trends discussed above, that the CRW is more sensitive to particle size than the DRW in the turbulent regime, and that the Fluent standard model struggles to predict turbulent deposition in the diffusion-impaction regime. It also shows how similarly the models perform for large (high inertia) particles, where turbulent effects are significantly reduced.

6.1.3 Summary

The existing model has been applied to simulations of a secondary air systems engine geometry. The CRW and DRW were shown to give similar predictions for large particles, but these simulations demonstrated the improved sensitivity of the CRW model to particle size.

6.2 Test case 2: impingement-driven deposition

Simulations of an array of particulate-laden impingement jets onto a flat plate are presented. This simulates the experimental work of Clum et al. (2014), who carried out experiments using Arizona road dust (ARD), with mass mean diameters (MMD) ranging from 2.3-7.4 µm. Differing build up patterns were observed based on flow conditions, and geometric and particle parameters. Deposition was measured using a laser-scanning technique to gather three-dimensional surface data. The fluid fluctuating velocity models, bounce-stick model, and DMM technique were applied.

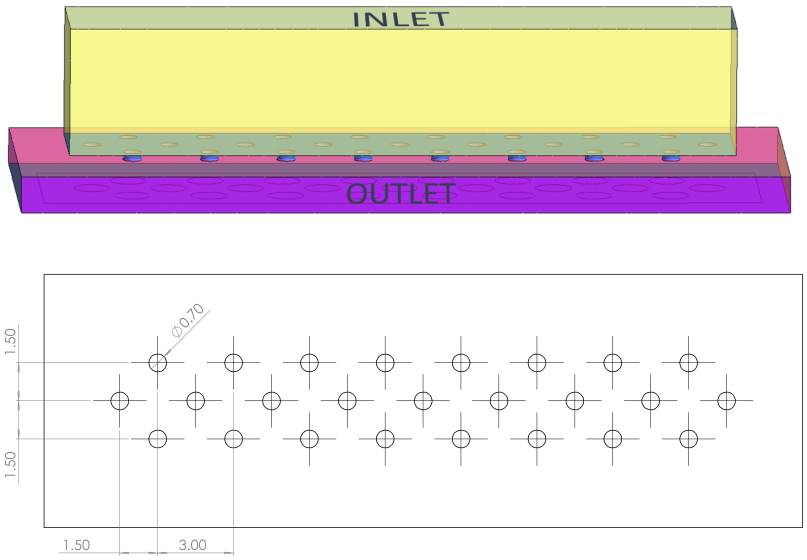

Figure 6.3: Computational domain for Clum et al. (2014). *Top*: schematic. Flow top to bottom from inlet, through impingement holes, onto impingement plate, and exhausted front and back from the lower volume. *Bottom*: Impingement hole geometry.

6.2.1 Computational set-up

A computational domain, Fig. 6.3, was constructed for test piece two (TP2) of the published work. The flow enters through an inlet (top), and passes vertically down through an array of 25 holes. Holes are arranged in three rows, and are 0.70 mm in diameter, spaced 1.50 mm between rows and 3.00 mm between holes in the same row. Neighbouring rows were offset in longitudinal direction by 1.50 mm onto the impingement plate. The impingement plate is spaced by 1.42 mm ($2D_h$) vertically from the impingement holes. Flow then vents to atmospheric pressure perpendicular to the impingement plate. An unstructured hybrid tet-prism mesh of 2.1 million elements was formed, with 5 prism layers (expansion ratio 1.1, initial cell height 5 µm, $y^+ < 1$ across domain). Initial simulations with finer meshes showed no significant differences in the initial flow field (see Appendix A).

Particle motion in an impingement regime is characterised by Stokes number,

$$Stk = \frac{\tau_p}{\tau_g} = \frac{\rho_p d_p^2}{18\mu_g} \frac{U_{jet}}{D_h}. \tag{6.2}$$

where characteristic velocity is the mean jet velocity U_{jet}, and the characteristic length the hole diameter D_h.

The constant backflow margin (BFM = $\frac{P_{ts}-P_{amb}}{P_{amb}}$) used by Clum et al. (4%) was specified as a pressure inlet condition to the computational domain. Conditions were

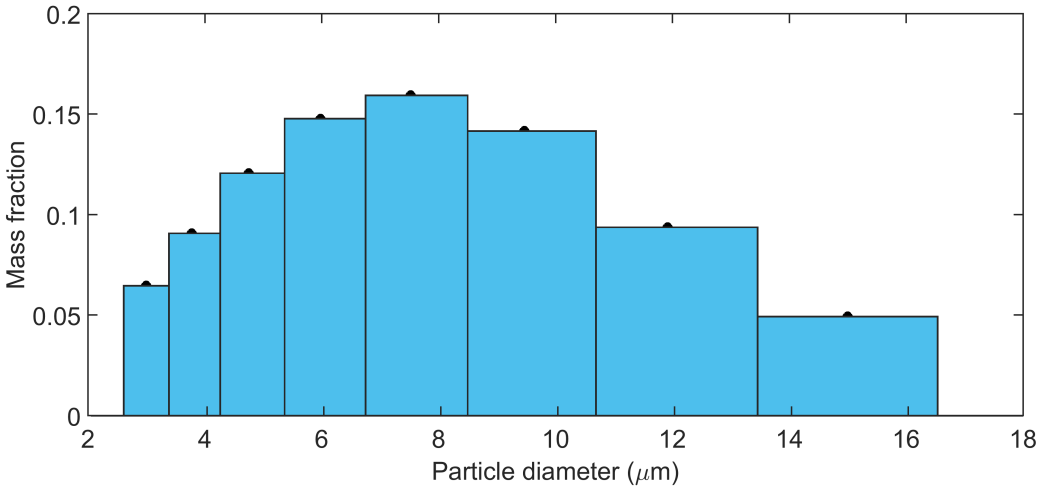

Figure 6.4: Particle size distribution for impingement simulations, as sampled from Clum et al. (2014).

set to match the experimental data presented in Figures 19 and 20 of the Clum et al. paper: gas temperature $T_g = 810$ K, impingement plate temperature $T_w = 1\,005$ K, with all other walls isothermal. Reynolds number based on impingement hole diameter was $Re_j = 1\,000$. The flow solution was calculated as sec. 5.1. Particle density was $\rho_p = 2\,000$ kg/m^3, and a logarithmic Rosin-Rammler (Rosin and Rammler, 1933) particle size distribution generated for eight particle sizes injected, Fig. 6.4, as sampled from the original paper. It is noted that this distribution is slightly narrower than that published. This was necessary as the bounce-stick model predicted all particles smaller than 2.5 µm would stick, which, when coupled with the aerodynamic focusing effect (see Clum et al. (2014) for details) due to particle Stokes number ~ 1, caused high deposition and deformation in the centre of the stagnation zone under the jet. Particles were injected into the domain from a uniform grid matching the fluid inlet plane. Particle velocity and temperature were matched to the gas temperature. For particle tracking the bounce-stick model was applied with parameters ($\sigma_y = 130$ MPa, $E_{comp} = 70$ GPa, $\mu_{imp} = 0.3$) as tuned and fitted for ARD by Bons et al. (2016) as part of the development of their bounce-stick model. A modified value of $\gamma = 0.5$ J/m^2 was implemented due to seeing extremely high deposition rates with $\gamma = 0.8$ J/m^2.

6.2.2 Simulation results

Build-up of small deposit mounds under the impingement holes is shown over the whole impingement plate in Fig. 6.5 as δ/D_h, for 15 and 30 mg injected mass respec-

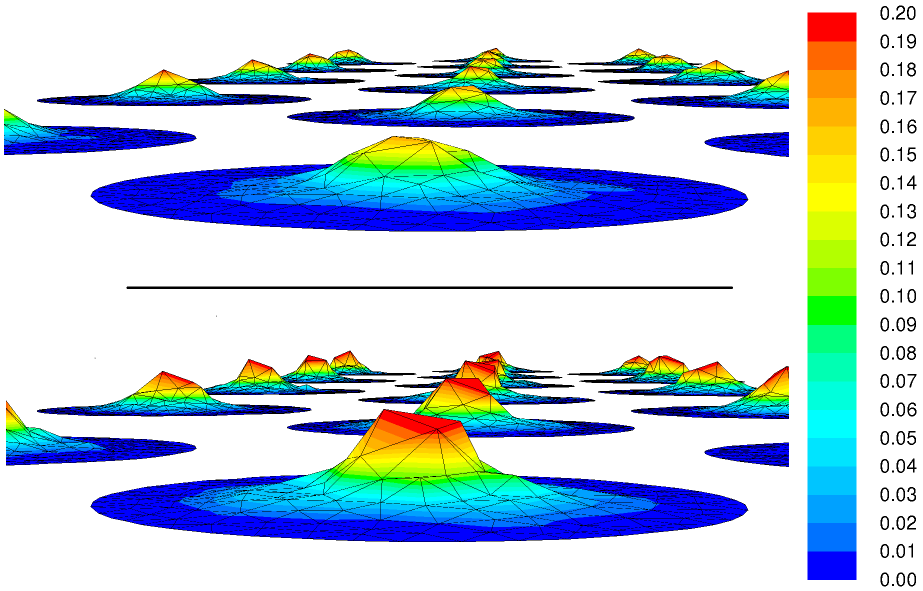

Figure 6.5: Build up of impingement plate surface due to particle deposition. *Top*: 15 mg injected. *Bottom*: 30 mg injected. Contours show δ/D_h, deposition height normalised by impingement hole diameter (0.71 mm).

tively. Peak deposition heights in the simulation were up to $1/7^{th}$ of the gap before the deformation became unmanageably distorted. The deposition profile under the nine central impingement holes was averaged and is presented in Fig. 6.6. This is the same processed as used by Clum et al. to develop their experimental profiles. Blue contours indicate equal injected mass (25 mg) in the simulation. Whilst the shape of the deposited mounds is qualitatively similar to the experimental data, it was not possible to fully capture the growth rate with time, or the substantial widening of the profile that occurs beyond 200 mg injected mass in the experiments. As described above, we use the parameters as tuned by Bons et al. for ARD, except γ. This indicates that the bounce-stick model cannot yet be used *a priori* for a given combination of materials, though as is shown below it performs significantly better than the 'all-stick' boundary condition.

6.2.3 Mesh updating methods and boundary conditions

An investigation was carried out into the differences between the iterative dynamic mesh morphing method and simply projecting a single iteration of deposition to a larger total injected mass. All injections are for the above distribution of mass, and contain the same total mass/injection. Fig. 6.7 shows comparisons between 25 iterations (25 mg injected) of the dynamic mesh morphing method, where the mesh is

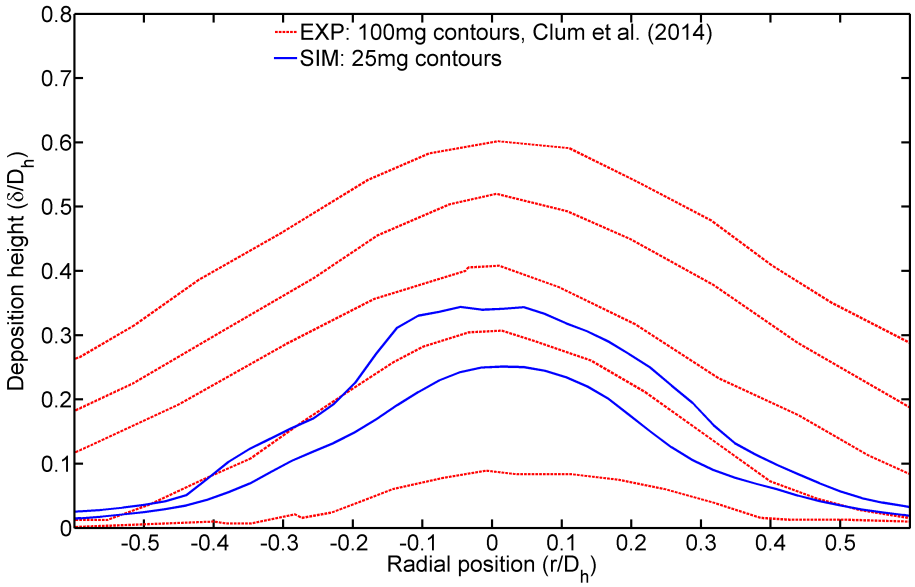

Figure 6.6: Averaged deposition profiles plotted on Clum et al. (2014) data. Contours of injected mass; simulation: 25 mg; experiment: 100 mg.

updated after every injection, and a single injection of 1 mg which has been projected out to 25 iterations linearly (pink line). The bounce-stick model is applied to both simulations. Whilst the peak height is reasonably well-matched, the shape is not; projecting a single iteration based on the initial, clean surface deposition trends is not able to capture the spreading of the deposition as the flow structure changes due to the deposition mound. This was noted by Bons et al. (2016) for projecting deposition widths on nozzle guide vanes external flow geometries. They report experiencing this exact tendency for the projected deposition traces to be narrower than those produced experimentally.

The stick-bounce model is also compared to the widely used 'all-stick' boundary condition (gold). It can be seen that whilst the single iteration matches the shape of the DMM 25 iteration curve, this is after only a single iteration, corresponding to 1 mg of injected material, 25 times less. This underlines the importance of accounting for particle-wall interaction when undertaking these simulations.

To take this further, the effect of mesh deformation on particle sticking trends and trajectories was assessed. The bounce-stick model was applied. 4 µm particles were injected into the undeformed/initial domain (Fig. 6.8a, left). The vast majority were found to stick (>99%, see Table 6.2). When the same injection is applied to the deformed domain, a 'deposition-on-deposition' case, Fig. 6.8a, right, far fewer particles are seen to stick; around 33%. From inspection of the plots it can be seen

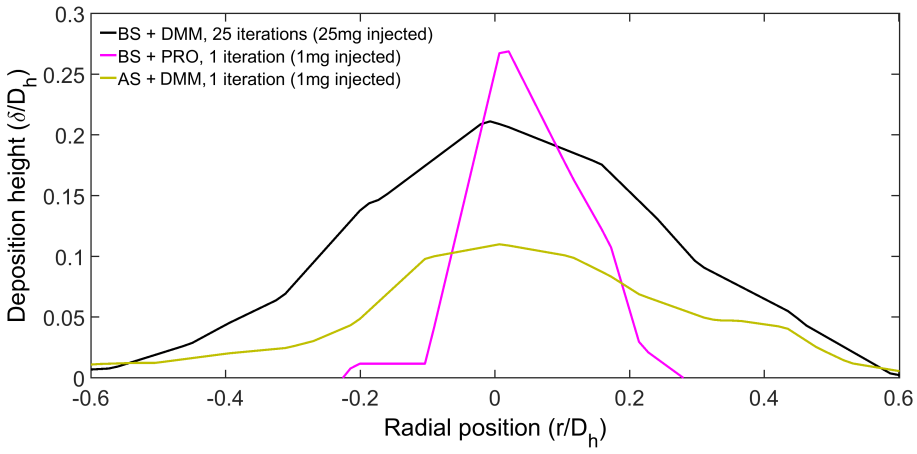

Figure 6.7: Effect of boundary conditions (BS: bounce-stick model; AS: all-stick model) on the transient nature of build up of deposition. 'PRO' (projected) indicates one deposition iteration (1 mg actual injection) projected out to 25 mg linearly.

Particle diameter	Initial mesh (% depositing)	Deformed mesh (% depositing)
4	99.5	34.0
7	0.80	1.16
10	0.00	0.16

Table 6.2: Percentage deposition for 4-10 µm ARD particles based on impacting undeformed or deformed meshes. 2 500 particles injected.

that whilst particle velocities are very similar, particles impacting the deposit do so at a more oblique angle in comparison to the highly normal impacts seen on the undeformed surface. This reduces the particle's surface normal velocity, reducing the plastic deformation undergone, and hence making a rebound more likely. The right hand plot also shows a number of secondary surface impacts, where a particle rebounding off the deposition then impacts either the deposition a second time, or the undeformed impingement plate. These particles may then impact and deposit in other locations within the geometry. The slight variations in particle trajectories at inlet is due to upstream stochastic effects from the CRW model.

The data in Table 6.2 also indicate why the 'all-stick' boundary condition shown in Fig. 6.7 predicts the deposition rate so poorly. Whilst a large number of the 4 µm particles stick in the undeformed case, the 7 & 10 µm particles are almost all seen to rebound due to their high normal velocities. In the deformed case more of these larger particles are seen to stick, again due to their lower surface normal velocities.

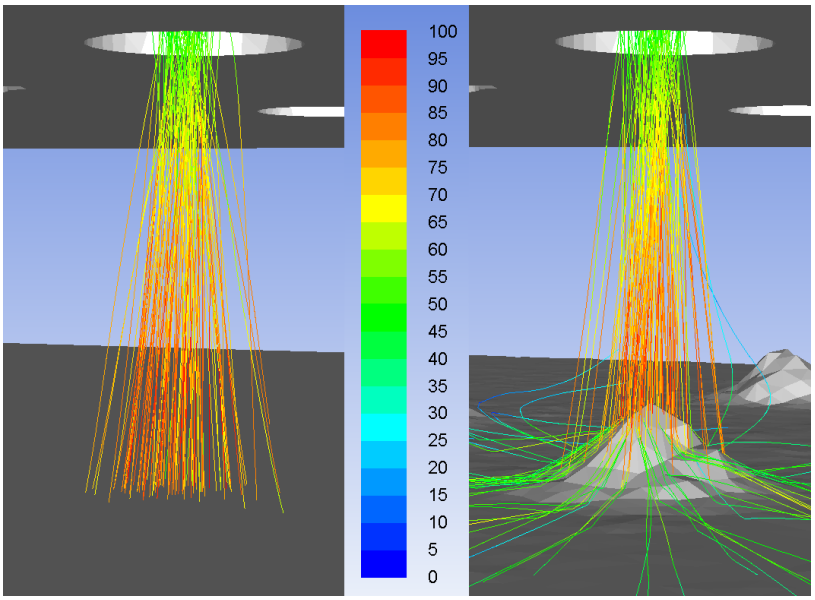

(a) Particle impacts on (left) initial, undeformed mesh, and (right) deformed mesh. Colour scale particle velocity magnitude (m/s). $d_p = 4\,\mu\text{m}$, peak displacement $\delta/D_h = 0.32$.

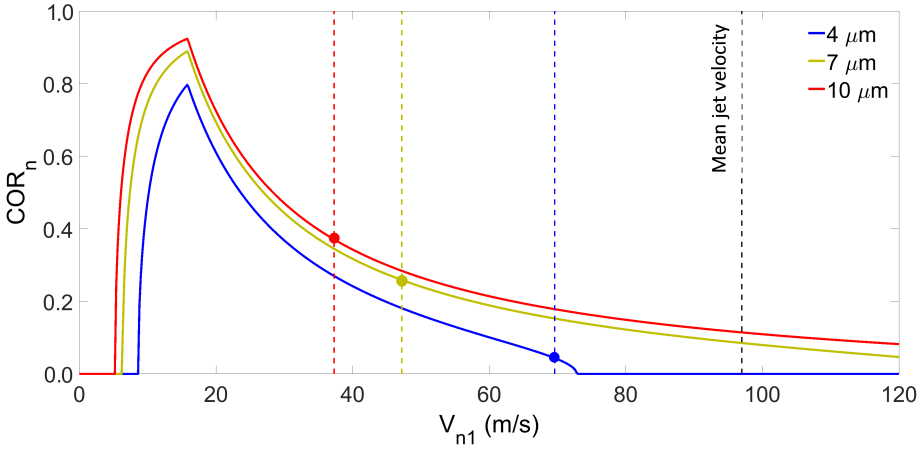

(b) Normal coefficient of restitution, CoR_n for particle sizes considered. Dashed lines and points indicate mean impact velocity for each particle size. Black dashed line indicates mean jet velocity.

Figure 6.8: Effect of previous deposition on current particle rebound characteristics. Deposition statistics in Table 6.2.

Fig. 6.8b shows normal coefficients of restitution as calculated by the bounce-stick model for the three particle sizes. Coloured dashed vertical lines indicate the mean impact velocity for each particle size. The black dashed line indicates the mean fluid jet velocity. It can be seen that for $4\,\mu\text{m}$ particles at highly normal angles, when $V_{n1} \approx V_1 = 65 - 90$ m/s, this is above the rebound upper velocity threshold, and sticking occurs. In the deposition on deposition simulation the impact angles are

more oblique, hence lower normal impact velocities, many of which fall into the 7-64 m/s range where rebound can occur. Some 7 µm particles experience a second impact occurring at a radial position of $r \sim D_h$, after a highly normal first impact. The second impact is highly oblique, giving a low enough normal velocity for some deposition to occur. Deposition of 10 µm particles in the deposition-on-deposition case is due to particles rebounding off the deposition mound to a second, oblique, impact on the impingement plate surface.

The combination of these factors helps explain how the deposition rate is a function of deposition history, and the transient manner in which this occurs. This complicated, coupled relationship between particle size, trajectory, and impact location indicates the importance of both adjusting the mesh to account for deposition and modelling particle-wall interactions.

Though particle on particle erosion hasn't been considered here numerically, it is likely to play a part in shaping the deposit mounds. At the highest jet Reynolds numbers tested, $Re_j = 1\,500$, removal of (whole) deposits was seen experimentally, which indicates that particle-particle, and particle-wall bonds are not strong at these temperatures, and hence that particle-particle erosion may have a significant effect.

6.2.4 Mesh dependency considerations

The dependency of the simulation results on the mesh is likely to be similar to that discussed in section 3.3.5. This current test case used the outcomes of mesh dependency analysis carried out during the development of the DMM method in chapter 3 to reduce this dependency where possible. A judgement must be made when the mesh has become too warped; at this point the simulation must be either stopped, or externally re-meshed.

6.2.5 Summary

Simulations of the build up of mounds under impingement jets, where the flow is particulate-laden, have shown than the dynamic mesh morphing method is able to capture some of the temporal effects of particle deposition. Simulations using the standard 'projected' method were shown to be a poor in comparison, unable to capture the spreading of the mound as more particulate mass is injected into the domain. This test case has highlighted the short-comings of current particle-wall modelling, and the need for better modelling of particle on particle deposition and erosion.

Main channel diameter, D_c	6 mm
Film cooling hole diameter, D_h	0.6 mm
Film cooling hole axial spacing	2 mm
Number of film-cooling holes per row	20
Film cooling hole circumferential angular spacing	120°
Film cooling hole inclination to passage axis	90°
Upstream distance before first hole	108 mm

Table 6.3: Dimensions and geometric ratios for experimental geometry of Wylie et al. (2017)

6.3 Test case 3: blockage of film-cooling holes

Simulations of the experimental work of Wylie et al. (2017), were carried out to demonstrate that the dynamic mesh morphing technique can be applied to the simulation of film-cooling hole blockage. The CRW, bounce-stick, and DMM models were applied. The Wylie et al. experiments used a geometry representative of a HPT blade leading edge internal cooling passage with film-cooling hole off takes to quantify the blockage due to ingested volcanic ash. A number of parameters were varied - geometry, ash characteristics, flow conditions. A view of the computational domain is shown in Fig. 6.9. Two full 3D computational domains were created from the geometry, extending 8 and 18 hydraulic diameters upstream from the first film-cooling hole. Full details of the experimental test piece are given in Table 6.3.

The authors reported hole blockage in terms of a flow parameter FP, a normalised mass flow rate,

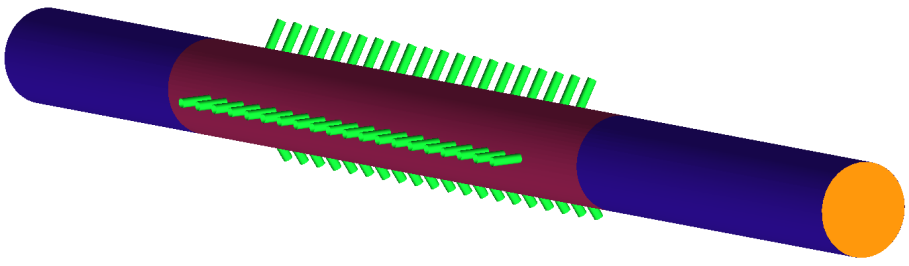

Figure 6.9: Computational domain of Wylie et al. test piece. Flow right to left. Orange: inlet; blue: upper/lower main channel; pink: main channel; green: film-cooling holes.

$$FP = \frac{\dot{m}_g \sqrt{T_g R}}{P_g D_c^2}, \tag{6.3}$$

where R is the specific gas constant, P_g the gas pressure, and D_c the main channel diameter. A reduction in flow parameter RFP, was also reported

$$RFP = \frac{FP_{start} - FP_{end}}{FP_{start}}. \tag{6.4}$$

Both flow parameters are generally taken at the same temperature condition, and reported as a percentage. Increasing RFP values indicates increasing blockage of the flow.

6.3.1 Computational set-up

Meshing of the computational domain was undertaken as described previously; the final mesh was 5.66 million cells with 5 prism layers, initial cell height $\delta_1 = 7\,\mu\text{m}$ (for film-cooling holes; main channel $\delta_1 = 20\,\mu\text{m}$), expansion ratio 1.1, $y^+ < 0.6$ for the holes. A mesh dependency analysis was undertaken. Outlet mass flow rates through each film-cooling hole was assessed for two cases: a short inlet length of 8 hydraulic diameters and a longer length of 18 hydraulic diameters. The mean absolute difference was found to be 0.23%, and the maximum 1.29%, hence the shorter mesh was used.

Solution of the continuous phase, particle tracking, and the dynamic mesh morphing processes were again carried out in ANSYS Fluent. A pressure inlet boundary condition was applied, driving a matched mass flow rate to that used by Wylie et al. (2017). Inlet conditions were conditioned by turbulence intensity, correlated based on Reynolds number for fully developed turbulent pipe flow (5.0% at $Re = 11\,000$), and hydraulic diameter (6 mm). Each of the 60 film-cooling holes was allocated as an individual pressure outlet. Walls were either adiabatic (ambient cases) or a fixed temperature to match the experimental work ($1\,193 < T_w < 1\,300$ K). The realisable k-ϵ turbulence model was used; computational scheme as discussed in sec. 5.1. Particles were injected using a uniform grid across the fluid inlet plane, with particle velocities and temperatures matched to the bulk gas conditions at this point. The initial CRW integration time step dt^*, Eq. 3.23, was used for these simulations.

6.3.2 Simulation results

6.3.2.1 Comparison to experimental deposition

A comparison of numerical and experimental deposition in the film-cooling holes and main channel is presented in Fig. 6.10. A particle size distribution to match the S1 sieving as used by Wylie et al. was implemented using a logarithmic Rosin-Rammler distribution of 6 discrete particle sizes, Fig. 6.11.

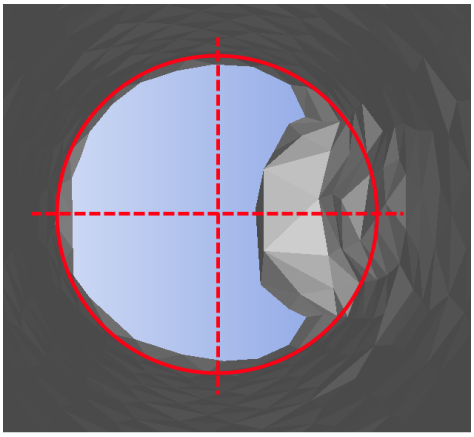

(a) Numerical deposition in film-cooling hole

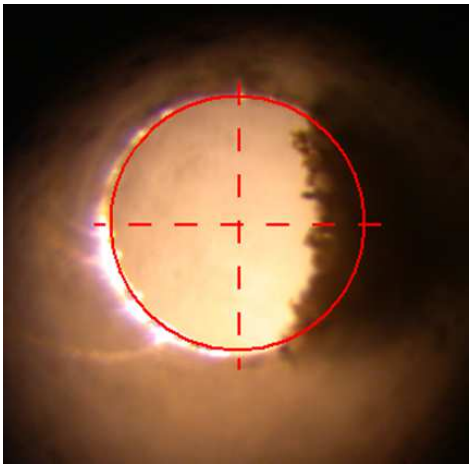

(b) Experimental deposition in film-cooling hole

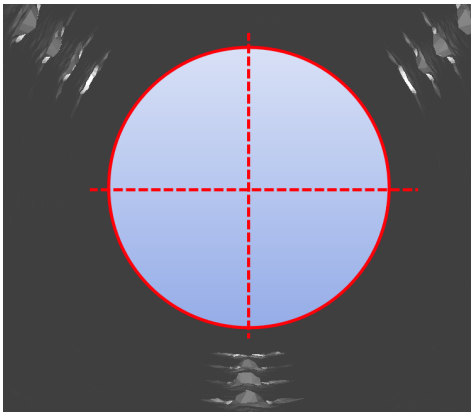

(c) Numerical deposition in main channel

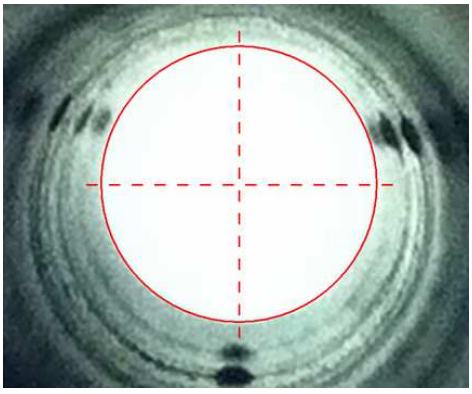

(d) Experimental deposition in main channel

Figure 6.10: Comparison of numerical and experimental deposition in the film-cooling holes (top row; flow in the main channel is left to right) and main channel (bottom row). Both looking into their respective flows. Photographs from preliminary work of Wylie et al. (2017).

The key deposition features seen in the experimental photographs are reproduced by the simulations. Deposition builds up on the downstream lip of the film-cooling holes, and can be seen causing blockage within the film-cooling holes, Fig. 6.10a.

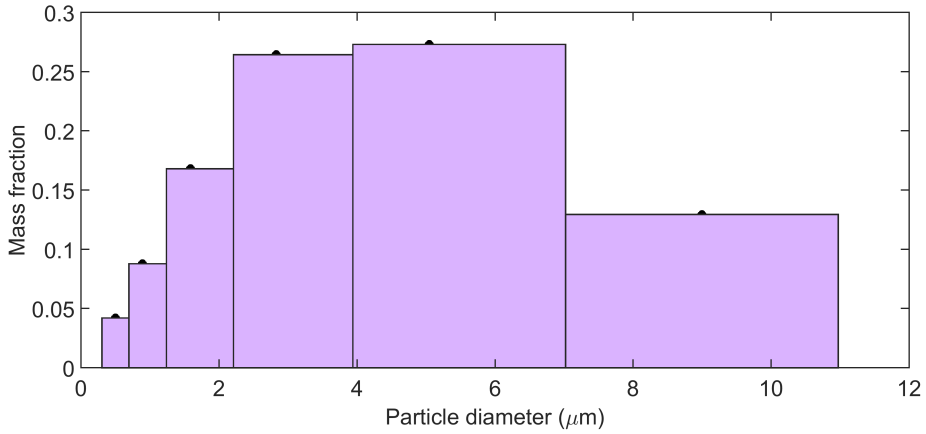

Figure 6.11: Particle size distribution from Wylie et al. (2017).

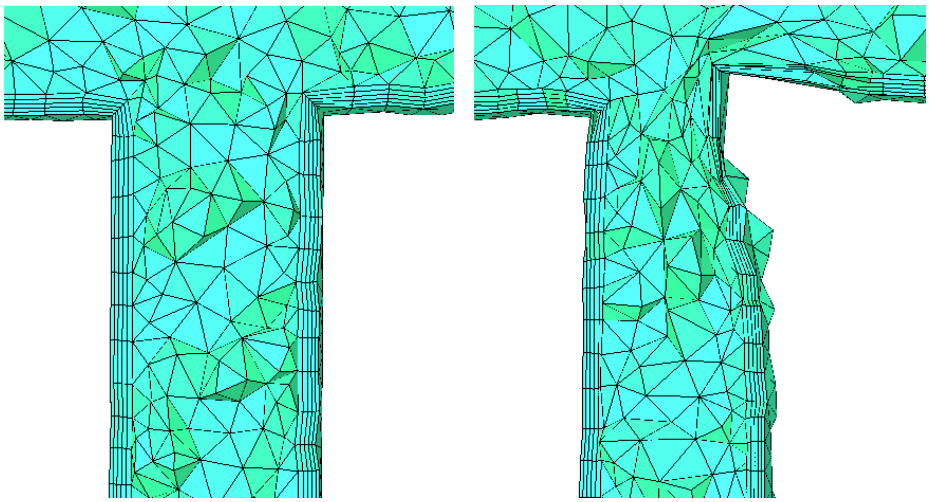

Figure 6.12: Mesh in film-cooling hole undeformed (left) and substantially deformed (right). Flow moved axially left to right, and down into film-cooling hole.

Due to the huge mesh that would be required, the simulation is not able to build the fine deposition structures seen in Fig. 6.10b, but that this blockage can in fact be simulated is a significant step forwards. Fig. 6.12 shows a cross-section of the mesh in a film-cooling hole before and after deformation. It can be seen that the hole becomes significantly closed, and that although the volume mesh becomes somewhat warped, the distortion is acceptable.

The upper part of this deposit is also seen growing up into the main channel, Fig. 6.10c. Again the shape and size of this deposit is a reasonable match for those seen in the experimental photographs. Small secondary mounds are seen experimentally building up on either side on the main mound; the presence of these was found to be strongly dependent on the bounce-stick model parameters chosen.

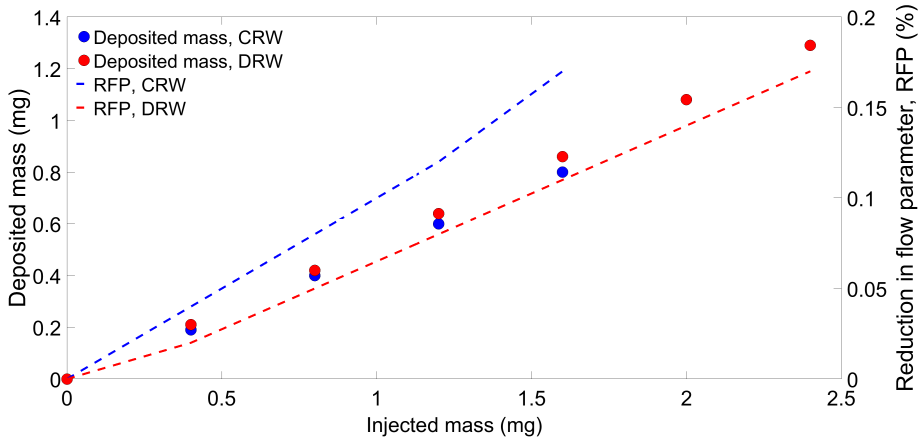

Figure 6.13: Comparison of deposited mass (points, left) and consequent reduction in flow parameter (lines, right) for CRW and DRW models. Circular markers to left scale, lines to right scale.

6.3.2.2 Comparison of particle tracking models

A comparison of the CRW and DRW models was made to investigate the effect of differing models for instantaneous fluid fluctuating velocity. An 'all-stick' boundary condition was used to allow the models to be directly compared. 1.6-2.4 mg of particulate matter at $d_p = 4.0\,\mu\text{m}$ and $\rho_p = 1\,500$ kg/m^3 was injected.

Fig. 6.13 demonstrates the difference between the deposition locations for the CRW and DRW models. Whilst the DRW model deposits more total mass (5-10%) than the CRW, the RFP values are significantly lower ($\sim$ 40%). This is due to the DRW depositing more particles in the main channel, and fewer in the film-cooling holes, where deposition significantly changes the flow parameter. This is borne out when integral deposition volume across the surfaces is considered; the DRW deposits 2.1$\times$ the total volume of particulate in the channel compared to the CRW, but the deposition is 75$\times$ that predicted by the CRW volume in the upper main channel (see Fig. 6.9). This deposition in the main channel was not observed experimentally by Wylie et al. Here $\tau_p^+ = 6.7$ for the 4 µm particles in the channel regime; as detailed in chapter 3 the DRW over-predicts deposition in this flow regime (diffusion-impaction) by up to three orders of magnitude. Using Fig. 3.12 as a guide, it is seen that compared to experimental data the DRW model over-predicts integral particle deposition by an order of magnitude for particles of this τ_p^+.

Compound	Chaiten	ARD	Eyja	JBPS SB
$Si0_2$	73.9	70	51.3	50
Al_20_3	14	10-15	10.9	11.5
Fe_2O_3	1.6	2.5	4.6	9.4
CaO	1.6	2-5	9.5	14.5
Na_2O	4.1	2.4	3.3	3.7
σ_y (MPa)	130		200	
E_{comp} (GPa)	72		85	
$c_{p,particle}$ (J/kg/K)	840		840	

Table 6.4: Material bulk chemical compositions (% wt), and model parameters chosen.

6.3.2.3 Effect of particle composition and temperature

Wylie et al. compared two volcanic ashes of different compositions: a mixed basaltic/ rhyolitic ash (Eyjafjallajökull, 'Eyja', Iceland 2010), and a silica-rich rhyolitic ash (Chaiten, Chile 2008). Chemical compositions are shown in Table 6.4, from Wylie et al. (2017). Two materials comparable by chemical composition are also shown, quoted from Bons et al. (2016). The Chaiten sample was seen to have a similar composition to Arizona road dust; both are silica-rich. The composition of the Eyja sample was similar to the sub-bituminous power station coal ash (JBPS SB) utilised in a number of Ohio State papers. Based on the compositional similarity, parameters for the bounce-stick model were chosen to match their respective similar materials. As the mechanical properties of both the Eyja or Chaiten ashes were unknown, matching based on chemical composition was an approximation (see section 2.3.6 for further discussion).

A dependency of particle yield stress on temperature, as fitted by Bons et al. for the sub-bituminous ash, was implemented for the Eyja ash,

$$\sigma_y\left(T_p\right) = 200 - 0.225\left(T_p - 1\,000\right) \text{ MPa}, \tag{6.5}$$

where T_p is in K. For particle temperatures below 1 000 K, the initial yield stress was used. Based on data for sand in Schmuecker (2012), a similar correlation was constructed for the ARD/Chaiten ash of $\sigma_y\left(T_p\right) = 130 - 0.075\left(T_p - 600\right)$ MPa. Both were limited to a minimum value of 80 MPa. Specific heat capacity was taken from Eppelbaum (2014), and considered equal for both ash types.

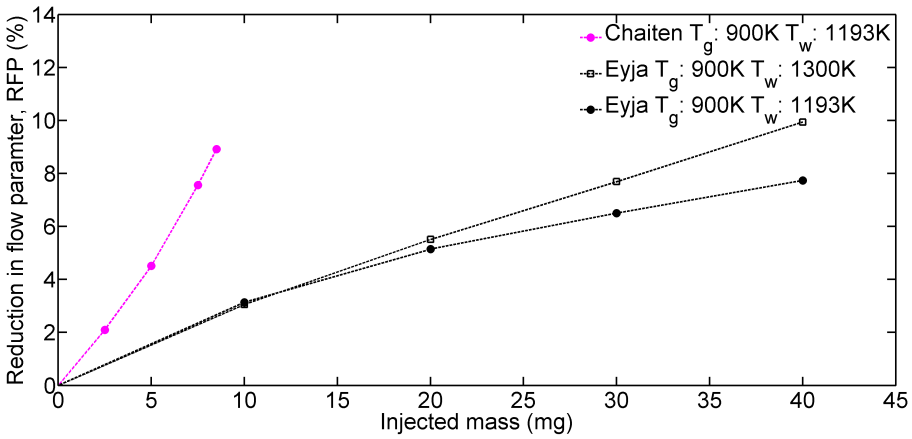

Figure 6.14: Comparison of different ash 'compositions' and temperatures. Experimental RFP values from Wylie et al. for 1 g injected ash: Chaiten $14 - 19\%$, Eyja ($T_w = 1\,193$ K): $< 0.5\%$, Eyja ($T_w = 1\,300$ K): 6%.

Comparing the implemented yield stress criteria, Fig. 6.14, it can be seen initially that for the Eyja and Chaiten traces at $T_g = 900$ K, $T_w = 1\,193$ K the lower yield stress of the Chaiten ash causes more blockage per unit injected mass, as would be expected. This temperature pairing was chosen as Wylie et al. reported very significant RFP at this temperature for the Chaiten ash ($14 - 19\%$ with 1 g ash injected), but negligible RFP for the Eyja ash at the same conditions ($< 1\%$). A second simulation with the Eyja ash was carried out, increasing the metal (wall) temperature to 1 300 K. It is observed that the rate of deposition then increases with time. Again it is noted that the simulations are depositing significantly more particle mass than would be expected if experimental deposition rates are projected linearly backwards. As with the impingement case above, the constants were taken as tuned by Bons et al. Many of the impacts in the main channel are at extremely oblique angles; these weren't addressed in the bounce-stick model as no experiments have been published for these shallow angles. This is an area of the bounce-stick model which needs further development to be able to fully assess its validity.

An important area of development required for the bounce-stick model is at high temperature. The manner in which the particles are bonded together is not addressed, nor the effect of temperature on this. The work of Kueppers et al. (2014); Clum et al. (2014); Lundgreen et al. (2016) showed that ARD, for example, behaves very differently in terms of deposition fraction and deposition 'strength' with increasing temperature: at 1 100 °C ARD deposits were observed to be still powdery, whereas by 1 265 °C partial glassification had occurred, and by 1 350 °C it was thought that

particle were at least partially liquid at impact due to the observed spreading. If particle on particle erosive effects were to be accounted for, the state and strength of the existing deposition would need to be modelled more appropriately. This is noted from Fig. 6.10, where the experimental deposition in the film-cooling hole has a fine structure towards the outward surface, rather than sintering into a solid mass, and could potentially be removed by impacting particles if the bond strength is not high.

6.3.3 Mesh dependency considerations

As can be seen from Fig. 6.12, substantial deformation of the mesh occurred during the DMM process, as would be expected. The recommendations of section 3.3.5 were followed were possible to give a robust solution, however by the nature of the DMM process, the grid will have an effect on the solution. The variation of the bounce-stick model parameters were seen to have a much more significant effect on the simulation results than the grid itself. Within the DMM process, adjustment of the distribution coefficient c to favour deposition towards the centroid (section 3.3.2.1) was seen to allow the deformation to grow in more realistic manner. In general, running the simulation in repeat for a set number of time steps, or repeating it from a set mid-point, using only the mean flow tracking model (no stochastic effects) would allow the divergence of results due to the grid to be assessed.

6.3.4 Summary

The above simulations indicate that the dynamic mesh morphing technique gives qualitative agreement with experimental deposition trends. Whilst still in development it can reproduce some of the key experimental findings for internal flows. The discussed transient nature of particle deposition rates implies that in order to truly be able to simulate particle deposition or optimise engine component designs, the particle deposition history must be accounted for.

6.4 Summary

This chapter has presented three test cases for the numerical tools developed in this study. The results have demonstrated that the continuous random walk, dynamic mesh morphing, and bounce-stick models are able to capture some of the salient features of the experimental work, and how they offer improvements over the more standard techniques used in the field.

The test cases have also highlighted key areas for further development, in particular deposition from more complex and rotating flows for the CRW model, and better modelling of particle deposition and erosion processes, in combination with thermal effects. These improvements would allow significant further progress to be made with such simulations.

Chapter 7

Conclusions and Further Work

7.1 Conclusions

This thesis has presented a number of studies designed to improve the modelling of small particulate motion in gas turbine engines. The continuous random walk model was further assessed and developed. The CRW model predicts the instantaneous fluid fluctuating velocity as seen by a particle. It is ideal for gas turbine modelling, as it can be applied post-simulation, is easily implemented, and is computationally inexpensive. It adds stochastic particle dispersion effects to steady flow simulations. A physics based approach to the definition of an appropriate integration time step was developed suitable for flowfields with substantial body forces and temperature gradients. This lead to improved matching of predicted deposition with published experimental data for vertical pipe flow by an order of magnitude.

The CRW model had not been validated at engine-representative temperatures; a new experimental rig was designed and run to provide high temperature particle deposition data not available in the open literature. A new deposition measurement technique was developed. Experiments at ambient temperatures matched published experimental data well for $\tau_p^+ < 7$, but showed a tail off of V_d^+ for $\tau_p^+ > 7$. This is thought to be a particle rebound or removal effect. At high temperatures, the data from isothermal conditions matched the ambient trends well, again with a tail-off at the highest τ_p^+ . Under thermophoretic conditions, large changes in deposition relative to isothermal conditions were seen; increasing by up to 4.8×, and decreasing by up to 560× dependent on the sign and magnitude of the temperature gradient.

These data enabled the CRW model to be assessed under gravitational and high temperature conditions for the first time. Horizontal simulations at ambient temperature showed adjustment of the integration time step was necessary to capture the gravitational effects on deposition. This is due to the crossing trajectories effect,

where external particle forces (gravity, for example) affect the rate at which particles move between turbulent eddies. At high temperature conditions, the same adjustment to the time step was made, bringing a significant improvement to the simulated results. The thermophoretic coefficient expression of Beresnev and Chernyak (1995) was shown to be superior for this high-Λ case to either that of Young (2011) or Talbot et al. (1980), despite the latter being extremely widely used.

Complementary to improved deposition site prediction, a dynamic mesh morphing method has been developed. This allows accurate topology of depositions to be used in subsequent flow modelling. Here computational surfaces are iteratively deformed in response to the deposition of particulate matter, incorporating the deposited mass: the boundary movement translated into the volume mesh. The effect of large-scale particle deposition can then be simulated, important for capturing the temporal effects of particle deposition, and deposition structure build-up. It is shown that the solution is substantially different when compared to the widely-used so called 'projected' method.

The CRW model was then applied with dynamic mesh morphing and a bounce-stick model to three gas turbine test cases - a rotor-stator cavity, an array of impingement jets, and an idealised row of film-cooling holes. The dynamic mesh morphing method was shown to be able to generate growth of deposition features. It was able to capture the spreading of the deposited mounds under impingement jets in a way which the projected method cannot. For the film-cooling geometry actual blockage of the holes was captured ($\sim 40\%$ of hole area), causing a reduction in mass flow rate through the geometry, and a changed flow distribution between holes. Experimental and fleet experience has shown that significant blockage of holes can occur; this is the first time it has been shown numerically to the author's knowledge.

These simulations also highlight the importance of the CRW modelling developments. The CRW model has been shown to lead to better predictions of particle deposition locations than the discrete random walk model. Most notably for the row of film-cooling holes fed from a cooling passage, the DRW was shown to erroneously deposit many particles within the main channel, while the CRW model deposited fewer, 1-2% of that deposited by the DRW in comparison. Such changes may change geometry features identified as critical deposition sites for the engine.

There is, of course a need for further work to improve the accuracy of the modelling. Particularly in the case of impingement flow the rate of deposition seen is too large compared to literature, though the total deposition height is not unrealistic ($\sim 30\%$ of hole diameter). This is unsurprising, as the 'all-stick' boundary condition

was, a priori, known to be inappropriate for fully modelling the particle-wall interaction. The applied bounce-stick model was able to improve predictions in relation to experimentally-reported values, however further work is required to develop the model to account for other physical processes, including erosion.

7.2 Further work

As this thesis has covered a range of numerical and experimental work with applications to gas turbines, there are a large number of avenues open for further study.

One of the key remaining limitations of this modelling has been shown to be the growth rate of the DMM-produced deformations being in excess of those seen experimentally. For the impingement case (section 6.2), the simulated mounds were seen to grow four times faster than experimentally. In the film-cooling hole offtake case, the RFP values simulated occurred at around $1/25^{\text{th}}$ the injected mass of particulate in comparison to the experiments. Two effects could be largely responsible for this; particle bounce-stick and particle-particle erosion. These are important areas for further development with regards to reducing the remaining disparities between simulations and experiments.

The effects of erosion of deposition by impacting particles should be investigated for gas turbine particulates. Appropriate work regarding particle-on-particle erosion, or shear removal, is essential for the further simulation of large-scale build up. Such effects have been noted experimentally in the literature, but are not currently accounted for. As a first step, models from the literature, such as that of Tabakoff et al. (1979), could be implemented and attempts made to tune appropriately for particle on particle erosion.

The Bons et al. model as described in chapter 3 has been indicated to be an improvement over existing models to some extent, however its applicability to the 'deposition on deposition' situation, for example section 6.2.3, is less certain, as the contact area will change. Temperature effects on particle properties are not currently captured by the model excluding tuning correlations for yield stress etc. The model cannot be considered for use a priori in gas turbine simulations until this aspect is addressed. The model has been tuned largely against non-aero gas turbine-specific materials - three of the five test cases (Bons et al., 2016) used coal fly ash which is not representative of volcanic ashes (Clarkson et al., 2016). Material data for more relevant materials must be gathered and/or generated experimentally for better assessment of the model for aero-engine applications.

The experimental simulations presented in chapter 5 indicated that the bounce-stick model was still struggling to reproduce the tail-off seen in the V_d^+ data at high τ_p^+. Deposition rates were up to 100× above those observed experimentally. Further research should be done here to address whether this is an impact (bounce-stick) effect, or some form of shear removal - discussion regarding a method for proceeding with this investigation is given in section 5.3.2.

The initial development of this DMM technique makes a step on in numerical simulations of particle-laden flows, and hence a number of areas can be further developed. Aspects to be addressed include stability, speed, and periodic capabilities. Shear, or impact removal of the deposition could be included. Longer-term aspects include development of capability to define the deposition as a third domain (after the fluid and wall), in order that conjugate heat transfer calculations could be carried out. This would require the simulation to generate a void between the wall and fluid domains, and be able to fill this with mesh.

The same current DMM approach could be applied to the (metal) erosion process in theory, though due to mesh size restrictions it might be challenging to capture the changes in component roughness seen as a primary effect of erosion. More attainable could be larger-scale erosion, for example compressor blade tips, or thinning of trailing edges (Dunn, 1990). Due to the increased scale of such damage, the aerodynamic loses would potentially be easier to capture.

The benefit of the DDM method is to allow heavy deposition to be simulated. This complements geometry optimisation methods, and is a primary application for the method. Using automated geometry optimisation it would be possible to trial hole geometries for improved blockage resistance for example, allowing a selected smaller number of experimental geometries to be assessed experimentally.

The continuous random walk model should be assessed against deposition data from more complex flows, including streamline curvature effects. Beyond flow through bends, almost no appropriate deposition validation data exists. An experiment including rotational effects could be designed, injecting particles onto a rotating disc. This would significantly increase the complexity of the calculation for assessment.

The experimental campaign discussed in chapter 4 indicated dependency on a number of variables which there was not time to address. The effects of exposure time on deposition rate, and the combination of exposure time and roughness should be investigated more thoroughly. The investigation of the interactions between gravity, particle diameter, and velocity was not conclusive, and needs further study. The

apparent rebound effect opens a range of possible directions for investigation; assessment of temperature effects, both isothermal and thermophoretic. Related to this would be the use of other salts - the previously used standard sea salt mixture. This would potentially introduce different crystal shapes, allowing this effect to be assessed. Recalibration of the swabbing technique would be necessary.

As indicated by Fig. 4.2, changing thermal conductivity ratio Λ significantly alters the thermophoretic coefficient for gas turbine conditions. Salt, sand, ash, and dust have differing thermal conductivities, the effects of which could easily be investigated; the current rig configuration would need little adaptation to inject solid particles - the installation of a fluidised bed powder atomiser would allow sand, ash, or dust to be injected. This would, though, require a different deposition measurement technique, potentially optical or mass-based.

Appendix A

Dynamic Mesh Morphing

A.1 Solver dependency

Due to the extremely small nature of the displacements carried out in each dynamic mesh morphing step, a comparison was carried out between full calculations using single or double precision solver. A single impingement jet was used, meshed as section 6.2. Radially averaged profiles are shown in Fig. A.1: single precision on left, double precision on right. Contours indicate equal mass injection. The maximum difference between the profiles was 1.8 %. The single precision calculation was 15 % faster under the same computational conditions.

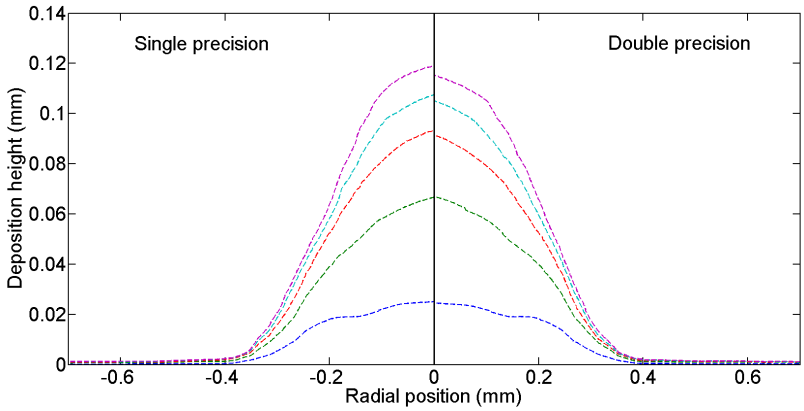

Figure A.1: Effect of solver precision on solution. *Left*: single precision. *Right*: double precision. Contours indicate equal mass injection; profiles averaged radially.

A.2 Grid dependency

Three mesh sizes were assessed - coarse, medium, and fine. Cell size was progressively halved. It was found that the fine mesh was extremely likely to deform into negative volumes. When the mass injected per iteration was reduced by an order of magnitude this was unable to correct the problem. The medium and fine meshes gave 2-5% differences in deformed volume, which was considered an acceptable difference.

Appendix B

Bounce-Stick Model

B.1 Model overview

The model considers elastic and plastic deformation, adhesion, and in the original shear removal. This was indicated to be negligible, and hence has been neglected from this current implementation. The below is a summary of the main effects of the model, see Bons et al. (2016) for the full derivation.

Fig. B.1 shows a typical plot of normal coefficient of restitution against normal impact velocity, highlighting the effect of the model. Four regimes of impact mechanics are be defined, labelled R1-4, along with the energy/deformation inequalities that define them.

R1: Stick: $W_{kn1} \leq W_a \sin(\alpha_1)$ Incoming normal kinetic energy is always less than the work of adhesion, hence sticking occurs at all impact velocities.

R2: Bounce: $w_{max} \leq w_{crit}$ and $W_{kn1} > W_a \sin(\alpha_1)$ Normal impact kinetic energy is larger than the work of adhesion so rebound occurs. Collision is fully elastic, the CoR_n increases with increasing V_{n1}.

R3: Bounce: $w_{max} > w_{crit}$ and $W_{crit} > W_a \sin(\alpha_1)$ High impact velocities cause plastic deformation to occur, hence increasing normal impact velocity increases the work of adhesion, reducing CoR_n.

R4: Stick: $W_a \sin(\alpha_1) > W_{crit}$ Plastic deformation is so large that the work of adhesion becomes larger than W_{crit}, the maximum elastic energy. Above this point only sticking occurs.

The normal and tangential coefficients of restitution are given by

$$CoR_n = \begin{cases} 0 & \text{for regimes R1 \& R4}(\textit{stick}), \\ \sqrt{\frac{\sigma_y^2}{\rho_p E_c} - \frac{2W_a \sin(\alpha_1)}{m_p}} \frac{1}{V_{n1}} & \text{for regimes R2 \& R3 (bounce)} \end{cases} \tag{B.1}$$

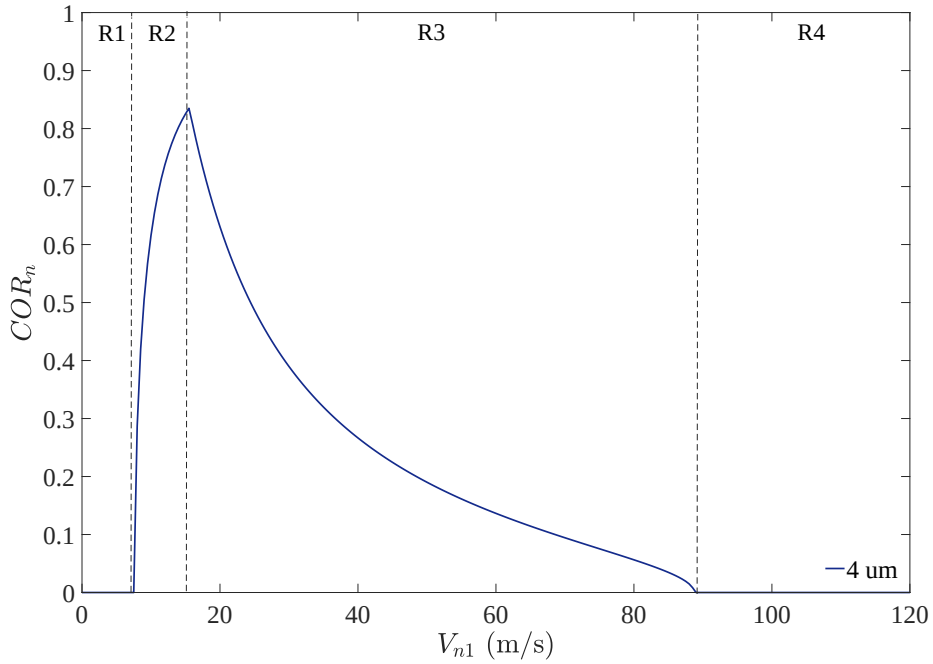

Figure B.1: Normal coefficient of restitution CoR_n against incoming normal impact velocity V_{n1} for a 4 µm particle. Four regimes of bounce/stick indicated, R1-4.

$$CoR_t = 1 - \mu_{imp}\left(\frac{V_{n1} + V_{n2i}}{V_{n1}}\right)\left(\frac{V_{n2}}{V_{n2i}}\right)\cos^2(\alpha_1)\,. \tag{B.2}$$

B.2 Validation of implementation

Three cases as published in the original Bons et al. paper are presented to indicate this implementation of the model works are the original. Solid lines indicate the new implementation, point markers the extracted data of Bons et al. The referenced experimental data is not shown for clarity.

B.2.1 Case 1: Quartz particles on aluminium

The model was assessed against impact data from quartz particles on an aluminium plate, Fig. B.2, from Bons et al. (2015). Experimentally both normal and tangential coefficients of restitution were measured. Incoming velocity was kept constant at 50 m/s, and plate angle varied to give impingement angles 10-80°.

Model parameters used were as follows: $d_p = 150\,\mu\text{m}$, $\rho_p = 2\,200$ kg/m^3, $\sigma_y = 120$ MPa, $E_c = 38$ GPa, $\gamma = 0.8$ J/m^2, $\mu_{imp} = 0.55$. It is very clear that the two implementations are producing the same results. The tangential coefficient of restitution

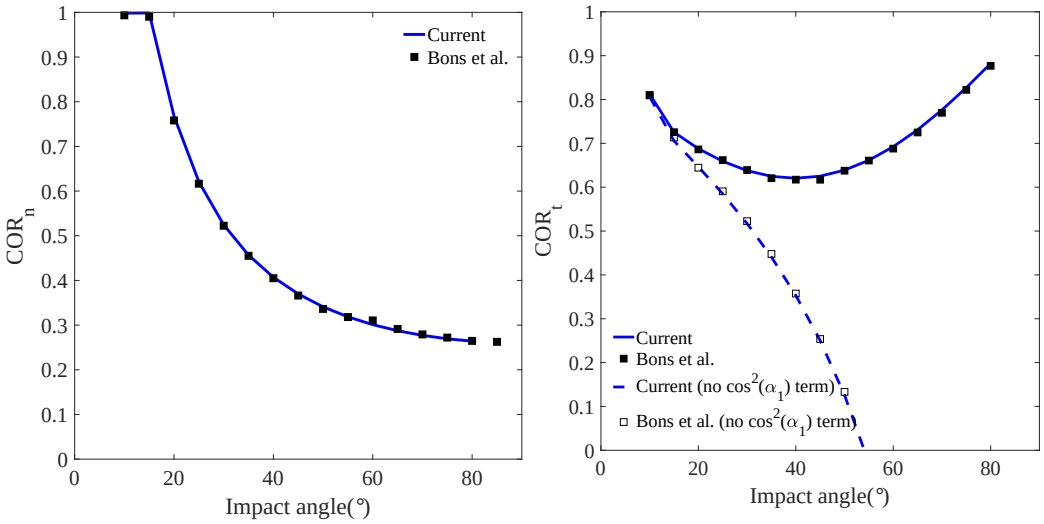

(a) Normal (b) Tangential

Figure B.2: Normal and tangential coefficients of restitution for case 1: quartz on aluminium. $d_p = 150\,\mu\text{m}$, $V_1 = 50$ m/s, $\alpha_1 = 10 - 80°$.

without the $\cos^2(\alpha_1)$ is shown; clearly this is not following the increasing CoR_t trend with increasing impingement angle above 30°, demonstrating the importance of the correction factor.

B.2.2 Case 2: Coal ash on stainless steel

The second assessment case for the current implementation was coal fly ash on stainless steel Whitaker and Bons (2015). The ash impacted at 'near normal' angles, with a range of velocities $5-120$ m/s, and a mean particle size of 60 µm. A single ash type, sub-bituminous, is shown here, Fig. B.3. Model parameters were $\rho_p = 2\,320$ kg/m^3, $\sigma_y = 200$ MPa, $E_c = 85$ GPa, $\gamma = 0.8$ J/m^2. No tangential coefficient of restitution data were recorded due to the highly normal impacts being induced.

As with case 1, the current implementation reproduces extremely closely the numerical results of Bons et al. Slight discrepancies are likely due to error in extracting data from the low-resolution published figures.

B.2.3 Case 3: Sand on stainless steel

The third assessment case was Arizona road dust (ARD) on stainless steel from the work of Reagle et al. (2014). A mean particle size of 30 µm was impacted onto the target plate at a velocity of 27 m/s, at angles from 20-80°. The experimental data compared against here, Fig. B.4 were acquired at ambient temperature. Model

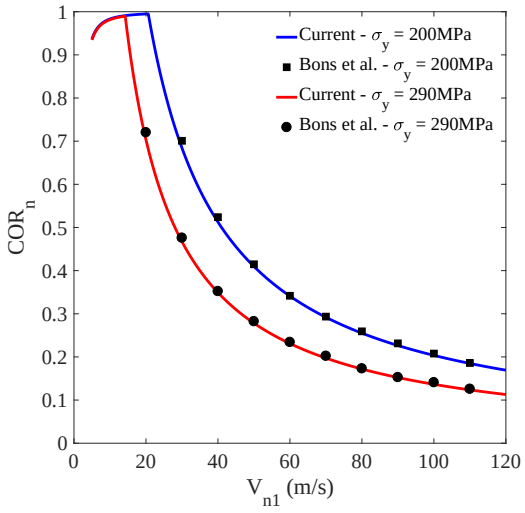

Figure B.3: Normal coefficients of restitution for coal ash impacting stainless steel. Particle size $d_p = 60\,\mu\text{m}$, impingement normal velocity $V_{n1} = 50$ m/s, impingement angle $\alpha_1 = 90°$.

parameters were $\rho_p = 2\,650$ kg/m^3, $\sigma_y = 130$ MPa, $E_p = 110 - 130$ GPa, $\gamma = 0.8$ J/m^2.

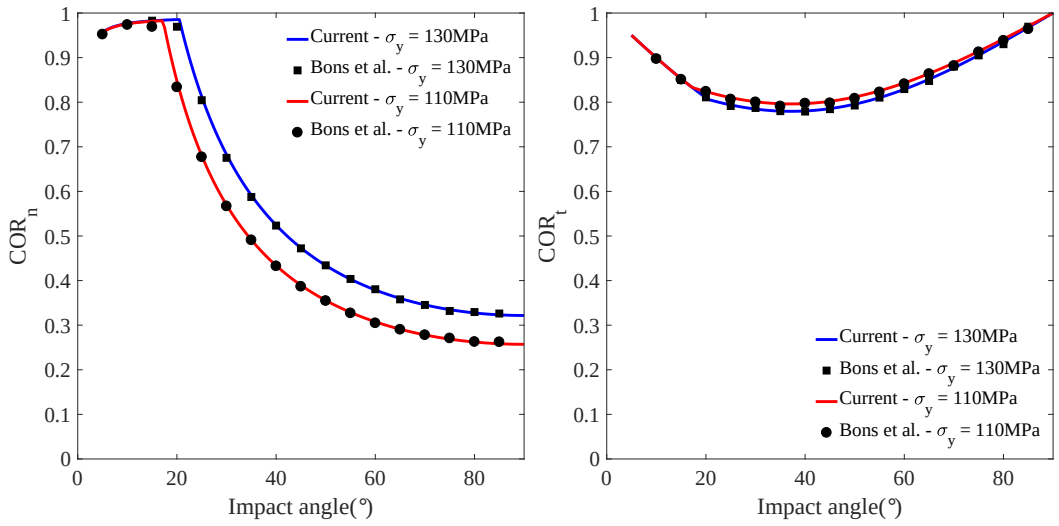

(a) Normal (b) Tangential

Figure B.4: Normal and tangential coefficients of restitution for case 3: sand on stainless steel. Particle size $d_p = 30\,\mu\text{m}$, impingement velocity $V_1 = 27$ m/s, impingement angles $\alpha_1 = 15 - 80°$.

Again it is clear that the current implementation of the bounce-stick model is reproducing the simulated results of Bons et al. extremely closely.

Appendix C

Experimental Design

C.1 Test piece design

The test section is coupled to the mixing chamber using a flanged joint and clamp, sealed using a copper O-ring. O-rings (32 mm OD, 30 mm ID, 2 mm thickness) were manufactured in-house. This method of joining was chosen as it allows the test section (and hence test insert) to be rotated through 360° about the main axis. This then allows gravitational effects to be investigated. Initial testing showed that some gravitational effects were seen; for the experimental campaign undertaken the test insert was always kept in the 'side' orientation to reduce gravitational effects where possible.

Overall length	420 mm
Diameter	18 mm
Test insert length	160 mm
Included angle of test insert	154.3°
Test insert area	3878 mm^2
Upstream distance from joint to mixing chamber	180 mm ($10D_h$)

Table C.1: Test piece dimensions

C.1.1 Optical particle sizer

The optical particle sizer (OPS), TSI model 3330, was used to provide both particle size distributions and bulk concentration measurements. The OPS uses a light scattering technique to calculate particle size. The OPS calibration for light intensity vs. particle size can be affected by particle refractive index. In the case of NaCl, the high

Bin	10	11	12	13	14	15	16	17
Original	2.2-2.7	2.7-3.3	3.3-4.2	4.2-5.2	5.2-6.5	6.5-8.0	8.0-10.0	> 10.0
Corrected	1.9-2.2	2.2-2.7	2.7-3.3	3.3-4.0	4.0-5.0	5.0-6.1	6.1-7.5	> 7.5
Bin width	0.4	0.5	0.6	0.7	0.9	1.1	1.4	-
Midpoint	2.1	2.5	3.0	3.7	4.5	5.5	6.8	-

Table C.2: Relevant OPS bin sizes (original and corrected as Eq. C.1), and midpoints. All sizes µm . Note bins 1-9 not shown here as below particle sizes of interest but recorded during experimental work.

refractive index of salt causes the OPS to size particles above their actual diameter. A linear fit was applied for optical to volume equivalent conversion,

$$d_{ve} = 0.72 d_{op} + 0.31, \tag{C.1}$$

which is shown as the blue line on Fig. 2.6, correlated from the experimental work of Chien et al. (2016). Here d_{ve} is the (spherical) volume equivalent particle diameter, d_{op} the particle diameter as sized by the OPS.

The OPS draws flow through the unit at 1.0 l/min. The number of particles per unit time in this flow are counted, n_c. If this is multiplied by the total volume flow rate at the point at which the sampling occurred, the total number of particles, N_c, can be found.

The model 3330 reported measured particle distribution in terms of a number of non-uniform bin widths, a maximum of 16 bins, and nominal particle diameters 0.3-10 µm. Bins 9-16, and 17 (all particle above maximum size) are shown in Table C.2. The upper bin size (6.1-7.5 µm) placed a restriction on the maximum particle size that could be measured; in order that there could be a bin above the maximum particle size generated (to show that the distribution was falling beyond this size), the largest particles generated in general were 6.0 µm.

C.1.2 Atomiser

A TSI model 3450 VOAG (Vibrating Orifice Aerosol Generator) was used to provide mono-dispersed NaCl particles from a saline solution. The atomiser pumps the solution through an orifice, which is oscillated using a signal generator and piezoelectric crystal. A single droplet is produced per cycle, hence from the frequency the number of potential particles is known.

d_p (µm)	2.0	2.5	3.0	4.0	4.2	5.0	6.0	6.5
C_m (ppm)	1107	2160	3727	8790	10161	17025	29059	36657
C_m (%)	0.1	0.2	0.4	0.9	1.0	1.7	2.9	3.7

Table C.3: NaCl concentrations by mass required for specific particle sizes used experimentally with 10 µm orifice.

Orifices of 10 and 20 µm were used, producing 25 and 40 µm droplets respectively. Careful and extensive tuning of the frequency was undertaken for each new particle size, and checked before each repeat test. This was most easily done using the optical particle sizer. Particles produced using the 10 µm orifice were found to have a higher quality distribution than those produced using the 20 µm orifice, likely due to them being closer to the 10 µm orifice's size. As $f \propto 1/D_d^3$, a smaller orifice will inject a larger mass flow rate of particles into the system for the same solution and same solution flow rate, which is desirable. Table C.3 indicates the NaCl concentrations required for the particle sizes used in the experiment when produced using the 10 µm orifice.

Atomiser efficiency $\eta_a = N_c/f_a$, where $N_c = n_c \left(\dot{Q}_{dil} + \dot{Q}_{dis}\right)$, the ratio of particles at mixing chamber entrance to atomiser frequency, was found to vary depending on d_p, f, $\dot{Q}_{dil}$, $\dot{Q}_{dis}$, $\dot{Q}_{sol}$, and tended to range 0.4-0.8. The loss of 'efficiency' is due to deposition of particles in both the drying column and transport pipe to the test section. A maximum allowable back pressure of 300 mbar could be placed upon the atomiser before the drying column would pop off its O-ring seal. This placed a significant limit on the maximum bulk Reynolds numbers that could be achieved, and the maximum pressure at which the experiment could run.

Appendix D

Calibration of Deposition Measurement Technique

D.1 Cell constant

The ECM cell constant was calibrated using standard potassium chloride (KCl) solutions as manufactured by Hanna Instruments. Single point calibrations were carried out for three different conductivity ranges (0.001-200 µS/cm, 200-2000 µS/cm, 2-200 mS/cm), using KCl calibration solutions at 84 µS/cm, 1413 µS/cm, 5000 µS/cm respectively. These calibration solutions are provided with a certificate of analysis and are stored in an opaque container to protect against light exposure.

D.2 Temperature compensation coefficient, α

Calibration of the ECM for temperature compensation coefficient was done by producing two NaCl solutions of varying and known concentration. A beaker of each solution was then heated in stages in a water bath, and the temperature allowed to stabilise (no temperature change to 1 decimal place for one minute). The solution conductivity and temperature were then measured. This was carried out for a range of appropriate temperatures (20-26 °C). Rearrangement of Eq. 4.16 and choice of a datum temperature (25 °C for convenience) allows the coefficient of temperature α to be calculated,

$$\alpha = \frac{G_{datum} - G_T}{G_{datum}\,(T_{sol} - T_{datum})}, \tag{D.1}$$

where temperatures are given in °C.

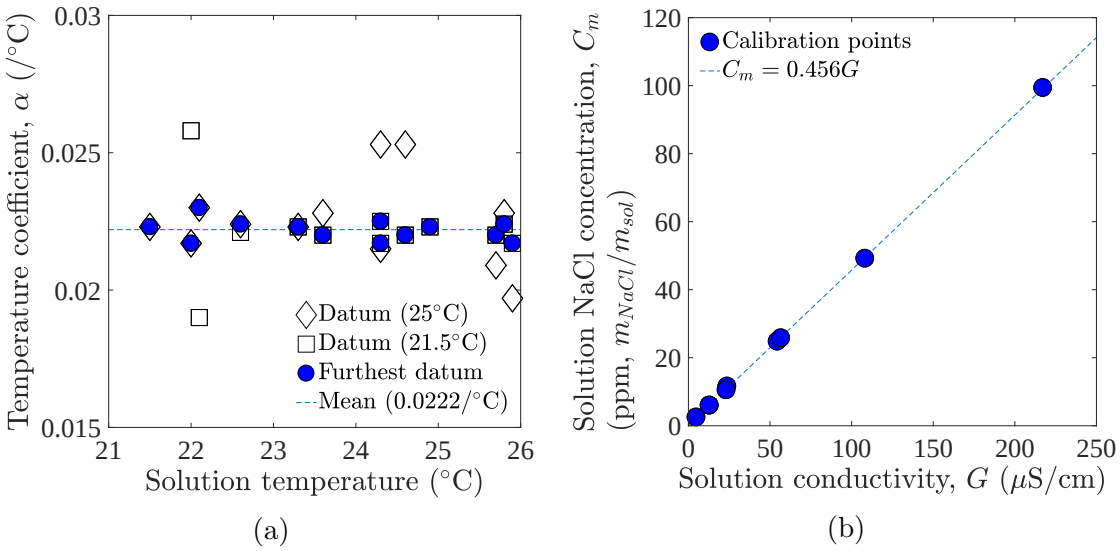

Figure D.1: *Left*: Coefficient of temperature compensation, α. Solution concentration: 60 ppm. Open shapes indicate the two datum points ($T_{sol} = 21.5$, 25°C). Solid blue circles indicate the value of α with the largest $T_{sol} - T_{datum}$. *Right*: Measured solution conductivity dependence on NaCl concentration. Plotting axis reversed as experimental analysis required $C_m = C_m\,(G)$. Conductivity at 25°C.

Fig. D.1a shows α as a function of solution temperature. Two datum points are shown, at 21.5 and 25°C, open square and diamond markers respectively. As $T_{sol} \to T_{datum}$, the variation in α is seen to increase, as measurement error becomes more significant. Hence two temperature datum points are used to show that a constant value of α is valid across the range of temperatures of interest.

A mean value of $\alpha = 0.022$/°C was calculated, with a standard deviation of 0.00038 (13 readings) at a solution concentration of 60 ppm. A further calibration was carried out at 19 ppm (not shown); this also gave a mean value of $\alpha = 0.022$/°C, and a standard deviation of 0.00032 (eight readings).

D.3 Conductivity to concentration

Solutions of known concentration were manufactured from pure NaCl, 2.5-99.4 ppm. The conductivity of these solutions was then measured. The resulting relationship between NaCl concentration and solution conductivity is seen to be highly linear ($r^2 > 0.999$), Fig. D.1b. A line of best fit of the form $C = mG$ (+0) gives the conversion from solution conductivity to NaCl concentration, where $m = 0.456$ ppm/(μS/cm). Dependent and independent variables are swapped as G is the dependent variable in the deposition experiments.

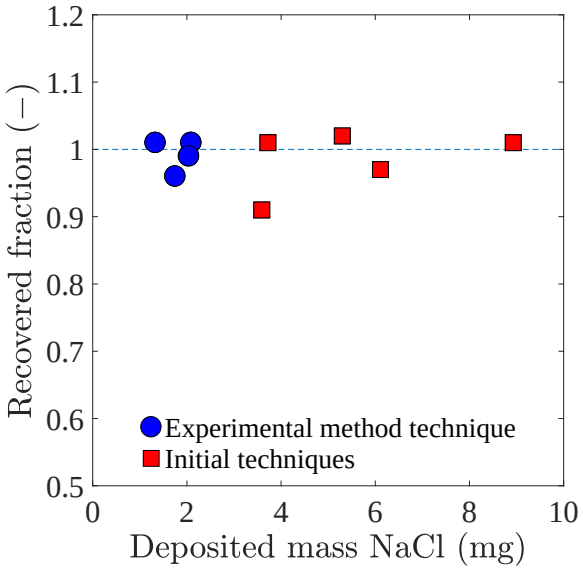

Figure D.2: Efficiency of swabbing technique. Blue circles indicate the finalised experimental swabbing method, red squares indicate initial methods as the technique was developed and improved.

D.4 Calibration of swabbing technique

A calibration of the swabbing technique used was undertaken. A measured amount of solution at a known concentration was deposited on to the test insert. This was then placed in the oven at 180 °C to evaporate the solute. The residual NaCl was then measured using the swabbing technique, in order to check the efficiency of the swabbing method.

Results are seen in Fig. D.2. All swabs returned > 0.90 efficiency, with the technique improved to give > 0.96 efficiency (blue circles). Due to measurement error, swabbing efficiencies slightly above 1.00 were seen for two of these samples. For the four experimental method tests, a mean swabbing efficiency of 0.99 with standard deviation 0.022 was seen. For all nine tests mean swabbing efficiency was also 0.99, with standard deviation 0.035.

This shows a significant improvement over previous swabbing techniques used, where a mean efficiency of 0.72, standard deviation 0.18 was seen. This improvement is largely due to (a) the ability to transfer the deposition directly from the test insert to the washing solution, without losses during swab transit inside the protective plastic bag, and (b) the ability to swab the surface until the measurement stabilises.

Appendix E

Uncertainty Analysis

An assessment of the uncertainties in individual experimental measurements was carried out, in preparation of overall uncertainties for the key reported experimental values (V_d^+, τ_p^+). Experimental uncertainly is not always been reported by experimentalists in this field, however those who did indicated values in the region 3-50%. A large fraction of published experimental data has tended to show significant spread in V_d^+, often in the region of an order of magnitude for matching τ_p^+. This suggests that experimental uncertainty is generally fairly high.

A list of uncertainties in the individual measurements taken in each test is given in Table E.1. The 'source' column indicates the origin of the value: manufacturer-specified (m), manually calibrated (c), assumed (a).

The Taylor series expansion method of Kline and McClintock (1953) (as then used by Coleman and Steele (2009)) for single-sample uncertainty analysis was used to calculate overall uncertainty values. For a small change in function R with dependent variables $X_1 ... X_i$,

$$R = R\left(X_1, X_2, ..., X_i\right), \tag{E.1}$$

this is expanded using a Taylor series, and truncated to only first order terms in $\partial R/\partial X_i$. The individual terms are assumed independent and therefore combined as sum of squares. Multiplying this expression by $(X_i/X_i)^2$ and dividing by R^2 leads to an expression for relative uncertainty U_R/R,

$$\left(\frac{U_R}{R}\right)^2 = \left(\frac{X_1}{R}\frac{\partial R}{\partial X_1}\right)^2 \left(\frac{U_{X1}}{X_1}\right)^2 + \left(\frac{X_2}{R}\frac{\partial R}{\partial X_2}\right)^2 \left(\frac{U_{X2}}{X_2}\right)^2 + \\ ... + \left(\frac{X_i}{R}\frac{\partial R}{\partial X_i}\right)^2 \left(\frac{U_{Xi}}{X_i}\right)^2, \tag{E.2}$$

Item	Measurement accuracy/uncertainty	Source
d_p	$\pm$0.5%	m
f_a	$\pm$0.01% reading	c
G	$\pm$1% reading	m/c
$\dot{m}_{mfc}$	$\pm$1% full scale	m
$\dot{m}_{op}$	$\pm$5% reading	c
m_{ws}	$\pm$0.01 g	m
P	$\pm$2% reading	c
$\dot{Q}_{sol}$	$\pm$1%	c
T_g, T_w	$\pm$2 °C	m
t	$\pm$1 s	a
η_c	7.2%	c
η_s	3.5%	c

Table E.1: Individual accuracies/uncertainties in experimentally measured values. 'Source' indicates origin of value; m: manufacturer-specified, c: calibrated, a: assumed.

where U_{Xi}/X_i is the relative uncertainty in variable X_i and $\frac{X_i}{R}\frac{\partial R}{\partial X_i}$ the uncertainty magnification factor. For V_d^+ and τ_p^+ this leads to total uncertainties of 11.5 and 10.4% respectively.

Appendix F

Experimental Method

The experimental test procedure is shown below. Around 5 hours were required for each test: 1.5 hours for preparation and heating, 1.5-2 hours experimental run time, 1 hour cooling time, 1 hour for dismantling experiment, measuring deposition, and processing data. Cold tests excluded heating and cooling processes.

1. Choose experimental conditions (T_g, T_w, Re, d_p). NaCl solution is produced in batches: dry NaCl and deionised water are weighed individually and mixed.

2. Commence heating of oven and main gas path. Use GP3 flow to bypass atomiser. Start atomiser once temperature approaching experimental conditions to allow output to stabilise. Once stable, measure outlet particle size distribution, and tune frequency and dispersion air flow rate as necessary.

3. Connect atomiser into system. Begin test. Monitor and adjust atomiser frequency generator and feed pressure wander, gas and metal temperatures as necessary. Gas and metal temperatures should be kept within ±3 °C of target nominal temperatures.

4. Once experiment complete, switch off heating elements and then gas flow. Remove test piece from oven and cool using external forced convection via a fan. Extractor fan unit removes hot gas from experimental room.

5. Once cool dismantle test piece and remove test insert. Inspect test insert and photograph any deposition characteristics of interest. Swab both test insert and remainder of circumference of passage (test piece body) as in section 4.3.5.2. Process data.

6. Clean test insert in ultrasonic bath in deionised water. Wash test section and scrub with bottle brush and scourer (due to size constraints of ultrasonic bath). Rinse both with deionised water. Rebuild test section.

Appendix G

Ambient temperature test matrix

$\dot{m}_g$ (g/s)	2.17	2.57	2.86	3.16	3.55	4.15	4.34	4.64	4.93	5.33	5.92	6.51	6.91
Re	8000	10000	11000	12000	14000	16000	17000	18000	19000	21000	23000	25000	27000
$u*$ (m/s)	0.46	0.53	0.59	0.64	0.70	0.79	0.84	0.90	0.93	1.01	1.11	1.23	1.27
EXPα													
2.5 µm	x												
3.0 µm	x		x		xxx				x	xx	xxx		x
4.0 µm	x		x		xxxxx				x		x		
5.0 µm		xx	x		xxxxx	x	xx		xx	xx	x		
6.0 µm	x			xx	x		xx	x	x			x	
6.5 µm					xxx								
EXPβ													
2.5 µm				x									
4.0 µm					xxx				xx				
5.0 µm			xxx		x								

Table G.1: Cold experimental campaign test matrix. Individual tests marked x

Appendix H

Ambient Experimental Results

H.1 Surface roughness

Roughness profiles are shown in Fig. H.1. These were measured using a Taylor Hobson surface profiliometer, 'Talysurf.' Probe tip diameter was 2.5 µm, a Gaussian high-pass filter with cut-off wavelength 0.8 mm applied to remove waviness. Roughness is characterised by the arithmetic mean deviation R_a, with measurements taken after 80 tests with EXPα , and four tests with EXPβ. Surface roughnesses were EXPα : $R_a = 0.22\,\mu\text{m}$, EXPβ: $R_a = 1.12\,\mu\text{m}$.

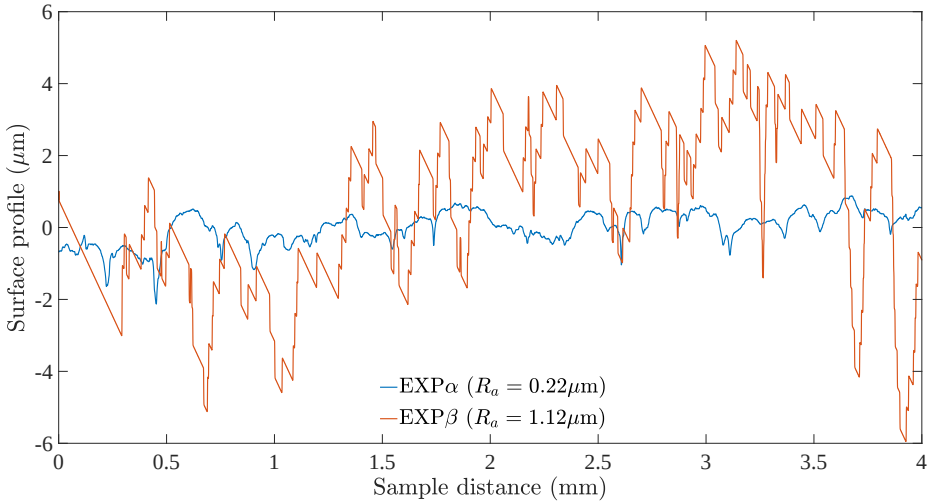

Figure H.1: Roughness profiles for test pieces EXPα, EXPβ as measured using Talysurf.

As both test pieces were machined by the same company, in the same manner (gun drilled, then honed), the difference in roughness is likely to be related to the cleaning process employed between tests. Until this point both test pieces were cleaned using a pan scrub, before washing in the ultrasonic bath and rinsing. As EXPα had undergone

this process many more times, it had been polished. In order to maintain the different surface finishes, EXPβ was not scrubbed for the remaining tests. Use of the ultrasonic bath and rising remained. EXPα continued to be cleaned as before. Swabbing of the test piece between cleaning and reassembly showed that no NaCl remained, despite the difference in cleaning method.

H.2 Repeatability

An enlargement of Fig. 4.8 is shown in Fig. H.2 with the scale adjusted for clarity. Only one point, $d_p = 4.0\,\mu\text{m}$, $Re = 14\,000$, point at [2.7, 0.0278], has a range of V_d^+ comparable to that of the data of Kvasnak et al.

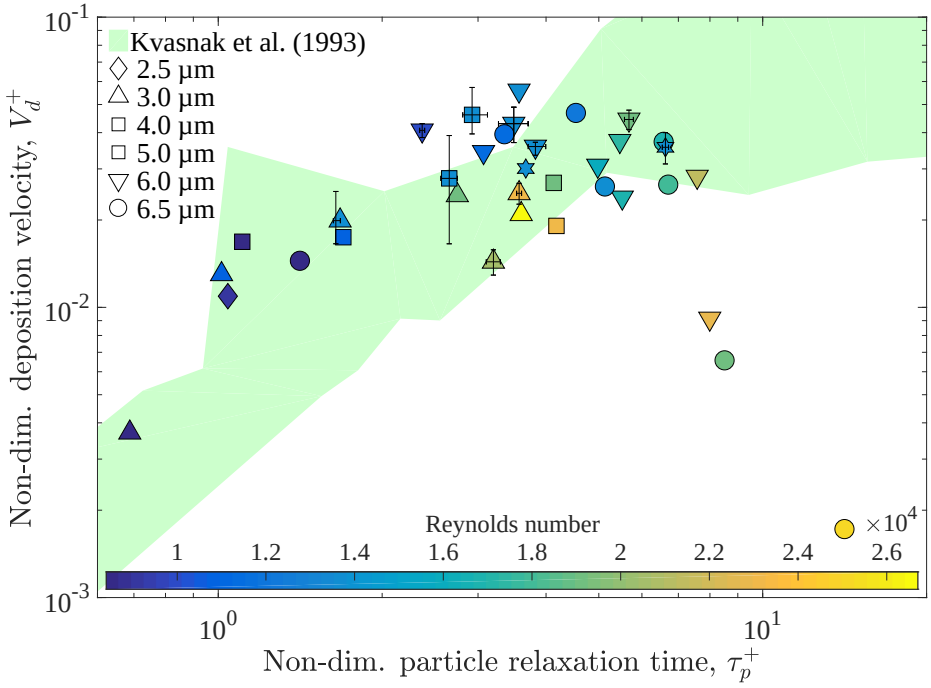

Figure H.2: V_d^+ against τ_p^+ for all EXPα ambient temperature tests. Markers by d_p, coloured by Re. Error bars show the spread for all repeated tests.

H.3 Secondary investigations

A number of secondary investigations were carried out by interrogating the above experimental data for other trends. As the experimental campaign was not conceived to assess these factors initially there are fewer usable data and hence the conclusions are somewhat more speculative.

H.3.1 Lift-off of deposited particles

Initially tests were carried out to assess the cooling of the experiment. Two schemes were used, (a) continuing to run the gas mass flow rate as in the test with the heaters off, hence cooling by internal convection for 30 mins, and (b) turning off the gas and heaters at the same time, cooling the rig by external convection via a fan. The first method was thought to potentially reduce the deposited mass by causing lift-off of deposited particles.

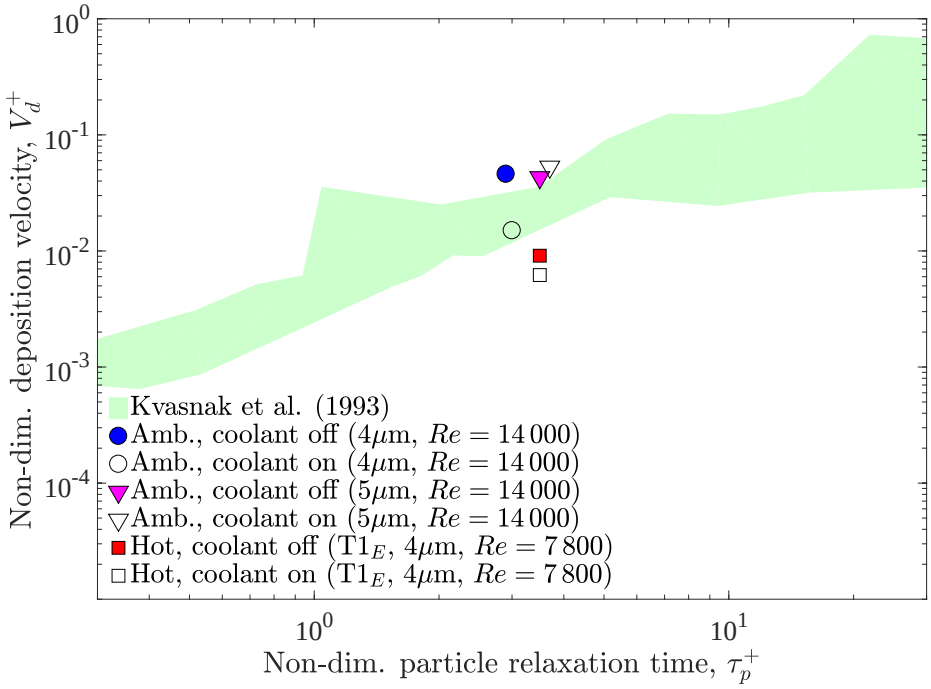

Figure H.3: Effects of lift-off of particles from test insert when gas was used to cool the rig internally

The deposition rate was reduced by 47%, Fig. H.3. A second pair of experiments were done at ambient conditions, with a simulated 'cooling' period of the same length. This is also seen on the same figure, causing a reduction in V_d^+ of 61%. A second set of ambient experiments, both repeated were done for $d_p = 5\,\mu\text{m}$ /$Re = 14\,000$. These indicated the reverse trend, with the 'coolant on' tests showing more deposition than the 'coolant off' experiments. As no gas was passing through the atomiser, no re-suspended particles could be entering the system from this location, and it is most likely that the effect is an artefact of experimental scatter. Due to the inconclusive nature of these experiments all further cooling was done with external convection and no internal coolant.

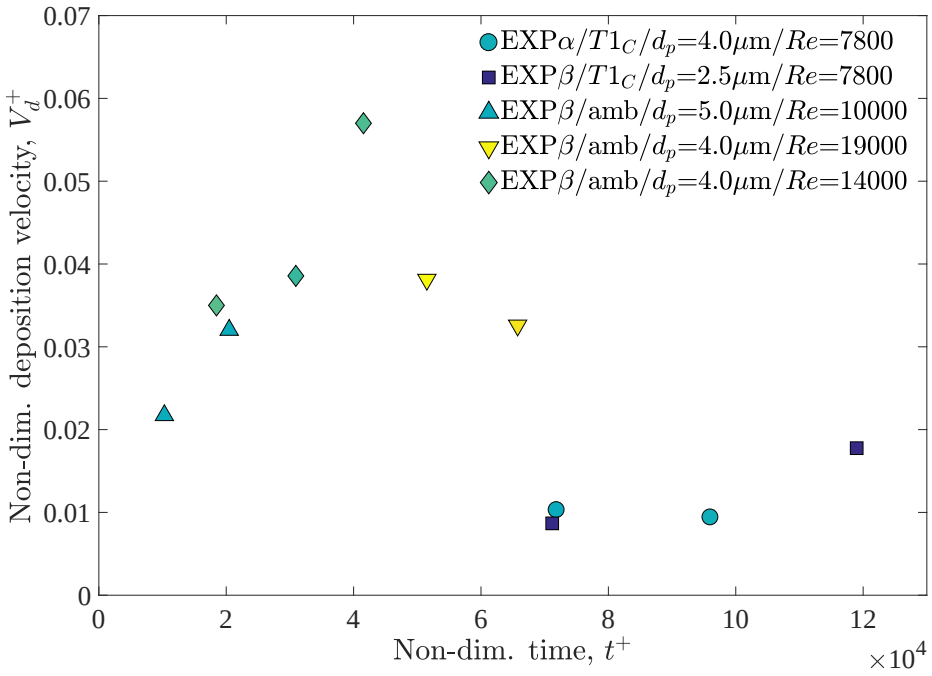

Figure H.4: Effect of exposure time t^+ on non-dimensional deposition velocity

H.3.2 Experimental test time

Assessment is made of the effect of test or exposure time on the deposition rate. Discussion of this effect in the open literature is very inconclusive. If a dependency exists, it is likely to be dependent on surface roughness R_a, particle size d_p. To make comparisons a non-dimensional experimental time t^+ was used,

$$t^+ = \frac{t\,(u^*)^2}{\nu^2}. \tag{H.1}$$

Only a small number of experimental data are suitable for these comparisons, as repeat experiments were usually carried out with the same test time. Deposition fraction is plotted against non-dimensional experimental time in Fig. H.4. Only a single pair of experiments were carried out at multiple t^+ for test piece EXPα (roughness $R_a = 0.22\,\mu$m). V_d^+ was seen to fall 3.3% with increasing t^+ (33%), inside experimental uncertainty. Tentatively this indicates that the smoother test piece saw a negligible time-dependency.

Assessment of varying experimental time using test piece EXPβ (roughness $R_a = 1.1\,\mu$m) indicated a much larger time-dependence for the rougher test piece. Three of the four data sets indicated increasing deposition rate with increasing time, with the ratio V_d^+/t^+ in the range $1.9e^{-7} - 1.7e^{-6}$. The effect was unexpected. The EXPβ

tests reported in chapter 4 are those closest to the EXPα experiments in terms of length, unless noted otherwise.

Deposition rate has been shown by other authors (El-Shobokshy, 1983, for example) to increase with increasing surface roughness. This increase with exposure time may be explainable in a similar manner. From Fig. 4.13 it is seen that the rougher test piece saw generally higher deposition rates than the smoother version. Deposition of these particles would be expected to increase the surface roughness as seen by the deposition salt particles, increasing the rate of deposition. This aspect of the investigation certainly requires more assessment.

Appendix I

High temperature test matrix

Temperature condition T1

d_p (µm)	2.0		2.5				3.0		4.0						5.0		6.0						
Re	7800		6500		7800		7800		6500		7800		10000		7800		7800		10000				
u^* (m/s)	1.7		1.44		1.7		1.7		1.46		1.7		2.1		1.7		1.7		2.1				
τ_p^+	0.4-0.5		0.61		0.7-0.8		1.0		1.3		1.9		2.8		3.3		4.6		6.7		T_w	T_g	$P_{Th}^+ d_p/\Phi$
Test piece	α	β	α	β	α	β	α	β	α	β	α	β	α	β	α	β	α	β	α	B	(°C)	(°C)	(m)
A ($T_{w,low}$)							x								x						357	390	1.86e-12
B ($T_{w,med.low}$)	x				x		x				x				x						383	390	4.01e-13
C (isothermal)			xx		x	xx				x	xx	xx	x		x	x	x		x		390	390	0.0
D ($T_{w,med.high}$)					x						x		x		x						480	390	-5.10e-12
E ($T_{w,high}$)											x		x		x						630	390	-1.27e-11

Temperature condition T2

d_p (µm)	4.0				
Re	7200				
u^* (m/s)	1.9				
τ_p^+	1.8		T_w	T_g	$P_{Th}^+ d_p/\Phi$
Test piece	α	β	(°C)	(°C)	(m)
C (isothermal)	x		480	480	0.0
D ($T_{w,med.high}$)	x		530	480	-2.49e-12
E ($T_{w,high}$)	x		730	480	-1.35e-11

Table I.1: Test matrix for hot experiments.

References

M. Abraham, J.W. Hoard, D. Assanis, D. Styles, and C.S. Sluder. An analytic study in thermophoretic particulate deposition in turbulent pipe flows. *Aerosol Science and Technology*, 44(9):785–795, 2010.

G. Agati, D. Borello, F. Rispoli, and P. Venturini. An innovative approach to model temperature influence on particle deposition in gas turbines. *ASME Turbo Expo*, 2016.

ANSYS. Fluent 14 Theory Guide . 2011a.

ANSYS. Fluent 14 User Guide. 2011b.

ANSYS. Fluent User Defined Function Manual. 2011c.

B. Arcen and A. Taniere. Simulation of a particle-laden turbulent channel flow using an improved stochastic Lagrangian model. *Physics of Fluids*, 21(4), 2009.

B. Arcen, A. Taniere, and B. Oesterle. Influence of the gravity field on the turbulence seen by heavy discrete particles in an inhomogeneous flow. *ERCOFTAC International Symposium on Engineering Turbulence and Measurements - ETMM6*, pages 949–958, 2005.

T. Barth, G. Lecrivain, and U. Hampel. Particle deposition study in a horizontal turbulent duct flow using optical microscopy and particle size spectrometry. *Journal of Aerosol Science*, 60(1):47–54, 2013.

T. Barth, J. Preuss, G. Mueller, and U. Hampel. Single particle resuspension experiments in turbulent channel flows. *Journal of Aerosol Science*, 71(1):40–51, 2014.

S. Beresnev and V. Chernyak. Thermophoresis of a spherical particle in a rarefied gas: Numerical analysis based on the model kinetic equations. *Physics of Fluids*, 7(7):1743–1756, 1995.

A. Berrouk, S., and D. Laurence. Stochastic modelling of aerosol deposition for LES of 90° bend turbulent flow. *International Journal of Heat and Fluid Flow*, 29: 1010–1028, 2008.

T.L. Bocksell and E. Loth. Random walk models for particle diffusion in free-shear flows. *AIAA Journal*, 39(6):1086–1096, 2001.

J.P. Bons, R. Blunt, and S. Whitaker. A comparison of techniques for particle rebound measurement in gas turbine applications, GT2015-43677. *ASME Turbo Expo*, 2015.

J.P. Bons, R. Prenter, and S. Whitaker. A simple physics-based model for particle rebound and deposition in turbomachinery, GT2016-56697. *ASME Turbo Expo*, 2016.

D. Borello, P. Venturini, F. Rispoli, and S.G.Z. Rafael. Prediction of multiphase combustion and ash deposition within a biomass furnace. *Applied Energy*, 101(1): 413–422, 2012.

D. Borello, D'Angeli, Salvagni L., Venturini A., and F. P., Rispoli. Study of particles deposition in gas turbine blades in presence of film cooling. *ASME Turbo Expo*, 2014.

R.W. Bosworth, A.L. Ventura, A.D. Ketsdever, and S.F. Gimelshein. Measurement of negative thermophoretic force. *Journal of Fluid Mechanics*, 805:207–221, 2016.

R.M. Brach. Mechanical impact dynamics : rigid body collisions. *John Wiley & Sons, ISBN 0471508454*, 1991.

R.M. Brach and and Dunn, P.F. A mathematical model of the impact and adhesion of microspheres. *Aerosol Science and Technology*, 16(1):51–64, 1992.

Y. Cao, J. Huang, Z. Xu, and J. Yin. Insight into rime ice accretion on an aircraft wing and corresponding effects on aerodynamic performance. *The Aeronautical Journal*, 120(1229):1101–1122, 2016.

M. Caporaloni, F. Tampeieri, F. Trombetti, and O. Vittori. Transfer of particles in nonisotropic air turbulence. *Journal of the Atmospheric Sciences*, 32(3):565–568, 1975.

N.D. Cardwell, K.A. Thole, and S.W. Burd. Investigation of sand blocking within impingement and film-cooling holes. *Journal of Turbomachinery*, 132:021020–1/10, 2010.

B. Casaday, C. Clum, and J.P. Bons. Particle deposition in internal cooling cavities of a nozzle guide vane part II: Analytical and computational modelling, GT2014-27155. *ASME Turbo Expo*, 2014a.

B. Casaday, R. Prenter., C. Bonilla, M. Lawrence, C. Clum, A.A. Ameri, and J.P. Bons. Deposition with hot streaks in an uncooled turbine vane passage. *Journal of Turbomachinery*, 136:041017–1/9, 2014b.

T.J. Casadevall. The 1989-1990 eruption of Mt. Redoubt volcano, Alaska: impacts on aircraft operations. *Journal of Volcanology and Geothermal Research*, 62:301–316, 1994.

J.C. Chambers. The 1982 encounter of British Airways 77 with the Mt. Galunggung eruption cloud. Paper no. 85-0097. *23rd Aerospace Sciences Meeting, Reno, Nevada*, 1985.

S. Chibbaro and J.-P. Minier. Langevin PDF simulation of particle deposition in a turbulent pipe flow. *Aerosol Science*, 39(7):555–571, 2008.

C.H. Chien, A. Theodore, C.Y. Wu, Y.M. Hsu, and B. Birky. Upon correlating diameters measured by optical particle counters and aerodynamic particle sizers. *Journal of Aerosol Science*, 101(1):77–85, 2016.

J.I. Choi, K. Yeo, and C. Lee. Lagrangian statistics in turbulent channel flow. *Physics of Fluids*, 16(3):779–793, 2004.

R.J. Clarkson, E.J.E. Majewicz, and P. Mack. A re-evaluation of the 2010 quantitative understanding of the effects volcanic ash has on gas turbine engines. *Proceedings of the IMechE Part G: Journal of Aerospace Engineering*, 230(12):2274–2291, 2016.

C. Clum, B. Casaday, E. Bokar, and J.P. Bons. Particle deposition in internal cooling cavities of a nozzle guide vane: Part I experimental investigation, GT2014-27150. *ASME Turbo Expo 2014, Dusseldorf*, 2014.

H.W. Coleman and W.G. Steele. Experimentation, validation, and uncertainty for engineers (third edition). *Wiley*, 2009.

A. Corsini, F. Rispoli, A.G. Sheard, and P. Venturini. Numerical simulation of coal fly-ash erosion in an induced draft fan. *Journal of Fluids Engineering*, 135(August): 081303–1/12, 2013.

T.C. Currie, D. Fuleki, and A. Mahallati. Experimental studies of mixed-phase sticking efficiency for ice crystal accretion in jet engines, Paper no. AIAA 2014-3049. *6th AIAA Atmospheric and Space Environments ConferenceAtlanta, GA*, 2014.

A. Dehbi. Turbulent particle dispersion in arbitrary wall-bounded geometries: A coupled CFD-Langevin-equation based approach. *International Journal of Multiphase Flow*, 34(9):819–828, 2008a.

A. Dehbi. A CFD model for particle dispersion in turbulent boundary layer flows. *Nuclear Engineering and Design*, 238(3):707–715, 2008b.

A. Dehbi. A stochastic Langevin model of turbulent particle dispersion in the presence of thermophoresis. *International Journal of Multiphase Flow*, 35(3):219–226, 2009.

A. Dehbi. Validation against DNS statistics of the normalised Langevin model for particle transport in turbulent channel flows. *Powder Technology*, 200(1):60–68, 2010a.

A. Dehbi. Validation against DNS statistics of the normalized langevin model for particle transport in turbulent channel flows. *Powder Technology*, 200(1):60–68, 2010b.

A. Dehbi. Prediction of extrathoracic aerosol deposition using RANS-random walk and LES approaches. *Aerosol Science and Technology*, 45(5):555–569, 2011.

A. Dehbi and F. de Crechy. Validation of the Langevin particle dispersion model against experiments on turbulent mixing in a T-junction. *Powder Technology*, 206 (3):312–321, 2011.

A. Dehbi and S. Martin. CFD simulation of particle deposition on an array of spheres using an Euler/Lagrange approach. *Nuclear Engineering and Design*, 241(8):3121–3129, 2011.

A. Dehbi, J. Kalilainen, T. Lind, and A. Auvinen. A large eddy simulation of turbulent particle laden flow inside a cubical differentially heated cavity. *Journal of Aerosol Science*, 103(1):67–82, 2017.

T.D. Dreeben and S.B. Pope. Probability density function and reynolds-stress modeling of near-wall turbulent flows. *Physics of Fluids*, 9(1):154–163, 1997.

L. Duan and M.P. Martin. Direct numerical simulation of hypersonic boundary layer. Part 4. Effect of high enthalpy. *Journal of Fluid Mechanics*, 684(1):25–59, 2011.

P. Dumaz, Y. Drossinos, and Drosik I. Capitao, J. Areia. Fission product deposition and revaporization phenomena in scenarios of large temperature differences. *ANS Proceedings 1993 National Heat Transfer Conference, American Nuclear Society, Atlanta, GA*, pages 348–358, 1993.

D. Dunham, J. Carrotte, and M. Zedda. Particle trajectories in a state of the art combustor. *NEWAC Deliverable D1.4.3B*, 2011.

M.G. Dunn. Performance deterioration of an operational F100 turbofan engine upon exposure to a simulated nuclear dust environment, Calspan Advanced Technology Center, Buffalo, NY, Technical Report No. DNA-TR-90-72-V1. 1990.

M.G. Dunn. Operation of gas turbine engines in an environment contaminated with volcanic ash. *Journal of Turbomachinery*, 134(5):051001, 2012.

P.A. Durbin. Near-wall turbulence closure modeling without 'damping functions'. *Theoretical Computational Fluid Dynamics*, 3(1):1–13, 1991.

M. El-Shobokshy. Experimental measurements of aerosol deposition to smooth and rough surfaces. *Atmospheric Environment*, 17(3):639–644, 1983.

L. Eppelbaum. Lecture notes in earth system sciences. *Applied Geothermics*, 2014.

P.S. Epstein. Zur Theorie des Radiometers. *Zeitschrift für Physik*, 54(7-8):537–563, 1929.

F.G. Fan and G. Ahmadi. A sublayer model for turbulent deposition of paticles in vertical ducts with smooth and rough surfaces. *Journal of Aerosol Science*, 24(1): 45–64, 1993.

Y. Feng and C. Kleinstreuer. Micron-particle transport, interactions and deposition in triple lung-airway bifurcations using a novel modeling approach. *Journal of Aerosol Science*, 71(1):1–15, 2014.

P.R. Forsyth, M. McGilvray, and D.R.H. Gillespie. Secondary flow and heat transfer coefficient distributions in the developing flow region of ribbed turbine blade cooling passages, GT2014-26737. *ASME Turbo Expo*, 2014.

P.R. Forsyth, D.R.H. Gillespie, and M. McGilvray. Validation and assessment of the continuous random walk model for particle deposition in gas turbine engines, GT2016-57332. *ASME Turbo Expo*, 2016.

P.R. Forsyth, D.R.H. Gillespie, and M. McGilvray. Development and applications of a coupled particle deposition dynamic mesh morphing approach for the numerical simulation of gas turbine flows, GT2017-63295. *ASME Turbo Expo*, 2017a.

P.R. Forsyth, D.R.H. Gillespie, and M. McGilvray. Experimental deposition of NaCl particles from turbulent flows at gas turbine temperatures. Paper no. 160. *ISROMAC*, 2017b.

P.R. Forsyth, M. McGilvray, and D.R.H. Gillespie. Secondary flow and heat transfer coefficient distributions in the developing flow region of ribbed turbine blade cooling passages,. *Experiments in Fluids*, 58(1), 2017c.

P.R. Forsyth, D.R.H. Gillespie, and M. McGilvray. Development and applications of a coupled particle deposition dynamic mesh morphing approach for the numerical simulation of gas turbine flows. *Journal of Engineering for Gas Turbines and Power*, 140(2), 2018.

S.K. Friedlander and H.F. Johnstone. Deposition of suspended particles from turbulent gas streams. *Industrial and Engineering Chemistry*, 49(7):1151–1156, 1957.

E. Ghahramani, O. Abouali, H. Emad, and G. Ahmadi. Numerical analysis of stochastic dispersion of micro-particles in turbulent flows in a realistic model of human nasal/upper airway. *Journal of Aerosol Science*, 67(1):188–206, 2014.

E. Ghahramani, O. Abouali, H. Emdad, and G. Ahmadi. Numerical investigation of turbulent airflow and microparticle deposition in a realistic model of human upper airway using LES. *Computers and Fluids*, 157(1):43–54, 2017.

A.D. Gosman and E. Ionnides. Aspects of computer simulation of liquid-fuelled combustors. *Journal of Energy*, 7(6):482–490, 1983.

A. Hamed and W. Tabakoff. Erosion and deposition in turbomachinery. *Journal of Propulsion and Power*, 22(2):356–360, 2006.

J.C. Han, S. Dutta, and S. Ekkad. Gas turbine heat transfer and cooling technology. *Taylor and Francis, ISBN 9781439855683*, 2000.

D.P. Healy and J.N. Young. An experimental and theoretical study of particle deposition due to thermophoresis and turbulence in an annular flow. *International Journal of Multiphase Flow*, 36(11):870–881, 2010.

J. Hilsenrath. Tables of thermal properties of gases : comprising tables of thermodynamic and transport properties of air, argon, carbon dioxide, carbon monoxide, hydrogen, nitrogen, oxygen, and steam. *U.S. Dept. of Commerce, National Bureau of Standards, Washington D.C.*, 1955.

and Gottuk D.T. andHall J.R. andHarada K. and Kuligowski E.D. Hurley, M.J. SFPR handbook of fire protection engineering. *Springer-Verlag New York, ISBN 978-1-4939-2564-3*, 2008.

I. Iliopoulos, Y. Mito, and T. Hanratty. A stochastic model for solid particle dispersion in a nonhomogeneous turbulent field. *International Journal of Multiphase Flow*, 29 (3):375–394, 2003.

P. Ireland. Technical report: Requirements for sulphidation experiments as Osney UTC. Report no. DNS168835. *RR Internal*, 2010.

J.W. Jensen, S.W. Squire, J.P. Bons, and T.H. Fletcher. Simulated land-based turbine deposits generated in an accelerated deposition facility. *Journal of Turbomachinery*, 127(3):462–470, 2004.

Potts I. Jin, C. and M.W. Reeks. A simple stochastic quadrant model for the transport and deposition of particles in turbulent boundary layers. *Physics of Fluids*, 27(5): 053305, 2016a.

Potts I. Jin, C. and M.W. Reeks. The effects of near wall corrections to hydrodynamic forces on particle deposition and transport in vertical turbulent boundary layers. *International Journal of Multiphase Flow*, 79(1):62–73, 2016b.

G.A. Kallio and M.W. Reeks. A numerical simulation of particle deposition in turbulent boundary layers. *International Journal of Multiphase Flow*, 15(3):433–446, 1989.

J.T. Kelly, B. Asgharian, J.S. Kimbell, and B.A. Wong. Particle deposition in human nasal airway replicas manufactured by different methods. Part I: Inertial regime particles. *Aerosol Science and Technology*, 38(11):1063–1071, 2004.

K. Kendall, M. Kendall, and F. Rehfeldt. Adhesion of cells, viruses, and nanoparticles. *Springer, Dordrecht, 978-90-481-2584-5*, 2011.

J. Kim, P. Moin, and R. Moser. Turbulence statistics in fully developed channel flow at low reynolds number. *Journal of Fluid Mechanics*, 177(1):133–166, 1987.

O.V. Kim and P.F. Dunn. A microsphere-surface impact model for implementation in computational fluid dynamics. *Journal of Aerosol Science*, 38(5):538–549, 2007.

C. Kleinstreuer and Z. Zang. Airow and particle transport in the human respiratory system. *Annual Review of Fluid Mechanics*, 42:301–334, 2010.

S. J. Kline and F.A. McClintock. Describing uncertainties in single-sample experiments. *Mechanical Engineering*, 75(1):3–8, 1953.

Y. Kousaka, K. Okuyama, M. Adachi, and K. Ebie. Measurement of electrica charge of aerosol particles generated by various methods. *Journal of Chemical Engineering of Japan*, 14(1):54–58, 1980.

U. Kueppers, C. Cimarelli, K.W. Hess, J. Taddeucci, F.B. Wadsworth, and D.B. Dingwell. The thermal stability of Eyjafjallajökull ash versus turbine ingestion test sands. *Journal of Applied Volcanology*, 3(4):1–11, 2014.

W. Kvasnak, G. Ahamadi, R. Bayer, and M. Gaynes. Experimental investigation of dust particle deposition in a turbulent channel flow. *Journal of Aerosol Science*, 34 (6):795–815, 1993.

G.Y. Lai. High-temperature corrosion and materials applications. *ASM International, ISBN: 978-0-87170-853-3*, pages 249–258, 2007.

P. Langevin. Sur la thorie du mouvement brownien. *Comptes Rendus de l'Acadmie des Sciences(Paris)*, 146:530–533, 1908.

B.K. Lee, D.S. Byun, G.N. Bae, and J.H. Lee. Thermophoretic deposition of ultrafine particles in a turbulent pipe flow: Simulation of ultrafine particle behaviours in an automobile exhaust pipe. *Journal of Aerosol Science*, 37(12):1788–1796, 2006.

B.Y.H. Liu and J.K. Agarwal. Experimental observation of aerosol deposition in turbulent flow. *Journal of Aerosol Science*, 5(2):145–155, 1974.

Y. Liu, E.A. Matilda, J. Gu, and M.R. Johnson. Numerical simulation of aerosol deposition in a 3-D human nasal cavity using RANS, RANS/EIM, and LES. *Journal of Aerosol Science*, 38(7):683–700, 2007.

J. Lou and E.H. Razinsky. Analysis of turbulent flow in 180 degree turning ducts with and without guide vanes. *Journal of Turbomachinery*, 131(2).

R. Lundgreen, C. Sacco, R. Prenter, and J.P. Bons. Temperature effects on nozzle guide vane deposition in a new turbine cascade rig, GT2016-57560. *ASME Turbo Expo*, 2016.

X. Luo and S. Yu. Deposition of particles in turbulent pipe flow. *China Particulogy*, 4(1):31–34, 2006.

J.M. MacInnes and F.V. Bracco. Stochastic particle dispersion modeling and the tracer-particle limit. *Physics of Fluids*, 4(12):2809–2824, 1992.

C. Marchioli, A. Giusti, M.V. Salvetti, and A. Soldati. Direct numerical simulation of particle wall transfer and deposition in upward turbulent pipe flow. *International Journal of Multiphase Flow*, 29(6):1017–1038, 2003.

C. Marchioli, A. Soldati, J.G.M. Kuerten, B. Arcen, A. Tanire, G. Goldensoph, K.d. Squires, M.F. Cargnelutti, and L.M. Portela. Statistics of particle dispersion in direct numerical simulations of wall-bounded turbulence: Results of an international collaborative benchmark test. *International Journal of Multiphase Flow*, 34 (9):879–893, 2008.

J.C. Mason-Flucke. Sulphidation life assessment for turbine blades. *RR Internal*, 2011.

E. A. Matida, W. H. DeHaan, W. H. Finlay, and C. F. Lange. Simulation of particle deposition in an idealized mouth with different small diameter inlets. *Aerosol Science and Technology*, 37(11):924–932, 2003.

H. Matsui, Y. Yoshida, M. Murata, and T. Ohata. Measurement of deposition fraction of aerosol particles in a horizontal straight metal pipe. *Journal of Nuclear Science and Technology*, 11(7):300–307, 1974.

M. McGilvray, P. Ireland, and C. Rees. Sulphidation experiments to investigate numerical modeling of particle deposition - rig commissioning report. *RR Internal*, 2011.

A. Mehel, A. Taniere, Oesterle., A., and J.-R. Fontaine. The influence of an anisotropic Langevin dispersion model on the prediction of micro- and nanoparticle deposition in wall-bounded turbulent flows. *Journal of Aerosol Science*, 41(8): 729–744, 2010.

Y. Mito and T.J. Hanratty. Use of a modified Langevin equation to describe turbulent dispersion of fluid particles in a channel flow. *Flow, Turbulence and Combustion*, 68(1):1–26, 2002.

T.L. Montgomery and M. Corn. Aerosol deposition in a pipe with turbulent airflow. *Aerosol Science*, 1(3):185–213, 1970.

R.D. Moser, J. Kim, and N.N. Mansour. Direct numerical simulation of turbulent channel flow up to $Re_\tau = 590$. *Physics of Fluids*, 11(4):943–945, 1999.

P.A. Mulheran. Surface free-energy calculations and the equilibrium shape of NaCl crystals. *Modelling and Simulation in Materials Science and Engineering*, 2(6): 1123–1131, 1994.

N. Narita, K. Higashida, T. Torii, and S. Miyaki. Crack-tip shielding by dislocations and fracture toughness in NaCl crystals. *Materials Transactions, JIM*, 30(11): 895–907, 1989.

A.M. Obukhuv. Description of turbulence in terms of lagrangian variables. *Advances in Geophysics*, 6(1):113–116, 1959.

J. Parry-Crooke. Sulphidation results 12/2012 (report). 2013.

W. Peng, T. Zhang, and Yu S. Sun, X. Thermophoretic and turbulent deposition of graphite dust in HTGR steam generators. *Nuclear Engineering and Design*, 300: 610–619, 2016.

S.B. Pope. A Lagrangian two-time probability density function equation for inhomogeneous turbulent flows. *Physics of Fluids*, 26:3448–3450, 1983.

R. Prenter, S.M. Whitaker, A. Ameri, and J.P. Bons. The effects of slot film cooling on deposition on a nozzle guide vane, GT 2014-27171. *ASME Tubro Expo*, 2014.

R. Prenter, A. Ameri, and J.P. Bons. Deposition of a cooled nozzle guide vane with nonuniform inlet temperatures. *Journal of Turbomachinery*, 138:101005–1/11, 2016.

D.Y.H. Pui, F. Romay-Novas, and B.Y.H. Liu. Experimental study of particle deposition in bends of circular cross section. *Aerosol Science and Technology*, 7(3): 301–315, 1987.

C.J. Reagle, J.M. Delimont, W.F. Ng, and S.V. Ekkad. Study of microparticle rebound characteristics under high temperature conditions. *Journal of Engineering for Gas Turbines and Power*, 136(1):11501–1/7, 2014.

M.W. Reeks. On the dispersion of small particle suspended in an isotropic turbulent fluid. *Journal of Fluid Mechanics*, 83(3):529–546, 1977.

F.J. Romay, S.S. Takagaki, D.Y.H. Pui, and B.Y.H. Liu. Thermophoretic deposition of aerosol particles in turbulent pipe flow. *Journal of Aerosol Science*, 29(8):943–959, 1998.

P. Rosin and E. Rammler. The laws governing the fineness of powdered coal. *Journal of the Institute of Fuel*, 7(1):29–36, 1933.

P.G. Saffman. The lift on a small sphere in a slow shear flow. *Journal of Fluid Mechanics*, 22(2):385–400, 1965.

B. Sagot. Thermophoresis for spherical particles. *Journal of Aerosol Science*, 65(1): 10–20, 2013.

B.L. Sawford. The basis for, and some limitations of, the Langevin equation in atmospheric relative dispersion modelling. *Atmospheric Environment*, 18(11):2405–2411, 1984.

B.L. Sawford. Lagrangian statistical simulation of concentration mean and fluctuation fields. *Journal of Climate and Applied Meteorology*, 24:1152–1166, 1985.

L. Schiller and A. Naumann. A drag coefficient correlation. *Zeitschrift des Vereins Deutscher Ingenieure*, 77:318–320, 1935.

M. Schmuecker. Einfluss von mineralstaeuben auf keramische solarabsorber. *DLR Presentation*, 2012.

G.A. Sehmel. Aerosol deposition from turbulent airstreams in vertical conduits. *AEC Research and Development Report*, 1968.

G.A. Sehmel. Particle eddy diffusivities and deposition velocities for isothermal flow and smooth surfaces. *Aerosol Science*, 4(1):125–138, 1972.

Z. Shen, G. Lin, J. Yu, Z. Bu, and C. Du. Three-dimensional numerical simulation of ice accretion at the engine inlet. *Journal of Aircraft*, 50(2):635–642, 2013.

S. Singh and D. Tafti. Predicting the coefficient of restitution for particle wall impacts in gas turbine components, GT2013-95623. *ASME Turbo Expo*, 2013.

M.R. Sippola and W.W. Nazaroff. Experiments measuring particle deposition from fully developed turbulent flow in ventilation ducts. *Aerosol Science and Technology*, 38(9):914–925, 2004.

M.R. Sippola and W.W. Nazaroff. Anisokinetic shrouded nozzle system for constant low-flow rate aerosol sampling from turbulent duct flow. *Aerosol Science and Technology*, 48(1):90–98, 2014.

S.A. Slater, A.D. Leeming, and J.B. Young. Particle deposition from two-dimensional turbulent gas flows. *International Journal of Multiphase Flow*, 29(5):721–750, 2003.

M. Sommerfeld. Analysis of collision effects for turbulent gasparticle flow in a horizontal channel: Part I. Particle transport. *International Journal of Multiphase Flow*, 29(4):675–699, 2003.

A. Suman, R. Kurz, N. Aldi, M. Morini, K. Brun, M. Pinelli, and P. Spina. Quantitative CFD analyses of particle deposition on a subsonic axial compressor blade - part I: Particle zones impact. *Journal of Turbomachinery*, 137(2):021009–021009–14, 2014a.

A. Suman, M. Morini, R. Kurz, N. Aldi, K. Brun, M. Pinelli, and P. Spina. Quantitative computational fluid dynamic analyses of particle deposition on a transonic axial compressor blade - Part II: Impact kinematics and particle sticking analysis. *Journal of Turbomachinery*, 137(2):021010–021010–12, 2014b.

A. Suman, M. Morini, R. Kurz, N. Aldi, K. Brun, M. Pinelli, and P. Spina. Estimation of the particle deposition of a subsonic axial compressor blade. *ASME Turbo Expo*, 2016.

K. Sun, L. Lu, H. Jiang, and H. Jin. Experimental study of solid particle deposition in 90° ventilated bends of rectangular cross section with turbulent flow. *Aerosol Science and Technology*, 47(2):115–124, 2013.

W. Tabakoff, R. Kotawal, and A. Hamed. Erosion study of different materials affected by coal ash particles. *Wear*, 52(1):161–173, 1979.

W. Tabakoff, M.F. Malak, and A. Hamed. Laser measurements of solid-particle rebound parameters impacting on 2024 aluminium and 6Al-4V titanium alloys. *AIAA Journal*, 25(5):721–726, 1987.

L. Talbot, R.K. Cheng, R.W. Schefer, and D.R. Willis. Thermophoresis of particles in a heated boundary layer. *Journal of Fluid Mechanics*, 101(4):737–758, 1980.

C. Taltavull, J. Dean, and T.W. Clyne. Adhesion of volcanic ash particles under controlled conditions and implications for their deposition in gas turbines. *Advanced Engineering Materials*, 18(5):803–813, 2016.

A. Taniere and B. Arcen. Prediction of a particle-laden turbulent channel flow: Examination of two classes of stochastic dispersion models. *International Journal of Multiphase Flow*, 30(1):1–10, 2014.

D.G. Thakurta, M. Chen, J.B. McLaughlin, and K. Kontomaris. Thermophoretic deposition of small particles in a direct numerical simulation of turbulent channel flow. *International Journal of Heat and Mass Transfer*, 41(24):4167–4182, 1998.

D.J. Thomson. Criteria for the selection of stochastic models of particle trajectories in turbulent flows. *Journal of Fluid Mechanics*, 180:529–556, 1987.

C. Thornton and Z. Ning. A theoretical model for the bounce/stick behaviour of adhesive, elastic-plastic spheres. *Powder Technology*, 99(1):154–162, 1998.

L. Tian and G. Ahmadi. Particle deposition in turbulent duct flows - comparisons of different model predictions. *Journal of Aerosol Science*, 38(4):377–397, 2006.

C.-J. Tsai, J.-S. Lin, S.G. Aggarwal, and D.-R. Chen. Thermophoretic deposition of particles in laminar and turbulent tube flows. *Aerosol Science and Technology*, 38 (2):131–139, 2004.

C.-J. Tsai, C.G. Lin, J.-S. nnd Deshpande, and L.C. Liu. Electrostatic charge measurement and charge neutralisation of fine aerosol particles during the generation process. *Part. Part. Syst. Charact*, 22:293–298, 2005.

TSI. Model 3450 Vibrating Orifice Aerosol Generator - operation and service manual. 2009.

TSI. Optical particle sizer model 3330. 2012.

D. Hanjali K. Venturini, P. Borello and F. Rispoli. Modelling of particles deposition in an environment relevant to solid fuel boilers. *Applied Thermal Engineering*, 49 (1):131–138, 2012.

T. Wakeman and W. Tabakoff. Measured particle rebound characteristics useful for erosion prediction, 82-GT-170. *ASME Turbo Expo*, 1982.

L. Waldmann. Uber die kraft eines inhomogen gases auf kleine suspendierte kugeln. *Z. Naturforschung*, 14(a):589599, 1959.

P.M. Walsh, A.N. Sayre, D.O. Loehden, L.S. Monroe, J.M. Beer, and A.F. Sarofim. Deposition of bituminous coal ash on an isolated heat exchanger tube: effects of coal properties on deposit growth. *Progress in Energy and Combustion Science*, 16 (4):327–345, 1990.

W.S. Walsh, K.A. Thole, and C. Joe. Effects of sand ingestion on the blockage of film-cooling holes, GT2006-90067. *ASME Turbo Expo*, 2006.

P. Webley and L. Mastin. Improved prediction and tracking of volcanic ash clouds. *Journal of Volcanology and Geothermal Research*, 186:1–9, 2009.

B. Wedd. Study of diffusion-impaction of environmental particulates in aircraft engines. *Fourth Year Project, University of Oxford*, 2014.

M.R. Wells and D.E. Stock. The effects of crossing trajectories on the dispersion of particles in a turbulent flow. *Journal of Fluid Mechanics*, 136(1):31–62, 1983.

S. Whitaker and J.P. Bons. Evaluation of elastic - plastic rebound properties of coal fly ash particles for use in a universal turbine deposition model, GT2015-43765. *ASME Turbo Expo*, 2015.

S. Whitaker, B. Peterson, A.F. Miller, and J.P. Bons. The effect of particle loading, size, and temperature on deposition in a vane leading edge impingement cooling geometry, GT2016-57413. *ASME Turbo Expo*, 2016a.

S. Whitaker, R. Prenter, and J.P. Bons. The effect of freestream turbulence on deposition for nozzle guide vanes. *Journal of Turbomachinery*, 137(12):121001, 2016b.

S.R. Wilson, L. Yuan, E.A. Matilda, and M.R. Johnson. Aerosol deposition measurements as a function of Reynolds number for turbulent flow in a ninety-degree pipe bend. *Aerosol Science and Technology*, 45(3):364–375, 2011.

N.D. Wood. A simple method for the calculation of turbulent deposition to smooth and rough surfaces. *Journal of Aerosol Science*, 12(3):275–290, 1981.

Z. Wu and J.B. Young. The deposition of small particles from a turbulent air flow in a curved duct. *International Journal of Multiphase Flow*, 44(1):34–47, 2012.

S. Wylie, A. Bucknell, P.R. Forsyth, M. McGilvray, and D.R.H. Gillespie. Reduction in flow parameter resulting from volcanic ash deposition in engine-representative cooling passages, GT2016-57296. *ASME Turbo Expo*, 2016.

S. Wylie, A. Bucknell, P.R. Forsyth, M. McGilvray, and D.R.H. Gillespie. Reduction in flow parameter resulting from volcanic ash deposition in engine-representative cooling passages. *Journal of Turbomachinery*, 139(3):031008–13, 2017.

S. Yamamoto, I. Ohno, and O.L. Anderson. High temperature elasticity of sodium chloride. *Journal of Physics and Chemistry of Solids*, 48(2):143–151, 1987.

J. Young and A. Leeming. A theory of particle deposition in turbulent pipe flow. *Journal of Fluid Mechanics*, 340:129–159, 1997.

J.B. Young. Thermophoresis of a spherical particle: Reassessment, clarification, and new analysis. *Aerosol Science and Technology*, 45(8):927–948, 2011.

M. Yudine. Physical considerations on heavy-particle diffusion. *Advances in Geophysics*, 6(1):185–191, 1959.

Z. Zhang and Q. Chen. Experimental measurements and numerical simulations of particle transport and distribution in ventilated rooms. *Atmospheric Environment*, 40(18):3396–3408, 2006.

F. Zonta, C. Marchioli, and A. Soldati. Particle and droplet deposition in turbulent swirled pipe flow. *International Journal of Multiphase Flow*, 56(1):172–183, 2013.

Further Publications

In addition to the papers published relating to the DPhil topic, the author has either written or contributed to four further papers regarding turbine blade cooling (own fourth year project), and volcanic ash blockage of film-cooling holes (fourth year project support).

Turbine blade rib turbulated internal cooling

P.R. Forsyth, M. McGilvray, and D.R.H. Gillespie. Secondary flow and heat transfer coefficient distributions in the developing flow region of ribbed turbine blade cooling passages,. *Experiments in Fluids*, 58(1), 2017c

P.R. Forsyth, M. McGilvray, and D.R.H. Gillespie. Secondary flow and heat transfer coefficient distributions in the developing flow region of ribbed turbine blade cooling passages, GT2014-26737. *ASME Turbo Expo*, 2014

Volcanic ash deposition experiments

S. Wylie, A. Bucknell, P.R. Forsyth, M. McGilvray, and D.R.H. Gillespie. Reduction in flow parameter resulting from volcanic ash deposition in engine-representative cooling passages. *Journal of Turbomachinery*, 139(3):031008–13, 2017

S. Wylie, A. Bucknell, P.R. Forsyth, M. McGilvray, and D.R.H. Gillespie. Reduction in flow parameter resulting from volcanic ash deposition in engine-representative cooling passages, GT2016-57296. *ASME Turbo Expo*, 2016